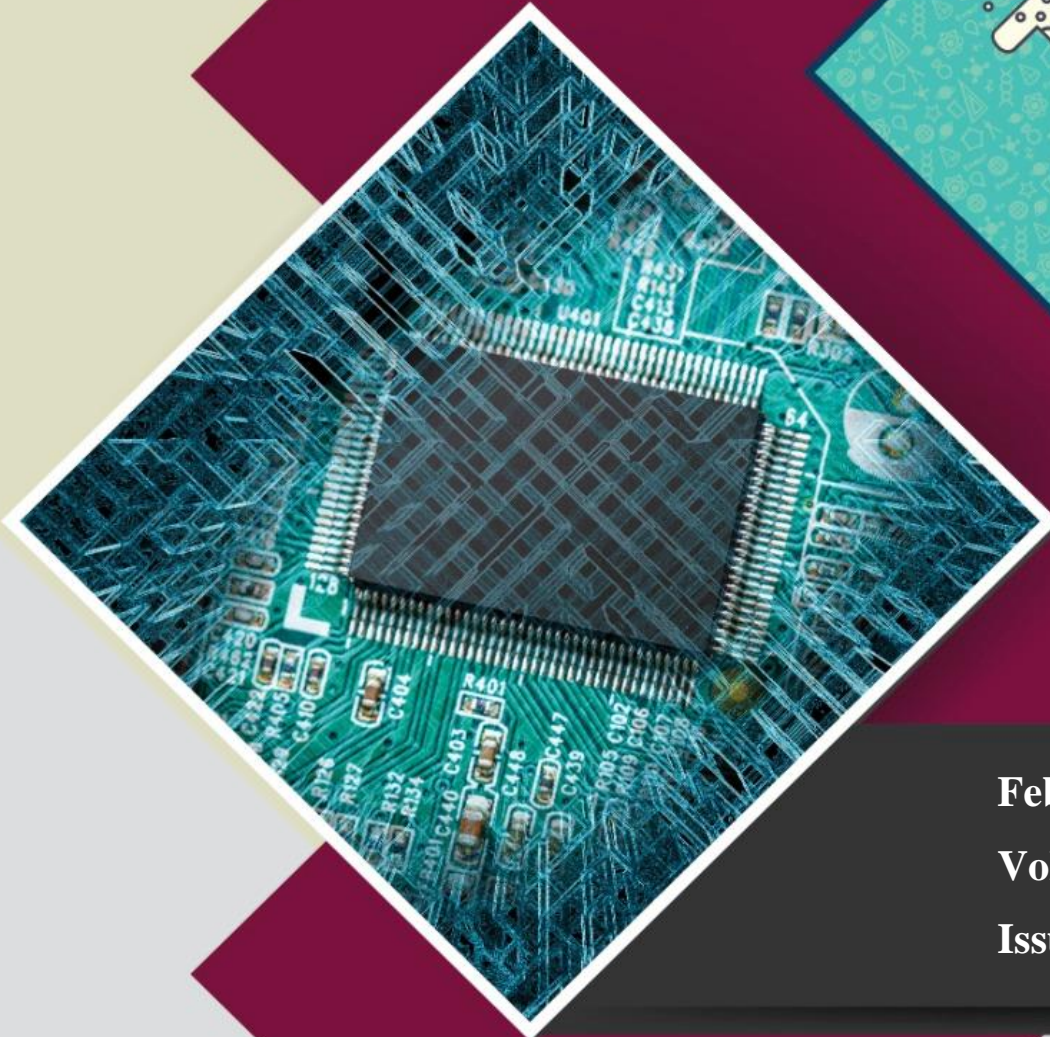


e-ISSN: 2822-2881



FUJECE

Firat University Journal of Experimental and Computational Engineering



February : 2025

Volume : 4

Issue : 1



<https://dergipark.org.tr/tr/pub/fujece>

Owner

On Behalf of Firat University

Rector

Prof. Dr. Fahrettin GÖKTAŞ

Editor-in-Chief

Prof. Dr. Mehmet YILMAZ, Firat University, Türkiye

Vice Editor-in-Chief

Prof. Dr. Ebru AKPINAR, Firat University, Türkiye

Prof. Dr. Ragıp İNCE, Firat University, Türkiye

Prof. Dr. Mete Onur KAMAN, Firat University, Türkiye

Assoc. Prof. Dr. Erkut YALÇIN, Firat University, Türkiye

Editorial Advisory Board

Prof. Dr. Yakup DEMİR, Firat University, Türkiye

Prof. Dr. Levent TAŞÇI, Firat University, Türkiye

Prof. Dr. Abdussamet ARSLAN, Gazi University, Türkiye

Prof. Dr. Ahmet ŞAŞMAZ, Firat University, Türkiye

Prof. Dr. Abdulkadir Cuneyt AYDIN, Atatürk University, Türkiye

Prof. Dr. Fatih CETİŞLİ, Pamukkale University, Türkiye

Prof. Dr. Bilal ALATAŞ, Firat University, Türkiye

Prof. Dr. Erhan AKIN, Firat University, Türkiye

Prof. Dr. Erkan KÖSE, Nuh Naci Yazgan University, Türkiye

Prof. Dr. Filiz KAR, Firat University, Türkiye

Prof. Dr. Hasan SOFUOĞLU, Karadeniz Technical University, Türkiye

Prof. Dr. Özge Kaya HANAY, Firat University, Türkiye

Prof. Dr. Yusuf AYVAZ, Yıldız Technical University, Türkiye

Prof. Dr. M. Şaban TANYILDIZI, Firat University, Türkiye

Doç. Dr. Tacettin GEÇKİL, İnönü University, Türkiye

Doç. Dr. José NORAMBUENA-CONTRERAS, Bio Bio University, Chile

Res. Assist. Dr. Ulaş Baran BALOĞLU, University of Bristol, England

Editorial Board

Prof. Dr. Mehmet YILMAZ (Editor-in-Chief)	Civil Engineering (Firat University)
Prof. Dr. Ebru AKPINAR (Vice Editor-in-Chief)	Mechanical Engineering (Firat University)
Prof. Dr. Ragıp İNCE (Vice Editor-in-Chief)	Civil Engineering (Firat University)
Prof. Dr. Mete Onur KAMAN (Vice Editor-in-Chief)	Mechanical Engineering (Firat University)
Assoc. Prof. Dr. Erkut YALÇIN (Vice Editor-in-Chief)	Civil Engineering (Firat University)
Prof. Dr. Ali TOPAL	Civil Engineering (Dokuz Eylul University)
Prof. Dr. Ali YAZICI	Software Engineering (Atilim University)
Prof. Dr. Ayşe Vildan BEŞE	Chemical Engineering (Atatürk University)
Prof. Dr. Bilge Hilal CADIRCI EFELİ	Bioengineering (Tokat Gaziosmanpasa University)
Prof. Dr. Kadir TURAN	Mechanical Engineering (Dicle University)
Prof. Dr. H. Soner ALTUNDOĞAN	Bioengineering (Firat University)
Prof. Dr. Mehmet Deniz TURAN	Metallurgy and Materials Eng. (Firat University)
Prof. Dr. Mustafa YANALAK	Geodesy and Photog. Eng. (Istanbul Tech. Univ.)
Prof. Dr. Nuno MENDES	Mechanical Engineering (University of Minho)
Prof. Dr. Rashid NADİROV	Chemical (Al-Farabi Kazakh National University)
Prof. Dr. Serdar Ethem HAMAMCI	Electrical-Electronics Engineering (İnönü Univ.)
Prof. Dr. Selçuk ALEMDAĞ	Geological Engineering (Gümüşhane University)
Prof. Dr. Mehmet KARAKÖSE	Computer Engineering (Firat University)
Prof. Dr. Alvaro Garcia HERNANDEZ	Civil Engineering (RWTH Aachen University)
Prof. Dr. Ömür GÖKKUŞ	Environmental Eng. (Sivas Cumhuriyet Univ.)
Assoc. Prof. Dr. Fatih DEMİR	Software Engineering (Firat University)
Lecturer Batuhan SELVİ (Language Editor)	English Language Teaching (Firat University)
Mustafa Gani GENÇER (Language Editor)	English Language Teaching (Firat University)
Res. Assist. Dr. Özge Erdoğan YAMAÇ (Secretariat)	Civil Engineering (Firat University)
Res. Assist. Beyza Furtana YALÇIN (Pub. Coordinators)	Civil Engineering (Firat University)
Ahmet BAL (Layout Editor)	Social Studies Education (Firat University)

Composition

Ahmet BAL

Correspondence Address

Firat University Faculty of Engineering Journal of Experimental and Computational Engineering Publishing

Coordinatorship

23119 Elazığ/TÜRKİYE

E-mail: fujece@firat.edu.tr

Web page: <http://fujece.firat.edu.tr/>

Firat University Journal of Experimental and Computational Engineering a peer-reviewed journal.

CONTENTS

Recommending Tolerance Value for SpO ₂ Devices with Linear Regression Based on Measuring Tape (Research Article) SpO ₂ Cihazlarında Ölçüm Bandına Göre Lineer Regresyon ile Tolerans Değeri Önerilmesi (Araştırma Makalesi) Özge ÜSTÜNER, Cafer BUDAK	1
Accurate Indoor Home Location Classification through Sound Analysis: The 1D-ILQP Approach (Research Article) Ses Analizi Yoluyla Doğru Ev İçi Konumu Sınıflandırması: 1D-ILQP Yaklaşımı (Araştırma Makalesi) Nura ABDULLAHI, Erhan AKBAL, Şengül DOĞAN, Türker TUNCER, Umut ERMAN	12
Covariance Estimation Of Millimeter Wave Channels Using Sparse Signal Recovery Algorithms In A Hybrid MIMO Architecture (Research Article) Karma Mimarideki Çok-Girişli Çok-Çıkışlı Sistemde Seyrek Sinyal Geriçatım Yöntemlerini Kullanarak Milimetrik Dalga Kanalı Uzamsal Kovaryansının Kestirilmesi (Araştırma Makalesi) Rıfat Volkan ŞENYUVA	30
Design and Experimental Validation Of FPGA Based Digital Control Scheme Of The Nearest Level Modulation Method For Modular Multilevel Converter Topology (Research Article) Modüler Çok Seviyeli Dönüştürücü Topolojisi İçin En Yakın Seviye Modülasyon Yönteminin FPGA Tabanlı Dijital Kontrol Şemasının Tasarımı ve Deneysel Doğrulaması (Araştırma Makalesi) Mehmet KURTOĞLU, Fatih EROĞLU, Ahmet Mete VURAL	44
Investigating Impact of Current Pulse Waveform and Simulation Frequency on Deep Brain Stimulation (Research Article) Elektriksel Akım Dalgasının and Frekansının Derin Beyin Stimülasyonu Üzerindeki Etkisinin Araştırılması (Araştırma Makalesi) Enver SALKIM	59
Interaction Prediction on BACE-1 Inhibitors Data for Alzheimer Disease using Message Passing Neural Network (Research Article) Mesaj Aktarma Sinir Ağını Kullanarak Alzheimer Hastalığı için BACE-1 İnhibitörleri Verilerine İlişkin Etkileşim Tahmini (Araştırma Makalesi) Suat TORAMAN, Bihter TAŞ	72
Fault Detection in Steel Belts of Tires Using Magnetic Sensors and Different Deep Learning Models (Research Article) Manyetik Sensörler ve Farklı Derin Öğrenme Modelleri Kullanarak Lastiklerin Çelik Kayışlarındaki Arıza Tespiti (Araştırma Makalesi) Sercan YALÇIN	85
Optimizing Unmanned Vehicle Navigation: A Hybrid PSO-GWO Algorithm for Efficient Route Planning (Research Article) İnsansız Araç Navigasyonunun Optimize Edilmesi: Verimli Rota Planlaması için Hibrit PSO-GWO Algoritması (Araştırma Makalesi) Gökhan ALTUN, İlhan AYDIN	100
Investigation of Compressive Strength and Energy Absorption of Cylinder Corrugated Sandwich Structures with Different Geometric Configurations (Research Article) Farklı Geometrik Konfigürasyonlara Sahip Silindir Oluklu Sandviç Yapıların Basma Mukavemetlerinin ve Enerji Emiliminin İncelenmesi (Araştırma Makalesi) İlyas BOZKURT	115
Investigation of Fragmentation and Abrasion Resistance of Basalt and Limestone Aggregates in Bitlis Region and the Relationship between MgSO ₄ and Flatness Index Values (Research Article) Bitlis Yöresindeki Bazalt ve Kireçtaşı Agregalarının Parçalanma ve Aşınma Direncinin Araştırılması ve MgSO ₄ ile Yassılık İndeksi Değerleri Arasındaki İlişkinin İncelenmesi (Araştırma Makalesi) Alev AKILLI EL	136

Short-Term Wind Speed Forecasting With Deep Learning (Research Article) Derin Öğrenme ile Kısa Vadeli Rüzgar Hız Tahmini (Araştırma Makalesi) Fatih KARAASLAN, Zeynep Mine ALÇİN, Muzzaffer ASLAN	151
Insights Into Air Pollution Dynamics and Quality: A Comprehensive Analysis Of Scholarly Research In Türkiye (Research Article) Hava Kirliliği Dinamikleri ve Kalitesine İlişkin İçgörüler: Türkiye'deki Akademik Araştırmaların Kapsamlı Bir Analizi (Araştırma Makalesi) Saliha ÇELİKCAN BİLGİN, Turgay Tugay BİLGİN	163
Examination of Lane Capacity at Fully Actuated Intersections (Research Article) Tam Denetimli Kavşaklarda Şerit Kapasitesinin İncelenmesi (Araştırma Makalesi) Nihat Can KARABULUT, Murat ÖZEN, Oruç ALTINAŞI	182
Machine Learning-Based Detection of Non-Technical Losses in Power Distribution Networks (Research Article) Dağıtım Şebekelerinde Teknik Olmayan Kayıpların Makine Öğrenme Yöntemleriyle Tespiti (Araştırma Makalesi) Mahmut TÜRK, Cem HAYDAROĞLU, Heybet KILIÇ	192
Predicting Three-Dimensional (3D) Printing Product Quality with Machine Learning-Based Regression Methods (Research Article) Makine Öğrenmesi Tabanlı Regresyon Metotları ile Üç Boyutlu (3B) Baskı Parça Kalitesinin Tahmini (Araştırma Makalesi) Ahmet Burak TATAR	206



SpO₂ Cihazlarında Ölçüm Bandına Göre Lineer Regresyon ile Tolerans Değeri Önerilmesi

Özge ÜSTÜNER^{1*}, Cafer BUDAK²

^{1,2}Elektrik-Elektronik Mühendisliği, Fen Bilimleri Enstitüsü, Dicle Üniversitesi, Diyarbakır, Türkiye.
¹ozgeustuner96@gmail.com, ²cafer.budak@dicle.edu.tr

Geliş Tarihi: 27.01.2024
Kabul Tarihi: 25.04.2024

Düzeltilme Tarihi: 10.03.2024

doi: <https://doi.org/10.62520/fujece.1426492>
Araştırma Makalesi

Alıntı: Ö. Üstüner ve C. Budak, "SpO₂ cihazlarında ölçüm bandına göre lineer regresyon ile tolerans değeri önerilmesi", Fırat Üni. Deny. ve Hes. Müh. Derg., vol. 4, no 1, pp. 1-11, Şubat 2025.

Öz

Kandaki oksijen değerinin izlenebilmesi, bronşit, zatürre, KOAH gibi çeşitli solunum yolu hastalıklarının ve COVID-19 hastaları da dahil olmak üzere kritik bakım hastalarının takibi için hayati önem taşımaktadır. SpO₂ cihazları, parmak ya da kulak memesi dokusundan alınan ölçümlerle kandaki oksijen yüzdesini hesaplayan tıbbi cihazlardır. Yapılan saha çalışmalarında edinilen izlenimler; cihaz kullanıcılarının, düşük oksijen saturasyonuna sahip hastalardan alınan ölçümlerde yüksek sapma görüldüğünü ve SpO₂ cihazı ölçümlerinin kusurlu olduğu izleniminde olduklarını sıklıkla belirtmeleri göz önünde bulundurularak, ölçümlerin doğru yorumlanabilmesi için bu çalışma gerçekleştirilmiştir. Bu çalışmada SpO₂ cihazlarının farklı ölçüm bantlarındaki % SpO₂ oranları makine öğrenmesinde lineer regresyon algoritması ile yorumlanarak kalite sınıflandırması yapılmış ve kullanıcılara her ölçüm bandı için tolerans değerleri ve göz önünde bulundurulması gereken sapma değerleri önerilmiştir. Ayrıca lineer regresyon yöntemi ile daha az veri kullanılarak sonuç tahmini ile kullanıcıya ve test uzmanına zaman kazandırarak daha çok cihazın izlenmesi ve cihazların daha sık test edilebilmesi hedeflenmiştir. Tahmin sonuçlarının gerçek değere çok yakın sonuçlar verdiği gözlemlenmiş ve bu çalışmanın testin sahada daha sık uygulanabilmesine ve hızlı yorumlanabilmesine katkı sağlayacağı öngörülmüştür. Çalışmada 80601-2-61 sayılı Avrupa standardının 201.12.1.101 sayılı maddesinde önerilen yöntem kullanılarak farklı üç marka pulse oksimetre cihazından; Contec marka MS100 model simülatör kullanılarak %70-79 SpO₂, %80-89 SpO₂, %90-100 SpO₂ olmak üzere üç ölçüm bandında ölçümler alınmıştır. Her ölçüm için lineer regresyon ile A_{rms} eğrisi grafiği oluşturulmuş, ortalama hata değerlerinin karesi (MSE) ve A_{rms} değerleri hesaplanarak iki değer arasındaki ilişkinin yorumlanmasıyla cihazların değerlendirilmesi gerçekleştirilmiştir. Sonuç olarak düşük oksijen saturasyonu seviyelerinde sapma oranının arttığı gözlemlenmiş ve her ölçüm bandı ve farklı kalitede cihazlar için göz önünde bulundurulması gereken %spo₂ sapma değeri önerilmiştir.

Anahtar kelimeler: SpO₂, Pulse oksimetre, Oksijen saturasyonu, A_{rms} , Lineer regresyon

*Yazışılan yazar

İntihal Kontrol: Evet – Turnitin

Şikayet: fujece@firat.edu.tr

Telif Hakkı ve Lisans: Dergide yayın yapan yazarlar, CC BY-NC 4.0 kapsamında lisanslanan çalışmalarının telif hakkını saklı tutar.



Recommending Tolerance Value for SpO₂ Devices with Linear Regression Based on Measuring Tape

Özge ÜSTÜNER^{1*} , Cafer BUDAK² 

^{1,2}Electrical and Electronics Engineering, Institute of Science and Technology, Dicle University, Diyarbakır, Turkey.
¹ozgeustuner96@gmail.com, ²cafer.budak@dicle.edu.tr

Received: 27.01.2024
Accepted: 25.04.2024

Revision: 10.03.2024

doi: <https://doi.org/10.62520/fujece.1426492>
Research Article

Citation: Ö. Üstüner and C. Budak, "Recommending tolerance value for spo₂ devices with linear regression based on measuring tape", *Firat Univ. Jour. of Exper. and Comp. Eng.*, vol. 4, no 1, pp. 1-11, February 2025.

Abstract

Monitoring blood oxygen levels is vital for tracking various respiratory diseases like bronchitis, pneumonia, COPD, and critical care patients, including those with COVID-19. SpO₂ devices, calculating oxygen percentage via finger or earlobe tissue, play a crucial role. Field studies have revealed concerns regarding the accuracy of SpO₂ measurements due to high deviations, particularly in patients with low oxygen saturation, prompting the initiation of this study to ensure accurate interpretation of the device's measurements. Using a linear regression algorithm, SpO₂ values from different bands were classified for quality. Tolerance values and deviation thresholds for each band were recommended. Additionally, linear regression aimed to save time by making result estimations with less data, facilitating more device monitoring and frequent testing. Results closely matched actual values, suggesting contributions to more frequent application and rapid interpretation. Following the European standard 80601-2-61, measurements were taken from three pulse oximeter brands (Contec MS100 model simulator) in three bands: 70-79%, 80-89%, and 90-100% SpO₂. For each measurement, an Arms curve graph was generated using linear regression, and the mean square error (MSE) and A_{rms} values were calculated to evaluate devices. In conclusion, deviation rates increase at low oxygen saturation levels, and recommended % SpO₂ deviation values were proposed for each band and device quality.

Keywords: SpO₂, Pulse oximetry, Oxygen saturation, A_{rms} , Linear regression

*Corresponding author

Plagiarism Checks: Yes – Turnitin

Complaints: fujece@firat.edu.tr

Copyright & License: Authors publishing with the journal retain the copyright to their work licensed under the CC BY-NC 4.0

1. Introduction

Oxygen saturation is an important measure for understanding the working capacity of the lung and for early detection of oxygen deficiency. The lungs first transfer oxygen to the capillaries, the oxygen mixed into the blood is sent to the heart and from the heart it is distributed to all organs that are supplied with oxygen. Since disruption in this cycle affects organs and therefore vital functions, monitoring oxygen saturation is extremely important. In a healthy person, oxygen saturation is between 95% and 100%. A drop in oxygen levels causes hypoxemia. Oxygen levels below 90% are considered low, and when they fall below 80%, they indicate severe hypoxemia, i.e. respiratory failure. Oxygen saturation is monitored during the diagnosis and treatment of many respiratory and chest diseases such as respiratory failure, pneumonia, bronchitis, covid-19, pneumothorax, smoking-related chest diseases [6-8, 19, 20, 29]. Pulse oximetry devices, which have started to be used for instant monitoring of oxygen saturation and pulse rate in surgical interventions, have been used for the last decade in monitoring the treatment processes of respiratory diseases, general condition monitoring of intensive care patients, and monitoring of patients treated in emergency and general wards [1, 3, 22, 23, 24, 27]. Due to the Covid-19 outbreak, the use of pulse oximetry devices has become widespread since the World Health Organization declared a pandemic in March 2020. Pulse oximetry devices are devices that examine oxygen saturation by recording the absorption rate of 600nm red light and 940nm infrared light by hemoglobin in the blood [10, 28]. The use of a non-invasive (non-surgical) measurement method and its low cost have made pulse oximetry devices easily accessible to users and easily usable for home care [19, 20]. However, despite the ease of use, clinical competence and knowledge of the technical features of the device are required for correct interpretation of the measurement results [2].

In Thomas Paul Walters' study of the impact of pulse oximeters in clinical practice, he conducted a literature review between 1980 and 2006 and found that nurses and physicians lacked the necessary level of knowledge about using pulse oximeters. Walters assessed the adequacy of the information obtained by speed reading and suggested that future research should be conducted to evaluate this information for clinical competence [3]. In a similar study, Malcom Elliott et al. reported that nurses, physicians and allied health personnel who frequently use the device have significant knowledge gaps and, worryingly, there are senior and experienced clinicians among them [4]. Bader conducted a questionnaire study with 50 participants, including nurses, physician assistants and respiratory therapists, and as a result of the analysis, the participants stated that there was a lack of knowledge in general principles, and as a result of the study, he stated that healthcare professionals need training on the basic working principles of pulse oximetry [26]. Kiekkas et al. observed that intensive care nurses had more correct answers compared to emergency nurses in their survey study with 207 participants and associated pulse oximetry device knowledge with longer experience and being an intensive care worker [23]. Jamieson et al. applied a questionnaire to healthcare personnel working in the neonatal service and stated that the participants had a significant lack of knowledge about the use of pulse oximetry and therefore, there was a need for continuous training on pulse oximetry devices [5]. Since the oxygen saturation value will affect the planning of the treatment process, it is very important to interpret it correctly. In case of low oxygen level, drug therapy, oxygen therapy, ventilation and mechanical ventilation methods may need to be applied depending on the patient's condition in order to provide the required oxygen level to the blood. For this reason, health personnel should not be in conflict with the oxygen saturation value during the diagnosis and treatment process [12].

In 2022, at a medical conference in Canada, M. Blanchet and colleagues shared the results of their research on 6 different brands of SpO₂ devices, but the results only contain summary information and are based on measurements taken from patients. In 2023, Giuliano et al. examined SpO₂ results in 28 healthy adult volunteers with 3 different brands of spo₂ devices under motion dysfunction and low perfusion. The fact that the results were not obtained with a reference device of known accuracy and were not obtained according to an international standard reduces the reliability rate [9, 17].

In order to evaluate the accuracy and effectiveness of pulse oximetry devices, the use of which has become more frequent with the Covid-19 pandemic; "Anesthesiology and Respiratory Therapy Devices Panel Medical Devices Advisory Board Meeting" was held on November 1, 2022 by the Food and Drug Administration (FDA) of the United States Ministry of Health. As a result of the panel, where experts in the

field took part and gave opinions and suggestions; FDA recommended to comply with the standard ISO 80601-2-61:2017 for the evaluation of the effectiveness of pulse oximetry devices [15, 16, 18].

Since the application of the tests included in the European Standard recommended by the FDA is not possible to be performed by healthcare personnel in the field due to the lack of technical competence and equipment required for the test, in this study, the % SpO₂ ratios of oxygen saturation measurement devices in the 70-79% SpO₂, 80-89% SpO₂, 90-100% SpO₂ measurement bands were examined and the deviation values to be considered for each measurement band were suggested to the device users. It is aimed to eliminate the uncertainties caused by user interpretation by predicting the results with linear regression. In the experimental phase of the study, Contec brand, MS100 model simulator device, which can perform SpO₂ and pulse rate simulation, was used in accordance with the test applications specified in the standard. Measurements were taken from three different brands of pulse oximeters that are widely used, these measurements were recorded and a measurement graph was created for each measurement by the method specified in the standard, and Arms and MSE values were recorded by applying linear regression algorithm to the measurements. As a result, in addition to the known factors such as dark skin and skin pigmentation, dark nail polish and artificial nails, probe placement, signal quality, medical residues such as blood etc. remaining on the sensor, the effect of the range of measurement results and the differences that may arise from sensor quality on the measurement accuracy was emphasized.

2. Materials and Methods

The basic physical property of the pulse oximeter is based on the Beer-Lambert law. According to Beer-Lambert's law, light passing through a solution is logarithmically inversely proportional to the path of light through the solution and the concentration of the solution, and directly proportional to the amount of light absorbed. For the two wavelengths of light of the pulse oximeter, red and near infrared light, the absorption rates of oxygenated hemoglobin and non-oxygenated hemoglobin are different. In general, pulse oximetry devices consist of an LED diode emitting light at two different wavelengths and a light detector (sensor) that senses the light in the opposite direction. Oxygen saturation is measured through a translucent region of the human body placed between the led light region and the sensor region [19, 20, 10].

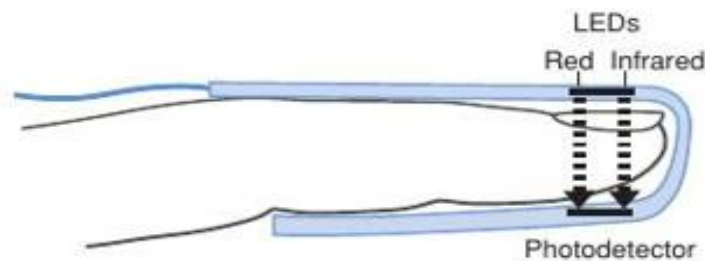


Figure 1. Finger-type pulse oximetry sensor [10]

One of the two LED diodes on the pulse oximeter device has red light at 660 nm wavelength and the other has infrared light at 940 nm wavelength. The absorption rates of these two different wavelengths of light by oxyhemoglobin (oxygenated hemoglobin) and deoxyhemoglobin (deoxygenated hemoglobin) are very different. The ratio of the difference in absorption between oxyhemoglobin and deoxyhemoglobin is calculated and compared with direct measurement of arterial oxygen to estimate peripheral oxygen saturation [19, 10].

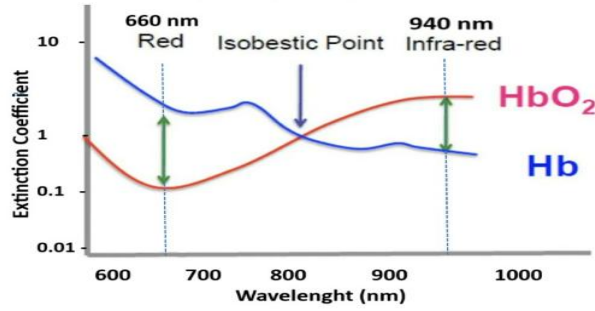


Figure 2. Hemoglobin light spectroscopy curve. (Black curve represents oxyhemoglobin, blue curve represents deoxyhemoglobin. The two vertical sections mark the wavelength points used in LEDs.) [10]

To apply the measurement accuracy test recommended in clause 201.12.1.101 of the European standard 80601-2-61 to the pulse oximetry device, a Contec, MS100 model SpO₂-pulse simulator with a SpO₂ range of 35-100% and a SpO₂ resolution of 1% was used.



Figure 3. Experiment-measurement setup

With the simulator device, which has four different light interference options: daylight, 50 Hz interference light, 60 Hz interference light and normal light source and has an amplitude setting in the range of 0.000-20.000%, measurements were made in the range of 70-100% SpO₂ with normal light source interference and 3.000% automatic amplitude setting [13].

With the test setup shown in Figure 3, the " SpO₂ accuracy test" in clause 201.12.1.101 of the ISO 80601-2-61:2017 standard recommended by the FDA was applied to three different brands of commonly used pulse oximetry devices. For the test setup described in the standard, the measurement points should consist of 31 measurement points ranging from 70% SpO₂ to 100% SpO₂ in 1% SpO₂ steps. At each measurement point set on the simulator device, the actual measurement results from the pulse oximeter device should be recorded and the deviation between the value set on the simulator (reference) device and the measurement value from the tested (pulse oximeter) device should be calculated and recorded. Arms values were calculated using the recorded deviation values and the accuracy value calculation equation [18].

$$A_{rms} = \sqrt{\frac{\sum_{i=1}^n (SpO2i - SRi)^2}{n}} \quad (1)$$

The A_{rms} (accuracy.root-mean-square difference) value calculated for the equation given in CC.2.5 of the standard should be ≤ 4% SpO₂ and the measurement results should form a linear curve as stated in CC.2.2 of

the standard under the heading 'effects of offset linearity errors'. [18] Considering the requirement that the measurement results should form a linear curve according to the standard, it is observed that the measurement results are suitable for the evaluation of the machine learning to be estimated with the linear regression algorithm application.

Linear regression is one of the machine learning algorithm methods that predicts the dependent variable by modeling the relationship between a dependent variable and an independent variable. [11] In the model, the set values in the measurements represent the independent variable and the actual measurement values represent the dependent variable to be predicted.

An example of the measurement records is given in figure 4 and examples of the obtained measurement results and linear curve graphs for 3 different devices of high, medium and low quality are given in figure 6, figure 7 and figure 8 under the heading "Experimental Results".

3. Experimental Results

Table 1. Example of measurement record

	First Measuring Band %70-79									Second Measuring Band %80-89									Third Measuring Band %90-100												
SET value (simulator device)	70	71	72	73	74	75	76	77	78	79	80	81	82	83	84	85	86	87	88	89	90	91	92	93	94	95	96	97	98	99	100
measurement value (pulse oximeter)	64	65	66	68	69	70	71	73	73	75	76	77	79	79	81	81	83	84	85	87	87	89	90	92	93	94	96	97	98	99	100
Deviation value	-6	-6	-6	-5	-5	-5	-5	-4	-5	-4	-4	-4	-3	-4	-3	-4	-3	-3	-3	-2	-3	-2	-2	-1	-1	-1	0	0	0	0	0

Table 1 shows a sample record of the measurements taken in the SpO₂ accuracy test application. By calculating the deviation values for each measurement value, the accuracy value expressed in the Arms equation was calculated and it was seen that the Arms value was 3.58 SpO₂ for the measurement values given in Table 1. It is seen that the Arms value obtained meets the ≤4% SpO₂ requirement for SpO₂ accuracy. When the accuracy curve of the measurement records is examined, it is seen that the linear curve condition required in the standard is also met. The graph of the Spo2 accuracy curve of the measurements in Table 1 is given in Figure 4.

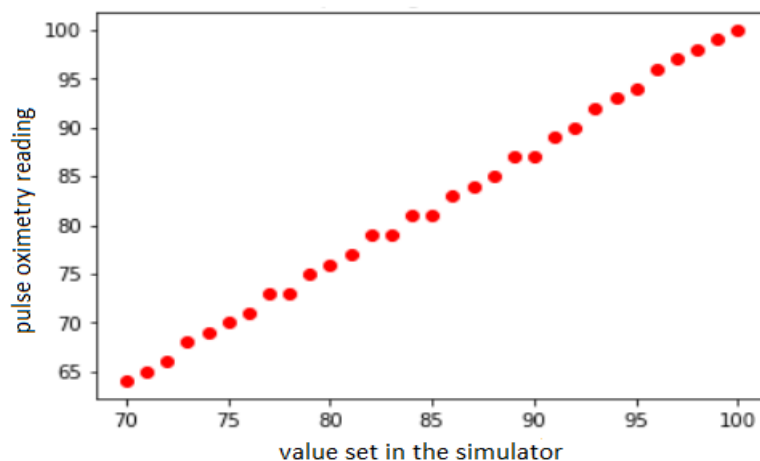


Figure 4. Linear curve plot of measurement data

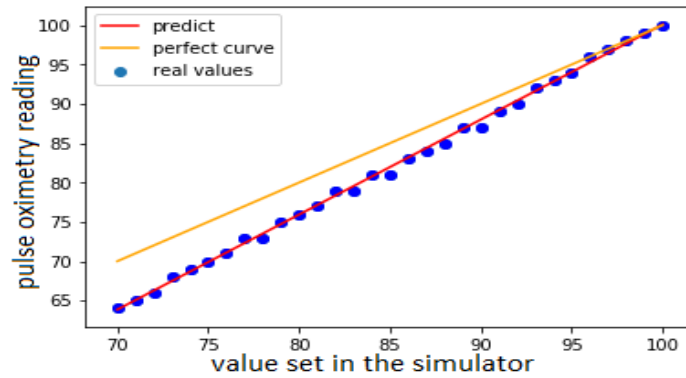


Figure 5. Example graph from a low quality device

A comparison of the curve of the predictions obtained by linear regression, the actual measurement values and the perfect curve in the absence of drift for the low quality device, for which the measurement record example is given in table 1, is given in Figure 5.

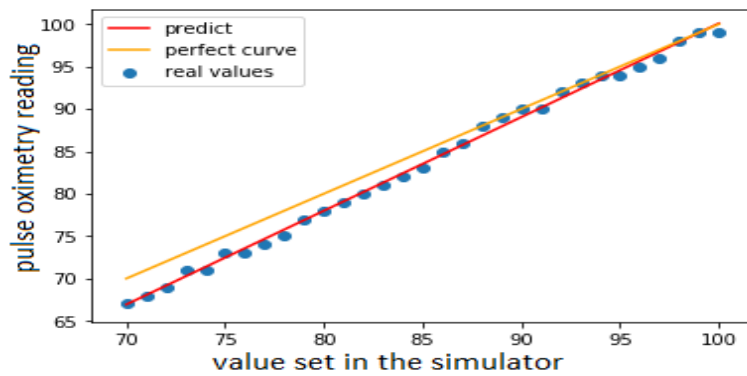


Figure 6. Example graph from a medium quality device

A comparison of the curve of predictions obtained by linear regression for a measurement from a medium quality device, the actual measurement values and the perfect curve in the absence of drift is given in Figure 6.

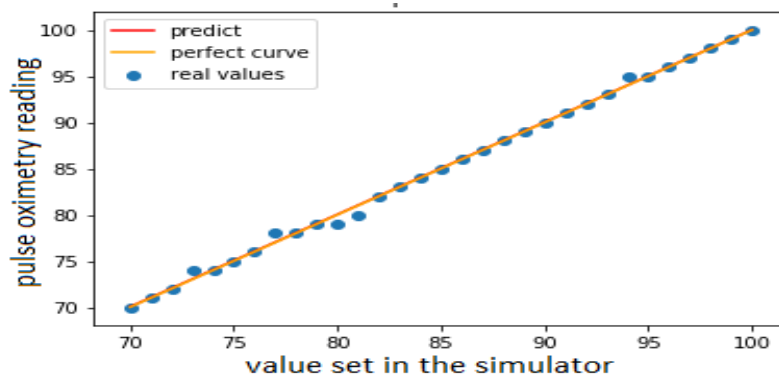


Figure 7. Example graph from a high quality device

A comparison of the curve of predictions obtained by linear regression for a measurement from a high quality instrument, the actual measurement values and the perfect curve in the absence of drift is given in Figure 7.

Table 2. Example of measurement record

	Low Quality Device (standard measurement)	Medium Quality Device (standard measurement)	High Quality Device (standard measurement)	Low Quality Device (10 Point measurement)
MSE Value	0,567	0,224	0,160	0,218
Arms Value	3,583	1,849	0,402	3,580

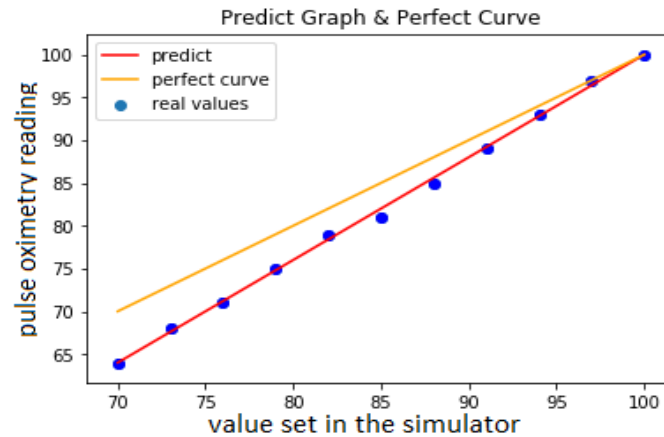


Figure 8. Prediction curve obtained with measurements from only 10 points

For the measurement results given in Table 1 (measurement from low quality device), only 10 measurement points were measured and the measurement results and prediction curve in Figure 8 were obtained. The comparison of the MSE values obtained for the 10 measurement points shown in Figure 8 with the MSE values obtained with the standard measurement is given in Table 2.

4. Results

When the measurement results were evaluated over different measurement bands in the measurements taken from three different brands of commonly used devices, it was observed that the deviation values in the lowest measurement band (70-79% SpO₂) found ~ 6% SpO₂ values, while the deviation values in the middle level measurement band (80-89% SpO₂) found ~ 4% SpO₂ values. In the measurement band with high oxygen saturation levels (90-100% SpO₂), it was observed to be less than 2% SpO₂. These results are the maximum values that can be tolerated in devices that comply with the standard observed in low quality devices with maximum deviation values.

It was observed that each device may show different deviation values depending on the sensor quality of the device and linear regression method was applied to predict the device measurement results in order to predict this by the user and to interpret the results correctly. In this study, by estimating the sensitivity of the device according to the MSE value calculated in the measurement results, the results that can be distributed according to the order of importance within the hospital, reduce the user's margin of error by estimating the deviation values of the devices and help the user to make healthier evaluations have been tracked. Although the sensitivities of different brands of devices make a difference in the measurements, the user will be able to make a healthier evaluation by considering the response of the devices under different measurement conditions by getting to know the devices more closely with the evaluation of the measurement results. When devices are classified according to sensor quality and MSE ratios are taken into account, it is predicted that the possibility of misdiagnosis of the monitored patient, such as severe hypoxemia instead of low saturation caused by the device, will be greatly reduced. Apart from the differences between the devices, the user will be able to make a healthier evaluation process by monitoring the points where the deviation from the actual

value increases with the change in the measurement values (change in the measurement bands) in the same device.

When the prediction values made with the measurement results taken from only 10 points for the same device are compared with the actual measurement values, it is observed that the predictions made with the linear regression method give very close values with fewer measurements. This study will provide an advantage in terms of monitoring more devices and testing devices more frequently by saving time for the user or tester while measuring the devices used in the field.

5. Discussion

A literature review of the studies conducted between 2006 and 2023 on the use of pulse oximetry device and its effects on diagnosis and treatment shows that healthcare professionals do not have sufficient knowledge about the use of pulse oximetry device, while the FDA has directed users to the ISO 80601-2-61 standard, which covers certain features for the required performance and basic safety of the pulse oximetry device in order to know the accuracy of the pulse oximetry device. The studies conducted do not provide efficient results for informing healthcare personnel working in the field and using the pulse oximetry device effectively. Observations made during field studies also revealed that health personnel were unable to correctly interpret the measurement differences between different brands of devices, and that there was a need for training on the use of devices and interpretation of results.

With the development of technology and the spread of epidemics, the usage area and need for SpO₂ devices are increasing and the variety of different brands is increasing in this direction. It is very important to check the accuracy of the devices used in the sector in certain periods and to inform the users regularly according to the classification and tolerances proposed in this study. Informing the health personnel in the field about the effects of the result of this test, which can be applied by an expert with the necessary equipment during the periodic maintenance-measurement of pulse oximetry devices, on the measurement performance of the device will increase the effective use of the pulse oximetry device. In this study, the accuracy test of the pulse oximeter device of the European Standard ISO 80601-2-61 was applied with the necessary equipment and in line with the experimental results, the deviation values that the device users can tolerate in different measurement bands while analyzing the measurement data were suggested and the applicability of the test was increased by making predictions close to the actual values with less data.

6. Author Contribution Statement

In the study, Author 1 contributed to forming the idea, making the design ,literature review, analysis of the results, provision of the materials and examination of the results; Author 2 contributed to checking the spelling and checking the article in terms of content.

7. Ethics Committee Approval and Conflict of Interest

There is no need for an ethics committee approval in the prepared article

8. References

- [1] T. Ş. Eyüboğlu, O. D. Güteryüz, E. Keleş, and I. Budakoğlu, “What do trainee physicians know about the use of pediatric pulse oximetry on patients?, *Gazi Med. J.*, vol. 29, pp. 119–122, 2018.
- [2] R. C. N. McMorro, and M. G. Mythen, “Pulse oximetry,” *Curr. Opin. Crit. Care*, vol. 12, pp. 269–271, 2006.
- [3] T. P. Walters, “Pulse oximetry knowledge and its effects on clinical practice,” *Br. J. Nurs.*, vol. 16, no. 21, pp. 1332–1340, 2007.
- [4] M. Elliott, R. Tate, and K. Page, “Do clinicians know how to use pulse oximetry? A literature review and clinical implications,” *Aust. Crit. Care*, vol. 19, no. 4, pp. 139–144, Nov. 2006.
- [5] K. Jamieson, M. J. Davey, and G. M. Nixon, “Oximetry knowledge in neonatal units in Victoria, Australia: Can we do better?,” *Acta Paediatr.*, vol. 108, no. 3, pp. 468–472, 2019.
- [6] S. Bagha and L. Shaw, “A real-time analysis of PPG signal for measurement of SpO₂ and pulse rate,” *Int. J. Comput. Appl.*, vol. 36, no. 11, pp. 45–50, 2015.
- [7] P. A. Assalim, M. T. P. Titisari, D. Caesarendra, and B. A. Prakoso, “Analysis of the effect of red LED and infrared flip flop frequency on SpO₂ measurement accuracy,” *Indones. J. Electron. Electromed. Eng. Med. Inform.*, 2022.
- [8] S. Seifi, A. Khatony, G. Moradi, A. Abdi, and F. Najafi, “Accuracy of pulse oximetry in detection of oxygen saturation in patients admitted to the intensive care unit of heart surgery: Comparison of finger, toe, forehead and earlobe probes,” *J. Clin. Monit. Comput.*, vol. 32, no. 6, pp. 1085–1090, 2018.
- [9] K. K. Giuliano, R. N. Bilkovski, J. Beard, and S. Lamminmäki, “Comparative analysis of signal accuracy of three SpO₂ monitors during motion and low perfusion conditions,” *J. Clin. Monit. Comput.*, vol. 33, no. 1, pp. 95–101, 2019.
- [10] Z. Xiong, and B. S. Kodali, “Pulse oximetry and capnograph,” in **The Essential Clinical Anesthesia Book*, pp. 186–190.
- [11] D. A. Freedman, **Statistical Models: Theory and Practice**, Cambridge: Cambridge Univ. Press, 2009.
- [12] *Respiratory Failure*, Akademisyen Kitabevi, pp. 233–247, 2021.
- [13] Contec MS100 SpO₂ Pulse Rate Blood Oxygen Simulator User Manual, [Online]. Available: <https://rfmedical.com.br/wp-content/uploads/2021/05/MANUAL-USUARIO-SIMULADOR-MS-100.pdf>. [Accessed: Jan. 13, 2023].
- [14] G. Ateş, and K. Polat, “Bulanik mantığa dayalı nabız oksimetresi kullanılarak oksijen saturasyonunun ölçülmesi,” *Tıbbi Ölçümler ve Başvurular Bildirileri*, pp. 1–6, 2012.
- [15] FDA, “Pulse oximeters - premarket notification submissions 510(k)s,” Document issued on: March 4, 2013.
- [16] FDA, “November 1, 2022: Anesthesiology and Respiratory Therapy Devices Panel of the Medical Devices Advisory Committee Meeting,” [Online]. Available: <https://www.youtube.com/watch?v=oQoF0XS9QNc>. [Accessed: Mar. 28, 2024].
- [17] M.A. Blanchet, G. Mercier, A. Delobel, E. Nayet, P.A. Bouchard, S. Simard, E. L'Her, R.D. Branson, F. Lellouche, “Accuracy of pulse oximetry (SpO₂) with different oximeters - Oxygap study,” ARF/ARDS Thematic Poster Session, Moscone Center, Hall F, Area G, Québec, Canada.
- [18] International Standard, ISO 80601-2-61:2017.
- [19] S. Çelik, “Oxygen saturation monitoring with pulse oximeter and nursing approaches,” *Health Soc.*, vol. 30, no. 2, pp. 11–15, 2020.
- [20] U. Yetkin, N. Karahan, and A. Gürbüz, “Pulse oximetry in clinical application,” *Van Med. J.*, vol. 9, no. 4, pp. 126–133, Oct. 2002.
- [21] M. Elliott, R. Tate, and K. Page, “Do retired know how to use pulse oximetry? A literature review and clinical implications,” *Aust. Crit. Care*, vol. 19, no. 4, pp. 139–144, Nov. 2006.
- [22] S. De Meulenaere, “Pulse oximetry: Uses and limitations,” *J. Nurse Pract.*, pp. 312–317, 2007.
- [23] P. Kiekkas et al., “Knowledge of pulse oximetry: Comparison among intensive care, anesthesiology and emergency nurses,” *J. Clin. Nurs.*, vol. 22, pp. 828–837, 2012.
- [24] J. J. Pretto, T. Roebuck, L. Beckert, and G. Hamilton, “Clinical use of pulse oximetry: Official guidelines from the Thoracic Society of Australia and New Zealand,” *Respirology*, vol. 19, pp. 38–46, 2014.

- [25] M. C. Seeley, L. McKenna, and K. Hood, "Graduate nurses' knowledge of the functions and limitations of pulse oximetry," *J. Clin. Nurs.*, vol. 24, pp. 3538–3549, 2015.
- [26] R. S. Bader, "Basic knowledge of the clinical applications of pulse oximetry technology among healthcare professionals in pediatrics," *J. Saudi Heart Assoc.*, vol. 19, no. 3, pp. 142–148, 2007.
- [27] J. P. Harper, "Post-anesthesia care unit nurses' knowledge of pulse oximetry," *J. Nurses Prof. Dev.*, vol. 20, no. 4, pp. 177–180, 2004.
- [28] E. C. Çelik and B. Çiftçi, "Cerebral oximetry and applications under anesthesia," *Ist Med. Fac. J.*, vol. 81, no. 1, pp. 33–36, 2018.
- [29] B. Hucuptan, "Pulse oximeter," [Online]. Available: <https://drbekir.com/nabiz-oksimetresi>. [Accessed: Jan. 9, 2025].



Ses Analizi Yoluyla Doğru Ev İçi Konumu Sınıflandırması: 1D-ILQP Yaklaşımı

Nura ABDULLAHI¹, Erhan AKBAL^{2*}, Sengul DOGAN³, Turker TUNCER⁴, Umut ERMAN⁵

^{1,2,3,4,5}Department of Digital Forensics Engineering, Technology Faculty, Fırat University, Elazığ, Türkiye.

¹191144116@firat.edu.tr, ²erhanakbal@firat.edu.tr, ³sdogan@firat.edu.tr, ⁴turkertuncer@firat.edu.tr,
⁵221144111@firat.edu.tr

Geliş Tarihi: 19.01.2024
Kabul Tarihi: 02.05.2024

Düzeltilme Tarihi: 17.03.2024

doi: <https://doi.org/10.62520/fujece.1422119>
Araştırma Makalesi

Alıntı: N. Abdullahi, E. Akbal, Ş. Dogan, T. Tuncer ve U. Erman, "Ses analizi yoluyla doğru ev içi konumu sınıflandırması: 1D-ILQP yaklaşımı", Fırat Üni. Deny. ve Hes. Müh. Derg., vol. 4, no 1, pp. 12-29, Şubat 2025.

Öz

Ev ortamlarındaki insan faaliyetlerinin tespit edilmesi, makine öğrenimi alanında temel bir zorluk teşkil etmektedir. Geleneksel olarak sensörler ve video kameralar, insan faaliyetinin tespitinde birincil araçlar olarak hizmet vermiştir. Ancak çalışmamız, çevresel ses sinyallerinin analizi yoluyla ev içi konumlarını belirlemeye yönelik yenilikçi hedefe sahiptir. Sonuç olarak, sekiz farklı lokasyondan gelen verileri kapsayan kapsamlı bir ses veri seti toplanmıştır. Bu ses veri kümesini kullanarak otomatik ev konumu algılamayı etkinleştirmek için, hassasiyete ve minimum hesaplama yüküne odaklanarak hafif bir makine öğrenimi modeli kullanılmıştır. Yaklaşımımızın temelinde, tek boyutlu Geliştirilmiş Yerel Dörtlü Model (GYDM) olarak adlandırılan yerel bir özellik oluşturucunun tanıtılması yer almaktadır. Bu yöntem, akustik sinyallerden dokusal özellikler üretmek için, özellik çıkarma sürecinde merkezi bir rol oynar. Yüksek seviyeli dokusal özelliklerin çıkarılmasını kolaylaştırmak için, sinyalleri ayrıştırmak için maksimum havuzlama uygulayarak evrişimli sinir ağı mimarisini taklit edilmiştir. Önerilen GYDM, orijinal sinyalin yanı sıra her ayrıştırılmış frekans bandından dokusal özelliklerini çıkarmaktadır. Daha sonra Komşu Bileşen Analizi tekniğini kullanarak en iyi 100 özellik seçilmiştir. Modelimizin son adımı sınıflandırmayı içermektedir. Bu aşamada karar ağaçları, doğrusal diskriminant analizi, ikinci dereceden diskriminant analizi, Naive Bayes, destek vektör makineleri, k-en yakın komşu, torbalanmış ağaçlar ve yapay sinir ağları dahil olmak üzere bir dizi sınıflandırıcı kullanılmıştır. Sonuçlar kapsamlı bir değerlendirmeye tabi tutulmuş ve tüm sınıflandırıcılar %80'in üzerinde sınıflandırma doğruluğuna ulaşmıştır. Özellikle k-en yakın komşu sınıflandırıcı, %99,75 gibi etkileyici bir değere ulaşarak en yüksek sınıflandırma doğruluğu sağlamıştır. Bulgularımız, GYDM'ye dayanan önerilen ses sınıflandırma modelinin, ev konumu ses veri setine uygulandığında oldukça tatmin edici sonuçlar verdiğini açıkça göstermektedir.

Anahtar kelimeler: Ev konum tespiti, Komşu bileşen analizi, Ses sınıflandırma, Makine öğrenmesi

*Yazılan yazar

İntihal Kontrol: Evet – Turnitin
Şikayet: fujece@firat.edu.tr

Telif Hakkı ve Lisans: Dergide yayın yapan yazarlar, CC BY-NC 4.0 kapsamında lisanslanan çalışmalarının telif hakkını saklı tutar.



Accurate Indoor Home Location Classification through Sound Analysis: The 1D-ILQP Approach

Nura ABDULLAHI¹ , Erhan AKBAL^{*2} , Sengul DOGAN³ , Turker TUNCER⁴ , Umut ERMAN⁵ 
^{1,2,3,4,5} Department of Digital Forensics Engineering, Technology Faculty, Firat University, Elazig, Turkey.
¹191144116@firat.edu.tr, ²erhanakbal@firat.edu.tr, ³sdogan@firat.edu.tr, ⁴turkertuncer@firat.edu.tr,
⁵221144111@firat.edu.tr

Received: 19.01.2024
Accepted: 02.05.2024

Revision: 17.03.2024

doi: <https://doi.org/10.62520/fujece.1422119>
Research Article

Citation: N. Abdullahi, E. Akbal, Ş. Dogan, T. Tuncer and U. Erman, "Accurate indoor home location classification through sound analysis: the 1D-ILQP approach", *Firat Univ. Jour. of Exper. and Comp. Eng.*, vol. 4, no 1, pp. 12-29, February 2025.

Abstract

Detecting human activities within domestic environments constitutes a fundamental challenge in machine learning. Conventionally, sensors and video cameras served as primary tools for human activity detection. However, our work is oriented towards the innovative objective of ascertaining home locations by analyzing environmental sound signals. Consequently, we compiled a comprehensive sound dataset from eight distinct locations. To enable automatic home location detection using this sound dataset, we employed a lightweight machine learning model designed with a paramount focus on precision and minimal computational overhead. At the core of our approach is the introduction of a local feature generator, referred to as the one-dimensional Improved Local Quadruple Pattern (1D-ILQP). This novel 1D-ILQP plays a central role in the feature extraction process, generating textural features from the acoustic signals. To facilitate the extraction of high-level textural features, we emulated the convolutional neural network (CNN) architecture, applying maximum pooling to decompose signals. The suggested 1D-ILQP extracts textural features from each decomposed frequency band as well as the original signal. Subsequently, we selected the top 100 features using the Neighborhood Component Analysis (NCA) technique. The final step of our model involves classification, wherein we employed a range of classifiers, including decision trees, linear discriminant analysis, quadratic discriminant analysis, Naive Bayes, support vector machines, k-nearest neighbor, bagged trees, and artificial neural networks. We subjected the results to a comprehensive evaluation, and all classifiers achieved classification accuracies exceeding 80%. Notably, the k-nearest neighbor classifier delivered the highest classification accuracy, reaching an impressive 99.75%. Our findings unequivocally demonstrate that the proposed sound classification model, based on the 1D-ILQP, has yielded highly satisfactory results when applied to the home location sound dataset.

Keywords: Home location detection, 1D-ILQP, Neighborhood component analysis, Sound classification, Machine learning

*Corresponding author

1. Introduction

Analyzing human behavior and activities holds significant potential across various domains [1]. Behavioral data can be invaluable for product development, design, and understanding human behavior in diverse settings. Humans spend the majority of their lives in a variety of locations, such as homes, shopping malls, offices, and restaurants. Analyzing usage patterns of these places can shed light on the complex relationships between individuals and their environments [2, 3]. Traditionally, cameras and sensors have been the preferred tools for monitoring human activities. However, these methods are often costly and present challenges in data analysis. Several studies have employed image data and intelligent techniques to describe human activities, but such approaches are susceptible to environmental conditions, such as variations in lighting, physical obstructions, and camera blind spots [4-8].

Numerous studies explored the detection of human activities using sensor data [1, 9-13]. Wearable technologies and mobile device sensors gained widespread use in this context [14-17]. However, a primary limitation of sensor-based methods is their dependency on the presence of sensors on individuals, which is not always feasible, especially within the confines of one's home [18]. When people are at home, they typically do not carry mobile devices or wear wearable technology products, making these methods less effective for indoor human activity and location data collection [19].

Sound-based detection of human activities and locations offers a more cost-effective and practical alternative to video recording and sensor technologies. Human behavior can be discerned from the sounds they produce or the sounds of objects they interact with, as these sounds often exhibit location-specific patterns [20]. Sound is readily propagated and can be captured at a distance, making it a viable option for monitoring human activities without the need for individuals to wear specific sensor-equipped devices [19].

Intelligent sound recognition systems employ algorithms to learn and interpret sound patterns, extracting valuable information from sound signals [21]. Sound recognition methods are typically categorized based on the type of sound signal and their intended purpose. Common classes include environmental sound determination [22-27], music recognition [28, 29], speaker recognition [30, 31], and emotional state detection [32-34]. Additionally, acoustic event detection focuses on identifying specific events within the acoustic environment, such as falls, breaks, and impacts [35-37], while acoustic scene classification aims to classify environments, events, or behaviors using multiple concurrent sounds in the environment [38-40]. This classification process helps differentiate environments such as crime scenes, schools, restaurants, barbershops, and cafes [41, 42].

Indoor activity and location detection intersect with both event detection and acoustic scene classification. Human indoor activities generate sound signals with varying frequencies and decibels. For example, sounds produced during activities like cooking or cleaning in a home may exhibit characteristics of both acoustic event recognition and acoustic scene classification. Nonetheless, indoor activities possess unique sound signal features specific to their respective locations [20].

In the existing literature, there are limited studies that employ sound signals for the classification of human activities and location recognition/classification. For instance, Jung and Chi [43] introduced a method for classifying human activities, utilizing a dataset of 10 different human activity sounds collected from YouTube. They extracted features from the sound signals using the Log Mel filter bank and achieved an 87.6% accuracy rate using a residual convolutional neural network. Galván-Tejada et al. [44] proposed a method to recognize the indoor location of humans based on sound signals generated during activities within a house. They used 11 different human activity sounds recorded in four distinct rooms of a house and achieved a classification accuracy of 95% using the random forest model. Do et al. [45] presented a sound-based human activity monitoring model by recognizing sound events in a home environment, achieving a classification accuracy of 92.41% for 12 activities across six locations using a two-level dynamic Bayesian network. Wang et al. [46] conducted a comparative study on different feature extraction and machine learning techniques for indoor environmental noise classification. They used 2500 indoor audio signals across five classes and demonstrated a 78%

classification accuracy using the LPCC and SVM model. Mesaros et al. [47] developed a system for acoustic event detection in real-life environments using hidden Markov models and achieved 24% accuracy in classifying sound events belonging to 61 isolated classes.

1.1. Motivation and our work

Sound activity classification is a critical aspect of building and design construction. Extracting meaningful information from environmental sounds is a valuable pursuit in this field. Deep learning models and networks are frequently employed to achieve high classification accuracy in sound categorization. However, these models are computationally expensive. Therefore, the development of lightweight learning models has emerged as a significant research challenge.

The primary objective of this research is to introduce a lightweight sound classification model. To achieve this, a novel hand-crafted feature extraction function has been devised to capture highly distinctive features. However, this hand-crafted extraction function is limited in its ability to generate high-level features. To address this limitation, we have emulated a deep learning network, specifically a convolutional neural network, to create hierarchical representations. These hierarchical representations enable the extraction of high-level features. For an accurate model, it is crucial to employ an effective feature selection function. We have applied Neighborhood Component Analysis (NCA) [48] to select the most distinctive features from the extracted set.

Additionally, we collected a new dataset specific to home activities, comprising eight distinct classes of sounds. Our proposed lightweight learning model has been applied to this newly collected sound dataset. To establish benchmark results, we have employed eight shallow classifiers for the classification process.

1.2. Novelties and contributions

In this research, we have introduced a novel Environmental Sound Classification (ESC) model utilizing environmental sounds from domestic settings. The key contributions of our study include:

- We collected a new and comprehensive sound dataset specifically designed for detecting home locations. This dataset serves as a valuable resource for the development and evaluation of our classification model.
- We have introduced a novel feature extraction function named 1D-ILQP. This function is instrumental in extracting informative features from the sound data, enabling the accurate classification of environmental sounds.
- Building upon the 1D-ILQP feature extraction, we have developed a new classification model. This model leverages the capabilities of 1D-ILQP and has demonstrated remarkable performance, achieving a classification accuracy exceeding 99%. Notably, this high accuracy is accomplished using only two shallow classifiers, highlighting the efficiency and effectiveness of our approach.

These contributions collectively enhance the field of environmental sound classification, particularly in the context of home locations, and offer valuable insights for future research in this area.

1.3. Organization

The organization of the remainder of this research is presented as follows: Section 2 details the dataset, Section 3 explains the proposed one-dimensional improved local quadruple pattern, and Section 4 presents the proposed feature engineering model. The results of this feature engineering model are given in Section 5. These results are discussed in Section 6, while the limitations and future work are presented in Section 7. Finally, Section 8 concludes the proposed research.

2. Dataset

In order to evaluate the performance of the proposed method, a new dataset containing indoor sounds was meticulously assembled. Different indoor locations within a home give rise to a diverse array of sounds produced by human activities. For instance, the kitchen might feature sounds associated with cooking, eating, and washing dishes, while the bedroom may exhibit sounds related to sleep. Each of these produced sound signals possesses distinct characteristics, which render them amenable to classification based on their unique features.

In our study, we identified eight distinct indoor locations within the home. For each location, we further delineated various sub-activities and selected recordings of these sub-activities. To accomplish this, we sourced material from open-access online video and audio platforms, including YouTube. Importantly, the audio and video recordings used in our dataset originate from a variety of recording devices and media sources. This diversity is intentional, as it reflects real-world conditions where data may be collected from different environments and devices. Collecting data from diverse sources is essential to ensure that our method's performance is robust and can generalize effectively across various settings. For our dataset, we incorporated 50 different videos for each of the selected locations. This process yielded a total of 500 sample sound signals for each location. Consequently, we created a balanced dataset, which comprises a total of 4,000 sound samples distributed across eight distinct location classes. These classes are as follows: (1) Bathroom, (2) Bedroom, (3) Dining room, (4) Dressing room, (5) Kitchen, (6) Living room, (7) Toilet, and (8) Washing room. Each audio sample is typically in the range of 1 to 2 seconds in duration, and all recordings have a signal frequency of 48 kHz. A detailed breakdown of the dataset's contents is presented in Table 1, providing a comprehensive overview of the dataset's composition and structure.

Table 1. Detail of collected sound dataset

Class No	Location Name	Class Activity Content	Number of used Recording	Number of sample sound signal
1	Bathroom	Showering, brushing teeth, hair care	50	500
2	Bedroom	Sleeping, breathing, and snore sounds	50	500
3	Dining room	Eating, drinking, and other eating sounds (spoon and fork)	50	500
4	Dressing room	Folding clothes, measuring, and hand movements	50	500
5	Kitchen	Cleaning and water flushing	50	500
6	Living room	Singing, Talking, Studying, Music, Clicking sound of keyboard and mouse	50	500
7	Toilet	Flushing	50	500
8	Washing room	Washing Machine sounds (watering, draining and spinning), Ironing	50	500
TOTAL			400	4.000

3. The Proposed One-Dimensional Improved Local Quadruple Pattern

In our research, we have introduced a novel feature extraction function named 1D-ILQP. The primary purpose of this function is to generate discriminative features from a given signal. The 1D-ILQP function operates by employing an overlapping block with a length of 16 and applying the signum function to create features. As a result, this feature extractor produces three map signals, each represented with eight bits. The cumulative outcome of this histogram-based extraction process amounts to 768 distinct features.

To elucidate the operation of the 1D-ILQP feature extraction function, we outline its steps below for a clearer understanding:

Step 1: Generate overlapping blocks with overlapping blocks with a length of 16.

Step 2: Apply vector to matrix transformation to obtain a 4×4 sized matrixes. The prime objective of this step is to apply the proposed pattern. Schematic description of the presented 1D-ILQP is shown in Figure 1.

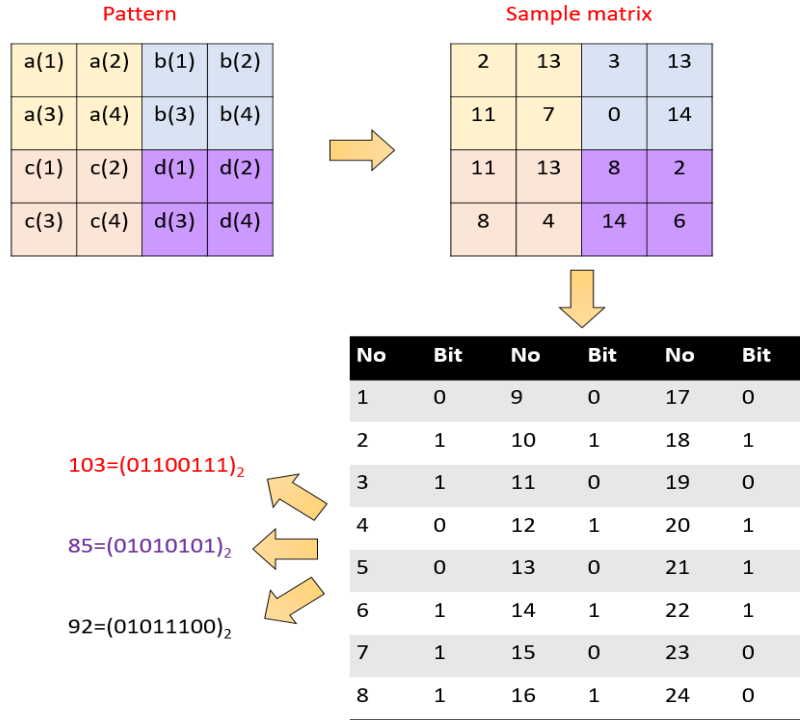


Figure 1. Binary feature extraction and decimal values creation diagram of the proposed 1D-ILQP

The proposed 1D-ILQP feature extraction function employs a binary feature extraction process, which subsequently leads to the creation of decimal values. The following diagram illustrates the binary feature extraction and decimal values creation process:

Here's a step-by-step description of this process:

- A 4x4-sized matrix is divided into four parts, each with a size of 2x2. These parts are denoted as 'a,' 'b,' 'c,' and 'd.'
- By comparing these four parts ('a,' 'b,' 'c,' and 'd'), 24 bits are extracted. These 24 bits are used to form three distinct groups of bits.
- These three bit groups serve as the basis for creating three map signals.
- Histograms of these map signals are generated to produce a feature vector.
- The three histograms are then combined, resulting in a feature vector with a total length of 768.

This feature extraction method yields a comprehensive set of features that can be utilized for subsequent analysis and classification tasks.

As can be seen Figure 1, the used pattern of the 1D-ILQP has been summarized.

Step 3: Extract binary features by using the quadruple pattern (see Figure 2). Pseudocode of the bit extraction process has been given in Algorithm 1.

Algorithm 1. Bit (binary features) generation of the proposed 1D-ILQP

Input: Matrix (m)

Output: Bit vector (bit)

```

01: Assign a, b, c and d values using m.
02: for j=1 to 4 do
03:   bit(j) = a(j) ≥ b(j);
04:   bit(j + 4) = a(j) ≥ c(j);
05:   bit(j + 8) = a(j) ≥ d(j);
06:   bit(j + 12) = b(j) ≥ c(j);
07:   bit(j + 16) = b(j) ≥ d(j);
08:   bit(j + 20) = c(j) ≥ d(j);
09: end for j
    
```

Step 4: Create three big groups with a length of eight like local binary pattern. These creation process is denoted in Equation 1.

$$b^g = bit(j + 8 \times (g - 1)), j \in \{1, 2, \dots, 8\}, g \in \{1, 2, 3\} \quad (1)$$

Herein, b^g defines g^{th} bit group.

Step 5: Generate three feature map signals using the generated bit groups.

$$map^g(i) = \sum_{j=1}^8 b^g(j) \times 2^{j-1} \quad (2)$$

where map^g represents g^{th} feature map signal.

Step 6: Extract histogram of each map signal.

Step 7: Merge the extracted histogram to create feature vector with a length of 768.

$$fv = H^g(h + 256 \times (g - 1)), h \in \{1, 2, \dots, 256\} \quad (3)$$

Herein H^g is histogram of the g^{th} map signal and fv defines feature vector with a length of 768.

4. Our Proposed Home Location Detection Method

The primary goal of this model is to efficiently detect home locations using sound signals, minimizing the computational time required. To achieve this, we have introduced a novel local feature extraction-based sound classification model, which comprises three key phases:

Feature Generation: This phase leverages the presented 1D-ILQP (One-Dimensional Improved Local Quadruple Pattern) and a maximum pooling-based feature extraction model. It involves the following steps:

- Creation of decomposed sub-bands of the sound signal using maximum pooling.
- Extraction of textural features from both the raw sound signal and the decomposed sub-bands using 1D-ILQP.
- Formation of a feature vector, which serves as input for the subsequent feature selection phase.

Feature Selection: In this phase, NCA is employed to select the most informative features. The NCA feature selection function is applied to the feature vector, leading to the identification and retention of the top 100 features.

Classification: The last phase involves classification using various machine learning methods. Eight classifiers are used to compute the classification results. These classifiers are evaluated through a 10-fold cross-validation procedure to ensure robustness and reliability of the model.

In summary, the model's workflow can be described as follows: raw sound signals are transformed into a feature vector through the application of 1D-ILQP and maximum pooling. Subsequently, feature selection using NCA is carried out, resulting in the identification of the most relevant features. Finally, the classification of home locations is performed using a range of classifiers with 10-fold cross-validation to validate the model's effectiveness. For a visual representation of this process, please refer to Figure 2 in our introduced 1D-ILQP feature extraction-based home location detection model.

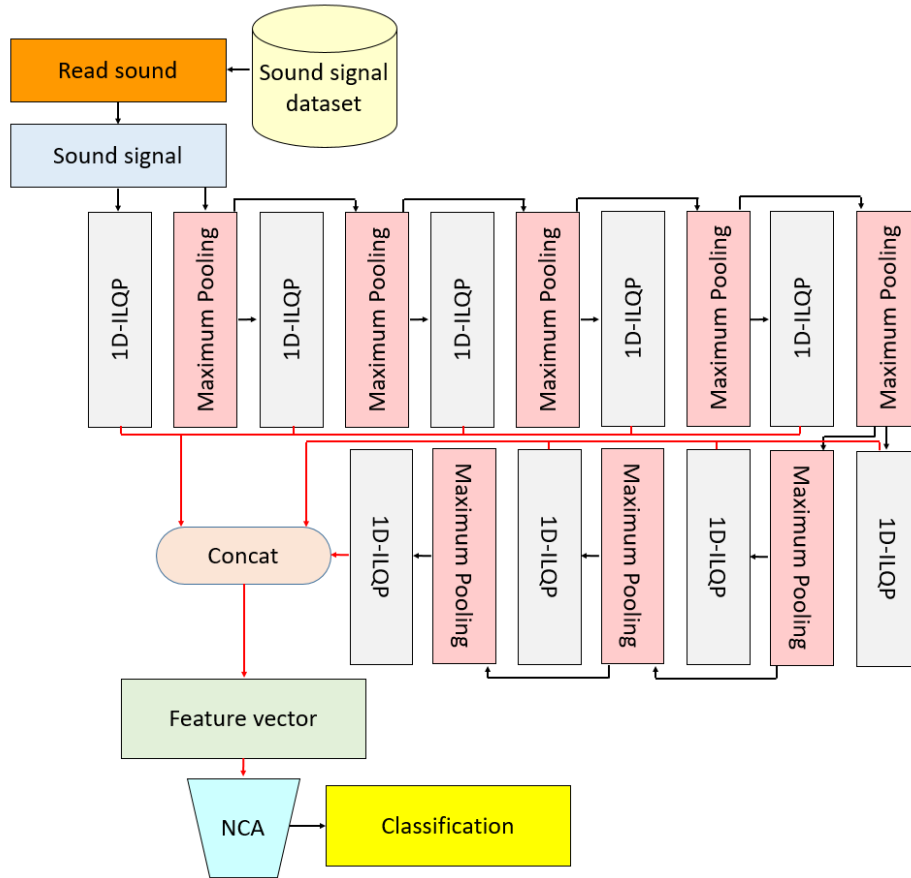


Figure 2. Block diagram of the 1D-ILQP-based sound signal classification model

This model mimics deep learning networks. It uses a manually crafted feature extractor to generate textural features. Maximum pooling is applied to create layers that function as a decomposition mechanism. These layers are instrumental in extracting high-level features. Throughout this process, the 1D-ILQP is applied nine times, extracting 768 features from each signal. During the fusion (concatenation) step, these features are combined to form a feature vector with a length of 6912 ($=768 \times 9$). From this pool of 6912 features, the top 100 features are selected using the NCA selector. The results are then obtained by applying these 100 features to eight conventional classifiers.

As can be seen from Figure 1, the used feature extraction function is 1D-ILQP. The definition of the 1D-ILQP is given below. General steps of the presented 1D-ILQP based model have been listed in below.

Step 1: Create sub-bands by deploying maximum pooling. In this work, eight compressed bands have been created. The number of compressed bands have been generated by using accuracy value. The optimal accuracy score has been attained using eight compressed bands. The compressed band generation formula is denoted in below.

$$sb^1 = \text{maxpool}(\text{sound}) \quad (4)$$

$$sb^t = \text{maxpool}(sb^{t-1}), t \in \{2, 3, \dots, 8\} \quad (5)$$

Herein, sb defines compressed bands and $\text{maxpool}(\cdot)$ is maximum pooling function using non-overlapping blocks with a length of two.

Step 2: Extract features from sound signal and compressed bands.

$$fv^1 = IQP(sound) \quad (6)$$

$$fv^t = IQP(sb^{t-1}), t \in \{2,3, \dots, 8\} \quad (7)$$

Herein, $IQP(.)$ defined the proposed 1D-IQP feature extraction function. In this step, the feature generation process has been defined.

Step 3: The extracted features have been merged to create final feature vector (X) with a length 6912.

$$X(q + 768 \times (t - 1)) = fv^t(q), q \in \{1,2, \dots, 768\}, t \in \{1,2, \dots, 8\} \quad (8)$$

Step 4: Choose the most discriminate/valuable 100 features from the generated 6912 features by applying NCA. NCA holds a significant place in feature selection literature and can be viewed as a feature selection variant of the k-nearest neighbors (kNN) method. NCA calculates a positive weight for each feature, with informative features receiving higher weight values and redundant features receiving lower weight values. This weighting process allows for the selection of the top 100 features based on the generated weights.

Step 5: Calculate results using the eight shallow classifiers with 10-fold cross-validation, it's important to understand the attributes of each classifier. Here's a summary of the attributes for each of the mentioned classifiers:

Decision Tree (DT): Decision trees are a non-linear model that uses a tree structure to make decisions. They split the dataset into subsets based on the most significant attribute at each node.

Linear Discriminant (LD): Linear discriminant analysis is a method used for dimensionality reduction and classification. It projects data into a lower-dimensional space while maximizing the separation between classes.

Quadratic Discriminant (QD): Quadratic discriminant analysis is a variant of linear discriminant analysis but assumes that each class has its own covariance matrix.

Naïve Bayes (NB): Naïve Bayes is a probabilistic classification algorithm based on Bayes' theorem. It assumes that features are conditionally independent.

Support Vector Machine (SVM): SVM is a powerful classification method that finds a hyperplane that best separates data points into different classes while maximizing the margin between the classes.

k-Nearest Neighbor (kNN): kNN is a simple classification algorithm that assigns a class label based on the majority class among its k-nearest neighbors in feature space.

Bagged Tree (BT): Bagging is an ensemble method that combines the predictions of multiple decision trees to reduce variance and improve accuracy.

Artificial Neural Network (ANN): Artificial neural networks are a family of machine learning models inspired by the human brain. They consist of interconnected nodes and layers and can be used for various classification tasks.

With the attributes of these classifiers in mind, you can now proceed to calculate results using each of them in your 10-fold cross-validation framework.

Table 2. Attributes of the classifiers

Classifier	Hyperparameters	Classifier	Hyperparameters
DT	Maximum number of splits: 100 Split criterion: Gini Surrogate decision split: Off	SVM	Kernel: Quadratic Box constraint level: 1 Kernel scale: Auto Multiclass method: One-vs-One
LD	Covariance structure: Full	kNN	k: 1 Distance metric: City block Weight: none
QD	Covariance structure: Full	BT	Ensemble: Bag Learner: DT Maximum number of splits: 1000 Number of learners: 30 Learning rate: 0.1
NB	Kernel: Gaussian Support: Unbounded	ANN	Number of fully connected layers: 1 Layer sizes: 100, 10, 10 Activation: ReLu Iteration limit: 1000 Lambda: 0

Results have been obtained by employing these eight shallow classifiers, with their respective hyperparameters as listed in Table 2.

5. Results

This section presents the experiments conducted in this research. The 1D-ILQP-based model was implemented in the MATLAB environment to evaluate the home location dataset used in this study. The dataset comprises 4000 sounds categorized into eight rooms, ensuring a balanced distribution. These sound samples were sourced from YouTube. The MATLAB implementation involves the utilization of several functions, including maximum pooling, 1D-ILQP, NCA, and a primary 'main' function.

To assess the model's performance, various metrics such as accuracy, precision, and F1-score were computed for each of the eight classifiers used in the study. Consequently, eight sets of results were generated. Furthermore, class-specific results for each classifier were also calculated. Initially, the comprehensive classification outcomes for each classifier are presented in Table 3.

Table 3. Overall classification performance results (%) of the used eight classifiers.

Classifier	Accuracy	Precision	F1
DT [49]	89.50	89.50	89.50
LD [50]	92.65	92.88	92.60
QD [51]	98.98	98.98	98.97
NB [52]	83.10	85.14	83.15
SVM [53]	99.68	99.68	99.68
kNN [54]	99.75	99.75	99.75
BT [55]	97.48	97.48	97.47
ANN [56]	98.95	98.95	98.95

Moreover, category-wise results have been denoted in Figure 3.

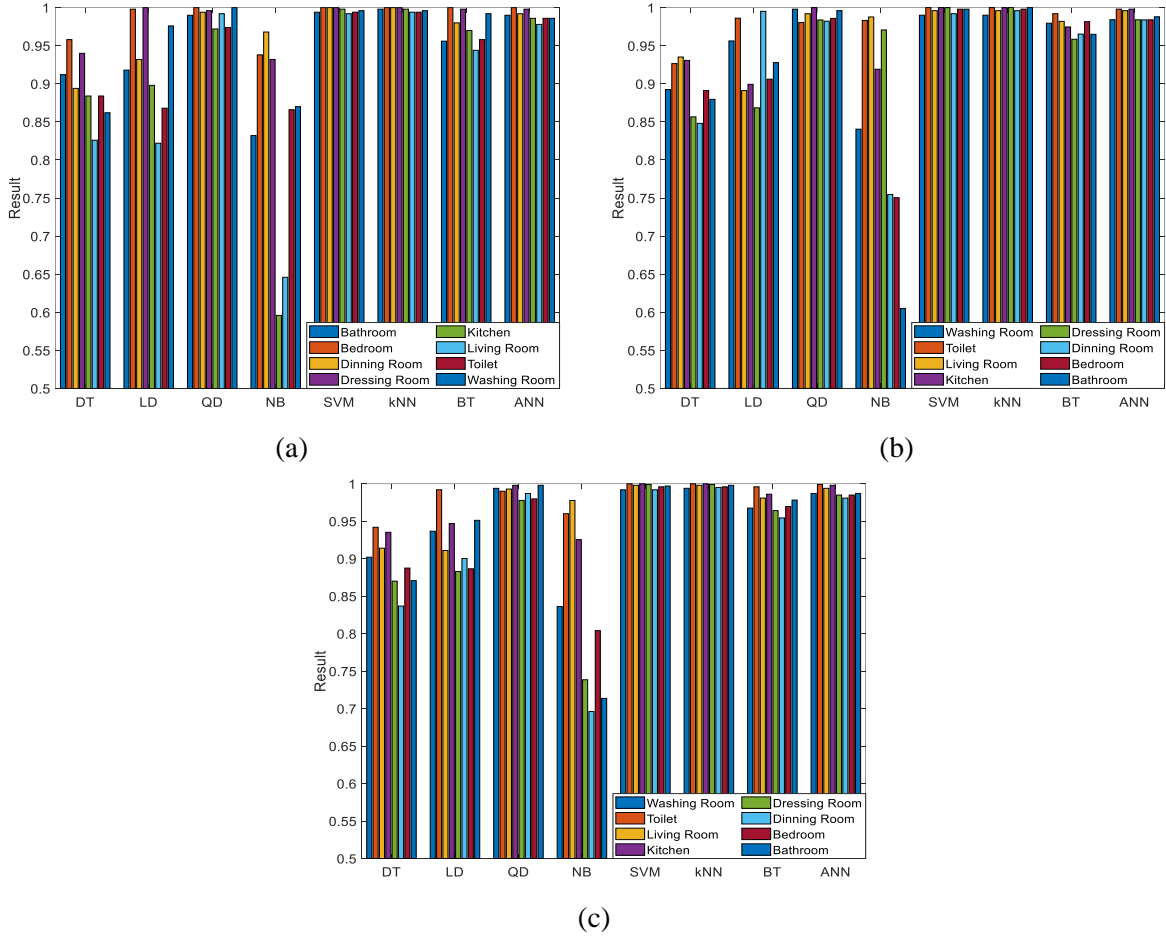


Figure 3. Category-wise classification accuracies according to the used classifiers.

Furthermore, the time complexity of the proposed 1D-ILQP pattern based sound classification has been calculated. In this model, the presented 1D-ILQP is a textural feature extractor and the time complexity of this function is equal to $O(n)$. To generate features at high levels, a simple decomposition model which is maximum pooling has been used. Maximum pooling halved the length of the used sound signal in each level. Therefore, the time burden of the presented feature extraction model is calculated as $O(n \log n)$. Moreover, we have used NCA feature selector. This feature selector is a simple feature selection function. In the classification phase, a shallow classifier has been employed to get results. In this respect, the time burden of this hand-crafted features based sound classification model is $O(n \log n + k + c)$. Herein, n is length of the sound signal, k is coefficient of NCA and c defines coefficient of the used classifier. According to this result, this model has linear time complexity.

6. Discussion

The primary objective of this research is to classify human activities within the home environment and determine the specific location within the home using sound data. This research introduces two noteworthy contributions: the compiled sound dataset and the novel 1D-ILQP function. The utilization of 1D-ILQP has facilitated the development of a novel classification model, inspired by Convolutional Neural Networks (CNNs). As previously mentioned, the presented feature extractor primarily generates low-level features. To enhance the feature extraction capabilities of 1D-ILQP, we introduce levels created through maximum pooling and subsequently generate decomposed/compressed sound signals. Our feature generator extracts feature from each of these compressed sound signals, resulting in multi-level feature extraction. An effective machine learning model must incorporate a feature extraction function to select the most valuable features and reduce the computational load on the classifier.

In this research, the Neighborhood Component Analysis (NCA) feature selector is employed, which selects the top 100 features from the 6912 initially used features. To evaluate the classification performance of the 1D-ILQP and NCA-based feature creation model, eight shallow classifiers are employed, yielding eight distinct results. The least performing classifier is Naïve Bayes (NB), which achieved an accuracy of 83.10% on the dataset. In contrast, the most successful classifier is k-Nearest Neighbor (kNN), attaining an accuracy of 99.75% on the same dataset. Additionally, the results are categorized by class for each classifier, and a comparative analysis is presented in Table 4.

Table 4. Comparative results to sound based human activity and location recognition/classification

Work and Year	Aim	Method	Number of Categories	Accuracy (%)
Mesaros et al. [47], 2010	Event detection	Hidden markov models	61 events	24
Tejada et al. [44], 2018	Indoor location estimation using activity	Contextual information extracted	10 activities, 4 locations	95
Wang et al. [46], 2019	Indoor human activity recognition	SVM model with LPCC feature	5 activities	78
Jung and Chi [43], 2020	Human activity classification	CNN	10 activities	87.6
Do et al. [45], 2021	Human activity monitoring	A two-level dynamic Bayesian network	12 activities, 6 locations	92.41
Our Work	Indoor home location classification	1D-ILQP	26 activities, 8 locations	99.75

According to Table 4, our proposed model attained 99.75% classification accuracy for eight locations classification. We proposed a hand-crafted features based model and the most of the previously presented sound classification methods used hand-crafted models except for Jung and Chi [43] method. Jung and Chi [43] used a CNN classification based model. They extracted spectrogram images from each sound and used these images as input for a residual network to compute results. In their study, they achieved an accuracy of 87.6% for a dataset with 10 classes. In contrast, our model is a manually designed learning approach, the 1D-ILQP-based model, which achieved a significantly higher classification accuracy of 99.75% for eight categories.

The benefits of the presented model are;

Advantages:

- The 1D-ILQP-based sound classification model achieved an impressive classification accuracy of 99.75% for eight categories, demonstrating the effectiveness of this novel approach in accurately detecting home locations using sound signals.
- The comprehensive evaluation of the model employed eight shallow classifiers. The classification results illustrate that the model's performance can vary based on the choice of classifier. The highest classification accuracy, 99.75%, was achieved using the k-Nearest Neighbor (kNN) classifier, while the Naïve Bayes (NB) classifier exhibited the lowest accuracy at 83.10%.
- The introduction of the 1D-ILQP function for feature extraction is a significant contribution. This function, when combined with maximum pooling and multi-level feature extraction, enhances the model's ability to generate informative features, improving the classification performance.

- The research utilized a balanced dataset comprising 4000 sound samples across eight categories, ensuring that each category was adequately represented. This balanced dataset contributes to the robustness and reliability of the model.
- The application of the NCA feature selector aids in selecting the most relevant features from a large set of 6912 features, optimizing the model's efficiency and effectiveness.

These findings highlight the strengths and weaknesses of the research, showcasing the promise of the 1D-ILQP-based model for indoor activity and location detection while acknowledging its specific limitations and areas for potential improvement.

7. Limitations and Future Works

In this section, the limitations of this research and future studies are presented.

The limitations of the research are presented below

- The research focuses on classifying activities and detecting locations within a home environment. The model's applicability may be limited to indoor settings and may not generalize well to other environments or broader contexts.
- While the 1D-ILQP function and feature extraction techniques are effective, manual feature engineering may not be the most scalable approach for more extensive datasets or evolving research needs.
- The model's performance is based on offline analysis, and its real-time applicability in home automation or security systems may require further development and optimization.

Future studies of the research are presented below

- Future work could focus on developing a real-time application of the 1D-ILQP-based sound classification model. This would involve optimizing the model's performance for immediate and continuous monitoring of activities and locations within a home environment, which could have applications in home automation and security systems.
- Extending the research to encompass a wider range of environments beyond the home, such as offices, public spaces, or outdoor settings, could expand the model's applicability. Addressing the challenges of noisy and dynamic environments presents an exciting research opportunity.
- Collecting and utilizing more extensive and diverse sound datasets would enable the model to generalize better and accommodate a broader spectrum of activities and locations. A larger dataset could also allow for more advanced machine learning techniques, such as deep learning models.
- Implementing an online learning framework could enable the model to adapt and improve its performance over time. This could be especially beneficial in environments where activities and sounds change or evolve continuously.
- Investigating how this technology can enhance human-computer interaction and user experience within smart homes or assistive technology settings is another exciting area. This research could focus on developing intuitive interfaces and control mechanisms based on sound classification.
- For applications in resource-constrained environments, such as IoT devices, research could concentrate on developing energy-efficient hardware solutions that can execute the sound classification model without significant power consumption.
- Further research into the modeling of human behavior patterns using sound signals could have implications in fields such as psychology, sociology, and healthcare. Understanding and predicting human behaviors can provide valuable insights.

These future works can advance the research in sound-based activity and location classification, offering innovative solutions for a wide range of applications and contributing to the evolving field of audio-based artificial intelligence. Furthermore, we are outlined our primary future objective in Figure 4.

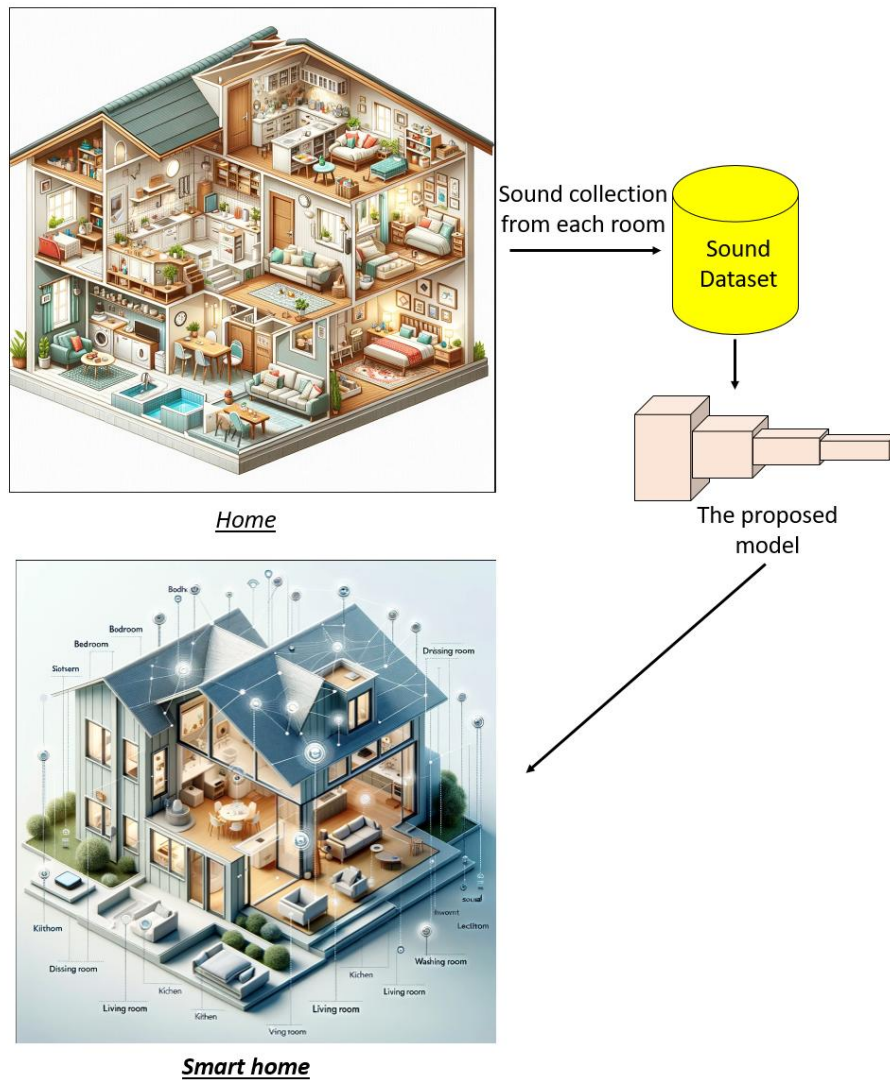


Figure 4. Converting to a smart home by implementing the proposed model

Figure 4 clearly demonstrates that the proposed model can be utilized in sound-based smart home applications. Furthermore, we can employ this model for digital forensics, particularly in sound forensics, as well as for cybersecurity and cybercrime analysis.

8. Conclusions

In this study, we presented a novel sound classification model, the 1D-ILQP-based model, aimed at classifying human activities within the home environment and accurately detecting the location of these activities using sound signals. The research has yielded significant insights and achieved remarkable results, which are summarized below:

The 1D-ILQP-based model demonstrated outstanding performance, achieving a classification accuracy of 99.75% for eight distinct categories, representing different rooms within a home. This exceptional accuracy underscores the model's ability to precisely identify activities and locations based on sound signals.

This research introduced an innovative approach to sound-based activity and location classification within a home environment. The exceptional classification accuracy, unique feature extraction techniques, and the robustness of the model are indicative of its potential for applications in home automation, security, and beyond.

As we move forward, future research will explore real-time implementation, scalability to diverse environments, and ethical considerations associated with sound-based monitoring. These endeavors aim to further enhance the applicability and responsible use of sound classification technology.

9. Author Contribution Statement

In the study, Author 1 and Author 2 contributed to the formation of the idea, design, literature review, evaluation of the results obtained, procurement of the materials used and examination of the results, Author 3 contributed to the writing of the original draft, methodology, visualization and experiments. Author 4 and Author 5, conceptualized the study and was involved in writing, reviewing and editing.

10. Ethics Committee Approval and Conflict of Interest Statement

There is no need to obtain ethics committee permission for the prepared article. There is no conflict of interest with any person/institution in the prepared article.

11. References

- [1] C. A. Ronao and S.B. Cho, "Human activity recognition with smartphone sensors using deep learning neural networks," *Expert Syst. Appl.*, vol. 59, pp. 235-244, 2016.
- [2] B. Dong and K. P. Lam, "Building energy and comfort management through occupant behaviour pattern detection based on a large-scale environmental sensor network," *J. Build. Perform. Simul.*, vol. 4, pp. 359-369, 2011.
- [3] J. G. Ortega, L. Han, N. Whittaker, and N. Bowring, "A machine-learning based approach to model user occupancy and activity patterns for energy saving in buildings," *Sci. Inf. Conf. (SAI)*, IEEE, pp. 474-482, 2015.
- [4] A. Khosrowpour, J. C. Niebles, and M. Golparvar-Fard, "Vision-based workplace assessment using depth images for activity analysis of interior construction operations," *Autom. Constr.*, vol. 48, pp. 74-87, 2014.
- [5] M. Zeng, L. T. Nguyen, B. Yu, O. J. Mengshoel, J. Zhu, P. Wu, and J. Zhang, "Convolutional neural networks for human activity recognition using mobile sensors," in *6th Int. Conf. Mob. Comput. Appl. Serv.*, IEEE, pp. 197-205, 2014.
- [6] A. Jalal, Y.-H. Kim, Y.-J. Kim, S. Kamal, and D. Kim, "Robust human activity recognition from depth video using spatiotemporal multi-fused features," *Pattern Recognit.*, vol. 61, pp. 295-308, 2017.
- [7] S. Kamal, A. Jalal, and D. Kim, "Depth images-based human detection, tracking and activity recognition using spatiotemporal features and modified HMM," *J. Electr. Eng. Technol.*, vol. 11, pp. 1857-1862, 2016.
- [8] A. Franco, A. Magnani, and D. Maio, "A multimodal approach for human activity recognition based on skeleton and RGB data," *Pattern Recognit. Lett.*, 2020.
- [9] M. M. Hassan, M. Z. Uddin, A. Mohamed, and A. Almogren, "A robust human activity recognition system using smartphone sensors and deep learning," *Future Gener. Comput. Syst.*, vol. 81, pp. 307-313, 2018.
- [10] Y. Chen and C. Shen, "Performance analysis of smartphone-sensor behavior for human activity recognition," *IEEE Access*, vol. 5, pp. 3095-3110, 2017.
- [11] H. F. Nweke, Y. W. Teh, M. A. Al-Garadi, and U. R. Alo, "Deep learning algorithms for human activity recognition using mobile and wearable sensor networks: State of the art and research challenges," *Expert Syst. Appl.*, vol. 105, pp. 233-261, 2018.
- [12] E. Lattanzi, L. Calisti, and P. Capellacci, "Lightweight accurate trigger to reduce power consumption in sensor-based continuous human activity recognition," *Pervasive Mob. Comput.*, 2023.
- [13] H. Feng, Q. Shen, R. Song, L. Shi, and H. Xu, "ATFA: Adversarial Time-Frequency Attention network for sensor-based multimodal human activity recognition," *Expert Syst. Appl.*, vol. 236, 2024.
- [14] Z. Chen, Q. Zhu, Y. C. Soh, and L. Zhang, "Robust human activity recognition using smartphone sensors via CT-PCA and online SVM," *IEEE Trans. Ind. Inf.*, vol. 13, pp. 3070-3080, 2017.
- [15] A. Ignatov, "Real-time human activity recognition from accelerometer data using Convolutional Neural Networks," *Appl. Soft Comput.*, vol. 62, pp. 915-922, 2018.
- [16] Z. Qin, Y. Zhang, S. Meng, Z. Qin, and K.-K. R. Choo, "Imaging and fusing time series for wearable sensor-based human activity recognition," *Inf. Fusion*, vol. 53, pp. 80-87, 2020.
- [17] F. S. Abuhoureyah, Y. C. Wong, and A. S. B. M. Isira, "WiFi-based human activity recognition through wall using deep learning," *Eng. Appl. Artif. Intell.*, vol. 127, 2024.
- [18] A. Mastakouris, G. Andriosopoulou, D. Masouros, P. Benardos, G.-C. Vosniakos, and D. Soudris, "Human worker activity recognition in a production floor environment through deep learning," *J. Manuf. Syst.*, vol. 71, pp. 115-130, 2023.
- [19] M. N.U. Hasan, and C. R. Stannard, "Exploring online consumer reviews of wearable technology: The Owlet Smart Sock," *Res. J. Text. Apparel*, 2022.
- [20] M. P. Buttner and L. D. Stetzenbach, "Monitoring airborne fungal spores in an experimental indoor environment to evaluate sampling methods and the effects of human activity on air sampling," *Appl. Environ. Microbiol.*, vol. 59, pp. 219-226, 1993.

- [21] A. Bansal and N. K. Garg, "Environmental Sound Classification: A descriptive review of the literature," *Intell. Syst. Appl.*, 2022.
- [22] Y. Chen, Q. Guo, X. Liang, J. Wang, and Y. Qian, "Environmental sound classification with dilated convolutions," *Appl. Acoust.*, vol. 148, pp. 123-132, 2019.
- [23] S. Abdoli, P. Cardinal, and A. L. Koerich, "End-to-end environmental sound classification using a 1D convolutional neural network," *Expert Syst. Appl.*, vol. 136, pp. 252-263, 2019.
- [24] A. Khamparia, D. Gupta, N. G. Nguyen, A. Khanna, B. Pandey, and P. Tiwari, "Sound classification using convolutional neural network and tensor deep stacking network," *IEEE Access*, vol. 7, pp. 7717-7727, 2019.
- [25] A. Bansal and N. K. Garg, "Environmental Sound Classification using Hybrid Ensemble Model," *Procedia Comput. Sci.*, vol. 218, pp. 418-428, 2023.
- [26] S. Dong, Z. Xia, X. Pan, and T. Yu, "Environmental sound classification based on improved compact bilinear attention network," *Digit. Signal Process.*, vol. 141, 2023.
- [27] M. YILDIRIM, "Automatic classification of environmental sounds with the mfcc method and the proposed deep model," *Firat Univ. J. Eng. Sci.*, vol. 34, pp. 449-457, 2022.
- [28] A. Baró, P. Riba, J. Calvo-Zaragoza, and A. Fornés, "From optical music recognition to handwritten music recognition: A baseline," *Pattern Recognit. Lett.*, vol. 123, pp. 1-8, 2019.
- [29] H. Tang, and N. Chen, "Combining CNN and Broad Learning for Music Classification," *IEICE Trans. Inf. Syst.*, vol. 103, pp. 695-701, 2020.
- [30] D. Snyder, D. Garcia-Romero, G. Sell, A. McCree, D. Povey, and S. Khudanpur, "Speaker recognition for multi-speaker conversations using x-vectors," *ICASSP 2019 - IEEE Int. Conf. Acoust., Speech, Signal Process. (ICASSP)*, pp. 5796-5800, 2019.
- [31] J. Villalba, N. Chen, D. Snyder, D. Garcia-Romero, A. McCree, G. Sell, J. Borgstrom, F. Richardson, S. Shon, F. Grondin, "State-of-the-art speaker recognition for telephone and video speech: The JHU-MIT submission for NIST SRE18," *Proc. Interspeech*, pp. 1488-1492, 2019.
- [32] J. Nicholson, K. Takahashi, and R. Nakatsu, "Emotion recognition in speech using neural networks," *Neural Comput. Appl.*, vol. 9, pp. 290-296, 2000.
- [33] Y.S. Seo, and J.-H. Huh, "Automatic emotion-based music classification for supporting intelligent IoT applications," *Electron.*, vol. 8, p. 164, 2019.
- [34] M. Yildirim, "Automatic diagnosis of snoring sounds with the developed artificial intelligence-based hybrid model," *Turk. J. Sci. Technol.*, vol. 17, pp. 405-416, 2022.
- [35] N. Takahashi, M. Gygli, B. Pfister, and L. Van Gool, "Deep convolutional neural networks and data augmentation for acoustic event detection," *arXiv preprint arXiv:1604.07160*, 2016.
- [36] X. Xia, R. Togneri, F. Sohel, and D. Huang, "Random forest classification based acoustic event detection utilizing contextual-information and bottleneck features," *Pattern Recognit.*, vol. 81, pp. 1-13, 2018.
- [37] X. Xia, R. Togneri, F. Sohel, and D. Huang, "Auxiliary classifier generative adversarial network with soft labels in imbalanced acoustic event detection," *IEEE Trans. Multimedia*, vol. 21, pp. 1359-1371, 2018.
- [38] F. Saki et al., "Open-set evolving acoustic scene classification system," 2019.
- [39] T. Doan, H. Nguyen, D. T. Ngo, L. Pham, and H. H. Kha, "Acoustic scene classification using a deeper training method for convolution neural network," *2019 Int. Symp. Electr. Electron. Eng. (ISEE)*, pp. 63-67, 2019.
- [40] J. Xie, and M. Zhu, "Investigation of acoustic and visual features for acoustic scene classification," *Expert Syst. Appl.*, vol. 126, pp. 20-29, 2019.
- [41] Y. Han, J. Park, and K. Lee, "Convolutional neural networks with binaural representations and background subtraction for acoustic scene classification," *Detec. and Classif. of Acou. Sce. and Events (DCASE)*, pp. 1-5, 2017.
- [42] L. Yang, L. Tao, X. Chen, and X. Gu, "Multi-scale semantic feature fusion and data augmentation for acoustic scene classification," *Appl. Acoust.*, vol. 163, p. 107238, 2020.
- [43] M. Jung, and S. Chi, "Human activity classification based on sound recognition and residual convolutional neural network," *Autom. Constr.*, vol. 114, p. 103177, 2020.
- [44] C.E. Galván-Tejada, F. López-Monteagudo, O. Alonso-González, J.I. Galván-Tejada, J.M. Celaya-Padilla, H. Gamboa-Rosales, R. Magallanes-Quintanar, L.A. Zanella-Calzada, "A generalized

- model for indoor location estimation using environmental sound from human activity recognition," *ISPRS Int. J. Geo-Inf.*, vol. 7, p. 81, 2018.
- [45] H. M. Do, K. C. Welch, and W. Sheng, "Soham: A sound-based human activity monitoring framework for home service robots," *IEEE Trans. Autom. Sci. Eng.*, 2021.
- [46] W. Wang, F. Seraj, N. Meratnia, and P. J. Havinga, "Privacy-aware environmental sound classification for indoor human activity recognition," *Proc. 12th ACM Int. Conf. Pervasive Technol. Assist. Environ.*, pp. 36-44, 2019.
- [47] A. Mesaros, T. Heittola, A. Eronen, and T. Virtanen, "Acoustic event detection in real life recordings," *18th Eur. Signal Process. Conf.*, pp. 1267-1271, 2010.
- [48] J. Goldberger, G. E. Hinton, S. Roweis, and R. R. Salakhutdinov, "Neighbourhood components analysis," *Adv. Neural Inf. Process. Syst.*, vol. 17, pp. 513-520, 2004.
- [49] S. R. Safavian and D. Landgrebe, "A survey of decision tree classifier methodology," *IEEE Trans. Syst. Man Cybern.*, vol. 21, pp. 660-674, 1991.
- [50] W. Zhao, R. Chellappa, and N. Nandhakumar, "Empirical performance analysis of linear discriminant classifiers," *Proc. IEEE Comput. Soc. Conf. Comput. Vision Pattern Recognit.*, pp. 164-169, 1998.
- [51] C. E. Thomaz, D. F. Gillies, and R. Q. Feitosa, "A new quadratic classifier applied to biometric recognition," *Int. Workshop Biometric Auth.*, Springer, pp. 186-196, 2002.
- [52] A. Y. Ng and M. I. Jordan, "On discriminative vs. generative classifiers: A comparison of logistic regression and naive bayes," *Adv. Neural Inf. Process. Syst.*, pp. 841-848, 2002.
- [53] V. Vapnik, "The support vector method of function estimation," *Nonlinear Modeling*, Springer, pp. 55-85, 1998.
- [54] L. E. Peterson, "K-nearest neighbor," *Scholarpedia*, vol. 4, p. 1883, 2009.
- [55] T. Hothorn and B. Lausen, "Bagging tree classifiers for laser scanning images: A data-and simulation-based strategy," *Artif. Intell. Med.*, vol. 27, pp. 65-79, 2003.
- [56] Q. K. Al-Shayea, "Artificial neural networks in medical diagnosis," *Int. J. Comput. Sci. Issues*, vol. 8, pp. 150-154, 2011.



Karma Mimarideki Çok-Girişli Çok-Çıkışlı Sistemde Seyrek Sinyal Geriçatım Yöntemlerini Kullanarak Milimetrik Dalga Kanalı Uzamsal Kovaryansının Kestirilmesi

Rıfat Volkan ŞENYUVA^{1*}

¹Elektrik-Elektronik Mühendisliği Bölümü, Mühendislik ve Doğa Bilimleri Fakültesi, Maltepe Üniversitesi, İstanbul, Türkiye.

¹rifatvolkansenyuva@maltepe.edu.tr

Geliş Tarihi: 21.01.2024

Kabul Tarihi: 7.06.2024

Düzeltilme Tarihi: 29.03.2024

doi: <https://doi.org/10.62520/fujece.1423312>

Araştırma Makalesi

Alıntı: R. V. Şenyuva, “Karma mimarideki çok-girişli çok-çıkışlı sistemde seyrek sinyal geriçatım yöntemlerini kullanarak milimetrik dalga kanalı uzamsal kovaryansının kestirilmesi”, Fırat Üni. Deny. ve Hes. Müh. Derg., vol. 4, no 1, pp. 30-43, Şubat 2025.

Öz

Bu çalışmada milimetrik dalga bandını kullanan darbant haberleşme sisteminde tek bir kullanıcıya ait kanalın kovaryans kestirimi incelenmektedir. Haberleşme sistemi zaman bölüşümlü çalışmaktadır ve kullanıcıdan baz istasyonu yönündeki kanal için kovaryans kestirimi yapılmaktadır. Baz istasyonu çok antenli ve radyo frekans (RF) zinciri hem analog hem sayısal birleştiricilerden oluşan çok-girişli çok-çıkışlı karma mimariye sahipken, kullanıcının tek anteni vardır. Ele alınan sistem modelinde ortak birleştirici matris yönteminin, milimetrik dalga kanalı uyum süresi boyunca gönderilen pilot bloklar için aynı birleştirici matrisinin uygulanması, kullanıldığı varsayılmaktadır. Seyrek sinyal geriçatım yöntemlerinden eşzamanlı normal uyum kovalama, çok ölçümlü seyrek Bayes öğrenme ve korelasyonlu seyrek Bayes öğrenmenin sistem modeline uygulanışı gösterilmektedir. İncelenen yöntemlerin sayısal sonuçları hesaplanarak normalleştirilmiş en küçük ortalama karesel hata başarımları değişen RF zincir sayısı ve milimetrik kanal seyreklik oranları için referans en küçük ortalama kare (EKOK) kestiricisiyle karşılaştırılmaktadır. Sayısal sonuçlar tüm deneylerde referans EKOK kestiricisine en yakın başarımların, korelasyonlu seyrek Bayes öğrenmeye ait olduğunu göstermektedir.

Anahtar kelimeler: Milimetrik dalga, Uzamsal kanal kovaryansı, Seyrek sinyal geriçatımı, Karma önkodlama

*Yazışılan Yazar

İntihal Kontrol: Evet – Turnitin

Şikayet: fujece@firat.edu.tr

Telif Hakkı ve Lisans: Dergide yayın yapan yazarlar, CC BY-NC 4.0 kapsamında lisanslanan çalışmalarının telif hakkını saklı tutar.



Covariance Estimation Of Millimeter Wave Channels Using Sparse Signal Recovery Algorithms In A Hybrid MIMO Architecture

Rıfat Volkan ŞENYUVA ^{1*} 

¹Department of Electrical-Electronics Engineering, Faculty of Engineering and Natural Sciences, Maltepe University, Istanbul, Türkiye.

¹rifatvolkansenyuva@maltepe.edu.tr

Received: 21.01.2024
Accepted: 7.06.2024

Revision: 29.03.2024

doi: <https://doi.org/10.62520/fujece.1423312>
Research Article

Citation: R. V. Senyuva, "Covariance estimation of millimeter wave channels using sparse signal recovery algorithms in a hybrid MIMO architecture", *Firat Univ. Jour. of Exper. and Comp. Eng.*, vol. 4, no 1, pp. 30-43, February 2025.

Abstract

In this paper, the channel covariance estimation of a single mobile station (MS) in a narrowband millimeter wave (mmWave) communication system was addressed. The communication system worked in time division duplex (TDD) mode and the channel covariance was estimated in the uplink communication. The base station (BS) had multiple antennas with a hybrid architecture of radio frequency (RF) chains made up of analog and digital combiners, while the MS had a single antenna. The investigated system model assumed the shared combining matrix scheme where the same combining matrix was used across multiple coherence blocks of the mmWave channel. The application of the sparse signal recovery algorithms including the simultaneous orthogonal matching pursuit (SOMP), the multiple response sparse Bayesian learning (MSBL), and the correlated sparse Bayesian learning (CSBL) to the system model were shown. The algorithms were evaluated numerically, and their normalized mean square error (NMSE) performances were compared against the benchmark oracle minimum mean square error (MMSE) estimator in multiple scenarios of varying number of RF chains at the BS and sparsity ratios for modeling the mmWave channel. The numerical results indicated that the CSBL algorithm provided the NMSE results closest to that of the oracle MMSE estimator in all the scenarios.

Keywords: Millimeter wave, Spatial channel covariance, Sparse signal recovery, Hybrid precoding

*Corresponding author

1. Introduction

Millimeter wave (mmWave) communication is one of the technologies considered for next-generation wireless systems [1-2]. The high data rate requirements of the next-generation wireless systems can be satisfied with the mmWave communication where the frequencies from 30 GHz up to 300 GHz with bandwidths as large as 2 GHz can be assigned to systems [1-2]. The signal processing at the mmWave frequencies is much more challenging than at lower frequencies due to new hardware constraints, different channel models, and the usage of large arrays. The power consumption and the high costs of circuits are important hardware constraints and to deal with them, the signal processing operations can be separated into analog and digital domains so that the number of analog-to-digital converters (ADC) can be reduced, or low-resolution ADCs may be used [3-5]. These hardware constraints have renewed the interest in the research of hybrid beamforming [6-7] and low-rate ADC methods [3-5]. The mmWave channel models must consider the drastic path loss due to attenuation at these frequencies. This makes estimation of the channel state information (CSI) of the mmWave systems very difficult since the signal-to-noise ratio (SNR) is poor without any application of beamforming. To mitigate the high propagation losses and improve the SNR, the mmWave systems need high beamforming gains which can only be achieved via large antenna arrays. These systems must employ hybrid analog-digital precoding techniques [6-7] to decrease the number of radio frequency (RF) chains needed at each antenna of the array so that the hardware costs can be maintained. The accurate full CSI is critical for the performance of these hybrid precoding techniques. Since the number of RF chains is less than the number of antennas in these hybrid systems, the received signal is lower dimensional which makes obtaining the full CSI even more challenging. There exist other hybrid precoding techniques which use spatial channel covariance instead of the full CSI. Thus, the channel covariance estimation is crucial in reaping the benefits of the hybrid mmWave systems.

A mmWave channel can be modeled as a sparse signal in the angular domain since the signals arrive in a small number of path clusters due to limited scatterers around the receiver. There is also spatial correlation since the antennas in the array are close to each other. Each signal with an angle of arrival correspond to a spatial frequency and the continuous domain of the spatial frequencies can be discretized into a finite set of grid points. If the true spatial frequencies are close to some of the grid points, the received signal at the t -th snapshot, $\tilde{\mathbf{y}}_t \in \mathbb{C}^{M \times 1}$, can be given as a linear system of equation,

$$\tilde{\mathbf{y}}_t = \Phi_t \mathbf{g}_t + \mathbf{z}_t, \quad t = 1, \dots, T. \quad (1)$$

In Equation (1), $\Phi_t \in \mathbb{C}^{M \times D}$ is the known dictionary matrix, $\mathbf{g}_t \in \mathbb{C}^{D \times 1}$ is the unknown mmWave channel vector, and the noise is shown as $\mathbf{z}_t \in \mathbb{C}^{M \times 1}$. This system of equations is underdetermined due to the reducing the number of RF chains via the hybrid precoding, i.e. $M \leq D$, and the unknown parameter vector \mathbf{g}_t is sparse with only $L \ll D$ nonzero entries. The covariance matrix, that determines the spatial correlation between the components of the channel vector, is assumed to remain constant during $t = 1, \dots, T$ snapshots. Finding a single solution amongst infinitely many requires imposing additional constraints in these underdetermined systems. Since the unknown mmWave channel vector is sparse, its nonzero entries can be estimated by applying the sparse signal recovery algorithms to Equation (1).

The point estimates of the correlated sparse mmWave channel of a single user can be obtained via the orthogonal matching pursuit (OMP) based algorithm proposed in [8]. However, the selection of the dictionary matrix, which must be done according to the restricted isometry property, determines the accuracy of the solutions provided by the OMP based algorithms. [9] proposes covariance estimation methods based on the simultaneous OMP (SOMP) algorithm for both fixed and varying dictionary matrices at each snapshot. The grid mismatch issue associated with the generation of the dictionary matrix for the greedy OMP and SOMP algorithms are addressed in the works [10-12]. While [10] proposes grid-less refinement steps for the OMP algorithm and a perturbation framework is given by [11] for the SOMP algorithm, [12] shows the implementation of a multigrid dictionary refinement scheme to be used with the SOMP algorithm. The out-of-band covariance information translated from a parallel sub-6 GHz system is used in the sparse recovery of the covariance of the wideband mmWave multiple-input multiple-output (MIMO) channel [13]. Multiple sparse Bayesian learning (MSBL) framework [14] utilizes expectation-maximization (EM) to find

probabilistic estimates of the unknown channel vector in Equation (1). Although the MSBL algorithm is more resilient to the selection of the dictionary matrix compared to the OMP based solutions, it uses a diagonal prior covariance matrix and so does not take the spatial correlation of the channel vector into account. The temporal correlation between the entries of the unknown channel vectors at different snapshots is considered in [15] where the measurement matrix made up from T measurements in Equation (1) is vectorized and a block MSBL algorithm is proposed. The correlated SBL (CSBL) algorithm [16] improves upon the MSBL algorithm by using a prior covariance matrix which is not diagonal and a much better model for the spatial correlation between the entries of the unknown channel vector. The CSBL algorithm has a computational disadvantage over the MSBL algorithm that it requires explicit calculation of the inverse of a precision matrix. A faster version of the CSBL algorithm with reduced complexity is proposed in [17]. The impact of the residual transceiver impairments in the components of the RF chain is examined for a narrowband mmWave hybrid MIMO system in [18]. A zero-attracting least mean square (ZALMS) adaptive filtering algorithm is proposed for the estimation of the downlink channel [18].

The covariance estimation of the mmWave channels in a narrowband hybrid MIMO communication system is investigated in this paper. In our system model a single mobile station (MS) with a single antenna is communicating to a base station (BS) with a mixture of analog and digital combiners in its RF chains and the estimation takes place during the uplink communication. Since the communication system works in time-division duplex (TDD) mode, the channel reciprocity allows the downlink communication to be precoded with the estimated uplink channel. The combining matrix is assumed to be shared across multiple pilot blocks transmitted by the MS within the coherence of the mmWave channel. We focus on covariance estimation methods using sparse signal reconstruction and show how the SOMP, the MSBL, and the CSBL algorithms can be applied to estimate the mmWave channel of a single MS communicating to a hybrid MIMO BS using the shared combining matrix scheme. The performances of the algorithms are compared in multiple scenarios with varying number of RF chains and mmWave channels with varying sparsity levels.

The remainder of this paper is arranged as: the models of the hybrid MIMO system and the mmWave channel are explained in Section 2. Then, the mmWave channel covariance estimation methods based on sparse signal recovery are presented in Section 3. The numerical evaluations of the methods are given in Section 4. Finally, Section 5 is the conclusions.

2. System Model

We consider a narrowband communication system operating in half-duplex TDD mode where either the BS or the MS is transmitting at one time. The total number of samples available within the coherence interval of the channel are divided into three subintervals: uplink data, uplink pilot, and downlink data [19]. The BS learns the CSI of the uplink channel via the symbols transmitted by the MS in the uplink pilot's subinterval of the coherence interval. Once the BS has acquired the uplink channel, it also has an estimate of the downlink channel due to the channel reciprocity that is the impulse response of the channel between any two antennas is the same [19]. In both uplink and downlink data transmissions, all complexity resides in the BS. In the uplink data transmission, the MS sets its power level and then transmits the data symbols, and the BS decodes the received symbols via either zero-forcing or maximum-ratio combining using the uplink channel estimate. Similarly in the downlink data transmission, the BS applies a linear precoding operation using either zero-forcing or maximum-ratio combining on the information bearing symbols before transmission [19]. The BS has a uniform linear array (ULA) of N antennas placed at equal distance from each other and M hybrid RF chains. An RF chain consists of components such as low-noise amplifiers, filters, mixers, converters, oscillators, ADCs, and automatic gain control [1,13,18]. The analog combiner connecting the antennas of the BS to its RF chains in Figure 1 is the RF combiner and it can be implemented using phase shifters which imposes unit norm entries in the analog combining matrix [1,18]. To convert the output of the RF chains to baseband, the BS must apply a second baseband combiner before the covariance of the channel can be estimated. The BS is communicating with a single MS which has a single antenna (Figure 1).

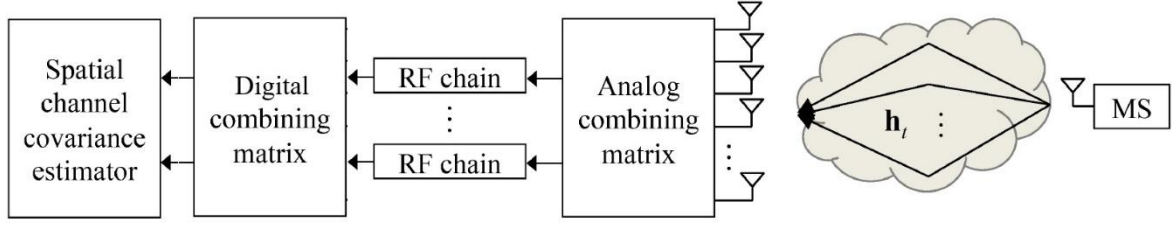


Figure 1. BS has N antennas and M RF chains while there is only a single antenna at the MS. The mmWave channel is represented with a narrowband geometric channel with L paths and the estimation of the channel covariance occurs in baseband [9]

The uplink mmWave channel from the MS and the BS is modeled according to the geometric channel model with L number of channel paths (Figure 1) as

$$\mathbf{h}_t = \sum_{l=1}^L \bar{g}_{t,l} \mathbf{b}(\phi_l) = \mathbf{B} \bar{\mathbf{g}}_t \quad (2)$$

where $\bar{\mathbf{g}}_t = [\bar{g}_{t,1} \ \cdots \ \bar{g}_{t,L}]^T \in \mathbb{C}^{L \times 1}$, $\bar{g}_{t,l}$ shows the gain of the l -th channel path at the t -th snapshot, and $\mathbf{B} = [\mathbf{b}(\phi_1) \ \cdots \ \mathbf{b}(\phi_L)] \in \mathbb{C}^{N \times L}$. A column of \mathbf{B} , i.e. $\mathbf{b}(\phi_l)$, is the array steering vector associated with the angle-of-arrival (AoA) of the l -th channel path, i.e. ϕ_l , is

$$\mathbf{b}(\phi_l) = [1 \ e^{-i\pi \cos \phi_l} \ \cdots \ e^{-i\pi(N-1) \cos \phi_l}]^T \quad (3)$$

In Equation (3) the spacing between the elements of the ULA at the BS is assumed to be equal to half of the wavelength and it is also assumed that the AoAs do not change for T snapshots.

A dictionary matrix, $\mathbf{A} = [\mathbf{a}(\phi_1) \ \cdots \ \mathbf{a}(\phi_D)] \in \mathbb{C}^{N \times D}$ can be built by creating a grid of $D \gg L$ points on the range of the spatial frequencies, i.e. $\mu_l = \cos \phi_l$, from -1 to +1 and Equation (2) can be rewritten using this dictionary matrix as

$$\mathbf{h}_t = \mathbf{A} \mathbf{g}_t \quad (4)$$

The path gain vector, $\mathbf{g}_t \in \mathbb{C}^{D \times 1}$, in Equation (4) has a support, the set of indices indicating to the nonzero entries, $\mathcal{S} = \{j: g_{t,j} \neq 0\}$, with L elements $|\mathcal{S}| = L$ and they correspond to the AoAs, $\{\phi_1, \dots, \phi_D\}$. The covariance matrix of the channel, $\mathbf{R}_h \in \mathbb{C}^{N \times N}$, can be written as

$$\mathbf{R}_h = \mathbb{E}\{\mathbf{h}_t \mathbf{h}_t^*\} = \mathbf{A} \mathbf{R}_g \mathbf{A}^* \quad (5)$$

in terms of $\mathbf{R}_g = \mathbb{E}\{\mathbf{g}_t \mathbf{g}_t^*\} \in \mathbb{C}^{D \times D}$, the covariance matrix of the path gains. $(\cdot)^*$ shows the Hermitian transpose. We assume that the components of the path gain vector, \mathbf{g}_t , are correlated with each other and so the entries of the covariance matrix are given as $[\mathbf{R}_g]_{(j,k)} = \rho_{j,k} \sqrt{\gamma_j} \sqrt{\gamma_k}$ where $\rho_{j,k}$ is correlation coefficient between the entries and γ_j is the variance of the j -th entry. The covariance matrix of the path gains can be written in matrix form as

$$\mathbf{R}_g = \mathbf{\Gamma}^{1/2} \mathbf{U} \mathbf{\Gamma}^{1/2} \quad (6)$$

where $\mathbf{\Gamma}^{1/2} = \text{diag}\{\sqrt{\gamma_1}, \dots, \sqrt{\gamma_D}\}$ and the entries of \mathbf{U} are $[\mathbf{U}]_{(j,k)} = \rho_{j,k}$.

The MS transmits a unit modulus pilot symbol, i.e. $|x_t| = 1$, and the received signal at the BS is

$$\mathbf{y}_t = \mathbf{A} \mathbf{g}_t x_t + \mathbf{n}_t \quad (7)$$

where $\mathbf{n}_t \in \mathbb{C}^{N \times 1}$ is the additive complex circularly symmetric Gaussian noise vector with the single-sided spectral density of each of its component being N_0 , i.e. $\mathbf{n}_t \sim \mathcal{CN}(\mathbf{0}, N_0 \mathbf{I})$. The received signal is multiplied with a hybrid combining matrix, $\mathbf{W}_t = \mathbf{W}_{\text{BB}} \mathbf{W}_{\text{RF}} \in \mathbb{C}^{M \times N}$, which is a cascade of the analog, $\mathbf{W}_{\text{RF}} \in \mathbb{C}^{M \times N}$, and digital, $\mathbf{W}_{\text{BB}} \in \mathbb{C}^{M \times M}$, combining matrices (Figure 1) and the conjugate of the pilot symbol, x_t^* , so that the result of this operation is the signal at baseband given as

$$\tilde{\mathbf{y}}_t = \mathbf{W}_t \mathbf{A} \mathbf{g}_t x_t x_t^* + \mathbf{W}_t \mathbf{n}_t x_t^* = \Phi_t \mathbf{g}_t + \mathbf{z}_t \quad (8)$$

where the overall sensing matrix is shown as $\Phi_t = \mathbf{W}_t \mathbf{A} \in \mathbb{C}^{M \times D}$ and the new noise vector, $\mathbf{z}_t = x_t^* \mathbf{W}_t \mathbf{n}_t \in \mathbb{C}^{M \times 1}$, is distributed as $\mathbf{z}_t \sim \mathcal{CN}(\mathbf{0}, |x_t|^2 N_0 \mathbf{W}_t \mathbf{W}_t^*)$. The conjugate transpose of a matrix is shown by superscript $(\cdot)^*$. Assuming that there are T snapshots in total and the hybrid combining matrix is fixed for each snapshot that is $\mathbf{W}_1 = \dots = \mathbf{W}_T = \mathbf{W}$, then the received signal vectors for $t = 1, \dots, T$ in Equation (8) can be rewritten as

$$\tilde{\mathbf{Y}} = \Phi \mathbf{G} + \mathbf{Z} \quad (9)$$

where the measurements are shown as $\tilde{\mathbf{Y}} = [\tilde{\mathbf{y}}_1 \dots \tilde{\mathbf{y}}_T] \in \mathbb{C}^{M \times T}$, the dictionary matrix is $\Phi = \mathbf{W} \mathbf{A} \in \mathbb{C}^{M \times D}$, $\mathbf{G} = [\mathbf{g}_1 \dots \mathbf{g}_T] \in \mathbb{C}^{D \times T}$, and $\mathbf{Z} = [\mathbf{z}_1 \dots \mathbf{z}_T] \in \mathbb{C}^{M \times T}$. The channel covariance estimation problem is to estimate \mathbf{R}_h given $\tilde{\mathbf{Y}}$.

3. Covariance Estimation Using Sparse Signal Reconstruction

Equation (9) is a multiple measurement vector problem, and the optimum solution can be found from

$$\min_{\tilde{\mathbf{G}}} \|\tilde{\mathbf{Y}} - \Phi \tilde{\mathbf{G}}\|_F \quad \text{subject to } \|\tilde{\mathbf{G}}\|_{\text{row-}0} \leq L \quad (10)$$

where the Frobenius norm of a matrix, $\tilde{\mathbf{Y}}$, is shown as $\|\tilde{\mathbf{Y}}\|_F = \left(\sum_m^M \sum_t^T |\tilde{y}_{m,t}|^2 \right)^{1/2}$ and the row- ℓ_0 quasi-norm of a matrix is defined as $\|\tilde{\mathbf{G}}\|_{\text{row-}0} = |\text{rowsupp}(\tilde{\mathbf{G}})|$ [7,16]. The row support of a matrix, $\tilde{\mathbf{G}}$, is the set of indices for its nonzero rows that is

$$\text{rowsupp}(\tilde{\mathbf{G}}) = \{j: [\tilde{\mathbf{G}}]_{(j,k)} \neq 0 \text{ for some } k\} \quad (11)$$

3.1. SOMP algorithm

The SOMP algorithm shown solves Equation (10). In each iteration the SOMP algorithm first finds the column of the dictionary matrix, Φ , that is best aligned with the current residual matrix \mathbf{V} [9,20-21] that is

$$j = \underset{d}{\text{argmax}} \|\phi_d^* \mathbf{V}\|_2, \quad d = 1, \dots, D. \quad (12)$$

The index set, Λ , is updated with the index of the best aligned column from Equation (12). Then a new residual is calculated by removing the projection of the measurement matrix along the direction of the chosen columns

$$\mathbf{V} = (\mathbf{I} - \Phi_\Lambda \Phi_\Lambda^*) \tilde{\mathbf{Y}} \quad (13)$$

where Φ_Λ is the submatrix constructed from the columns of Φ that correspond to the indices in the set, Λ [9,20-21].

The steps of the SOMP algorithm are shown in Figure 2. The SOMP algorithm iterates between steps 5-7. The computational complexity is dominated by the orthogonalization during the update of the residual matrix

in step 7. To reduce the computational complexity, the matrix decompositions such as Cholesky or QR can be applied. The SOMP algorithm implementing the QR matrix decomposition can terminate with a solution in $O(DML)$ operations [21].

```

1. begin
2. input:  $\Phi = \mathbf{W}\mathbf{A}, \tilde{\mathbf{Y}}, L$ 
3. initialize:  $\mathbf{V} = \tilde{\mathbf{Y}}, \Lambda = \emptyset, \hat{\mathbf{G}}_{\text{SOMP}} = \mathbf{0}$ 
4. for  $l = 1:L$  do
5.      $j = \underset{d}{\operatorname{argmax}} \|\phi_d^* \mathbf{V}\|_2$ 
6.      $\Lambda = \Lambda \cup \{j\}$ 
7.      $\mathbf{V} = (\mathbf{I} - \Phi_\Lambda \Phi_\Lambda^*) \tilde{\mathbf{Y}}$ 
8. end for
9.  $[\hat{\mathbf{G}}_{\text{SOMP}}]_{(\Lambda,:)} = \Phi_\Lambda^* \tilde{\mathbf{Y}}$ 
10. output:  $\hat{\mathbf{G}}_{\text{SOMP}}, \hat{\mathbf{H}}_{\text{SOMP}} = \mathbf{A}_\Lambda \hat{\mathbf{G}}_{\text{SOMP}}$ 

```

Figure 2. The pseudocode of the SOMP algorithm

Once the path gains, \mathbf{g}_t 's are estimated via $\hat{\mathbf{G}}_{\text{SOMP}}$, then the covariance channel matrix can be found using $\hat{\mathbf{R}}_{\mathbf{g}} = (1/T)\hat{\mathbf{G}}_{\text{SOMP}}\hat{\mathbf{G}}_{\text{SOMP}}^*$ as in

$$\hat{\mathbf{R}}_{\mathbf{h}} = \mathbf{A}\hat{\mathbf{R}}_{\mathbf{g}}\mathbf{A}^* \quad (14)$$

3.2. MSBL algorithm

The MSBL algorithm calculates the maximum a posteriori (MAP) estimates of the channel path gains using the expectation-maximization (EM) method [14-15]. Given $\tilde{\mathbf{y}}_t$, the posterior conditional density of the path gain vector, \mathbf{g}_t , is circularly symmetric complex Gaussian with $\mathbf{g}_t \sim \mathcal{CN}(\boldsymbol{\mu}_{\text{MSBL}_t}, \boldsymbol{\Sigma}_{\text{MSBL}})$ [14]. The expectation step (E-step) of the MSBL algorithm calculates the mean and the covariance of the Gaussian distribution according to

$$\boldsymbol{\mu}_{\text{MSBL}_t} = \boldsymbol{\Gamma}_{\text{MSBL}} \boldsymbol{\Phi}^* \boldsymbol{\Omega}_{\text{MSBL}}^{-1} \tilde{\mathbf{y}}_t \quad (15)$$

$$\boldsymbol{\Sigma}_{\text{MSBL}} = \boldsymbol{\Gamma}_{\text{MSBL}} - \boldsymbol{\Gamma}_{\text{MSBL}} \boldsymbol{\Phi}^* \boldsymbol{\Omega}_{\text{MSBL}}^{-1} \boldsymbol{\Phi} \boldsymbol{\Gamma}_{\text{MSBL}} \quad (16)$$

respectively. In Equations (15) and (16), $\boldsymbol{\Gamma}_{\text{MSBL}} = \operatorname{diag}\{\hat{\boldsymbol{\gamma}}_{\text{MSBL}}\} \in \mathbb{C}^{D \times D}$ and $\boldsymbol{\Omega}_{\text{MSBL}} = N_0 \mathbf{I} + \boldsymbol{\Phi} \boldsymbol{\Gamma}_{\text{MSBL}} \boldsymbol{\Phi}^* \in \mathbb{C}^{M \times M}$ [14]. The maximization step (M-step) of the algorithm updates $\hat{\boldsymbol{\gamma}}_{\text{MSBL}} = [\hat{\gamma}_1, \dots, \hat{\gamma}_D]$ according to

$$\hat{\gamma}_d = \frac{1}{T} \left\| [\mathbf{M}_{\text{MSBL}}]_{(d,:)} \right\|_2^2 + [\boldsymbol{\Sigma}_{\text{MSBL}}]_{(d,d)}, d = 1, \dots, D \quad (17)$$

The posterior mean matrix shown as \mathbf{M}_{MSBL} in Equation (17) is the concatenation of the mean vectors that is $\mathbf{M}_{\text{MSBL}} = [\boldsymbol{\mu}_{\text{MSBL}_1}, \dots, \boldsymbol{\mu}_{\text{MSBL}_T}] \in \mathbb{C}^{D \times T}$ and the d -th row of \mathbf{M}_{MSBL} is shown as $[\mathbf{M}_{\text{MSBL}}]_{(d,:)}$ [14].

The pseudocode of the MSBL algorithm shown in Figure 3. The MSBL algorithm requires the variance of the noise, N_0 , to be supplied as an input. The first step of the MSBL is the initialization of the variance parameter vector

$$\hat{\boldsymbol{\gamma}}_{\text{MSBL}} = [\hat{\gamma}_1, \dots, \hat{\gamma}_D] = [1, \dots, 1] = \mathbf{1}_D \quad (18)$$

where $\mathbf{1}_D$ is a column vector of size $D \times 1$ with all its elements equal to 1. Then the MSBL iterates between the E- and M-steps, lines 6-9 (Figure 3), until convergence is achieved, or a fixed number of loops have been run. There is no need to explicitly invert the matrix, $\boldsymbol{\Omega}_{\text{MSBL}}$, in steps 7 and 8. Instead the Moore-Penrose pseudo-inverse which is way more efficient than explicit matrix inversion can be calculated. The computational complexity of the MSBL algorithm is $O(DM(M + T))$ [16].

```

1. begin
2. input:  $\Phi = \mathbf{W}\mathbf{A}$ ,  $\tilde{\mathbf{Y}}$ ,  $N_0$ 
3. initialize:  $\hat{\mathbf{y}}_{\text{MSBL}} = [1, \dots, 1] = \mathbf{1}$ 
4. for  $i = 1$ : maxIter do
5.      $\mathbf{\Gamma}_{\text{MSBL}} = \text{diag}\{\hat{\mathbf{y}}_{\text{MSBL}}\}$ 
6.      $\mathbf{\Omega}_{\text{MSBL}} = N_0\mathbf{I} + \Phi\mathbf{\Gamma}_{\text{MSBL}}\Phi^*$ 
7.      $\mathbf{\Sigma}_{\text{MSBL}} = \mathbf{\Gamma}_{\text{MSBL}} - \mathbf{\Gamma}_{\text{MSBL}}\Phi^*\mathbf{\Omega}_{\text{MSBL}}^{-1}\Phi\mathbf{\Gamma}_{\text{MSBL}}$ 
8.      $\mathbf{M}_{\text{MSBL}} = \mathbf{\Gamma}_{\text{MSBL}}\Phi^*\mathbf{\Omega}_{\text{MSBL}}^{-1}\tilde{\mathbf{Y}}$ 
9.      $\hat{y}_d = (1/T)\|\mathbf{M}_{\text{MSBL}}\|_{(d,:)}\|_2^2 + [\mathbf{\Sigma}_{\text{MSBL}}]_{(d,d)}, \forall d$ 
10. end for
11. output:  $\hat{\mathbf{G}}_{\text{MSBL}} = \mathbf{M}_{\text{MSBL}}$ ,  $\hat{\mathbf{H}}_{\text{MSBL}} = \mathbf{A}\hat{\mathbf{G}}_{\text{MSBL}}$ ,  $\hat{\mathbf{Y}}_{\text{MSBL}}$ 

```

Figure 3. The pseudocode of the MSBL algorithm

3.3. CSBL algorithm

The CSBL algorithm uses a nondiagonal prior covariance matrix to model the correlations between the entries of the path gain vector. The posterior conditional probability density function of \mathbf{g}_t given $\tilde{\mathbf{y}}_t$ is circularly symmetric complex Gaussian with $\mathbf{g}_t \sim \mathcal{CN}(\boldsymbol{\mu}_{\text{CSBL}_t}, \boldsymbol{\Sigma}_{\text{CSBL}}^{-1})$ where the mean vector, $\boldsymbol{\mu}_{\text{CSBL}_t}$, and the posterior precision matrix, $\boldsymbol{\Sigma}_{\text{CSBL}}$, are given [16-17]

$$\boldsymbol{\mu}_{\text{CSBL}_t} = (1/N_0)\boldsymbol{\Sigma}_{\text{CSBL}}^{-1}\Phi^*\tilde{\mathbf{y}}_t \quad (19)$$

$$\boldsymbol{\Sigma}_{\text{CSBL}} = (1/N_0)(\Phi^*\Phi) + \boldsymbol{\Omega}_{\text{CSBL}} \quad (20)$$

respectively. The precision matrix, $\boldsymbol{\Omega}_{\text{CSBL}}$, in Equation (20) is given as

$$\boldsymbol{\Omega}_{\text{CSBL}} = \text{diag}\{\mathbf{c}\}\mathbf{U}^{-1}\text{diag}\{\mathbf{c}\} \quad (21)$$

where i -th entry of the parameter vector $\mathbf{c} \in \mathbb{C}^{D \times 1}$ is $c_i = 1/\sqrt{\hat{y}_i}$ and \mathbf{U}^{-1} is the inverse of the correlation coefficient matrix, \mathbf{U} [16-17]. The M-step of the EM algorithm calculates the new parameter vector, \mathbf{c}_{new} , using the old parameter vector, \mathbf{c}_{old} , as in

$$\mathbf{c}_{\text{new}} = [\Re\{\mathbf{U}^{-1} \odot \hat{\mathbf{R}}_{\mathbf{g}}^T\}]^{-1} \mathbf{c}_{\text{old}} \quad (22)$$

where \odot is the elementwise Hadamard product between two matrices of same dimensions and $\Re\{\cdot\}$ takes the real part of its argument. The estimate of the covariance matrix of the path gain vector in Equation (22) is [16-17]

$$\hat{\mathbf{R}}_{\mathbf{g}} = \boldsymbol{\Sigma}_{\text{CSBL}}^{-1} + \frac{1}{T} \sum_{t=1}^T \boldsymbol{\mu}_{\text{CSBL}_t} \boldsymbol{\mu}_{\text{CSBL}_t}^* \quad (23)$$

The pseudocode of the CSBL algorithm is given in Figure 4. The CSBL algorithm requires the coefficient matrix, \mathbf{U} , in addition to the noise variance when compared to the pseudocode of the MSBL algorithm in Figure 3. As it can be observed from the pseudocode of the CSBL algorithm (Figure 4), there are two explicit matrix inversion operations in step 8, i.e. the inversion of the post precision matrix $\boldsymbol{\Sigma}_{\text{CSBL}}^{-1}$, and in step 9, i.e. the inversion of the coefficient matrix \mathbf{U}^{-1} . Instead of inverting the whole coefficient matrix which is of size $D \times D$, only the submatrix of size $L \times L$ residing within the rows and columns of \mathbf{U} corresponding to the indices of the nonzero entries of \mathbf{c} should be inverted since the rest of nondiagonal elements of the matrix is zero [17]. The computational complexity of the CSBL algorithm is $O(DM(M+T) + D^3)$ [16].

```

1. begin
2. input:  $\Phi = \mathbf{W}\mathbf{A}, \tilde{\mathbf{Y}}, \mathbf{U}, N_0$ 
3. initialize:  $\mathbf{c}_0 = [1, \dots, 1] = \mathbf{1}_D$ 
4. for  $i = 1$ : maxIter do
5.      $\mathbf{\Omega}_{\text{CSBL}} = \text{diag}\{\mathbf{c}_i\}\mathbf{U}^{-1}\text{diag}\{\mathbf{c}_i\}$ 
6.      $\mathbf{\Sigma}_{\text{CSBL}} = (1/N_0)(\Phi^*\Phi) + \mathbf{\Omega}_{\text{CSBL}}$ 
7.      $\mathbf{M}_{\text{CSBL}} = [\boldsymbol{\mu}_{\text{CSBL}_1}, \dots, \boldsymbol{\mu}_{\text{CSBL}_T}] = (1/N_0)\mathbf{\Sigma}_{\text{CSBL}}^{-1}\Phi^*\tilde{\mathbf{Y}}$ 
8.      $\hat{\mathbf{R}}_{\mathbf{g}} = \mathbf{\Sigma}_{\text{CSBL}}^{-1} - (1/T)(\mathbf{M}_{\text{CSBL}}\mathbf{M}_{\text{CSBL}}^*)$ 
9.      $\mathbf{c}_i = [\Re\{\mathbf{U}^{-1}\odot\hat{\mathbf{R}}_{\mathbf{g}}^T\}]^{-1}\mathbf{c}_{i-1}^{-1}$ 
10. end for
11. output:  $\hat{\mathbf{G}}_{\text{CSBL}} = \mathbf{M}_{\text{CSBL}}, \hat{\mathbf{H}}_{\text{CSBL}} = \mathbf{A}\hat{\mathbf{G}}_{\text{CSBL}}, \hat{\mathbf{Y}}_{\text{CSBL}} = \mathbf{c}_i^{-1}$ 

```

Figure 4. The pseudocode of the CSBL algorithm

4. Numerical Results

We now compare the normalized mean squared error (NMSE) results of the algorithms. The NMSE obtained via one of the algorithms is calculated as

$$\text{NMSE}_o = 10 \log_{10} \left(\frac{1}{R} \sum_{r=1}^R \frac{\|\hat{\mathbf{H}}_{o,r} - \mathbf{H}_r\|_F^2}{\|\mathbf{H}_r\|_F^2} \right) \quad (24)$$

where the total number of Monte Carlo iterations is fixed as $R = 1000$ for each numerical result. $\hat{\mathbf{H}}_{o,r}$ in Equation (24) denotes the estimate of the channel matrix at the r -th Monte Carlo iteration, $\mathbf{H}_r = [\mathbf{h}_1 \dots \mathbf{h}_T] \in \mathbb{C}^{N \times T}$, provided by the algorithms, $o \in \{\text{SOMP}, \text{MSBL}, \text{CSBL}\}$. The NMSE results are shown versus the pilot-to-noise-ratio (PNR) which is defined as

$$\text{PNR} = 10 \log_{10}(1/N_0). \quad (25)$$

For all the presented numerical results, the NMSE curves from Equation (24) is plotted against the PNR (Equation (25)) range between 0 dB to 20 dB. For the dictionary matrix, Φ , to be an equal-norm equiangular tight frame, the analog combining matrix is generated according to [9]

$$\mathbf{W} = \mathbf{W}_{\text{BB}} \mathbf{W}_{\text{RF}} = (\mathbf{W}_{\text{RF}} \mathbf{W}_{\text{RF}}^*)^{-1/2} \mathbf{W}_{\text{RF}} \quad (26)$$

where $(\mathbf{W}_{\text{RF}} \mathbf{W}_{\text{RF}}^*)^{1/2}$ is the principal square root of the matrix $\mathbf{W}_{\text{RF}} \mathbf{W}_{\text{RF}}^*$ and each element of \mathbf{W}_{RF} has a constant amplitude, $1/\sqrt{N}$, and a random phase independent and identically uniformly distributed in $[0, 2\pi]$ [9,16]. The conventional least squares (LS) and minimum mean-squared-error (MMSE) estimators are used as benchmark against the algorithms. The LS and MMSE estimators are given as

$$\hat{\mathbf{H}}_{\text{LS}} = (\Phi_{\mathcal{S}}^* \Phi_{\mathcal{S}})^{-1} \Phi_{\mathcal{S}}^* \tilde{\mathbf{Y}} \quad (27)$$

$$\hat{\mathbf{H}}_{\text{MMSE}} = \mathbf{R}_{\mathbf{g}} \Phi_{\mathcal{S}}^* \left(\Phi_{\mathcal{S}} \mathbf{R}_{\mathbf{g}} \Phi_{\mathcal{S}}^* + \frac{1}{N_0} \mathbf{I}_M \right)^{-1} \tilde{\mathbf{Y}} \quad (28)$$

where $\Phi_{\mathcal{S}} = \mathbf{W}\mathbf{A}_{\mathcal{S}}$ and $\mathbf{A}_{\mathcal{S}}$ is the submatrix constructed by extracting the columns from \mathbf{A} corresponding to the support of the path gain vector, \mathcal{S} . Since these estimators require the support of the path gain vector, \mathcal{S} , to be known prior, they are called oracle LS and oracle MMSE respectively. For all the numerical results, the numbers of antennas at the BS and snapshots are fixed at $N = 64$ and $T = 10$ respectively. The column size of the dictionary matrix is set to $D = 128$ and the support of the path gain vector, \mathcal{S} , randomly sampled from $\{1, \dots, D\}$ at each Monte Carlo iteration. The entries of the correlation coefficient matrix, \mathbf{U} , is generated according to $\rho_{j,k} = \rho^{|j-k|}$ where $\rho = 0.95$.

The NMSE curves plotted in Figure 5 are obtained when the number of nonzero entries of the channel path gain vector is fixed at $L = 4$ and the number of RF chains at the BS is taking values from $M \in \{32,48\}$. The effect of M on the estimation performance is critical since hybrid precoding requires $M < N$ to be power efficient. For both M values, the lowest NMSE results are obtained via the two benchmark methods: the LS and the MMSE estimators. Also due to the small L , the performances of the MMSE and the LS are almost equal for high PNR of 20 dB. There is about 2 dB gap between the MMSE for $M = 32$ and the MMSE for $M = 48$. This means that decreasing M from 48 to 32 incur 2 dB penalty on the best attainable estimation performance. Decreasing the number of RF chains result in extra additional noise on the measurements which causes all the NMSE results to increase. The overall best performing algorithm is the CSBL algorithm, while the MSBL algorithm takes the second place. For $M = 48$, the NMSE of the SOMP is the closest to the benchmark methods up to 10 dB. The SOMP results become saturated as the PNR increases beyond 10 dB. This advantage of the SOMP algorithm disappears when the number of RF chains is decreased to $M = 32$. The SOMP algorithm is more sensitive to M compared to the rest of the algorithms.

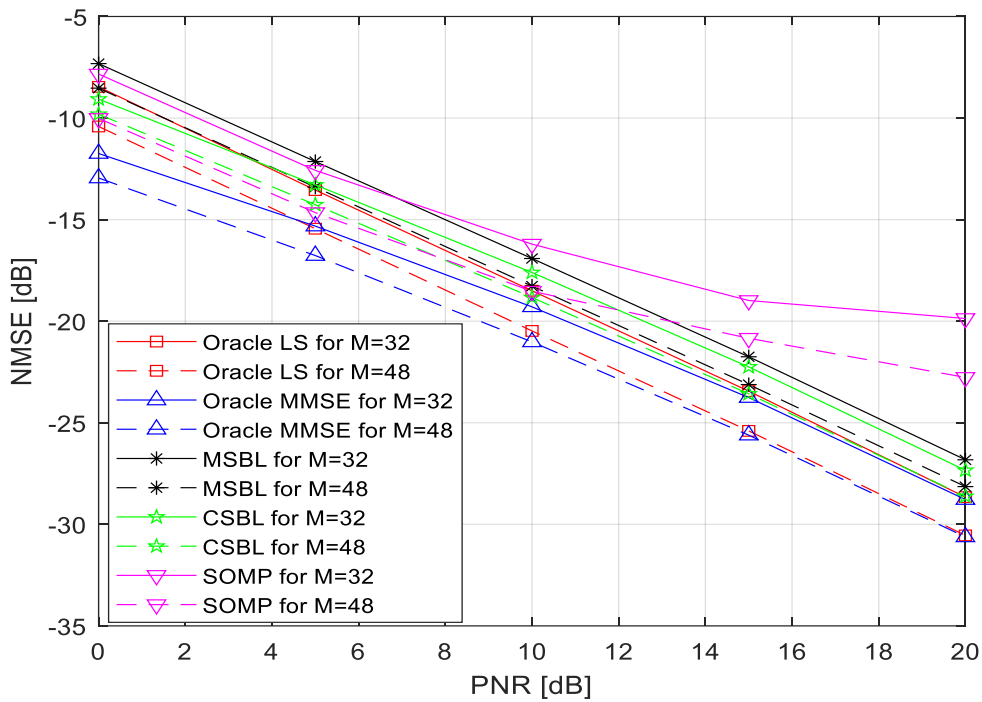


Figure 5. NMSE versus PNR for $N = 64$, $T = 10$, $M \in \{32,48\}$ and $L = 4$

Figure 6 shows the NMSE results when the number of RF chains is fixed at $M = 48$ and the number of nonzero taps of the channel path gain vector is taking values from $L \in \{4,16\}$. When L is increased from 4 to 16, the NMSE results of all the algorithms degrades. Also, the correlations between the nonzero entries of the channel vector become more critical on the estimation performance. Since the CSBL algorithm exploits the correlations of the channel vector, its performance remains close to the MMSE estimator. The MSBL algorithm can perform as good as the oracle LS estimator and unlike the oracle LS estimator, the MSBL algorithm does not need the prior knowledge of the path gain vector support. Since the channel is less sparse due to the increased sparsity ratio, the greedy SOMP algorithm gives the highest NMSE curve. For $L = 16$, the CSBL algorithm can follow the lowest NMSE curve obtained via the oracle MMSE estimator with a less than 2 dB PNR gap. The MSBL algorithm is as good as the oracle LS estimator and even better for the PNR range less than 5 dB.

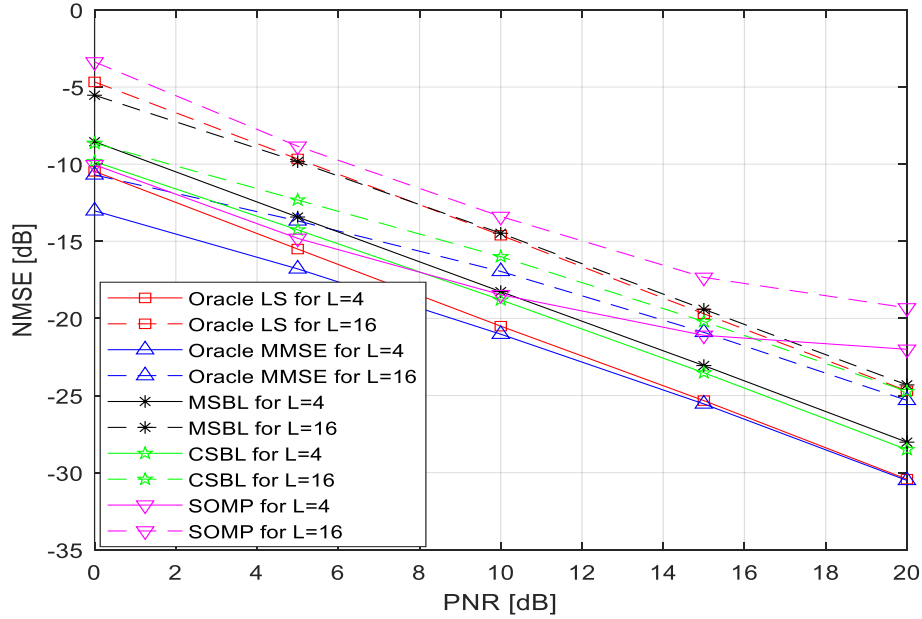


Figure 6. NMSE versus PNR for $N = 64, T = 10, M = 48$ and $L \in \{4,16\}$

The convergence of the NMSE results versus the number of iterations is shown in Figure 7. The number of the mm Wave channel taps and the PNR are fixed at $L = 4$ and 15 dB respectively. The number of the RF chains is $M \in \{32,48\}$ and the number of iterations is varying as $\maxIter \in [10,100]$. The SOMP algorithm always run for fixed number of iterations which is the number of the mmWave channel taps and so its NMSE performance remains constant across varying iterations. The performances of the EM based MSBL and CSBL algorithms depend on the number of iterations. For $M = 32$ at 10 iterations, the gap between the CSBL and the MSBL is almost 10 dB. As the number of iterations increase, the gap diminishes to less than 1 dB. The CSBL algorithm can converge at 60th iteration, while the MSBL algorithm requires 100 iterations for both M values. The CSBL algorithm converges faster and to a lower NMSE level than the MSBL algorithm.

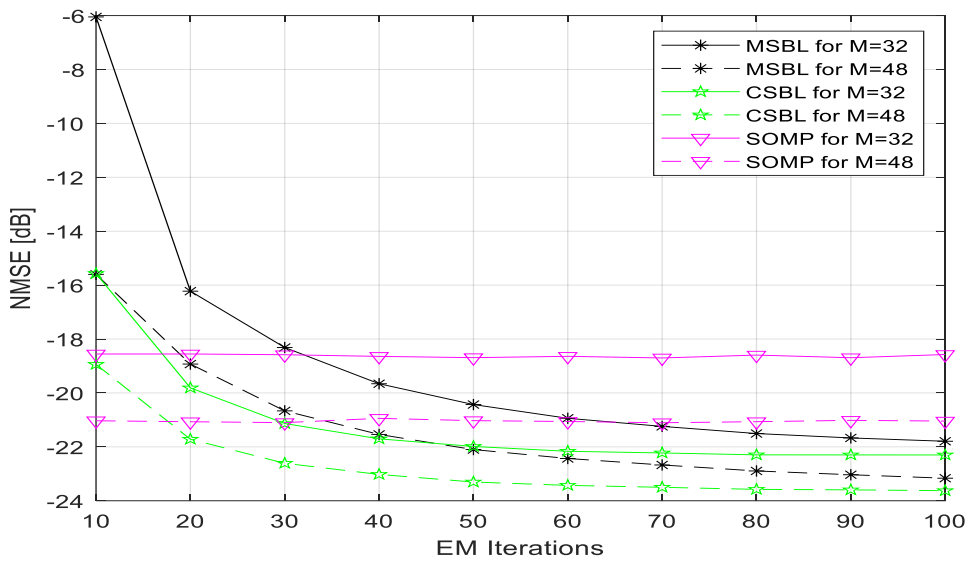


Figure 7. NMSE versus number of iterations for $N = 64, T = 10, M \in \{32,48\}$ and $L = 4$

5. Conclusion

This paper investigates sparse signal recovery based covariance estimation of the uplink channel of a single MS in a MIMO mmWave communication system. The BS has a hybrid RF chain and applies the same combining matrix for multiple coherence blocks of the channel estimation phase. We present how the sparse signal recovery algorithms including the SOMP, the MSBL, and the CSBL algorithms can be applied to estimate the covariance of the mmWave channel using the shared combining matrix scheme. The performances of the algorithms are compared in terms of their NMSE against the benchmark oracle MMSE and LS estimators under multiple scenarios with varying number of RF chains and sparsity levels for the mmWave channel. The numerical results show that the performance of the CSBL is superior to the MSBL and the SOMP algorithms for all the considered scenarios. Although the CSBL has superior performance, its computational complexity is the highest due to explicit matrix inversions. The CSBL can exploit the correlations between the nonzero entries of the mmWave channel vector, but the coefficient matrix must be supplied as an input. The coefficient matrix holding the correlations of the mmWave channel vector must be learned before the CSBL can be applied. The MSBL algorithm can be implemented without matrix inversions and so its complexity is much lower compared to the CSBL. However, the MSBL cannot estimate as well as the CSBL and requires the noise variance as an input. The SOMP algorithm, on the other hand, requires the least input and has the lowest computational complexity. Decreasing the number of the RF chains or increasing the number of nonzero entries of the mmWave channel is detrimental to its performance.

6. Author Contribution Statement

In the study, Author 1 contributed to conceptualization, data curation, formal analysis, investigation, methodology, validation, visualization, writing – original draft, writing - review and editing.

7. Ethics Committee Approval and Conflict of Interest

Ethics committee approval is not needed for preparing the article. There is no conflict of interest for this article.

8. References

- [1] R. W. Heath, N. González-Prelcic, S. Rangan, W. Roh, and A. M. Sayeed, "An Overview of Signal Processing Techniques for Millimeter Wave MIMO Systems," *IEEE J. Sel. Topics Signal Process.*, vol. 10, no. 3, pp. 436-453, 2016.
- [2] T. S. Rappaport, Y. Xing, O. Kanhere, S. Ju, A. Madanayake, and S. Mandal, "Wireless Communications and Applications Above 100 GHz: Opportunities and Challenges for 6G and Beyond," *IEEE Access*, vol. 7, pp. 78729-78757, 2019.
- [3] J. Mo, P. Schniter, and R. W. Heath, "Channel Estimation in Broadband Millimeter Wave MIMO Systems with Few-Bit ADCs," *IEEE Trans. Signal Process.*, vol. 66, no. 5, pp. 1141-1154, 2018.
- [4] S. Huang, D. Qiu, and T. D. Tran, "Bayesian Massive MIMO Channel Estimation with Parameter Estimation Using Low-Resolution ADCs," in *IEEE ICASSP*, Toronto, Canada, pp. 4830-4834, 2021.
- [5] R. Zhang, L. Yang, M. Tang, W. Tan, and J. Zhao, "Channel Estimation for mmWave Massive MIMO Systems with Mixed-ADC Architecture," *IEEE Open J. Comm. Soc.*, vol. 4, pp. 606-613, 2023.
- [6] X. Yu, J. -C. Shen, J. Zhang, and K. B. Letaief, "Alternating Minimization Algorithms for Hybrid Precoding in Millimeter Wave MIMO Systems," *IEEE J. Sel. Topics Signal Process.*, vol. 10, no. 3, pp. 485-500, 2016.
- [7] X. Xue, Y. Wang, L. Yang, J. Shi, and Z. Li, "Energy-Efficient Hybrid Precoding for Massive MIMO mmWave Systems With a Fully-Adaptive-Connected Structure," *IEEE Trans. Comm.*, vol. 68, no. 6, pp. 3521-3535, 2020.
- [8] J. Lee, G. -T. Gil, and Y. H. Lee, "Channel Estimation via Orthogonal Matching Pursuit for Hybrid MIMO Systems in Millimeter Wave Communications," *IEEE Trans. Comm.*, vol. 64, no. 6, pp. 2370-2386, 2016.
- [9] S. Park, and R. W. Heath, "Spatial Channel Covariance Estimation for the Hybrid MIMO Architecture: A Compressive Sensing-Based Approach," *IEEE Trans. Wireless Comm.*, vol. 17, no. 12, pp. 8047-8062, 2018.
- [10] L. Weiland, C. Stöckle, M. Würth, T. Weinberger, and W. Utschick, "OMP with Grid-Less Refinement Steps for Compressive mmWave MIMO Channel Estimation," in *IEEE 10th SAM*, pp. 543-547, 2018.
- [11] C. K. Anjinappa, A. C. Gürbüz, Y. Yapıcı, and İ. Güvenç, "Off-Grid Aware Channel and Covariance Estimation in mmWave Networks," *IEEE Trans. Comm.*, vol. 68, no. 6, pp. 3908-3921, 2020.
- [12] R. V. Şenyuva, and E. Anarım, "Multigrid Based Sparse Recovery Method for Multidimensional Harmonic Retrieval," in *IEEE 28th SIU*, pp. 1-4, 2020.
- [13] A. Ali, N. González-Prelcic, and R. W. Heath, "Spatial Covariance Estimation for Millimeter Wave Hybrid Systems Using Out-of-Band Information," *IEEE Trans. Wireless Comm.*, vol. 18, no. 12, pp. 5471-5485, 2019.
- [14] D. P. Wipf, and B. D. Rao, "An Empirical Bayesian Strategy for Solving the Simultaneous Sparse Approximation Problem," *IEEE Trans. Signal Process.*, vol. 55, no. 7, pp. 3704-3716, 2007.
- [15] Z. Zhang, and B. D. Rao, "Sparse Signal Recovery with Temporally Correlated Source Vectors Using Sparse Bayesian Learning," *IEEE J. Sel. Topics Signal Process.*, vol. 5, no. 5, pp. 912-926, 2011.
- [16] D. Prasanna, and C. R. Murthy, "mmWave Channel Estimation via Compressive Covariance Estimation: Role of Sparsity and Intra-Vector Correlation," *IEEE Trans. Signal Process.*, vol. 69, pp. 2356-2370, 2021.
- [17] J. N. Pisharody, A. Rajoriya, N. Gupta, and R. Budhiraja, "Fast Correlated SBL Algorithm for Estimating Correlated Sparse Millimeter Wave Channels," *IEEE Comm. Letters*, vol. 27, no. 5, pp. 1407-1411, 2023.
- [18] V. B. Shukla, R. Mitra, O. Krejcar, V. Bhatia, and K. Choi, "Performance Analysis of Sparse Channel Estimators for Millimeter Wave Hybrid MIMO Systems With Non-Ideal Hardware," *IEEE Trans. on Veh. Tech.*, vol. 72, no. 9, pp. 11913-11923, 2023.
- [19] T. L. Marzetta, E. G. Larsson, H. Yang, and H. Q. Ngo, *Fundamentals of Massive MIMO*, Cambridge: Cambridge University Press, 2016.

- [20] J. A. Tropp, A. C. Gilbert, and M. J. Strauss, "Algorithms for simultaneous sparse approximation. Part I: Greedy pursuit," *EURASIP J. Signal Process.*, vol. 86, pp. 572-588, 2006.
- [21] B. L. Sturmfels, and M. G. Christensen, "Comparison of orthogonal matching pursuit implementations," in *20th EUSIPCO*, pp. 220-224, 2012.



Modüler Çok Seviyeli Dönüştürücü Topolojisi İçin En Yakın Seviye Modülasyon Yönteminin FPGA Tabanlı Dijital Kontrol Şemasının Tasarımı ve Deneysel Doğrulaması

Mehmet KURTOĞLU^{1*}, Fatih EROĞLU², Ahmet Mete VURAL³

¹Elektrik-Elektronik Mühendisliği Bölümü, Mühendislik ve Doğa Bilimleri Fakültesi, İskenderun Teknik Üniversitesi, Hatay, Türkiye.

²TOFAŞ Türk Otomobil Fabrikası A.Ş., ARGE, Güç Sistemleri Müdürlüğü, Bursa, Türkiye.

³Elektrik-Elektronik Mühendisliği Bölümü, Mühendislik Fakültesi, Gaziantep Üniversitesi, Gaziantep, Türkiye.

¹mehmet.kurtoglu@iste.edu.tr, ²fatih.eroglu2@tofas.com.tr, ³mvural@gantep.edu.tr

Geliş Tarihi: 23.03.2024
Kabul Tarihi: 12.06.2024

Düzeltilme Tarihi: 24.05.2024

doi: <https://doi.org/10.62520/fujece.1457671>
Araştırma Makalesi

Alıntı: M. Kurtoglu, F. Eroglu ve A. M. Vural, "Modüler çok seviyeli dönüştürücü topolojisi için en yakın seviye modülasyon yönteminin FPGA tabanlı dijital kontrol şemasının tasarımı ve deneysel doğrulaması", Fırat Üni. Deny. ve Hes. Müh. Derg., vol. 4, no 1, pp. 44-58, Şubat 2025.

Öz

Modüler çok seviyeli dönüştürücü (MÇD), en yakın seviye modülasyonu (ESM) tekniğinin çoğunlukla MÇD'nin kol gerilimlerini kontrol etmek için kullanıldığı endüstriyel uygulamalar için tercih edilen bir devre topolojisi haline gelmiştir. ESM yönteminin MÇD topolojisi üzerinde dijital kontrol teknikleri kullanılarak uygulanması; esnek tasarım, tam kontrol edilebilirlik, yeniden yapılandırılabilir özellik ve modüler gerçekleştirme nedeniyle araştırmacılar arasında önem kazanmaktadır. Bu amaca ulaşmak için yüksek hız performansı ve paralel işlem yapabilme gibi avantajları sayesinde alanda programlanabilir kapı dizileri (FPGA'lar) kullanılmaktadır. Buna göre, bu makalede, tek fazlı beş seviyeli MÇD topolojisi için ESM yönteminin FPGA tabanlı kontrol şeması önerilmiştir. Bu bağlamda, çok yüksek hızlı tümeleşik devre donanım tanımlama dili (VHDL) modülleri, uygulamada kullanılan her bir VHDL modülü ve algoritması sunularak ESM yönteminin önerilen mimari tasarımını gerçekleştirmek için tasarlanmıştır. ESM yönteminin FPGA'da gerçekleştirilmesinin mimari adımları ayrıntılı olarak sunulmuştur. MÇD topolojisindeki anahtarlama elemanlarının kapı sinyalleri simülasyon ortamında gözlemlenmiştir. Son olarak, ESM yönteminin dijital kontrol şemasının uygulanabilirliğini doğrulamak için, tek fazlı beş seviyeli MÇD topolojisi kullanılarak bir deney düzeneği oluşturulmuş ve deneysel bulgular sunulmuştur. Bu çalışmada elde edilen sonuçlara göre, RL yükü kullanılarak kapı sinyalleri, kol gerilimleri ve çeşitli modülasyon indeksi değerleri için çıkış gerilimleri ile akımları içeren sonuçlar sunulmuştur.

Anahtar kelimeler: Çok seviyeli dönüştürücü, Modülasyon, Alanda programlanabilir kapı dizisi, Dijital kontrol

*Yazışılan Yazar

İntihal Kontrol: Evet – Turnitin

Şikayet: fujece@firat.edu.tr

Telif Hakkı ve Lisans: Dergide yayın yapan yazarlar, CC BY-NC 4.0 kapsamında lisanslanan çalışmalarının telif hakkını saklı tutar.



Design and Experimental Validation Of FPGA Based Digital Control Scheme Of The Nearest Level Modulation Method For Modular Multilevel Converter Topology

Mehmet KURTOĞLU^{1*} , Fatih EROĞLU² , Ahmet Mete VURAL³ 

¹Department of Electrical-Electronics Engineering, Faculty of Engineering and Natural Sciences, İskenderun Technical University, Hatay, Türkiye.

²TOFAŞ Türk Otomobil Fabrikası A.Ş., R&D, Propulsion Systems Management, Bursa, Türkiye.

³Department of Electrical-Electronics Engineering, Faculty of Engineering, Gaziantep University, Gaziantep, Türkiye.
¹mehmet.kurtoglu@iste.edu.tr, ²fatih.eroглу2@tofas.com.tr, ³mvural@gantep.edu.tr

Received: 23.03.2024
Accepted: 12.06.2024

Revision: 24.05.2024

doi: <https://doi.org/10.62520/fujece.1457671>
Research Article

Citation: M. Kurtoglu, F. Eroglu ve A. M. Vural, "Design and experimental validation of FPGA based digital control scheme of the nearest level modulation method for modular multilevel converter topology", *Firat Univ. Jour. of Exper. and Comp. Eng.*, vol. 4, no 1, pp. 44-58, February 2025.

Abstract

Modular multilevel converter (MMC) has become a preferable circuit topology for industrial applications, where the nearest level modulation (NLM) technique is mostly used to control the arm voltages of the MMC. Implementation of the NLM method on MMC topology using digital control techniques is gaining importance among researchers because of flexible design, full controllability, re-configurable property and modular realization. In order to achieve this aim, field programmable gate arrays (FPGAs) are preferred thanks to their benefits such as high speed performance and parallel processing ability. Accordingly, in this article, FPGA based control scheme of the NLM method was proposed for single-phase five-level MMC topology. In this context, very high-speed integrated circuit hardware description language (VHDL) modules were designed to achieve the proposed architectural design of the NLM method by presenting each VHDL module and algorithm used in the implementation. The architectural steps of the FPGA realization of the NLM method were presented in detail. Gate signals of the switching devices of the MMC topology were observed in simulation environment. Finally, in order to validate the applicability of the digital control scheme of the NLM method, an experimental setup was built using single-phase five-level MMC topology and experimental findings were presented. According to the obtained results of this study, the outcomes including gate signals, arm voltages and output voltages with currents were presented for various modulation index values using the RL load.

Keywords: Multilevel converter, Modulation, Field programmable gate array, Digital control

*Corresponding author

1. Introduction

Modular multilevel converter (MMC) is an effective converter for power electronics based industrial applications [1-2]. The primary application fields of the MMC consist of high-voltage direct current networks [3], battery systems [4], motor drive applications [5], static synchronous compensator [6], renewable energy system [7], active power filter [8] and power electronic transformer [9].

In the literature, pulse width modulation (PWM) strategies using carrier signals were employed to manage the upper and lower arm voltage of the MMC in the past decade. The most popular ones of them are phase-shifted PWM [10] and level-shifted PWM [11] including phase-disposition PWM [12], phase-opposition-disposition PWM [13] and alternative phase-opposition-disposition PWM [14]. In addition to techniques with carriers, the nearest level modulation (NLM) method is stated as carrier-less technique, which has flexible implementation and directly controls the arm voltages [15].

Recently, digital platforms instead of analog systems have been adopted by the researchers for the implementation of the NLM method because of more practical design and debugging ability. Among digital platforms, field programmable gate arrays (FPGAs) and digital signal processors (DSPs) are the attractive components to realize the NLM method [16]. Design of cascaded H-bridge multilevel inverter is presented using FPGA by implementing multiple carrier phase disposition modulation method. The developed system is confirmed by simulation and experimental findings in [17]. Reference [18] suggests a control method using Xilinx system generator by implementing the phase disposition modulation method for five-level asymmetric stacked multilevel converter. The authors in [19] develop a FPGA implementation of a real-time simulation with the help of a model design method for MMC-H-bridge DC transformer. FPGA based MMC voltage controller implementing bucket odd-even hybrid voltage sorting method using Xilinx VC709 board is reported in [20]. Research reported in [21] presents a FPGA based digital switching controllers of selective harmonic elimination and sinusoidal PWM by designing minimal hardware complexity and logic utilization for a 21-level cascaded H-bridge multilevel inverter. In the implementation process of the NLM method for MMC topology, one of the most important points is that there may be too many semiconductor devices that require to be triggered in parallel. Accordingly, several packages of DSPs are insufficient to synchronously drive too many switches. Therefore, FPGAs are incorporated into the digital control systems of the NLM method as an ideal option thanks to their parallel processing capability [22]. In this context, several publications have focused on the FPGA implementation of the NLM method for MMC topology in recent years. Digital control of the NLM method using FPGA is presented for MMC topology in [23, 24]. However, in these studies, digital implementation of the NLM method is not comprehensively discussed by presenting the each very high-speed integrated circuit hardware description language (VHDL) module and algorithm on FPGA controller platform. In this paper, FPGA based control scheme of the NLM method was proposed for single-phase five-level half-bridge submodule (HBSM) based MMC topology. The major target of this proposal was to suggest the architectural steps of the FPGA realization of the NLM method.

The structure of this article is as follows. In Section 2, MMC topology is introduced. Section 3 reports the basic properties of the NLM method. Section 4 presents the proposed architectural design of FPGA implementation of the NLM method for MMC topology. Simulation and experimental study is provided by showing the gate pulses of the switching elements and experimental findings of the MMC topology in Section 5. Section 6 concludes the presented article.

2. MMC Topology

In Figure 1, circuit configuration of the single-phase MMC is depicted. As shown, DC source is used in the left side while a resistive or resistive-inductive characterized load is attached to the right side of the MMC topology. Upper and lower arm structures are included in a phase. Identical N submodules (SMs) and arm inductances are built in each arm. Output AC phase voltage and current are symbolized with V_{AC} and i_{AC} , respectively. HBSM structure is also illustrated in Figure 1. HBSM contains two semiconductor switches as S_1 and S_2 , respectively.

Each HBSM also includes a DC capacitor, which should be connected in parallel. The operation logic of HBSM is tabulated in Table 1. According to this logic operation, there are two available states as 0 and V_C . Furthermore, semiconductor devices S_1 and S_2 are operated in the opposite manner. HBSM generates V_C voltage when S_1 is in the conduction region. Contrarily, HBSM generates zero voltage when S_2 is in the conduction region. As can be understood from these definitions, HBSM is simply controlled, which makes it more preferable in the MMC based power electronics applications [25].

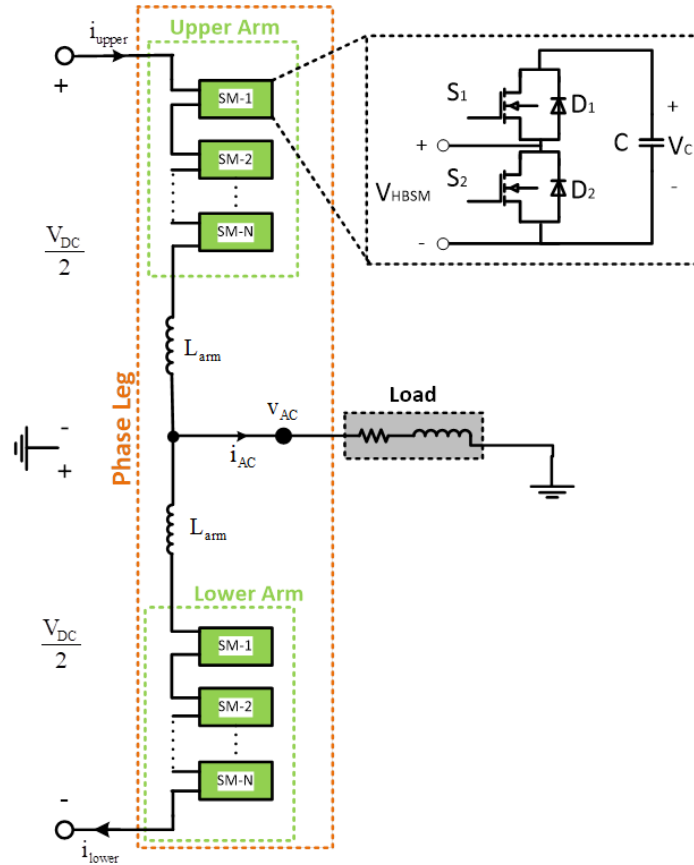


Figure 1. MMC single-phase circuit diagram including HBSM structure

Table 1. Switching states of HBSM

S_1	S_2	Arm Current	Capacitor	V_{HBSM}
1	0	Positive	Charging	V_C
1	0	Negative	Discharging	V_C
0	1	Positive	Unvaried	0
0	1	Negative	Unvaried	0

3. NLM Method

NLM is gaining more interest due to its simple implementation and it is adopted by digital controller applications of MMC to control the arm voltages of the MMC. Also, NLM method avoids the use of carrier signals. The operating principle of the NLM is depicted in Figure 2. Each arm can be effectively regulated with the help of this method.

Equivalent single-phase circuit form of the MMC is represented in Figure 3. Mathematical relations of this circuit are derived in the equations below.

Arm voltages could be computed as follows:

$$V_{upper} = \frac{V_{DC}}{2} - V_{AC} - L_{arm} \frac{di_{upper}}{dt} \quad (1a)$$

$$V_{lower} = \frac{V_{DC}}{2} + V_{AC} - L_{arm} \frac{di_{lower}}{dt} \quad (1b)$$

where L_{arm} is the arm inductance. Upper and lower arm equations are defined under steady-state condition as follows:

$$V_{upper} = \frac{V_{DC}}{2} - V_{AC} - v_L \quad (2a)$$

$$V_{lower} = \frac{V_{DC}}{2} + V_{AC} - v_L \quad (2b)$$

where v_L denotes the voltage drop on the arm inductor and it is negligible. The modulation signal could be defined as given below:

$$V_{AC} = M \frac{V_{DC}}{2} \sin(\omega_0 t + \phi) \quad (3)$$

where M , ω_0 and ϕ represent the modulation ratio, angular frequency and phase angle, respectively. In this context, upper and lower arm voltages could be computed using Equation (2a), (2b) and (3) as follows:

$$V_{upper} = \frac{V_{DC}}{2} - M \frac{V_{DC}}{2} \sin(\omega_0 t + \phi) \quad (4a)$$

$$V_{lower} = \frac{V_{DC}}{2} + M \frac{V_{DC}}{2} \sin(\omega_0 t + \phi) \quad (4b)$$

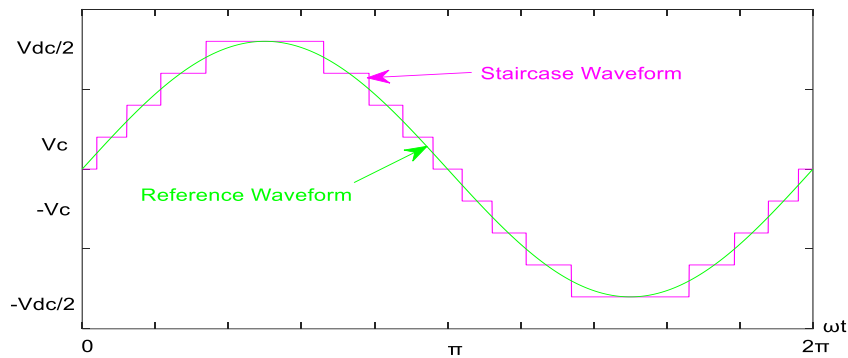


Figure 2. Main principle of the NLM method

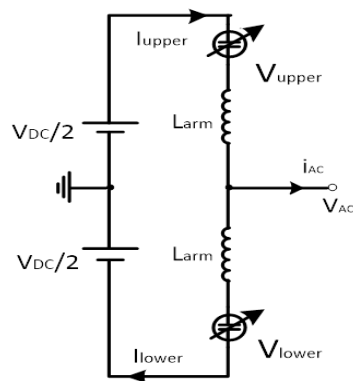


Figure 3. MMC single-phase circuit

The total DC supply voltage could be expressed with regard to the number of SMs and SM capacitor voltage as follows:

$$V_{DC} = NV_c \quad (5)$$

After substituting (5) into (4a) and (4b), the Equations are obtained as given below:

$$V_{upper} = \frac{NV_c}{2} - M \frac{NV_c}{2} \sin(\omega_0 t + \phi) \quad (6a)$$

$$V_{lower} = \frac{NV_c}{2} + M \frac{NV_c}{2} \sin(\omega_0 t + \phi) \quad (6b)$$

where V_c specifies the step value of the output voltage. If the Equations (6a) and (6b) are normalized, following relations are derived for arm voltages as follows:

$$V_{upper}^n = \frac{N}{2} [1 - M \sin(\omega_0 t + \phi)] \quad (7a)$$

$$V_{lower}^n = \frac{N}{2} [1 + M \sin(\omega_0 t + \phi)] \quad (7b)$$

4. The Proposed Architectural Design of the NLM Method

Details of the architectural design of the NLM method using FPGA are addressed in this section. VHDL is used to carry out the structural design of the method. The modules and algorithm employed in the system are explained in detail.

4.1. Sinusoidal reference creation and rounding module

Sinusoidal signal, which is employed to modulate the arms in MMC topology, is created in this module. Then, rounding function is operated to obtain the nearest voltage level from the sinusoidal reference. Initially, externally created samples of a sinusoidal reference signal with unity amplitude are kept in a look-up table (LUT). On the FPGA, LUT values are saved for subsequent use. One of the important points is to determine the modulation ratio for the generated sinusoidal reference values in the previous step. Normally, modulation index is multiplied with the sine value which is taken from LUT.

Since 10 bit string is used, modulation index (M) is considered based on 2^{10} (1024). Therefore, for the M=0.9, 92 is selected instead of 90, which results 0.89 modulation index value. According to this approach, for different M values, constant k-terms are selected. The required k-term and some of the M values are given in Table 2.

Herein, normal process is applied to multiply M with the sine value which is received from the LUT. But on an FPGA, dividing a number requires several clock cycles. Amplitude of sine signal is between -1024 and 1024. After sine signal is subtracted from 1024, it is multiplied with 2. Then, the obtained value is summed with 512 for rounding process and it is sent to upper and lower arm modules. This process is performed in each sampling period and modulation process is completed.

Table 2. The required k-terms and M values

Desired M	Actual M	k-terms	Selected k-terms
0.9	0.89	90	92
0.8	0.82	80	82
0.7	0.7	70	72
0.6	0.58	60	62

4.2. Clock divider

In digital implementation of the NLM using FPGA, special clocks are generated using the master clock of FPGA. Clock frequency of used FPGA is 100 MHz, which is also known as master clock [26]. The clock frequency can be different depending on the used FPGA card in the implementation [27]. Special clock is necessary for sinusoidal reference. The number of samples used to create the signal is included in the clock period change. In order to create other clocks from the master clock, the counter counts the number of rising edges of it up to previously determined value. When the required edge is completed, new clock is logically changed in the opposite form. Identical number of clock ticks is counted and similar procedure is continuously performed. To generate clocks for special application inside FPGA, clock of sine module is investigated. Herein, 400 samples are used to create a period of sine reference. Therefore, sampling period is computed by

$$T_{s,sine} = \frac{\text{Period of sinusoidal reference}}{\text{Number of samples}} = \frac{20 \text{ ms}}{400} = 0.05 \text{ ms} \quad (8)$$

The counter value can be computed using Equation (8) as stated below:

$$\text{counter}_{sine} = \frac{T_{s,sine}}{2T_{master}} = \frac{0.05 \text{ ms}}{2 \cdot 10 \text{ ns}} = 2500 \quad (9)$$

Similar procedures using the Equation (8) and (9) are performed to generate clocks for special application within FPGA.

4.3. SM on and SM off nodules

The used semiconductor switches of HBSM, explained in Section 2, are triggered in the opposite manner. When S_1 and S_2 are logically 1 and 0, respectively, the SM becomes ON. Otherwise, when S_1 and S_2 are logically 0 and 1, respectively, the SM becomes OFF. In other words, while SM ON means that the output of HBSM gives the balanced capacitor voltage, SM OFF means that the output of HBSM gives zero voltage. According to this triggering information, SM ON and SM OFF modules are separately created. The details of the SM ON and SM OFF process are presented in the algorithms as given in Figure 4.

4.4. Upper and lower arm gate signal modules

Outputs of sine rounding, SM ON and SM OFF module as well as clock divider become inputs of upper and lower arm modules. Depending on the number of activated SM/SMs in each arm, gate signals of HBSMs are created. While the number of active SM/SMs is equal to N_{active} for upper arm, the number of active SM/SMs is equal to $(4-N_{active})$ for lower arm. Depending on the N_{active} , both upper and lower arm gate signal modules generate logic signals for semiconductors of used HBSMs in the implementation of MMC topology. Eventually, switching patterns are created for each HBSM. But, dead time module should be designed and it is required between the triggering pulses of two switching elements on any HBSM to protect from the short circuits during switching variations. For this reason, dead time module is established in the architectural design of this work.

SM ON Module Algorithm	SM OFF Module Algorithm
<pre> library IEEE; use IEEE.STD_LOGIC_1164.ALL; use IEEE.NUMERIC_STD.ALL; entity sm_on is Port (clk_on : in STD_LOGIC; reset : in STD_LOGIC; S1_on : out STD_LOGIC; S2_on : out STD_LOGIC); end sm_on; architecture Behavioral of sm_on is signal logic_s1_on, logic_s2_on : std_logic := '0'; begin process(clk_on,reset,logic_s1_on,logic_s2_on) begin if reset = '1' then logic_s1_on <= '0'; logic_s2_on <= '0'; else if rising_edge(clk_on) then logic_s1_on <= '1'; --ON signals for SM (S1=1, S2=0) logic_s2_on <= '0'; end if; end if; S1_on <= logic_s1_on; S2_on <= logic_s2_on; end process; end Behavioral; </pre>	<pre> library IEEE; use IEEE.STD_LOGIC_1164.ALL; use IEEE.NUMERIC_STD.ALL; entity sm_off is Port (clk_off : in STD_LOGIC; reset : in STD_LOGIC; S1_off : out STD_LOGIC; S2_off : out STD_LOGIC); end sm_off; architecture Behavioral of sm_off is signal logic_s1_off, logic_s2_off : std_logic := '0'; begin process(clk_off,reset,logic_s1_off,logic_s2_off) begin if reset = '1' then logic_s1_off <= '0'; logic_s2_off <= '0'; else if rising_edge(clk_off) then logic_s1_off <= '0'; --OFF signals for SM (S1=0, S2=1) logic_s2_off <= '1'; end if; end if; S1_off <= logic_s1_off; S2_off <= logic_s2_off; end process; end Behavioral; </pre>

Figure 4. SM ON and SM OFF module algorithms

4.5. Dead time generator module

Since a semiconductor needs a little amount of time to be ON or OFF, it is well known that turning it on and off instantly is not practical. Hence, if no dead time is provided between the switching instants of the semiconductors on any HBSM, they can all be ON at the same time. This situation causes short circuits and extremely high currents to flow through the semiconductors, possibly damaging the HBSM. Accordingly, a dead time that is greater than the ON and OFF timings of the semiconductors should be incorporated into the switching instants of the semiconductors on the HBSM [28]. Final gate pulses of the semiconductors of HBSMs are created on the output of this module. Note that 200 ns time was selected as a dead time for triggering of the MOSFETs in this implementation.

4.6. Top module

This module combines every VHDL module. The architecture accepts the FPGA's master clock and a reset button as inputs, and it generates gate pulses for every HBMS on the upper and lower arms as the output, then, these pulses are sent to the real circuit. General architecture of the NLM method for single-phase five-

level MMC topology is illustrated in Figure 5. As seen, the top module includes the aforementioned VHDL modules.

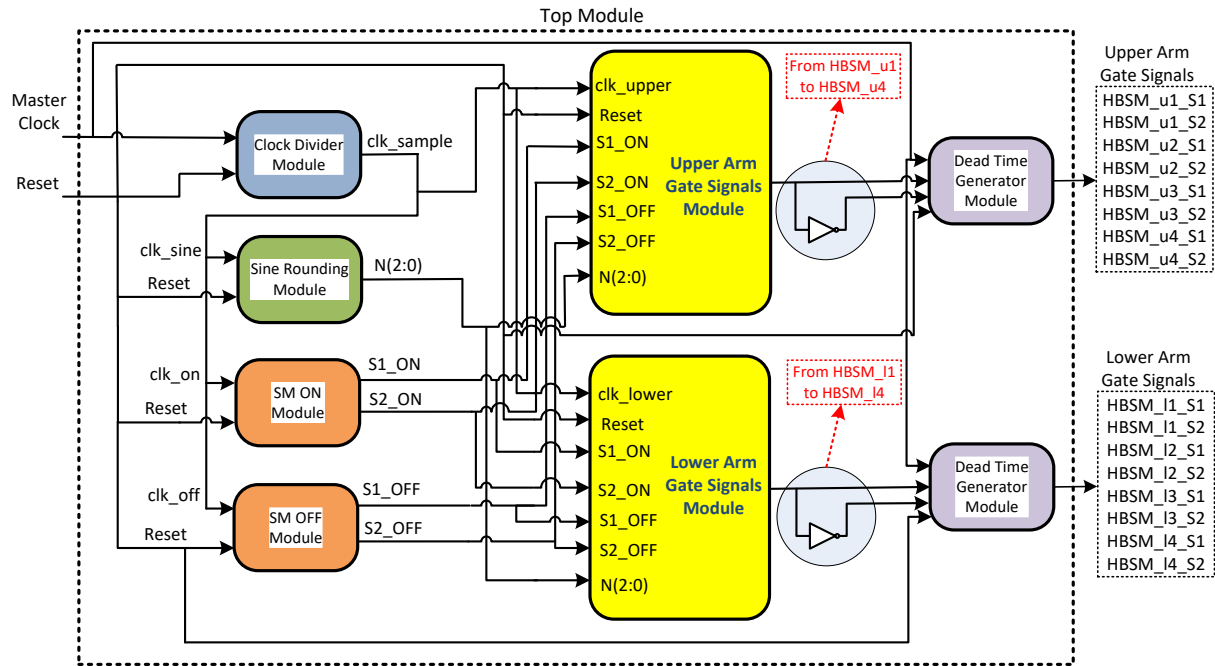


Figure 5. The proposed architectural design of the VHDL modules that creating the gate pulses of single-phase five-level MMC topology on FPGA

5. Simulation and Experimental Study

In this section, in simulation environment, the simulation results of the proposed architectural scheme using FPGA were presented to confirm the suitability of the created gate signals. The NLM method was implemented on Xilinx SPARTAN-6 FPGA controller (100 MHz master clock frequency). Xilinx ISE design computer program was utilized for the purpose of supervising and controlling the modules introduced in the previous section in real time. Table 3 demonstrates the device utilization summary of the used FPGA in the implementation by considering the number of slice registers, LUTs, used as memory and input-outputs (IOs) as performance indicators. According to the Table 3, utilization performance of resources seems satisfactory and the NLM method uses relatively few resources.

Moreover, Figure 6 shows the gate signals during a period. Four HBSM gate signals are presented for upper and lower arm, respectively. Also, clock signal and reset pulse are given. The gate signals are logically changed depending on the N value. It is clearly shown that gate signals of first and second semiconductor of any HBSM are created in the opposite manner. Although the gate signals of the semiconductors on the HBSM appear to be exact inverse of each other in Figure 6, a dead-time exists between the ON/OFF instants of the devices as explained before. A zoomed version of the dead-times between the first and second gate pulses of the HBSM is observed in Figure 7. The dead time value between S_1 and S_2 semiconductors of first HBSM of upper arm is clearly specified.

In addition, Figure 8 represents the gate signals when N value is set to 2. Herein, the gate signals remain continuously same logics since N value is constant. Again, all the gate signals of HBSMs for the arms are exhibited.

Table 3. Device utilization summary

Slice logic utilization	Utilized	Available	Utilization (%)
Number of slice registers	155	18224	1
Number of slice LUTs	250	9112	2
Number utilized as memory	7	2176	1
Number of bonded IOs	18	232	7

To verify the applicability of gate signals for the NLM method, an experimental setup was established. Table 4 describes the circuit parameters used in the MMC topology. A photograph of the experimental prototype is shown in Figure 9 and it contains the components as follows:

- FPGA controller.
- DC supplies to provide balanced capacitor voltages for the HBSMs.
- MMC SMs with gate drivers (consisting of MOSFET and gate driver) [29].
- Oscilloscope to observe the results.

Table 4. Tabulated form of experimental parameters

Item	Value
DC-link supply	40 V
Fundamental frequency	50 Hz
Number of SMs per arm	4
Arm inductor	29 mH
Balanced capacitor voltage	10 V
Load resistor	10 ohm
Load inductor	29 mH

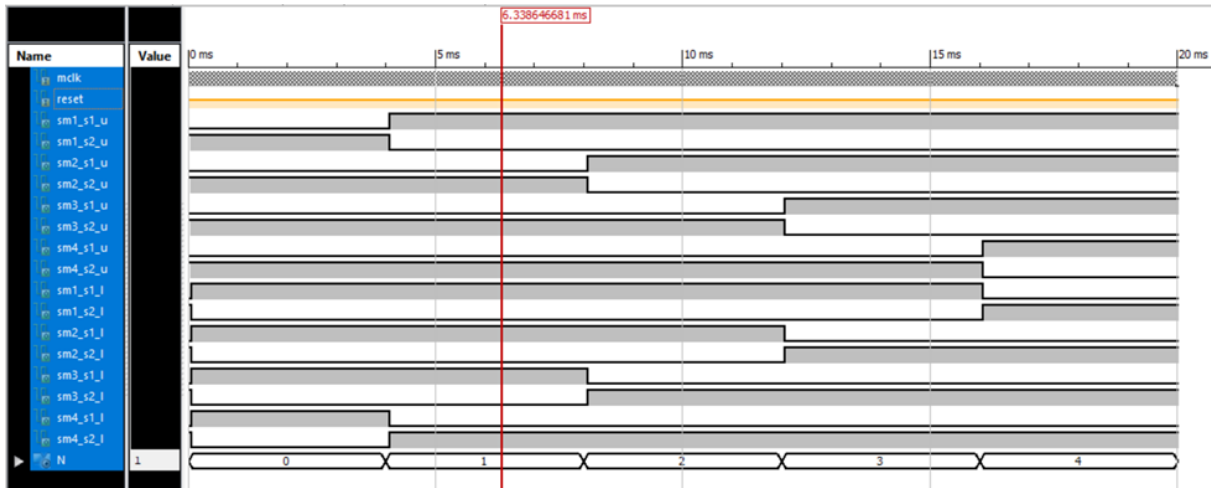


Figure 6. Gate pulses created in Xilinx program for MMC topology

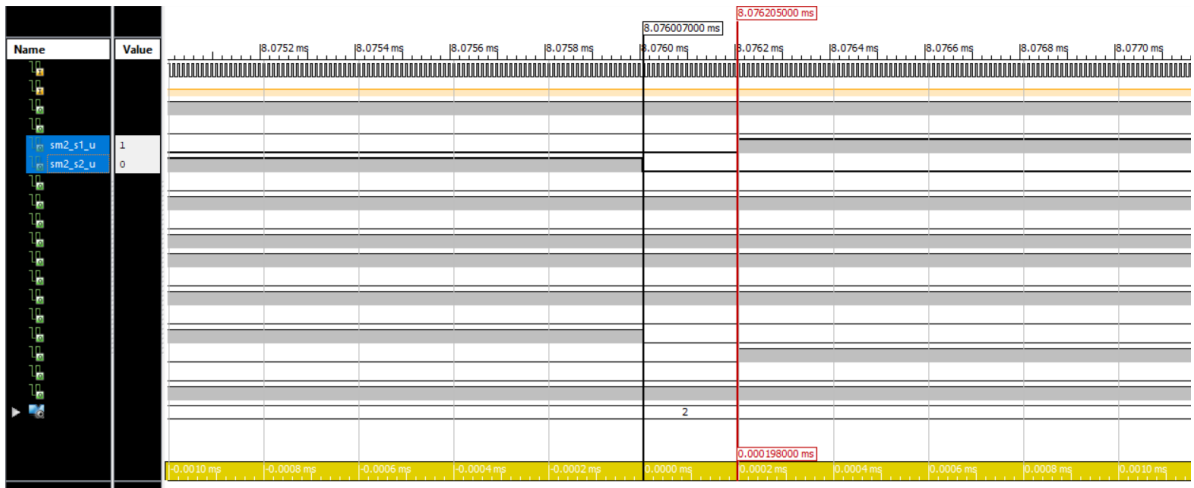


Figure 7. Dead-time between gate pulses in the upper arm

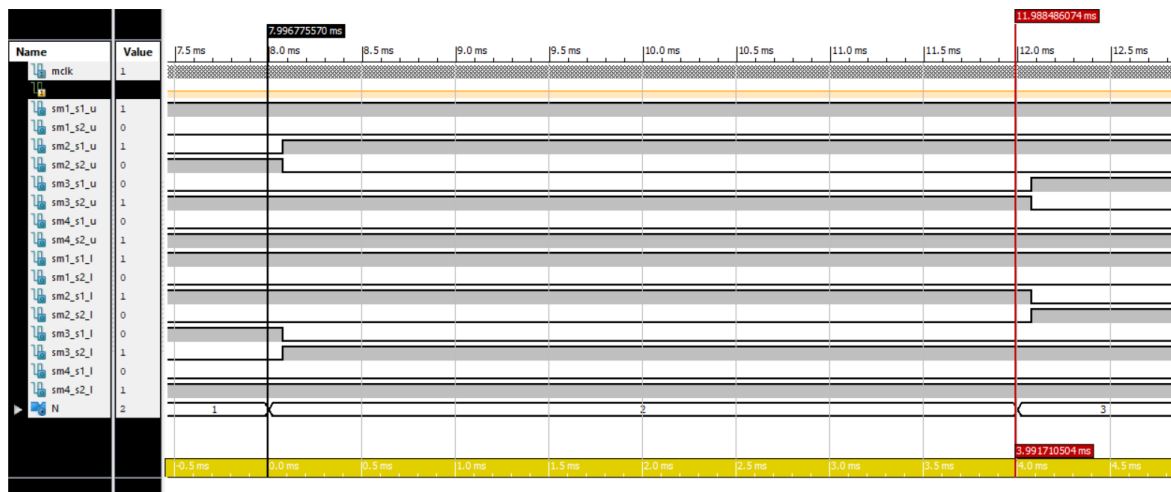


Figure 8. A view of the gate signals when N value is set to 2

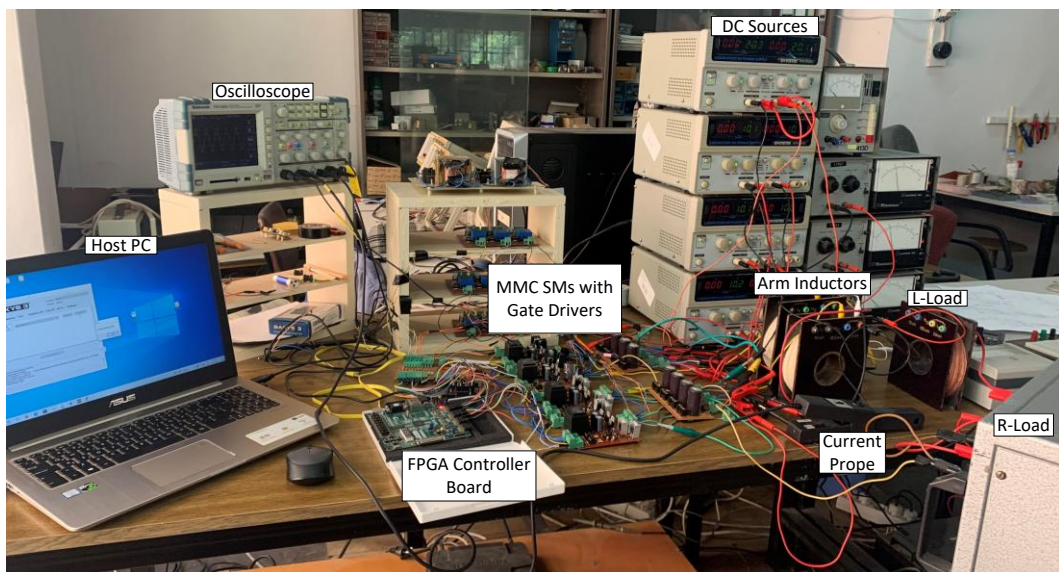


Figure 9. Experimental setup of the MMC topology

Firstly, gate signals of S_1 (channel (3)) and S_2 (channel (4)) semiconductors of HBSM1 for upper arm are presented in Figure 10(a). As seen in the screenshot of the oscilloscope, the triggering pulses are generated in the opposite manner. S_1 and S_2 semiconductors are driven by signal indicated as pink one and green one, respectively. Upper and lower arm voltages are shown in Figure 10(b), which is created as 5 levels and 50 Hz frequency for each arm.

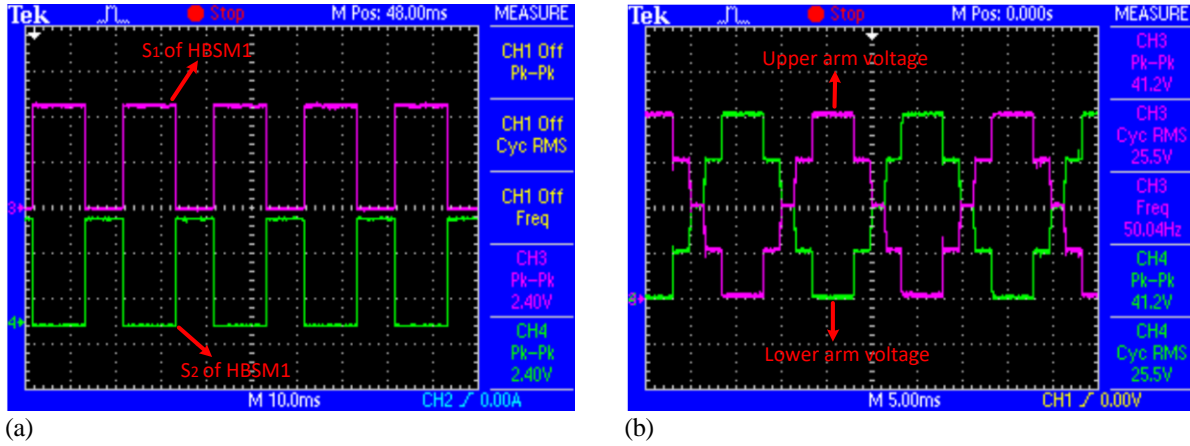


Figure 10. (a) a view of the gate signals of S_1 and S_2 semiconductors of HBSM1 for upper arm, (b) arm voltages

Secondly, output voltage and current waveforms of the MMC topology are demonstrated in Figure 11(a) and Figure 11(b), respectively. Fundamental output frequency of the waveforms is generated as 50 Hz. In the screenshots, output voltage and current are visualized when $M=0.9$ in Figure 11(a) and $M=0.6$ in Figure 11(b), respectively. As seen in Figure 11(a), output voltage is generated as 5 levels and equal to nearly 10.5 Vrms value while output current is equal to nearly 0.54 Arms. Furthermore, as indicated in Figure 11(b), output voltage is generated as 3 levels and equal to nearly 6.67 Vrms value while output current is equal to nearly 0.36 Arms.

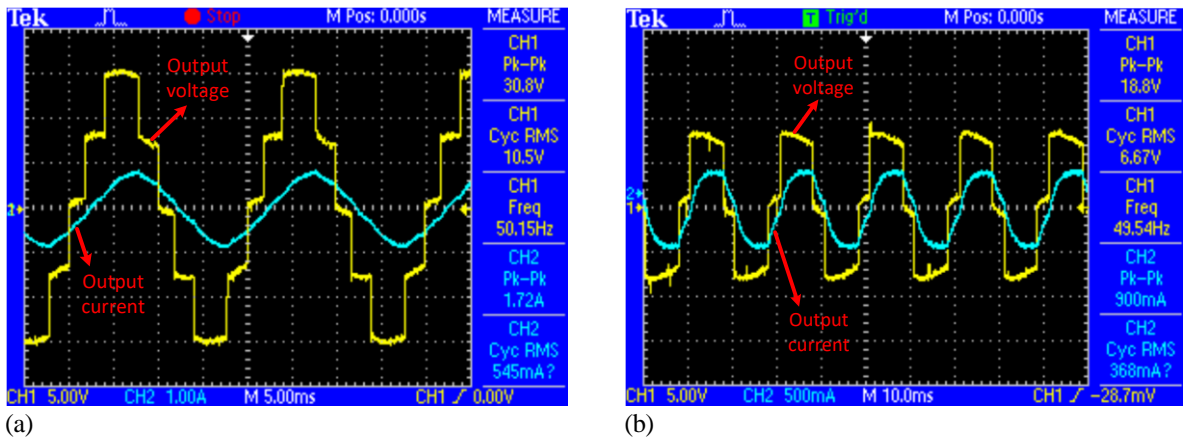


Figure 11. Output voltage and current waveforms (a) when $M=0.9$; (b) when $M=0.6$

6. Conclusions

The implementation of the NLM method on MMC using digital control methods is gaining popularity among scholars because of adaptive controllability and modular realization. In order to accomplish this aim, FPGAs are preferred due to their benefits such as high speed performance and parallel processing ability. For this reason, FPGA based control scheme of the NLM method has been proposed for single-phase five-level MMC topology. In this regard, VHDL modules have been utilized to perform the proposed architectural scheme of the NLM method by presenting each VHDL module and algorithm used in the implementation. The architectural steps of the FPGA realization of the NLM method have been presented

in detail. Gate signals of the switching devices of the MMC topology have been investigated in simulation environment. To confirm the feasibility of the NLM on MMC topology, an experimental setup has been established and experimental results have been presented. According to the obtained findings of this study, validation of the NLM method using the proposed architectural design for single-phase five-level MMC topology has been performed and its practical implementation has been shown. In addition, the outcomes including gate signals, arm voltages and output voltages with currents have been presented for various modulation index values by utilizing the RL load.

7. Author Contribution Statement

Author 1 carried out the literature review, analyzed the proposed architectural design of the NLM method and prepared the paper. Author 1 also carried out the simulation and experimental study. Author 2 contributed data collection, design of the proposed architectural design of the NLM method and evaluating the obtained results. Author 3 contributed the supervising all stages in the paper.

8. Ethics Committee Approval and Statement of Conflict of Interest

There is no need to obtain ethics committee permission for the article prepared. There is no conflict of interest with any person/institution in the prepared article.

9. References

- [1] M. A. Perez, S. Ceballos, G. Konstantinou, J. Pou, and R. P. Aguilera, "Modular multilevel converters: Recent achievements and challenges," *IEEE Open Journal of the Industrial Electronics Society*, vol. 2, pp. 224–239, 2021.
- [2] M. Kurtoğlu, F. Eroğlu, A. O. Arslan, and A. M. Vural, "Recent contributions and future prospects of the modular multilevel converters: A comprehensive review," *Int. Trans. Electr. Energy Syst.*, vol. 29, no. 3, 2019.
- [3] F. Xu, Z. Xu, H. Zheng, G. Tang, and Y. Xue, "A tripole HVDC system based on modular multilevel converters," *IEEE Trans. Power Del.*, vol. 29, no. 4, pp. 1683–1691, 2014.
- [4] F. Eroğlu, M. Kurtoğlu, and A. M. Vural, "Bidirectional DC–DC converter based multilevel battery storage systems for electric vehicle and large-scale grid applications: A critical review considering different topologies, state-of-charge balancing and future trends," *IET Renew. Power Gener.*, vol. 15, no. 5, pp. 915–938, 2021.
- [5] J. J. Jung, H. J. Lee, and S. K. Sul, "Control strategy for improved dynamic performance of variable-speed drives with Modular Multilevel Converter," *IEEE J. Emerg. Sel. Top. Power Electron.*, vol. 3, no. 2, pp. 371–380, 2015.
- [6] H. P. Mohammadi and M. T. Bina, "A transformerless medium-voltage STATCOM topology based on extended modular multilevel converters," *IEEE Trans. Power Electron.*, vol. 26, no. 5, pp. 1534–1545, 2011.
- [7] A. M. Vural, M. Kurtoğlu, and F. Eroğlu, "An efficient capacitor voltage balancing scheme for modular multilevel converter based wind energy conversion system," *Adv. Electr. Comput. Eng.*, vol. 21, no. 4, pp. 31–42, 2021.
- [8] F. T. Ghetti, A. A. Ferreira, H. A. C. Braga, and P. G. Barbosa, "A study of shunt active power filter based on modular multilevel converter (MMC)," in *Proc. 2012 10th IEEE/IAS Int. Conf. Ind. Appl.*, Fortaleza, Brazil, Nov. 5-7, 2012, pp. 1–6.
- [9] F. Briz, M. Lopez, A. Rodriguez, and M. Arias, "Modular power electronic transformers: Modular multilevel converter versus cascaded H-Bridge solutions," *IEEE Ind. Electron. Mag.*, vol. 10, no. 4, pp. 6–19, 2016.
- [10] S. Lu, L. Yuan, K. Li, and Z. Zhao, "An improved phase-shifted carrier modulation scheme for a hybrid modular multilevel converter," *IEEE Trans. Power Electron.*, vol. 32, no. 1, pp. 81–97, 2017.
- [11] R. Darus, G. Konstantinou, J. Pou, S. Ceballos, and V. G. Agelidis, "Comparison of phase-shifted and level-shifted PWM in the modular multilevel converter," in *Proc. 2014 Int. Power Electron. Conf. (IPEC-Hiroshima 2014 - ECCE ASIA)*, Hiroshima, Japan, May 18-21, pp. 1488–1493, 2014.
- [12] F. Martinez-Rodrigo, D. Ramirez, A. B. Rey-Boue, S. De Pablo, and L. C. Herrero-De Lucas, "Modular multilevel converters: Control and applications," *Energies*, vol. 10, no. 11, 2017.
- [13] A. Ferreira-António, C. Collados-Rodríguez, and O. Gomis-Bellmunt, "Modulation techniques applied to medium voltage modular multilevel converters for renewable energy integration: A review," *Electr. Power Syst. Res.*, vol. 155, pp. 21–39, 2018.
- [14] S. Debnath, J. Qin, B. Bahrani, M. Saedifard, and P. Barbosa, "Operation, control, and applications of the modular multilevel converter: A review," *IEEE Trans. Power Electron.*, vol. 30, no. 1, pp. 37–53, 2015.
- [15] M. Kurtoğlu and A. M. Vural, "A novel nearest level modulation method with increased output voltage quality for modular multilevel converter topology," *Int. Trans. Electr. Energy Syst.*, 2022.
- [16] X. Ma, W. A. Najjar, and A. K. Roy-Chowdhury, "Evaluation and acceleration of high-throughput fixed-point object detection on FPGAs," *IEEE Trans. Circuits Syst. Video Technol.*, vol. 25, no. 6, pp. 1051–1062, 2015.
- [17] S. Chitra and K. R. Valluvan, "Design and implementation of cascaded H-Bridge multilevel inverter using FPGA with multiple carrier phase disposition modulation scheme," *Microprocess. Microsyst.*, vol. 76, 2020.
- [18] M. Q. Kasim et al., "Control algorithm of five-level asymmetric stacked converter based on Xilinx system generator," in *Proc. 2021 IEEE 9th Conf. Syst., Process Control (ICSPC 2021)*, pp. 1–5, 2021.

- [19] L. Wu et al., "Design and FPGA implementation of a real-time simulation platform for an MMC-H DC transformer," in Proc. 2022 IEEE Energy Conversion Congr. Expos. (ECCE), pp. 1–5, 2022.
- [20] K. Xiong, G. Wang, J. Zhang, and G. He, "FPGA-based modular multilevel converter (MMC) controller for efficient voltage balancing in real-time simulation," in Proc. 16th IET Int. Conf. AC DC Power Transm. (ACDC 2020), Online Conf., pp. 1851–1856, 2020.
- [21] E. Noorsal et al., "Design of FPGA-based SHE and SPWM digital switching controllers for 21-level cascaded H-bridge multilevel inverter model," *Micromachines*, vol. 13, no. 2, 2022.
- [22] N. Fujita, R. Kobayashi, Y. Yamaguchi, and T. Boku, "Parallel processing on FPGA combining computation and communication in OpenCL programming," in Proc. 2019 IEEE Int. Parallel Dist. Process. Symp. Workshops (IPDPSW), Rio de Janeiro, Brazil, May 20-24, pp. 1–6, 2019.
- [23] M. Moranchel, E. J. Bueno, F. J. Rodriguez, and I. Sanz, "Implementation of nearest level modulation for modular multilevel converter," in Proc. 2015 IEEE 6th Int. Symp. Power Electron. Distrib. Gener. Syst. (PEDG), Aachen, Germany, Jun. 22-25, pp. 1–6, 2015.
- [24] T. H. Cuong, P. V. Phuong, T. V. Phuong, and T. T. Minh, "Experiment on nearest level modulation algorithm for FPGA based modular multilevel converters," in Proc. 2019 10th Int. Conf. Power Electron. ECCE Asia (ICPE 2019 - ECCE Asia), Busan, South Korea, May 27-30, pp. 1–6, 2019.
- [25] M. Kurtoğlu, A. O. Arslan, F. Eroğlu, and A. M. Vural, "Comparison of different submodule topologies in modular multilevel converters," in Proc. 2019 3rd Int. Symp. Multidiscip. Stud. Innov. Technol. (ISMSIT), Ankara, Turkey, Oct. 11-13, pp. 1–6, 2019.
- [26] Digilent Inc., "Nexys 3™ FPGA Board Reference Manual," 2016.
- [27] M. Sönmez and A. Akbal, "Design of a new BPSK modulator," *Pamukkale Univ. J. Eng. Sci.*, vol. 23, no. 5, pp. 492–496, 2017.
- [28] F. Eroğlu and A. M. Vural, "Digital implementation of level-shifted pulse width modulation for multilevel converters," in Proc. 2022 Int. Congr. Human-Comput. Interact., Optim. Robotic Appl. (HORA), Ankara, Turkey, Jun. 9-11, pp. 1–6, 2022.
- [29] International Rectifier, "Mosfet, hexfet power, Irfz44N," URL: <https://datasheetspdf.com/pdf-file/509097/InternationalRectifier/IRFZ44N/1>, (Visited on Mar. 23, 2024).



Elektriksel Akım Dalgasının and Frekansının Derin Beyin Stimülasyonu Üzerindeki Etkisinin Araştırılması

Enver SALKIM^{1,2*}

¹Elektronik ve Elektrik Mühendisliği Bölümü, College London (UCL) Üniversitesi, Londra, Birleşik Krallık.

²Elektronik ve Otomasyon Bölümü, Teknik Bilimler Meslek Yüksekokulu, Muş Alparslan Üniversitesi, Muş, Türkiye.

¹e.salkim@ucl.ac.uk, ²e.salkim@alparslan.edu.tr

Geliş Tarihi: 09.04.2024

Kabul Tarihi: 12.06.2024

Düzeltilme Tarihi: 17.05.2024

doi: <https://doi.org/10.62520/fujece.1467198>

Araştırma Makalesi

Alıntı: E. Salkım, "Elektriksel akım dalgasının ve frekansının derin beyin stimülasyonu üzerindeki etkisinin araştırılması", Fırat Üni. Deny. ve Hes. Müh. Derg., vol. 4, no 1, pp. 59-71, Şubat 2025.

Öz

Biyo-hesaplamalı modellerin tıbbi cihazların tasarımı ve geliştirilmesi üzerinde önemli bir etkisi vardır. Bu yaklaşım, deneysel test kullanılarak tasarlanması mümkün olmayan çeşitli tıbbi cihaz parametre ayarlarının araştırılmasına olanak tanır. Bu nöromodülatör sistemler için en uygun parametrelerin kullanılması hasta güvenliği açısından çok önemlidir. Hesaplamalı modelleme, derin beyin stimülasyonunda (DBS) hedefleme ve stimülasyon parametrelerini iyileştirme mücadelesinde temel bir araçtır. Spesifik olarak, simülasyon dalga biçimi şekli, darbe genişliği ve amplitüdünün yanı sıra pasif faktörler de dahil olmak üzere birçok parametredeki farklılıklar nedeniyle DBS'yi birleştiren Parkinson hastalığı için optimal bir nöromodülatörün tasarlanması zor olabilir. Bu çalışma, bu tür gelişmiş biyo-hesaplamalı modelleme sistemlerini kullanarak farklı darbe genişliklerine dayalı farklı dalga formlarının kullanılmasının etkisini araştırmaktadır. Bir insan kafasının hacim iletkeni, temel doku katmanları da dahil olmak üzere ortalama insan kafası kalınlığına dayanılarak oluşturulmuştur. Daha sonra, farklı frekans aralıklarını kullanarak sonuçları analiz etmek için DBS elektrot dizisi tasarlandı ve hesaplamalı modelle birleştirildi. Ayrıca hesaplamalı model tasarımcıları için hesaplamalı model geliştirmenin temelleri vurgulandı. Daha sonra sonuçlar, zamana dayalı simülasyon kullanılarak elektrik ve akım yoğunluğu dağılımlarına göre hesaplandı. Simülasyon frekansının ve simülasyon dalga biçimi şeklinin sonuç üzerinde önemli bir etkiye sahip olduğu gösterilmiştir. Sonuçlar, ilgilenilen bölgedeki elektrik potansiyeli, akım yoğunluğu ve elektrik alan dağılımları üzerinde önemli bir etkiye sahip olması nedeniyle kapasitif etkinin daha yüksek frekans seviyelerinde göz ardı edilemeyeceğini göstermiştir.

Anahtar kelimeler: Biyo-hesaplamalı modelleme, Kapasitif etki, Derin beyin stimülasyonu, Simülasyon frekansı, Stimülasyon dalga formu

*Yazışılan yazar



Investigating Impact of Current Pulse Waveform and Simulation Frequency on Deep Brain Stimulation

Enver SALKIM^{1,2*} 

¹Department of Electronic and Electrical Engineering, University College London (UCL), London, United Kingdom.

²Department of Electronic and Automation, Vocational School of Technical Sciences, Muş Alparslan University, Muş, Türkiye.

¹e.salkim@ucl.ac.uk, ²e.salkim@alparslan.edu.tr

Received: 09.04.2024
Accepted: 12.06.2024

Revision: 17.05.2024

doi: <https://doi.org/10.62520/fujece.1467198>
Research Article

Citation: E. Salkim, "Investigating impact of current pulse waveform and simulation frequency on deep brain stimulation", *Firat Univ. Jour. of Exper. and Comp. Eng.*, vol. 4, no 1, pp. 59-71, February 2025.

Abstract

Bio-computational models have a significant impact on the design and development of medical devices. This approach allows investigation of various medical device parameter settings which would be infeasible to design by using the experimental test. Using the optimal parameters for these neuromodulator systems is crucial for the patient safety. Computational modelling is a fundamental tool in the challenge to improve targeting and stimulation parameters in deep brain stimulation (DBS). Specifically, it may be difficult to design an optimal neuromodulator for Parkinson's disease fusing DBS due to variations in many parameters including simulation waveform shape, pulse width, and amplitude as well as passive factors. This study investigates the impact of using different waveforms based on different pulse widths using such advanced bio-computational modelling systems. The volume conductor of a human head was generated based on average human head thickness including fundamental tissue layers. Then, the DBS electrode array was designed and merged with the computational model to analyse the results using different frequency ranges. Also, the fundamentals of the computational model developments were highlighted for the computational model designers. Then, the results were calculated based on electrical and current density distributions using time-based simulation. It was shown that the simulation frequency and simulation waveform shape have a significant impact on the outcome. The results suggested that the capacitive effect cannot be ignored at the higher frequency levels due to having a significant impact on the electrical potential, current density, and electric field distributions in the region of interest.

Keywords: Bio-computational modelling, Capacitive effect, Deep brain stimulation, Simulation frequency, Stimulation waveform

*Corresponding author

1. Introduction

It has been shown that it may not be possible to investigate the impact of the neuromodulator parameters on the target tissue layer using different electrode features based on experimental test or it is difficult to design an optimal medical device for individuals using clinical methods due to associated risks [1-3]. Computational modelling has been proven to be an effective tool for designing and analysing neuromodulator devices to treat health-related disorders and diseases. The general workflow for computational modelling of a neural stimulation device includes finite element (FE) models (FEM) involving, a volume conductor model representing various, anatomical structures and the electrodes by their respective conductivities and appropriate boundary conditions [4], as shown in Fig. 1 and 2.

It is possible to calculate the electrical potential distributions within the volume conductor of the computational models using available commercial FEM software packages (e.g., COMSOL Multiphysics, ANSYS). FEM has matured as a numerical. COMSOL Multiphysics (COMSOL, Ltd, Cambridge, UK) includes many matured numerical toolsets for solving bioelectric field problems with complex geometric features and anisotropic tissue properties [5-7]. However, it is not always clear how to generate the current source and implement the required boundary conditions accordingly. It has been shown that many studies were conducted based on the quasi-static approximation by neglecting capacitive and magnetic various applications. For example, the capacitive and magnetic affects were ignored when the electrode insertion guidance was analysed using FEM modelling approach [9, 10]. Also, the required stimulus current thresholds nerve fibers activation for various neuromodulator systems was calculated based on quasi-static approximation by ignoring capacitive affect using advanced bio-computational modelling [5, 8, 11-14]. There is not much information on designing current sources based on transient simulation using different simulation waveforms (e.g., sinusoidal, rectangular) simulation modes (biphasic, monophasic) as shown in Fig. 3. Designing and simulation of such parameters are crucial during the modelling as the results are used for many neural prostheses and therapies (include upper and lower limb prostheses for spinal cord injury and stroke and deep brain stimulation (DBS)) during the clinical tests. Then, the medical devices are designed and developed depending on the trial outcome [15].

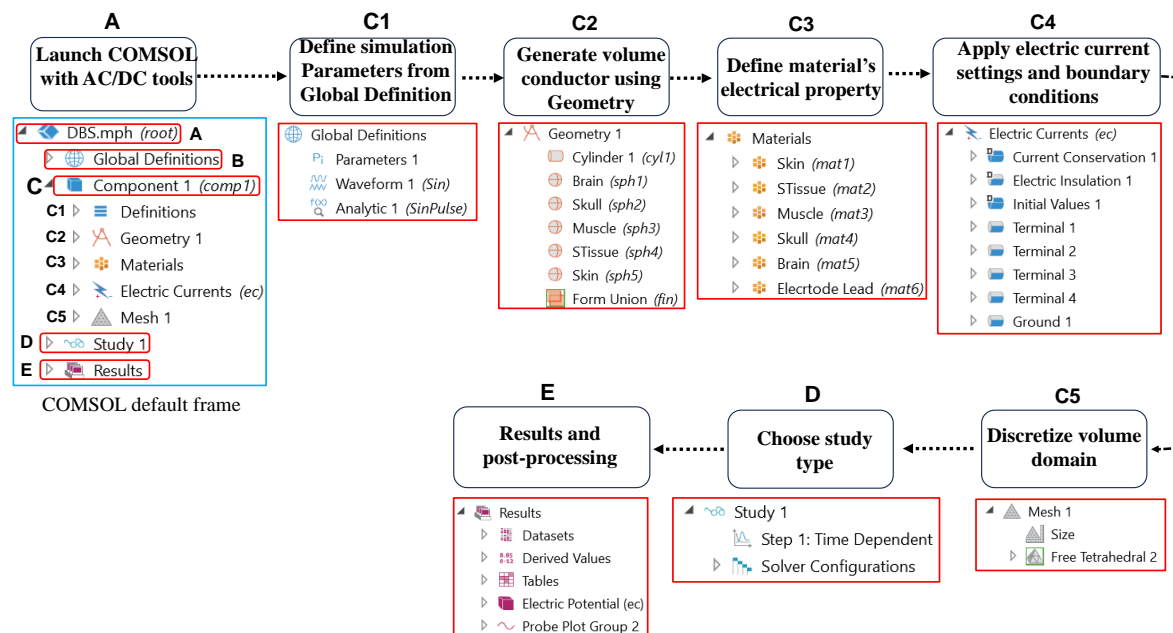


Figure 1. General workflow of COMSOL for AC/DC module. The default steps for AC/DC are shown. The steps for generating a computational model are numbered (from A to E)

The DBS is a neurosurgical procedure where an electrical stimulator is implanted in a specific brain region to treat multiple neuropsychiatric disorders, including Parkinson's disease. The DBS is a surgical procedure involving implantation of electrodes into deep the brain as shown in Fig. 2(a). The electrodes are placed to

the ROI using stereotactic or computer-assisted guidance techniques. The DBS has several advantages compared to the other surgical methods. Namely, the DBS is reversible, less interference with future intervention and adjustable to optimize benefit and reduce side effect. The main disadvantages of the DBS

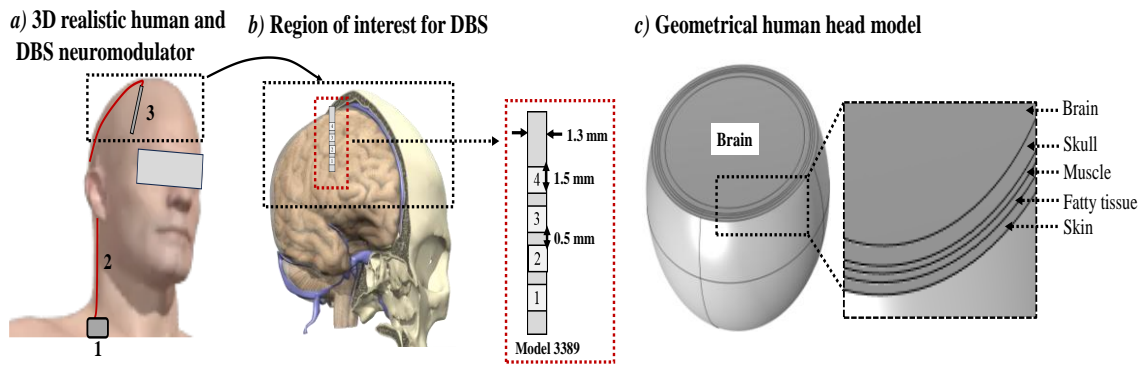


Figure 2. (a) Shows a simplified representation of the DBS system and its implementation inside the patient's head. (b) Shows the region of interest for the DBS. The electrode contacts are equally spaced, and the pitch of the electrode is set to 2 mm. (c) Shows the geometrical human head model that is generated based on the fundamental tissue layers

maybe it is more expensive, more time consuming, and it has complications related to device and the battery should be replaced periodically [16].

It has been shown that there are many parameters that affect the performance of the DBS neuromodulator including waveform shape, frequency, pulse width and amplitude as well as passive factors [17]. The dielectric properties of the tissue are frequency dependence and may have a significant impact on the outcome. In particular, the electric field distribution is strongly influenced by the dielectric properties of the tissue layers, which have a heterogeneous, locally anisotropic, and dispersive nature. Also, the electrical field may show different results using a wide range of frequencies [18, 19]. Furthermore, the capacitive properties of grey and white matter cannot be disregarded for current-controlled stimulations [20]. Therefore, it is necessary to investigate the impact of such parameters. It is not feasible to investigate the impact of these various DBS neuromodulator parameters using experimental tests. Computational models of DBS generally rely on FEM to solve for the electrical potential distribution in the brain from the DBS pulses which otherwise impossible to do with experimental tests. The model used to solve for the DBS electrical potential distribution is called a volume conductor (VC) model [20]. The electrical potential distributions within the VC for DBS were extracted using isotropic dielectric parameters of each tissue layer [15]. The procedures of defining the DBS electrode contacts, the simulation settings and boundary conditions that represented in the finite element model can also affect the outcome as detailed in method section.

This paper investigates the impact of the simulation pulse waveform shape as well as the effect of dielectric properties of the anatomical layers based on different frequency on the current density and electrical potential distribution on the region of interest (ROI) (e.g. brain). Thus, current source based on different waveforms were designed in COMSOL Multiphysics using different electrode arrangements for DBS. Then, the time-based electric potential and current density distributions were calculated using conventional DBS electrode settings as shown in Fig. 2(b). The VC of the human head was developed using smooth geometrical shapes to analyse the impact of the current source waveforms based on the electrical potential distributions [3, 4]. The human head volume conductor was developed based on the fundamental tissue layers based concentric geometric shapes (e.g., sphere) as shown in as shown in Fig. 2(c). To mimic the realistic human head model, the layers were developed based on their average thickness [3], [4]. The main contributions of this study are:

- The human head model was developed, and the conventional DBS electrode model merged to analyse the impact of the different current pulse waveforms and simulation frequency levels on the outcome.
- The electrical potential and current density distributions were examined at the RIO by considering the safety criteria.

- By analysing the impact of the representations of the current sources for the electrical potential distribution using neuromodulator settings of DBS, the procedures of the more accurate and efficient simulation detailed, and useful recommendations were provided for the bio-computational model's designers.

The paper is organized as follows. The method section presents the development of the current source and boundary condition models; the results give the electrical potential distributions of chosen current source and the discussion and conclusion are given, respectively.

2. Methods

For all the subsequent simulations and operations, a computer with an Intel i7-8550U CPU @ 1.80GHz with 16GB RAM was used.

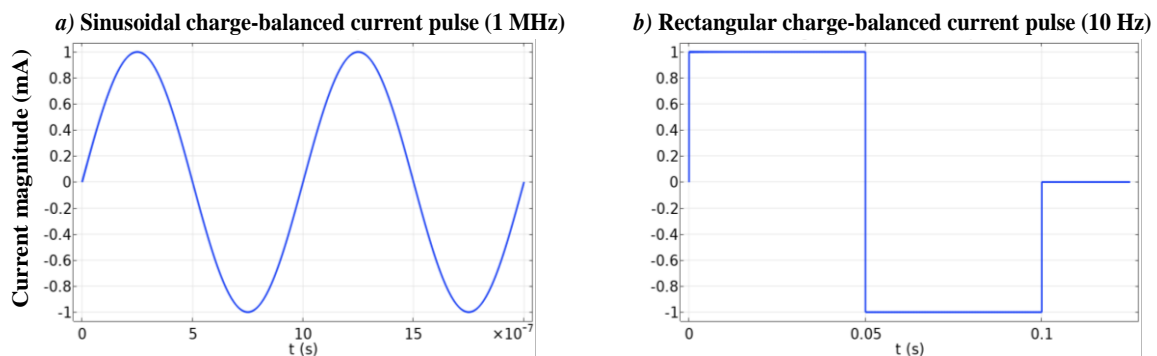


Figure 3. (a) Shows 1 MHz sinusoidal charge – balanced current pulse. (b) shows 10 Hz rectangular charge – balanced current pulse

2.1. Multi-layered model development

The computational model was generated using COMSOL Multiphysics based on the AC/DC module. The AC/DC module provides a unique environment for the simulation of electrical potential simulation in 2D and 3D. This module is a powerful tool for detailed analysis of the components of biomedical neuromodulators for various disorders.

The human head was generated using smooth geometrical shapes to investigate the impact of the simulation current source on the electrical potential distributions of DBS. The head model consisted of five concentric spheres to represent skin, fatty tissue, muscle, skull, and brain as detailed in Fig 2(c). Each layer was developed using its standard thickness (skin: 2.8 mm, fat: 2 mm, muscle: 1.7 mm, skull: 5.5 mm) to represent average individuals. Since the region of interest is the brain, and the electrical parameters of the grey and white matters are identical; the white and grey matters were combined and modelled as the brain. The brain layer was designed based on the average human brain diameter.

2.2. Electrode design

The DBS electrodes were designed based on commercially available neurostimulator for DBS therapy settings (Medtronic 3389) using smooth geometric shapes in COMSOL and the electrode model was inserted into the head model. The diameter of each electrode was set to 1.3 mm. The pitch of electrodes was chosen as 2 mm, as shown in Fig. 2(b). Each DBS lead included four contacts (4, 3, 2, 1) each contact has a length of 1.5 mm. The electrode was positioned in the ROI.

In the practical DBS, the electrical signal with a specific frequency was delivered to the target brain region via the neurostimulator, which is a pacemaker-like device installed subcutaneously near the clavicle of the

patient. However, the generated signal was directly applied to the electrode contacts as detailed in the following section.

2.3. Simulation source design

Since the simulation pulse of the DBS may affect the outcome, there is a need to investigate the impact of different pulse waveform shapes on the electrical potential and current density on the RIO. In general, the charge balanced pulse is used for the safety criteria [15] COMSOL Multiphysics allows researchers to design various current waveforms based on different pulse widths. Thus, the rectangular and sinusoidal balanced current pulses were generated based on 10 Hz and 1 MHz, respectively as shown in Fig. 3. After generating the current pulse, each pulse was named and applied to the electric contact of DBS electrode arrangements in the Electric current section. The current pulse for each contact was defined as in (1). It was noted that the current was given by Ampere (A) by default. Thus, if the lower amplitude is applied, the current should be converted to A. Since 1 mA current pulse was applied to the contacts, this value was used in (1).

$$I_0 = (0.001) * W(t)(A) \quad (1)$$

where I_0 is time-based the electrode contact current based on sinusoidal waveform. $W(t)$ shows type of waveform source. Since the charge-balanced sinusoidal and rectangular current pulses were used in this study, $W(t) = \text{Sin}(\omega t)$ was used for the sinusoidal current pulse and $W(t) = \text{Rec}(\omega t)$ was applied to the electrode contacts for the rectangular current pulse, ω shows angular frequency.

Table 1. Dielectric properties of human head anatomical layers are based on different frequency levels.

Anatomical layers	Conductivity (σ) (10 Hz)	Relative permittivity (ϵ_r) (10 Hz)	Conductivity (σ) (1 MHz)	Relative permittivity (ϵ_r) (1 MHz)
Skin	2.00e-4	1.14e+3	1.32e-2	9.91e+2
Fatty tissue	3.77e-2	5.03e+6	4.41e-2	5.08e+1
Muscle	2.02e-1	2.57e+7	5.03e-1	1.84e+3
Skull	2.00e-2	5.52e+4	2.44e-2	1.45e+2
Brain	4.75e-2	4.07e+7	1.85e-1	1.14e+3

2.4. Electric properties of tissue and boundary conditions

The dielectric properties of the human head tissue layers were attained based on Table 1 for each simulation waveform. Since each tissue layer has different dielectric properties, each simulation was separately run by attaining associated features. The current simulation was designed based on a charge-balanced pulse for both waveforms to mimic the practical conditions. Thus, 1 mA current was applied to the anode contact and -1 mA was applied to the cathode contact for each simulation. Each electrode was defined as a contact boundary. Each electrode contact was defined as *Terminal* in COMSOL (*Terminal 1*, *Terminal 2*, *Terminal 3*, *Terminal 4*). The lead shaft was designed as an insulator with a conductivity of $10e-16$ S/m, and the contacts were modelled as platinum/iridium with a conductivity of $5.3e6$ S/m. The boundary components were built and consequently subtracted from the DBS lead model which resulted in external boundaries that were defined using boundary conditions. The Dirichlet boundary condition ($V = 0$) was applied at the near end of the electrode lead.

2.5. Finite element simulation

The accuracy of the simulation that can be obtained from any FEM is related to the finite element mesh settings during domain discretization. The finite element mesh is used to subdivide the defined domains into

smaller domains called elements to solve electrical potential distributions using underlying differential equations.

The VC of the human head and DBS electrode was discretized using the free tetrahedral element method as shown in Fig. 4(a). Since the electrode domain is relatively smaller in size, it was more finely meshed by modifying the maximum and minimum element size as shown in Fig. 4(b). The remaining domains were relatively coarsely meshed to reduce the computation time. These settings were applied until no significant difference was observed in the electrical potential variations based on given settings. This resulted in about 0.4 million tetrahedral elements and about 0.5 million degrees of freedom.

The transient time response of the given stimulation current pulses was studied based on the time-dependent electrical current approximation of Maxwell's equations using (2).

$$\nabla \cdot \left(\sigma \nabla V - \epsilon_0 \epsilon_r \nabla \frac{\partial V}{\partial t} \right) \quad (2)$$

where σ is the conductivity of each of the tissues, V is the electrical potential in the representative geometry, $\epsilon_0 \epsilon_r$ is the tissue permittivity.

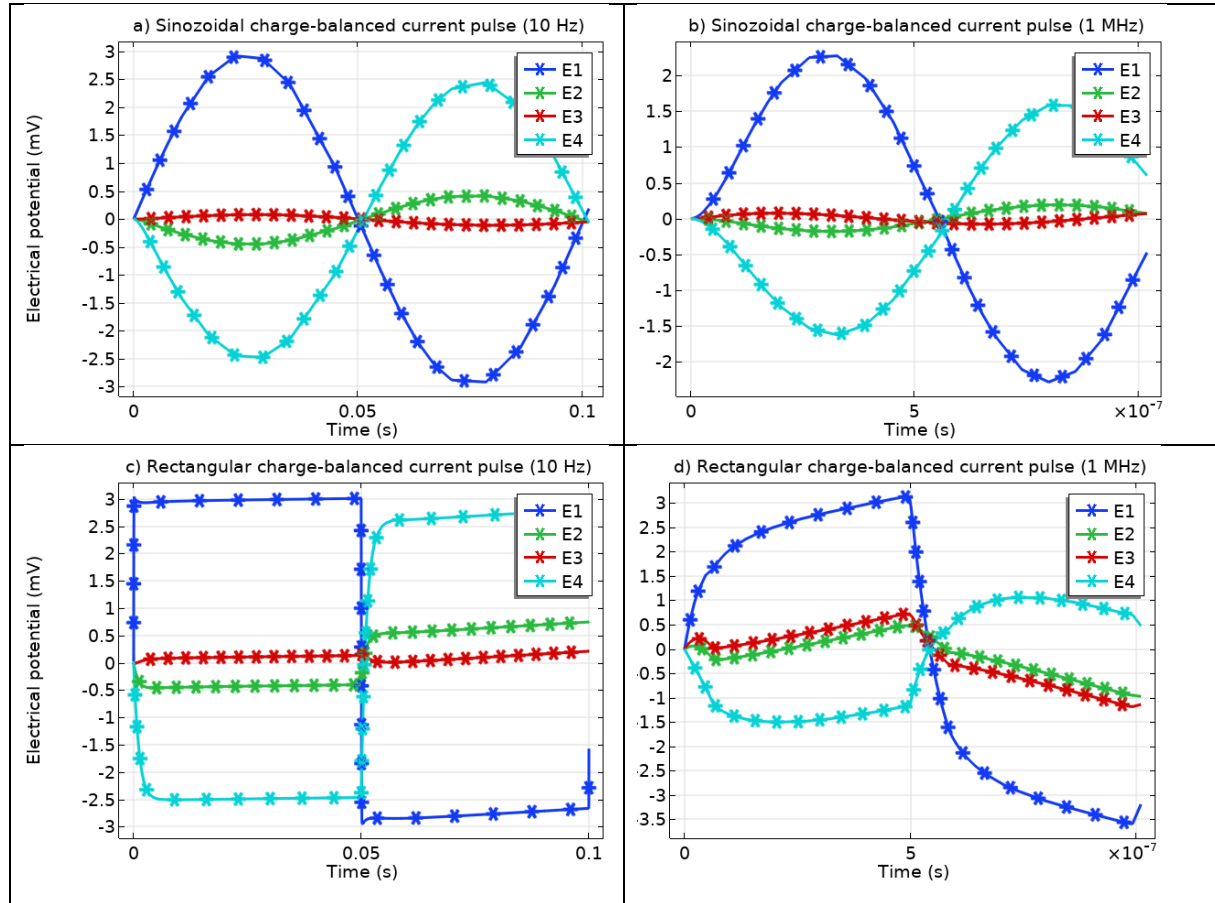


Figure 4. (a) Shows the electrical potential variation for 10 Hz using sinusoidal waveform. (b) shows the electrical potential variation for 1 MHz using sinusoidal waveform. (c) shows the electrical potential variation for 10 Hz using rectangular waveform. (d) shows the electrical potential variation for 1 MHz using rectangular waveform

The dielectric properties of each layer were attained using based on available data [3]. The electrode-tissue interface contact impedance was assumed to be zero and appropriate continuity conditions were implemented at the boundary of the different domains to have a unique solution. The current density distributions for 10

Hz and 1 MHz were compared using the same settings (e.g., the same contour number) for fair comparison. The results were recorded for each simulation as shown in Fig. 4(c).

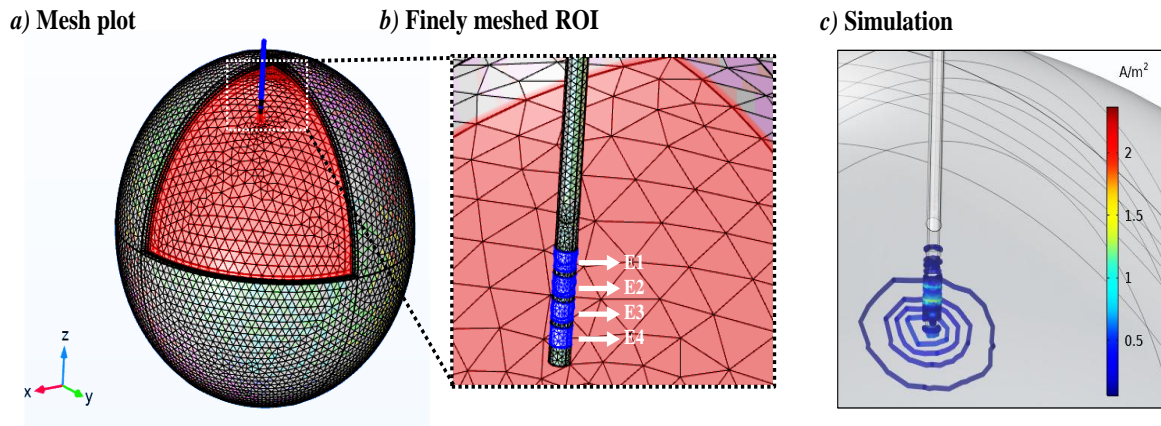


Figure 5. a) Shows volume conductor mesh plot. (b) Shows the region of interest (RIO) is relatively finely meshed. The electrode contacts are highlighted in blue and labelled in order (e.g. E1 to E4). (c) The results are recorded for each simulation pulse and frequency level

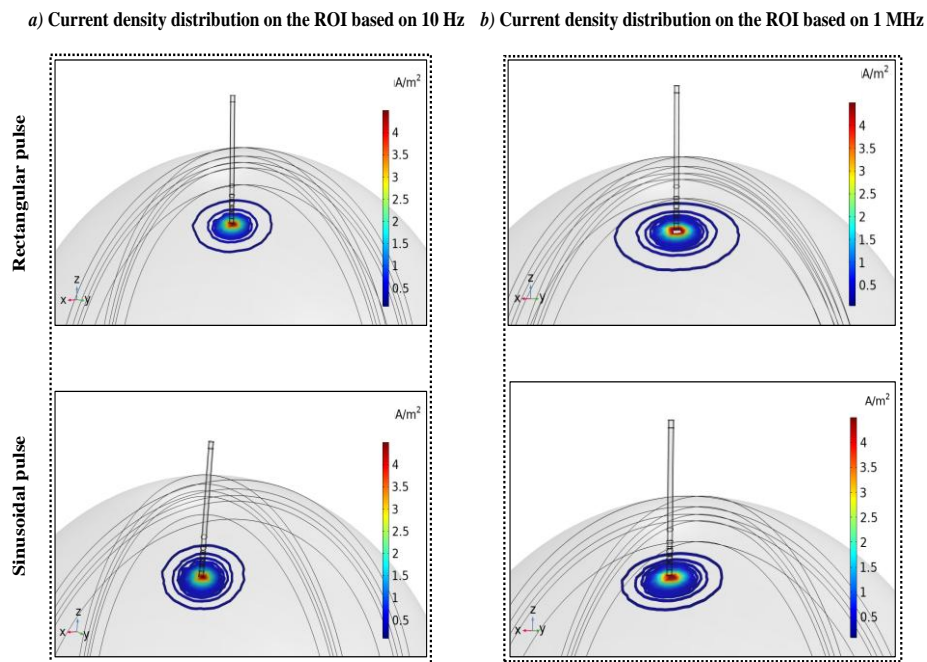


Figure 6. (a) Shows the current density variation for rectangular and sinusoidal waveforms based on 10 Hz. (b) Shows the current density variation for rectangular and sinusoidal waveforms based on 1 MHz

3. Results

3.1. Electrical potential

The electrical potential variation on the RIO for different simulation waveforms based on different simulation frequencies is shown in Fig. 5. The electrical potential variation was recorded for each frequency based on sinusoidal and rectangular simulation waveforms. The electrical potential variation based on sinusoidal

waveform is shown in Fig. 5(a) and (b). The electrical potential variation based on rectangular waveform is shown in Fig. 5(c) and (d). Each waveform is evaluated based on used frequencies as follows.

It is clearly shown that there is distortion in the stimulus current waveforms for both frequency ranges. The induced electrical potential range is about 6 mV for the 10 Hz frequency range. This is about 4 mV for the 1 MHz. The highest electrical potential variation is recorded for *Terminal 1* for both frequencies. Also, the lowest electrical potential induced on *Terminal 3* for both frequencies range.

Interestingly, the induced positive electrical potential range is higher for 1 MHz compared to 10 Hz using a rectangular stimulation waveform. However, the electrical potential range is the same for both simulation frequencies. The electrical potential value varies from -3 mV to 3 mV for 10 Hz. This varies from -0.5 mV to 5.5 mV for the 1 MHz. The recorded lowest electrical potential is observed on Terminal 3 for 10 Hz. The same trend is not observed for the 1 MHz.

It is also shown that the distortion in the rectangular electrical potential waveform is significantly distorted for 1 MHz, compared to the results for 10 Hz as shown in Fig. 5(d).

3.2. Current density

The current density variation on the RIO based on different frequency ranges using different simulation waveforms is shown in Fig. 6. The results for the 10 Hz and 1 MHz are shown in Fig. 6(a) and (b), respectively. The current density distributions are visualized with contours. The number of contours is the same for both simulation pulses and different frequency levels. The VC is unified based on grey colour and the current density variation is ranged with colormap in COMSOL to visualise current density over the RIO in more detail.

It is shown that the induced current density variation range was about the same for all waveforms and frequencies. It is clearly shown that the current density has a wide-spread range when 1 MHz current pulse is used, compared to 10 Hz. The current density has the same variation based on different current pulse waveforms for 10 Hz. It is noted that the results for the rectangular current pulse based on 1 MHz spread more on the RIO, compared to the sinusoidal current pulse based the 1 MHz.

3.3. Electrical Field

The electrical field distribution over the RIO based on different frequency ranges using different simulation waveforms is shown in Fig. 7. The electrical field is calculated based on *streamlines* in COMSOL to visualize variation on the surface of the RIO. The results for the 10 Hz and 1 MHz are shown in Fig. 7(a) and (b), respectively.

The higher value of the electric field is recorded for the rectangular waveform pulse for both frequency levels, compared to the sinusoidal current pulse. The electric field range is 0 to 60 V/m for the rectangular current pulse using 10 Hz frequency. This range varies from 0 to 140 V/m for the same waveform using 1 MHz current pulse.

When the sinusoidal current pulse is applied, the recorded electric field range is 0 to 25 V/m for 10 Hz and 0 to 45 V/m for 1 MHz current pulses. Thus, the simulation frequency is proportional to the induced electric field over the RIO. It is interestingly shown that the direction of the lower simulation frequency is from the outer to towards to the centre. However, this is from the centre to towards the outer for the higher frequency level. This is valid for both simulation waveforms. It is noted that the electric field distribution is smoother for the higher simulation frequency compared to the lower frequency level.

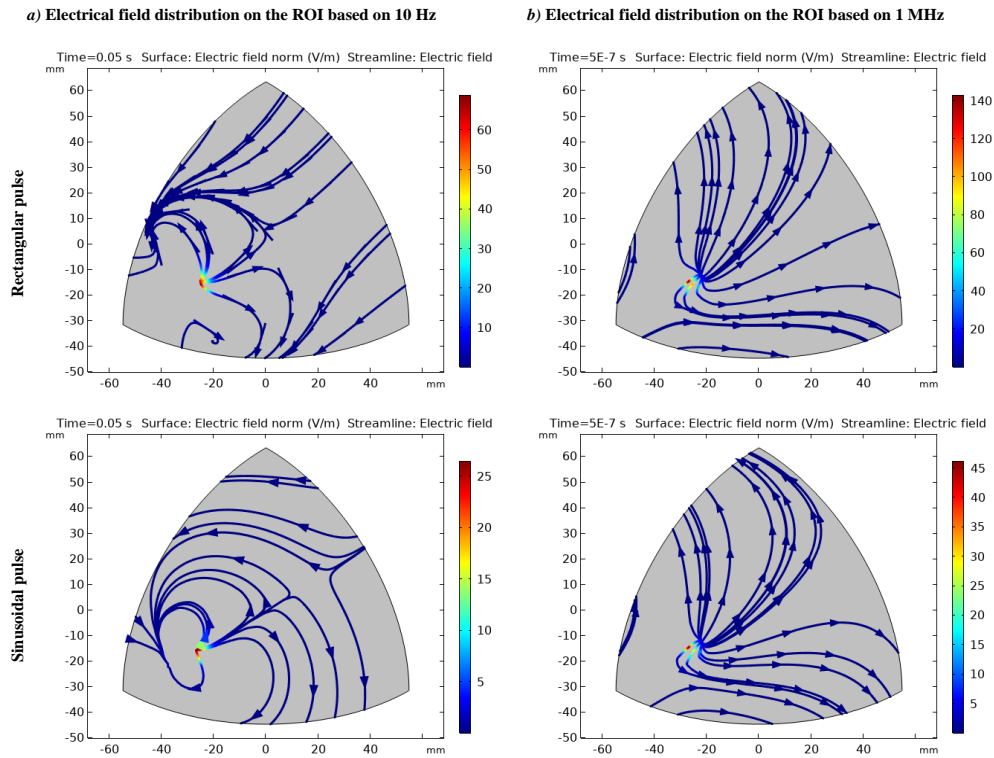


Figure 7. (a) Shows electric field distribution over the RIO for rectangular and sinusoidal waveforms based on 10 Hz. (b) Shows electric field distribution over the RIO for rectangular and sinusoidal waveforms based on 1 MHz.

4. Discussion

It has been shown that there are various factors influencing the DBS performance including waveform shape, frequency, pulse width [17]. It may not be feasible to deeply investigate the impact of such parameters on the outcome using experimental tests. Bio-modelling is increasingly becoming an alternative option to the design and optimization of biomedical devices. Thus, the impact of the simulation waveform shape and frequency level on the current density, electrical potential and electrical field variations was evaluated using such bio-computational modelling methods. A multi-layered bio-computational model of the human head was developed based on the previous study [3]. The electrode model was generated based on commercially available device parameters to analyse the impact of device stimulation waveforms using different frequencies. Also, the framework of the existing simulation software was highlighted for bio-computational model designers. The important steps of the generation of the volume conductor were emphasized. The results were calculated based on the time-dependent study by including the capacitive effect of the tissue layers.

The results showed that the amplitude of the electrical potential variation was reduced when the higher simulation frequency was applied as shown in Fig. 5. This can be associated with the composition of the body. When the higher frequency was used, the current penetrates to the inner structures as the simulation current pulse based on the higher frequency penetrates easily through the inner structures [15], and this led to lower induced electrical potential variation according to (2). Also, it was shown that the capacitive effect was more dominant when the higher frequency level was used based on rectangular waveform shape. This may be related to the sharp transition region of the rectangular pulse compared to the sinusoidal pulse.

It is shown that the induced electrical potential variation on the simulation electrodes distorted when the rectangular simulation waveform was used. This may be associated with sharpness of the transition region. Since the sinusoidal waveform has a smooth transition from anode to cathode region, whereas, rectangular has a significant sharp transition when the polarity was changed from anode to cathode (or vice-versa), thus, the results for rectangular waveform were more distorted based on higher frequency ranges.

Although the induced current density range is nearly the same for the different frequency levels and simulation waveform shapes, it was indicated in Fig. 6 that current density has more spread contours using a higher frequency. It is well known that the neuromodulator device based on higher frequency stimulation may spread the inner structure of the biological tissue layers with ease. The reason for current density range is nearly the same for the different frequency levels may be related to the geometric features of the electrode and the applied current level. Since the same electrode and the same current amplitude were used for this study; it is expected to be the same amount of the current density at the RIO for different simulation waveforms and frequency levels.

In Fig. 7, it was shown that the electric field variation was proportional to the simulation frequency for both simulation waveform types. This may be associated with the composition of the body as the simulation frequency increased and the induced electric field also increased.

Although some previous studies did not include the capacitive effect when the DBS based on FEM was studied [21, 22], the other was considered to compute the potential and current distribution that was resulting from the DBS [23]. The result of this study is in agreement with the existing study [23] regarding the capacitive effect. It has been shown that the capacitive affect has a substantial impact on the outcome. However, only this study investigates the impact of the different pulse waveforms based on different frequency levels using FEM procedures.

Overall, it can be deduced from the results of this study that the simulation waveform shape and simulation frequency level affect the performance of the DBS neuromodulator. The capacitive effect should not be ignored at the higher frequency levels, and it was also suggested that current density evenly distributed over the RIO at the higher frequency levels. These steps should be considered when a DBS neuromodulator is designed.

5. Conclusion

The multilayered bio-computational model was used to analyse the electrical potential, current density, and electric field variations within the human head model via DBS electrodes that are commonly used in clinical research studies. The goal of this study was to investigate the impact of the stimulation waveform shape and simulation frequency level on the outcome using the DBS system. The results for the sinusoidal and rectangular charge-balanced stimulation waveforms were recorded based on different frequency ranges. Also, the general flow of the computational model development was highlighted. The results showed that the stimulation waveforms have a significant impact on the electrical and current density distributions on the RIO.

6. Author Contribution Statement

In the study, Author 1 contributed to forming the idea, making the design and finalising the work.

7. Ethics committee approval and conflict of interest statement

There is no conflict of interest with any person / institution in the article prepared.

8. References

- [1] N. A. Pelot, B. J. Thio, and W. M. Grill, "Modeling current sources for neural stimulation in COMSOL," *Front. Comput. Neurosci.*, vol. 12, no. June, pp. 1–14, 2018.
- [2] L.-J. Ren, Y. Yu, Y.-H. Zhang, X.-D. Liu, Z.-J. Sun, W.-J. Yao, T.-Y. Zhang, C. Wang, C.-L. Li, "Three-dimensional finite element analysis on cochlear implantation electrode insertion," *Biomech. Model. Mechanobiol.*, Apr. 2022.
- [3] E. Salkim, A. Shiraz, and A. Demosthenous, "Impact of neuroanatomical variations and electrode orientation on stimulus current in a device for migraine: A computational study," *J. Neural Eng.*, vol. 17, no. 1, 2020.
- [4] E. Salkim, A. Shiraz, and A. Demosthenous, "Influence of cellular structures of skin on fiber activation thresholds and computation cost," *Biomed. Phys. Eng. Express*, vol. 5, no. 1, p. 015015, 2018.
- [5] A. Fellner, A. Heshmat, P. Werginz, and F. Rattay, "A finite element method framework to model extracellular neural stimulation," *J. Neural Eng.*, vol. 19, no. 2, Apr. 2022.
- [6] J. Martinek, Y. Stickler, M. Reichel, W. Mayr, and F. Rattay, "A novel approach to simulate Hodgkin-Huxley-like excitation with COMSOL Multiphysics," *Artif. Organs*, vol. 32, no. 8, pp. 614–619, 2008.
- [7] F.-J. Pettersen, and J. O. Høgetveit, "From 3D tissue data to impedance using Simpleware ScanFE+IP and COMSOL Multiphysics – a tutorial," *J. Electr. Bioimp.*, vol. 2, pp. 13–32, 2011.
- [8] P. Marianelli, M. Capogrosso, L. B. Luciani, A. Panarese, and S. Micera, "A computational framework for electrical stimulation of vestibular nerve," *IEEE Trans. Neural Syst. Rehabil. Eng.*, vol. 4320, no. c, pp. 1–13, 2015.
- [9] L.-J. Ren, Y. Yu, Y.-H. Zhang, X.-D. Liu, Z.-J. Sun, W.-J. Yao, T.-Y. Zhang, C. Wang, C.-L. Li, "Three-dimensional finite element analysis on cochlear implantation electrode insertion," *Biomech. Model. Mechanobiol.*, Apr. 2022.
- [10] E. Salkim, M. Zamani, D. Jiang, S. R. Saeed, and A. Demosthenous, "Insertion guidance based on impedance measurements of a cochlear electrode array," *Front. Comput. Neurosci.*, vol. 16, Jun. 2022.
- [11] E. Salkim, A. N. Shiraz, and A. Demosthenous, "Computational study on transcutaneous frontal nerve stimulation: Simplification of human head model," in *Proc. COMSOL Conf.*, Rotterdam, pp. 1–4, 2017.
- [12] M. Zelechowski, G. Valle, and S. Raspopovic, "A computational model to design neural interfaces for lower-limb sensory neuroprostheses," *J. Neuroeng. Rehabil.*, vol. 17, no. 1, pp. 1–13, 2020.
- [13] Y. Ge et al., "Mediating different-diameter A β nerve fibers using a biomimetic 3D TENS computational model," *J. Neurosci. Methods*, vol. 346, Dec. 2020.
- [14] S. Raspopovic, S. Capogrosso, and M. Micera, "A computational model for the stimulation of rat sciatic nerve using a transverse intrafascicular multichannel electrode," *IEEE Trans. Neural Syst. Rehabil. Eng.*, vol. 19, no. 4, pp. 333–344, 2011.
- [15] S. F. Cogan, "Neural stimulation and recording electrodes," *Annu. Rev. Biomed. Eng.*, vol. 10, no. 1, pp. 275–309, 2008.
- [16] K. M. Prakash, "An overview of surgical therapy for movement disorders," *Neurology*.
- [17] N. Yousif, R. Bayford, and X. Liu, "The influence of reactivity of the electrode-brain interface on the crossing electric current in therapeutic deep brain stimulation," *Neuroscience*, vol. 156, no. 3, pp. 597–606, Oct. 2008.
- [18] E. Salkim, "Analysis of tissue electrical properties on bio-impedance variation of upper limbs," *Turk. J. Electr. Eng. Comput. Sci.*, vol. 30, no. 5, pp. 1839–1850, 2022.
- [19] E. Salkim, and Y. Wu, "Modeling of transcutaneous recording for bio-impedance analysis on the upper-arm," *IEEE Access*, vol. 11, pp. 107184–107193, 2023.
- [20] C. R. Butson, and C. C. McIntyre, "Tissue and electrode capacitance reduce neural activation volumes during deep brain stimulation," *Clin. Neurophysiol.*, vol. 116, no. 10, pp. 2490–2500, Oct. 2005.
- [21] J. D. Johansson, and P. Zsigmond, "Comparison between patient-specific deep brain stimulation simulations and commercial system SureTune3," *Biomed. Phys. Eng. Express*, vol. 7, no. 5, Sep. 2021.

- [22] A. M. Frankemolle-Gilbert, B. Howell, K. L. Bower, P. H. Veltink, T. Heida, and C. C. McIntyre, "Comparison of methodologies for modeling directional deep brain stimulation electrodes," *PLoS One*, vol. 16, no. 12, Dec. 2021.
- [23] K. Butenko, C. Bahls, M. Schröder, R. Köhling, and U. Van Rienen, "OSS-DBS: Open-source simulation platform for deep brain stimulation with a comprehensive automated modeling," *PLoS Comput. Biol.*, vol. 16, no. 7, Jul. 2020.



Mesaj Aktarma Sinir Ağını Kullanarak Alzheimer Hastalığı için BACE-1 İnhibitörleri Verilerine İlişkin Etkileşim Tahmini

Suat TORAMAN^{1*} , Bihter DAS² 

¹Hava Trafik Kontrol Bölümü, Sivil Havacılık Yüksekokulu, Fırat Üniversitesi, Elazığ, Türkiye.

²Yazılım Mühendisliği Bölümü, Teknoloji Fakültesi, Fırat Üniversitesi, Elazığ, Türkiye.

¹storaman@firat.edu.tr, ²bihterdas@firat.edu.tr

Geliş Tarihi: 08.04.2024
Kabul Tarihi: 30.07.2024

Düzelme Tarihi: 13.05.2024

doi: <https://doi.org/10.62520/fujece.1466902>
Araştırma Makalesi

Alıntı: S. Toraman ve B. Daş, "Mesaj aktarma sinir ağını kullanarak alzheimer hastalığı için BACE-1 inhibitörleri verilerine ilişkin etkileşim tahmini", Fırat Üni. Deny. ve Hes. Müh. Derg., vol. 4, no 1, pp. 72-84, Şubat 2025.

Öz

Beyin hücrelerinin zamanla ölmesine bağlı olarak hafıza kaybı, demans ve bilişsel işlevlerde genel bir azalma şeklinde gelişen tıbbi duruma Alzheimer hastalığı denir. Bu hastalık, bilişsel işlevlerde kademeli bir düşüşe ve sonuçta kişinin günlük yaşamını etkileyen ciddi hafıza kayıplarına yol açabilmektedir. Alzheimer hastalığına neden olan mekanizma tam olarak anlaşılmasına rağmen beyindeki plaklar ve nörofibriler demetler gibi bazı yapısal değişikliklerle ilişkilendirilmiştir. Bu çalışma, Alzheimer hastalığının tedavisinde ümit verici olan BACE-1 inhibitörlerinin keşfi için geometrik derin öğrenme yönteminin kullanımını araştırmaktadır. Eğitim sürecinde İletişim Geçiş Sinir Ağı ve Tamamen Bağlantılı Ağ kullanılarak özelleştirilmiş bir model geliştirilmiştir. Bu model, moleküler yapıların karmaşık özelliklerini yakalamak için grafik yerleştirmelerin ve tamamen bağlantılı ağların birleşimi yoluyla molekül etkileşimlerini tahmin etmektedir. Sonuçlar, geliştirilen modelin BACE-1 inhibitörlerinin etkileşimlerini başarılı bir şekilde tahmin edebildiğini göstermektedir. Modelin performans oranı %87,7 olarak belirlenmiştir. Bu çalışma, Alzheimer hastalığına yönelik yeni BACE-1 inhibitörlerinin keşfedilmesi ve geliştirilmesi için umut verici bir yol haritası sunmaktadır.

Anahtar kelimeler: BACE-1 ilaç etkileşimi, Alzheimer hastalığı, Geometrik derin öğrenme, Grafik ağı, BACE-1 inhibitörleri

*Yazışılan Yazar

İntihal Kontrol: Evet – Turnitin

Şikayet: fujece@firat.edu.tr

Telif Hakkı ve Lisans: Dergide yayın yapan yazarlar, CC BY-NC 4.0 kapsamında lisanslanan çalışmalarının telif hakkını saklı tutar.



Interaction Prediction on BACE-1 Inhibitors Data for Alzheimer Disease using Message Passing Neural Network

Suat TORAMAN^{1*} , Bihter DAS² 

¹Air Traffic Control, Civil Aviation High School, Firat University, Elazig, Türkiye.

²Department of Software Engineering, Technology Faculty, Firat University, Elazig, Türkiye.

¹storaman@firat.edu.tr, ²bihterdas@firat.edu.tr

Received: 08.04.2024
Accepted: 30.07.2024

Revision: 13.05.2024

doi: <https://doi.org/10.62520/fujece.1466902>
Research Article

Citation: S. Toraman and B. Daş, "Interaction prediction on bace-1 inhibitors data for alzheimer disease using message passing neural network", *Firat Univ. Jour.of Exper. and Comp. Eng.*, vol. 4, no 1, pp. 72-84, February 2025.

Abstract

The medical condition that develops as memory loss, dementia, and a general decrease in cognitive functions due to the death of brain cells over time is called Alzheimer's disease. This disease can lead to a gradual decline in cognitive functions and eventually severe memory losses that affect a person's daily life. Although the exact mechanism that causes Alzheimer's disease is not fully understood, it has been associated with certain structural changes in the brain, such as plaques and neurofibrillary bundles. This study investigates the use of geometric deep learning methods for the discovery of BACE-1 inhibitors that are promising in addressing Alzheimer's disease. Our study builds on these advancements by integrating GDL with pharmacological criteria, such as the QED criterion and Lipinski's rule, to predict BACE-1 inhibitors with enhanced accuracy and drug-like properties. Our model, which combines message-passing neural networks (MPNNs) and fully connected network (FCN) architectures, achieved a success rate of 87.7%. This performance not only surpasses that of previous studies but also ensures the practical applicability of our findings in drug discovery for Alzheimer's disease. The dual focus on prediction accuracy and drug likeness sets our work apart, providing a more comprehensive approach to identifying effective therapeutic agents.

Keywords: BACE-1 drug interaction, Alzheimer's disease, Geometric deep learning, Graph network, BACE-1 inhibitors.

*Corresponding author

1. Introduction

Alzheimer's disease is a form of dementia that progresses slowly and increases with age, leading to cognitive impairment, memory loss, and eventually difficulty in activities of daily living. The disease is characterized by nerve cells in the brain becoming damaged and dying over time [1,2]. It is the most prevalent form of dementia and usually has a progressive course. The pathophysiology of Alzheimer's disease revolves around two key features, namely the accumulation of beta amyloid plaques and the formation of neuronal fibrillary tangles. These plaques and tangles block communication between nerve cells and lead to neuronal death. Alzheimer's disease is a health problem that is common in the elderly population and still has no cure. The pathophysiology of this disease is complex and is affected by factors such as the accumulation of beta amyloid ($A\beta$) plaques and abnormal accumulation of tau protein leading to neuronal toxicity. In the beginning of these pathological processes, the BACE-1 enzyme, also known as beta-secretase, plays a critical role [3,4]. Beta-secretase 1 (BACE-1), which plays a critical role in the production of beta amyloid ($A\beta$) peptides, is an enzyme associated with Alzheimer's disease [5]. BACE-1 initially produces the $A\beta_{42}$ peptide by cleaving the amyloid precursor protein (APP). $A\beta_{42}$ is one of the main components of toxic amyloid beta plaques that accumulate in the pathological process of Alzheimer's disease and cause the death of nerve cells. Therefore, the inhibition or diminishment of BACE-1 activity is being explored as a strategy to treat or prevent AZ. Inhibitors targeting the BACE-1 enzyme have garnered significant attention in research and development as potential therapeutic avenues for addressing AZ. Understanding the role of this enzyme's function is crucial in elucidating the pathophysiology of AZ and devising potential treatment modalities [6].

The geometric deep learning (GDL) approach is the application of advanced geometry techniques to drug data used to predict drug interactions by providing precise representations of molecular structures. Numerous studies in the literature delve into drug interactions using geometric deep learning. For instance, the work by Shen et al. [7] showcases the efficacy and promise of geometric deep learning in molecular data analysis. Specifically, research shows that molecular graphs composed solely of non-covalent bonds can yield comparable or superior results compared to those based on covalent bonds, which are conventionally accepted as the standard for representing molecular topology at the atomic level. In the context of geometric deep learning (GDL), molecules are typically modeled as molecular graphs, density functions, or molecular surfaces, and these representations are analyzed using various deep learning models such as (3D) convolutional neural networks (CNNs), graph neural networks (GNNs), recurrent neural networks (RNNs), and others [8-10]. In another investigation, researchers applied geometric deep learning techniques to drug discovery and the design processes of bioorganic and medicinal chemistry. Authors investigated the potential of geometric deep learning in tasks such as molecular property prediction, ligand binding site and location prediction, and structure-based new molecule design [11]. Additional studies [12-15] delve into the integration of symmetry information into 3D molecular representations and its incorporation into neural network architectures. These studies assess the efficacy of these methods, particularly in structured learning processes, and their utilization in structure-based drug design. Furthermore, a comprehensive review [16] offers insights into recent literature on GDL studies for drug discovery and symmetry learning. The review highlights GDL's applications in drug discovery, including tasks like molecular property prediction, interactions, design, conformation prediction, and 3D pretraining, while also addressing associated challenges. Nugroho et al. developed and optimized a fingerprint-based artificial neural network (ANN) model using three different Bat Algorithm strategies to predict Beta-secretase 1 (BACE-1) inhibitors as therapeutic agents for Alzheimer's disease [17]. More recently, Feinberg et al. [18] applied 3D convolutional neural networks (3D-CNNs) to molecular surfaces, achieving high accuracy in predicting protein-ligand binding affinities. Their study highlighted the importance of three-dimensional molecular representations in capturing interaction nuances. Ragoza et al. [19] developed a deep learning model that incorporates both 2D and 3D information of molecules for drug-target interaction predictions. Their model achieved state-of-the-art performance, showcasing the advantages of integrating multiple molecular representations.

In our study, we leverage both GDL and pharmacological criteria to predict interactions of BACE-1 inhibitors. Unlike previous studies, our model integrates MPNN and fully connected network (FCN) architectures, achieving a success rate of 87.7%. This study also advances the literature by providing a quantifiable success rate, which is often missing in previous studies. By incorporating pharmacological

criteria such as the QED criterion and Lipinski's rule, our model ensures not only effective interaction predictions but also favorable drug-like properties of the inhibitors. This dual focus enhances the practical applicability of our findings, offering a more comprehensive approach to drug discovery for Alzheimer's disease.

In this paper, we aim to use a geometric deep learning approach to perform interaction predictions for Alzheimer's disease on BACE-1 data. GDL has indeed emerged as a powerful method in molecular interaction prediction because it allows more precise representation of molecular structures and more accurate modeling of interaction mechanisms. This study also targets to make valuable contributions to the discovery of new therapeutic targets and drug development for the treatment and prevention of Alzheimer's disease. Application of geometric deep learning methods to interaction predictions on BACE-1 data may lead to the discovery of potential BACE-1 inhibitors and the development of innovative approaches to the treatment of Alzheimer's disease. This study aims to offer a new perspective in the fight against Alzheimer's disease and shed light on advancing treatment strategies. The main contributions of this study are outlined below:

- It offers a new approach to drug interaction prediction for Alzheimer's disease by investigating the use of geometric deep learning methods on BACE-1 data.
- Interaction predictions obtained through the use of MPNN based method can guide the design and optimization of BACE-1 inhibitors.
- The study contributes to a better understanding of the molecular interactions between the BACE-1 enzyme and potential inhibitors. This allows for the development of more effective strategies during the drug design process.

The structure of this paper as follows: Section 2 presents an in-depth exploration of the materials and methods employed. Section 3 delves into the experimental findings and discussions. Following that, Section 4 outlines the limitations encountered and suggests future avenues of research. Finally, Section 5 concludes the study of the paper.

2. Materials and Method

This section outlines the materials and methodologies employed in the study for the prediction of interactions with BACE-1 inhibitors. It encompasses the dataset description, model architecture, training procedure, and evaluation metrics utilized in the experiment. The proposed algorithm encompasses three key steps: dataset collection, training, and prediction. Additionally, Figure 1 shows the block diagram of the proposed model, providing a visual representation of the methodology employed in the study.

This section outlines the materials and methodologies employed in the study for the prediction of interactions with BACE-1 inhibitors. It encompasses the dataset description, model architecture, training procedure, and evaluation metrics utilized in the experiment. The proposed algorithm encompasses three key steps: dataset collection, training, and prediction. Additionally, Figure 1 shows the block diagram of the proposed model, providing a visual representation of the methodology employed in the study.

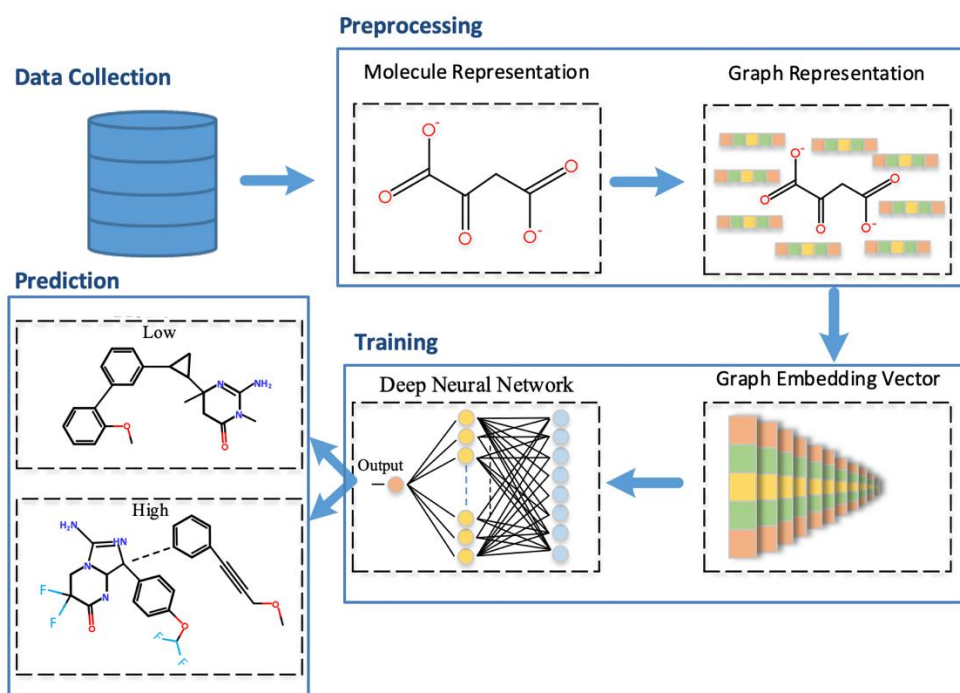


Figure 1. The block diagrams of the GDL based model

2.1. Data collection

This section provides an overview of the dataset employed in the study. It includes quantitative (IC50) measurements and qualitative (binary label) binding outcomes, obtained from experiments conducted on a range of compounds targeting human β -secretase 1 (BACE-1). BACE-1 is an enzyme involved in the production of beta-amyloid peptides, which accumulate in the brains of Alzheimer's patients, contributing to the disease's progression. The BACE dataset includes a variety of columns and parameters that are crucial for developing and evaluating potential BACE-1 inhibitors. These features are broadly categorized into molecular descriptors, activity measurements, and annotations related to Alzheimer's disease. The dataset originates from the BACE data, specifically curated for research on Alzheimer's disease therapeutics. The dataset utilized in this study was sourced from <https://moleculenet.org/datasets-1> database [20]. It comprises 1513 compounds represented in the SMILES format. The dataset is partitioned into training of 80%, validation of 10%, and test of 10% subsets. Additionally, the dataset's scaffold and rec-split methods were employed to ensure diverse representation and robust evaluation. 1D and 2D descriptive features were used to represent the compounds in the study. Basic molecular feature information such as molecular weight, number of hydrogen bond donors and acceptors, and LogP (partition coefficient) were selected as 1D descriptors. These descriptors are necessary to evaluate the drug-likeness of compounds based on Lipinski's rule of five. 2D descriptors, on the other hand, capture the molecular topology and include features such as the number of rings, the number of rotatable bonds, and the presence of specific functional groups. They provide a more detailed representation of the structure of the molecule. Table 1 shows the dataset used in the experiment.

Table 1. The detailed features of the dataset

Mol	CID	Class	pIC50	MW	AlogP	HBA	HBD	RB	Heavy Atom Count	Chiral Center Count	Chiral Center CountAll	Ring Count	PSA	Estate	MR	Polar
<chem>O1CC[C@@H](NC(=O)[C@@H](Cc2cc3cc(ccc3nc2N)-c2ccccc2C)CC1(C)C</chem>	BACE_1	1	9.1549015	431.56979	4.4014001	3	2	5	32	2	2	4	77.239998	67.251999	129.9039	58.397999
<chem>Fc1cc(cc(F)c1)C[C@H](NC(=O)[C@@H](N1CC[C@](NC(=O)C)(CC(C)C)C1=O)CCc1ccccc1)[C@H](O)[C@@H]1[NH2+][C][C@H](OCCC)C1</chem>	BACE_2	1	8.8538723	657.81073	2.6412001	5	4	16	47	6	6	4	124.58	115.417	173.6176	76.254997
<chem>S1(=O)(=O)N(c2cc(cc3c2n(cc3CC)CC1)C(=O)N[C@H]([C@H](O)C[NH2+])Cc1cc(OC)ccc1)Cc1ccccc1)C</chem>	BACE_3	1	8.6989698	591.74091	2.5499001	4	3	11	42	2	3	5	125.86	96.585999	160.12421	75.639
<chem>O=C(NCC1CCCC1)[C@@H](Cc1cc2cc(ccc2nc1N)-c1ccccc1)CCC</chem>	BACE_4	1	7.9586072	443.6236	7.0788999	2	2	8	33	1	1	4	68.010002	66.001999	137.3194	61.431
<chem>S1(=O)(=O)C[C@@H](Cc2cc3c([nH]cc3CC(F)F)cc2)[C@H](O)[C@@H]([NH2+])Cc2cc(ccc2)C(C)(C)C1</chem>	BACE_5	1	7.2596374	505.6402	2.7595999	2	3	8	35	3	4	4	95.150002	87.500999	132.3071	60.943001
<chem>O1[C@@H]2COCC[C@@]2(N=C1N)c1cc(ccc1)-c1cncnc1</chem>	BACE_6	0	4.0030508	296.32379	0.87709999	5	0	2	22	2	2	4	82.620003	47.750999	80.689301	37.137001
<chem>[NH+]=1[C@](N=C(c2ccccc2)C=1N)(C)c1cc(ccc1)-c1cncnc1</chem>	BACE_7	0	327.4024	1.4339	2	0	3	25	1	1	4	65.239998	49.251999	97.589897	48.525002	
<chem>n1ccccc(NCc2cc(ccc2)-c2ccccc2)c1N</chem>	BACE_8	0	276.33569	2.2346001	2	2	4	21	0	0	3	63.830002	44.334999	86.700699	41.577	
<chem>O1CCC(OC(=O)[C@@H]2[NH2+][C][C@]3(C2)c2c(NC3=O)ccc2)CC1</chem>	BACE_9	0	3.9430952	317.35959	-1.0807	4	2	3	23	2	2	4	81.239998	53.084	80.653801	36.096001
<chem>O=C1NC(=NC(=C1)CCc1cc2[nH]c2cc1)N</chem>	BACE_10	0	3.8860567	254.2872	1.7381001	2	3	3	19	0	0	3	87.559998	44.001999	75.263802	34.915001

2.2. Pre processing

This section describes the preprocessing steps applied to prepare the dataset for training the geometric deep learning-based model. In the experimental study, raw data represented in SMILES (Simplified Molecular Line Entry System) format was first converted into molecular graphs. The choice to use the SMILES format is to represent the structure of chemical compounds efficiently and concisely. The preprocessing steps began with parsing each compound's SMILES string to generate its corresponding molecular graph, identifying atoms and bonds, and constructing a graph where atoms are nodes and bonds are edges. These molecular graphs were then processed to extract node features such as atom types, hybridization states, and aromaticity, along with edge features like bond types and bond orders, which are crucial for accurately representing the molecules' chemical properties. Next, these molecule representations were used to construct graph structures suitable for input into the Message Passing Neural Network (MPNN), where each node (atom) was represented by a feature vector and each edge (bond) by an attribute vector. Feature normalization was applied to ensure that all input features were on a similar scale, enhancing the stability and performance of the neural network.

2.3. Training

This section elucidates the training protocol for our proposed model, which integrates a Message Passing Neural Network (MPNN) to forecast interactions with BACE-1 inhibitors. The training unfolds in two pivotal stages: MPNN and FCN. MPNN, a specialized neural network architecture tailored for processing molecular data depicted as graphs [21], plays a central role. It facilitates the conversion of graph data structure into a vector termed as a graph embedding. This embedding vector undergoes iterative updates grounded on messages exchanged among nodes within the graph. Leveraging MPNN, node feature vectors are transmuted into a distinct space, thereby enabling the generation of graph embedding [22-24]. Originally introduced by Gilmer et al., this approach reshapes spatial and spectral architectures within graph networks through two discernible phases: message passing and readout. Moreover, MPNN serves as a supervised learning framework for graphs, empowering the redefinition of spatial and spectral architectures within graph networks. MPNN's message passing and readout stages contribute to the model's ability to capture intricate structural and functional characteristics of molecules. By incorporating MPNN into our training pipeline, we aim to exploit the rich information present in molecular structures to accurately predict interactions with BACE-1 inhibitors.

In the GDL-based model used, the metric space is created by excluding the reading function. Since the entire graph is examined to predict molecule interactions with BACE inhibitors for results, simply placing node proximity information in the embedding field will not be sufficient. Within the proposed GDL framework, embedding values undergo processing through a fully connected layer to facilitate prediction. This layer comprises four dense layers, with a dropout rate of 20% implemented in the first three layers to counter overfitting. The initial dense layer encompasses 92 neurons, succeeded by 46 neurons in the second layer, 23 neurons in the third layer, and a solitary neuron in the output layer. Activation functions encompass ReLu for the first three layers and sigmoid for the final layer. The architecture of the methodology employed in the experimental application is delineated in Figure 2.

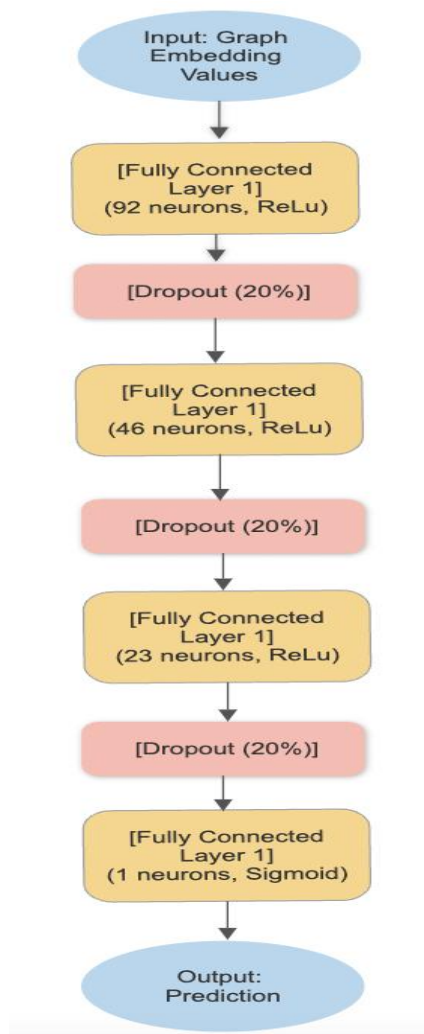


Figure 2. The Architecture of the FC Network Component

2.4. Prediction of interaction

In estimating the interaction of BACE-1 inhibitors, the Quantitative Estimates of Drug-likeness (QED) criterion is utilized [25,26]. This criterion allows quantitative evaluation of a combination of a compound's biological effect, drug properties, and pharmacological properties. This measure is calculated by evaluating molecular properties through a series of mathematical and statistical analyses. A compound with a higher QED score is considered to be more likely to succeed in the drug development process. Therefore, QED is used as an important tool in drug design and discovery processes. Figure 3 shows the interaction rates of QED on the BACE-1 inhibitors.

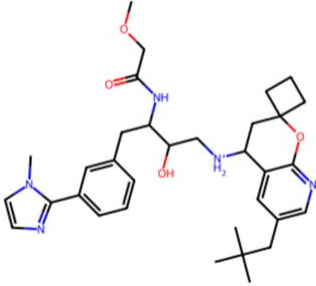
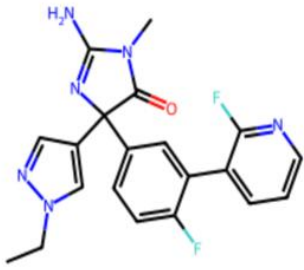
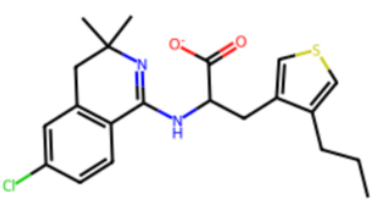
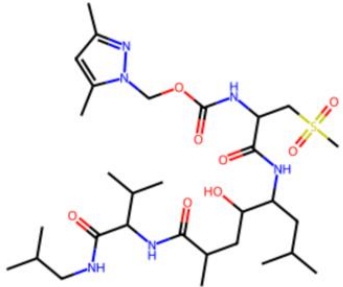
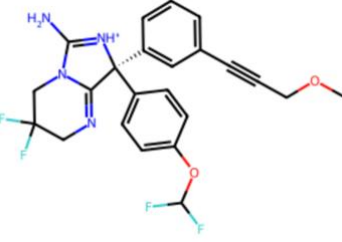
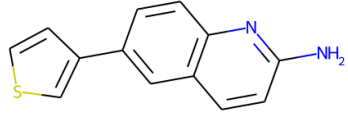
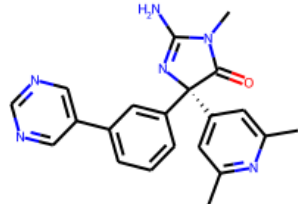
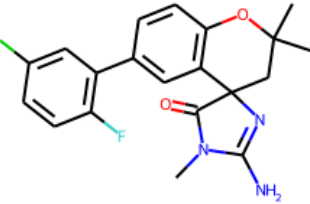
		
<chem>O1c2ncc(cc2C([NH2+])CC(O)C(NC(=O)COC)Cc2cc(ccc2)-c2nccn2C)CC12CCC2) CC(C)(C)C</chem>	<chem>O=C1N(CCCCC)C(=NC1(C1CCCCC1)C1CCCCC1)N</chem>	<chem>Fc1ccc(cc1-c1cccnc1F)C1(N=C(N)N(C)C1=O)c1cn(nc1)CC</chem>
$y_true/y_pred = 1/0.87$	$y_true/y_pred = 0/0.21$	$y_true/y_pred = 1/0.80$
		
<chem>Clc1cc2CC(N=C(NC(Cc3csc3CCC)C(=O)[O-])c2cc1)(C)C</chem>	<chem>S(=O)(=O)CC(NC(OCn1nc(cc1C)C)=O)C(=O)NC(C(O)CC(C=O)NC(C(C)C)C(=O)NCC(C)C)CC(C)C</chem>	<chem>FC1(F)CN2C(=NC1)[C@]([NH+]=C2N)(c1cc(ccc1)C#CCOC)c1ccc(OC(F)F)cc1</chem>
$y_true/y_pred = 0/0.15$	$y_true/y_pred = 1/0.50$	$y_true/y_pred = 1/0.87$
		
<chem>s1cc(cc1)-c1cc2c(nc(N)cc2)cc1</chem>	<chem>O=C1N(C)C(=N[C@]1(c1cc(nc1)C)C)C1ccc(cc1)-c1cncnc1)N</chem>	<chem>Clc1cc(-c2cc3c(OC(CC34N=C(N)N(C)C4=O)(C)C)cc2)c(F)cc1</chem>
$y_true/y_pred = 1/0.16$	$y_true/y_pred = 0/0.64$	$y_true/y_pred = 1/0.50$

Figure 3. The QED results for interaction on BACE-1 inhibitors

3. Experimental Results and Discussion

In this study, Lipinski's rule was also taken into account for the prediction of drug interactions of BACE-1 inhibitors. The Lipinski rule consists of a set of rules used to evaluate whether oral bioavailability of a compound is likely [27]. This rule is important for determining the pharmacokinetic properties of a compound and is widely used in the development of drug candidates. Lipinski's rules are [28]:

- The molecular weight of the molecule has not been more than 500.
- The total number of hydrogen bonds (sum of N and O atoms) has not been more than 5.
- The number of donor hydrogen bonds has not been more than 5.
- To determine the lipophilicity of the molecule, the distribution coefficient (LogP) value should not be more than 5.

The BACE-1 drug interaction prediction performance value obtained by using the GDL model was determined as 0.877. To assess the effectiveness of the GDL model, the area under the curve (AUC) was calculated, indicating the accuracy of the proposed model. The ROC curve was used to provide a clearer

visual interpretation of the drug prediction of BACE-1 inhibitors. Figure 4 shows the results of the AUC, F1 score and negative predictive value performance values of the proposed model. Figure 4 shows that the AUC value approaches 90. In the ROC curve, the under the curve is defined as AUC. The desired situation is for the ROC curve to be close to 1. This shows that the discrimination of the system is high. In Figure 4a, the high AUC value shows that the discrimination of the system is high.

Accuracy is a performance criterion that is frequently used to measure the success of a model, but is not sufficient to measure system performance. F1 score is used to avoid making a wrong choice, especially when there is an imbalance in data between classes. Figure 4b shows the F1 score values for the training and validation data sets. As seen in Figure 4b, the F1 score reached approximately 80% at the end of 60 epochs.

When a test result is negative, the value that indicates the probability of the result actually being negative is called Negative Predictive Value. As can be seen in Figure 4c, it was actually negative, but the percentage defined as negative in the system was approximately 78%.

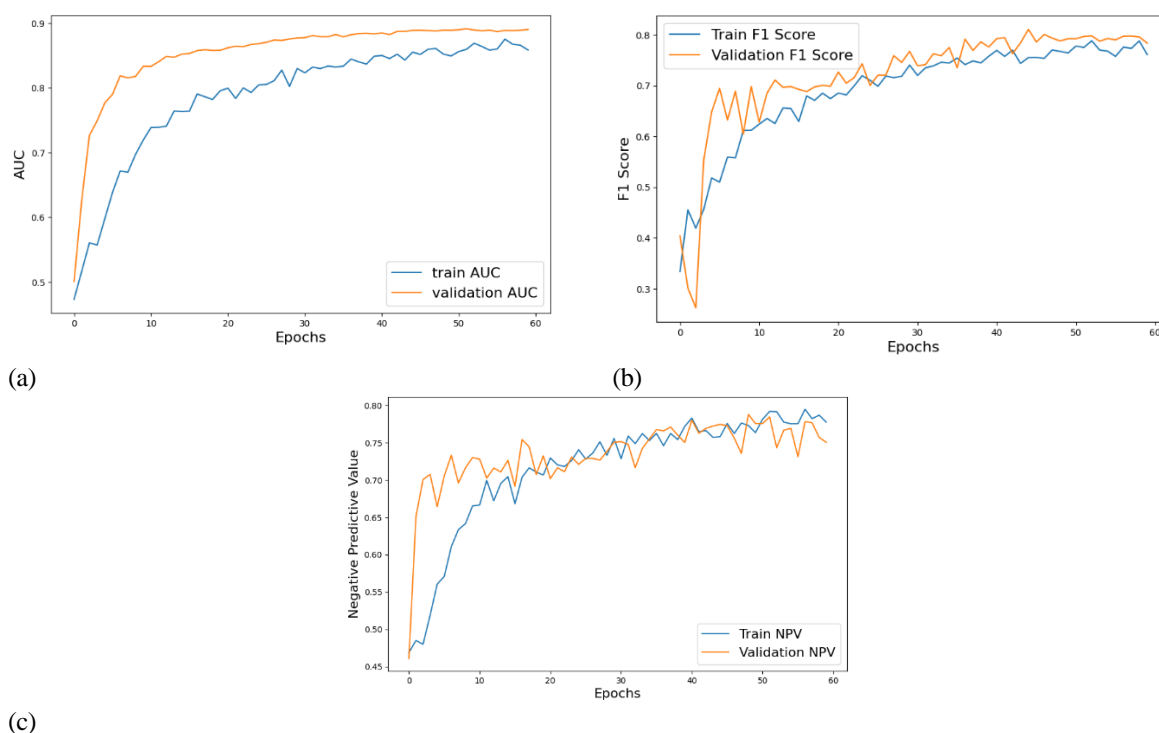


Figure 4. (a) The AUC (b) The F1 Score (c) The Negative Predictive Value performance of GDL based model

This study examined the potential role of BACE-1 inhibitors in the treatment of Alzheimer's. When we review other studies in the existing literature [29-32], there is sample evidence that BACE-1 inhibitors are an important therapeutic strategy targeting AD pathology. In particular, BACE-1 inhibitors have been shown to inhibit A β oligomerization and consequent amyloid plaque formation and thus may slow disease progression. Other studies in the literature reveal that BACE-1 inhibitors often face significant challenges in terms of their selectivity and drug-like properties. In this study, we showed that the GDL model we developed provides a high accuracy in predicting the efficacy of BACE-1 inhibitors. It is important to highlight the potential use of this model as a tool in the design and screening of BACE-1 inhibitors. However, the current study has some limitations. For example, the data set used was limited and only covered a specific chemical space. Additionally, further work is required on the generalizability and applicability of the GDL model to other molecular targets. Additionally, we think this study is an important step to further investigate the potential of BACE-1 in the treatment of AD. In the future, with further experimental studies and clinical trials, it will be possible to realize this potential and develop an effective therapeutic strategy in the treatment of AD.

Upon reviewing the literature, it is evident that many studies in the field do not explicitly report success rates in a manner that allows for direct comparison. For example, studies by Korolev et al. [33], Wang et al. [34], and Ghosh et al. [35] focus primarily on clinical and biochemical evaluations, providing valuable insights into binding mechanisms and pharmacokinetic properties, but do not offer quantifiable success rates for predictive modeling. This study makes significant contributions to the literature by leveraging geometric deep-learning techniques to predict interactions of BACE-1 inhibitors, an approach not widely explored in previous studies. Unlike traditional methods, our model utilizes the Message Passing Neural Network (MPNN) and Fully Connected Network (FCN) to effectively capture and represent complex molecular structures and their interactions. A key superiority of our study is the quantifiable success rate of 87.7%, which demonstrates the robustness and accuracy of our predictive model. This metric provides a clear benchmark for future research and offers a measurable improvement over previous studies that often lack explicit success rates.

4. Conclusion

This study assessed the applicability of geometric deep learning techniques in forecasting interactions of BACE-1 inhibitors for addressing Alzheimer's disease. During the training process, a customized model was developed using a Communication Transition Neural Network (MPNN) and Fully Connected Network (FCN). This model predicts molecule interactions through the combination of graph embedding and fully connected networks to capture complex structural and functional features in molecular structures. Our results show that the geometric deep learning model we developed can successfully predict the interactions of BACE-1 inhibitors. The performance rate of our model was evaluated based on the curve under area (AUC) value and was determined as 87.7%. By using pharmacological criteria such as the QED criterion and Lipinski's rule, the effectiveness of our model has further increased. These findings offer a novel approach for identifying and developing potential BACE-1 inhibitors aimed at treating Alzheimer's disease.

5. Acknowledgement

This work is supported by the Turkish Scientific and Technical Research Council (TUBITAK) project named "Development of a New Model for the Discovery of Anti-HIV Effective Molecules Using Geometric Deep Network Approaches" and project code 123E098. This study was supported by Scientific Research Projects Unit of Firat University (FUBAP) under the Grant Number ADEP.22.06. The authors thank to FUBAP for their supports.

6. Author Contribution Statement

S.T. contributed to the design, analysis of the data, interpretation of the results, spelling check and content, and B.D. contributed to the creation of the idea, literature review, analysis of the data, interpretation of the results, spelling check and checking the paper in terms of content.

7. Ethics Committee Approval and Conflict of Interest

There is no need for an ethics committee approval in the prepared paper. There is no conflict of interest with any person/institution in the prepared paper.

8. References

- [1] L. Baldini, E. Lenci, C. Faggi, and A. Trabocchi, "Identification of BACE-1 inhibitors through directed C(sp³)-H activation on 5-oxo-pyrrolidine-3-carboxylic acid derivatives," *Org. Biomol. Chem.*, vol. 22, no. 14, pp. 2754–2763, Apr. 2024.
- [2] Y. Nomura, M. Kaneko, R. Saito, Y. Okuma, Y. Kitamura, K. Takata, A. Nish, "A novel therapeutic target against Alzheimer's disease: HRD1 as endoplasmic reticulum stress-related ubiquitin ligase," *Neurobiol. Aging*, vol. 35, p. S17, Mar. 2014.
- [3] Z. Wang, J. Zhou, B. Zhang, Z. Xu, H. Wang, Q. Sun, N. Wang, "Inhibitory effects of β -asarone on lncRNA BACE1-mediated induction of autophagy in a model of Alzheimer's disease," *Behav. Brain Res.*, vol. 463, p. 114896, Apr. 2024.
- [4] Z. Chang, B. Zhu, J. Liu, H. Dong, Y. Hao, Y. Zhou, J. Travas-Sejdic, and M. Xu, "'Signal-on' electrochemical detection of BACE1 for early detection of Alzheimer's disease," *Cell Rep. Phys. Sci.*, p. 101632, Oct. 2023.
- [5] P. Gehlot, S. Kumar, V. Kumar Vyas, B. Singh Choudhary, M. Sharma, and R. Malik, "Guanidine-based β amyloid precursor protein cleavage enzyme 1 (BACE-1) inhibitors for the Alzheimer's disease (AD): A review," *Bioorg. Med. Chem.*, vol. 74, p. 117047, Nov. 2022.
- [6] S. M. Roy, B. R. Mehta, S. Trivedi, B. K. Sharma, and D. R. Roy, "Biological activity of some thiazolyl-thiadiazines as BACE-1 inhibitors for Alzheimer's disease in the light of density functional theory based quantum descriptors," *J. Phys. Org. Chem.*, 2022.
- [7] C. Shen, J. Luo, and K. Xia, "Molecular geometric deep learning," *Cell Rep. Methods*, vol. 3, no. 11, p. 100621, Nov. 2023.
- [8] J. Gilmer, S. S. Schoenholz, P. F. Riley, O. Vinyals, and G. E. Dahl, "Neural message passing for quantum chemistry," in *Proc. 34th Int. Conf. Mach. Learn.*, vol. 70, pp. 1263–1272, 2017.
- [9] P. W. Battaglia et al., "Relational inductive biases, deep learning, and graph networks," *arXiv Preprint*, arXiv:1806.01261, 2018.
- [10] H. Wua, J. Liua, R. Zhanga, Y. Lua, G. Cui, Z. Cui, Y. Ding, "A review of deep learning methods for ligand-based drug virtual screening," *Fundam. Res.*, Mar. 2024.
- [11] M. Liu, C. Li, R. Chen, D. Cao, and X. Zeng, "Geometric deep learning for drug discovery," *Expert Syst. Appl.*, vol. 240, p. 122498, Apr. 2024.
- [12] C. Isert, K. Atz, and G. Schneider, "Structure-based drug design with geometric deep learning," *Curr. Opin. Struct. Biol.*, vol. 79, p. 102548, Apr. 2023.
- [13] J. I. B. Janairo, "Chapter 6 - Support vector machine in drug design," in *Cheminformatics, QSAR and Machine Learning Applications for Novel Drug Development*, K. Roy, Ed., Acad. Press, pp. 161–179, 2023.
- [14] S. Kearnes, K. McCloskey, M. Berndl, V. Pande, and P. Riley, "Molecular graph convolutions: moving beyond fingerprints," *J. Comput. Aided Mol. Des.*, vol. 30, no. 8, pp. 595–608, Aug. 2016.
- [15] E. Shim, J. Kammeraad, Z. Xu, A. Tewari, T. Cernak, and P. M. Zimmerman, "Predicting reaction conditions from limited data through active transfer learning," *Chem. Sci.*, vol. 13, no. 22, pp. 6655–6668, 2022.
- [16] W. Hu et al., "Deep learning methods for small molecule drug discovery: A survey," *IEEE Trans. Artif. Intell.*, vol. 5, no. 2, pp. 459–479, Feb. 2024.
- [17] A. F. Nugroho, R. Rendian Septiawan, and I. Kurniawan, "Prediction of human β -secretase 1 (BACE-1) inhibitors for Alzheimer therapeutic agent by using fingerprint-based neural network optimized by bat algorithm," in *Proc. Int. Conf. Comput. Sci. Inf. Technol. Eng. (ICCoSITE)*, Jakarta, Indonesia, pp. 257–261, 2023.
- [18] E. N. Feinberg et al., "PotentialNet for molecular property prediction," *ACS Cent. Sci.*, vol. 4, no. 11, pp. 1520–1530, Nov. 2018.
- [19] M. Ragoza et al., "Protein–ligand scoring with convolutional neural networks," *J. Chem. Inf. Model.*, vol. 57, no. 4, pp. 942–957, 2017.
- [20] Z. Wu, B. Ramsundar, E. N. Feinberg, J. Gomes, C. Geniesse, A. S. Pappu, K. Leswing, and V. Pande, "MoleculeNet: A benchmark for molecular machine learning," *arXiv Preprint*, arXiv:1703.00564, 2017.

- [21] X. P. Zhou and K. Feng, "MPNN-based graph networks as learnable physics engines for deformation and crack propagation in solid mechanics," *Int. J. Solids Struct.*, vol. 291, p. 112695, Apr. 2024.
- [22] M. Tang, B. Li, and H. Chen, "Application of message passing neural networks for molecular property prediction," *Curr. Opin. Struct. Biol.*, vol. 81, p. 102616, Aug. 2023.
- [23] X. Han, M. Jia, Y. Chang, Y. Li, and S. Wu, "Directed message passing neural network (D-MPNN) with graph edge attention (GEA) for property prediction of biofuel-relevant species," *Energy AI*, vol. 10, p. 100201, Nov. 2022.
- [24] B. Das, M. Kutsal, and R. Das, "A geometric deep learning model for display and prediction of potential drug-virus interactions against SARS-CoV-2," *Chemometr. Intell. Lab. Syst.*, vol. 229, p. 104640, Oct. 2022.
- [25] T. J. Ritchie and S. J. F. Macdonald, "How drug-like are 'ugly' drugs: do drug-likeness metrics predict ADME behaviour in humans?," *Drug Discov. Today*, vol. 19, no. 4, pp. 489–495, Apr. 2014.
- [26] B. Das, M. Kutsal, and R. Das, "Effective prediction of drug–target interaction on HIV using deep graph neural networks," *Chemometr. Intell. Lab. Syst.*, vol. 230, p. 104676, Nov. 2022.
- [27] M. A. Abbasi et al., "Synthesis of novel N-(1,3-thiazol-2-yl)benzamide clubbed oxadiazole scaffolds: Urease inhibition, Lipinski rule and molecular docking analyses," *Bioorg. Chem.*, vol. 83, pp. 63–75, Mar. 2019.
- [28] R. Barret, "Lipinski's Rule of Five," in *Therapeutical Chemistry*, R. Barret, Ed., Elsevier, pp. 97–100, 2018.
- [29] M. Martins et al., "Towards the development of potential dual GSK- β /BACE-1 inhibitors: a strategy to fight Alzheimer's disease," *Toxicol. Lett.*, vol. 350, pp. S110–S111, Sep. 2021.
- [30] A. Kumar, G. Srivastava, and A. Sharma, "A physicochemical descriptor-based method for effective and rapid screening of dual inhibitors against BACE-1 and GSK-3 β as targets for Alzheimer's disease," *Comput. Biol. Chem.*, vol. 71, pp. 1–9, Dec. 2017.
- [31] X. Zhang et al., "Low anticoagulant heparin oligosaccharides as inhibitors of BACE-1, the Alzheimer's β -secretase," *Carbohydr. Polym.*, vol. 151, pp. 51–59, Oct. 2016.
- [32] H. Fu et al., "Promising anti-Alzheimer's dimer bis(7)-tacrine reduces β -amyloid generation by directly inhibiting BACE-1 activity," *Biochem. Biophys. Res. Commun.*, vol. 366, no. 3, pp. 631–636, Feb. 2008.
- [33] I. O. Korolev, "Alzheimer's Disease: A Clinical and Basic Science Review," *Med. Student Res. J.*, vol. 4, pp. 24–33, 2014.
- [34] Y. Wang, F. Yang, D. Yan, Y. Zeng, B. Wei, J. Chen, and W. He, "Identification mechanism of BACE1 on inhibitors probed by using multiple separate molecular dynamics simulations and comparative calculations of binding free energies," *Molecules*, vol. 28, no. 12, p. 4773, Jun. 2023.
- [35] A. K. Ghosh and H. L. Osswald, "BACE1 (β -secretase) inhibitors for the treatment of Alzheimer's disease," *Chem. Soc. Rev.*, vol. 43, no. 19, pp. 6765–6813, Oct. 2014.



Manyetik Sensörler ve Farklı Derin Öğrenme Modelleri Kullanarak Lastiklerin Çelik Kayışlarındaki Arıza Tespiti¹

Sercan YALÇIN^{1*}

¹Bilgisayar Mühendisliği Bölümü, Mühendislik Fakültesi, Adiyaman Üniversitesi, Adiyaman, Türkiye.
¹svancin@adiyaman.edu.tr

Geliş Tarihi: 02.08.2024
Kabul Tarihi: 09.09.2024

Düzeltilme Tarihi: 29.08.2024

doi: <https://doi.org/10.62520/fujece.1527246>
Araştırma Makalesi

Alıntı: S. YALÇIN, "Manyetik sensörler ve farklı derin öğrenme modelleri kullanarak lastiklerin çelik kayışlarındaki arıza tespiti", Fırat Üni. Deny. ve Hes. Müh. Derg., vol. 4, no 1, pp. 85-99, Şubat 2025.

Öz

Lastik arızaları önemli güvenlik riskleri oluşturur ve ileri seviye inceleme tekniklerini gerektirir. Bu araştırma, lastiklerin çelik kuşaklarındaki kusurları tespit etmek için manyetik sensörlerin ve derin öğrenmenin uygulanmasını incelemektedir. Kusurların neden olduğu manyetik alan değişimlerini yakalayıp, sağlam ve doğru bir arıza tespit sistemi geliştirilmesi amaçlanmaktadır. Bu çalışmada, manyetik görüntü sensör devresi tasarlanmış ve daha sonra ondan elde edilen görüntüler, hata olmayan, çatlak ve delaminasyon tipi çelik kuşak hataları olarak sınıflandırılmıştır. Çeşitli derin öğrenme modelleri ve bunların hibrit mimarileri araştırılmış ve karşılaştırılmıştır. Deneysel sonuçlar tüm modellerin güçlü bir performans sergilediğini, Transformatör modelinin %96.12'lik en yüksek doğruluğa ulaştığını göstermektedir. Geliştirilen sistem, endüstrilerde lastik güvenliğini iyileştirmek ve bakım maliyetlerini düşürmek için potansiyel bir çözüm sunmaktadır.

Anahtar kelimeler: Derin öğrenme, Çelik kayışlar, Manyetik sensör, Arıza tespiti

*Yazışılan Yazar

İntihal Kontrol: Evet – Turnitin
Şikayet: fujece@firat.edu.tr
Telif Hakkı ve Lisans: Dergide yayın yapan yazarlar, CC BY-NC 4.0 kapsamında lisanslanan çalışmalarının telif hakkını saklı tutar.



Fault Detection in Steel Belts of Tires Using Magnetic Sensors and Different Deep Learning Models

Sercan YALÇIN¹ * 

¹Department of Computer Engineering, Faculty of Engineering, Adiyaman University, Adiyaman, Türkiye.

svancin@adiyaman.edu.tr

Received: 02.08.2024
Accepted: 09.09.2024

Revision: 29.08.2024

doi: <https://doi.org/10.62520/fujece.1527246>
Research Article

Citation: S. YALÇIN, "Fault detection in steel belts of tires using magnetic sensors and different deep learning models", *Firat Univ. Jour. of Exper. and Comp. Eng.*, vol. 4, no 1, pp. 85-99, February 2025.

Abstract

Tire failures pose significant safety risks, necessitating advanced inspection techniques. This research investigates the application of magnetic sensors and deep learning for detecting defects in steel belts of the tires. It was aim to develop a robust and accurate fault detection system by measuring magnetic field variations caused by defects. In this study, the magnetic image sensor circuit had been designed and then the images obtained from it have been classified as none, crack, and delamination type steel belt errors. Various deep learning models and their hybrid architectures, were explored and compared. Experimental results demonstrate that all models exhibit strong performance, with the Transformer model achieving the highest accuracy of 96.12%. The developed system offers a potential solution for improving tire safety and reducing maintenance costs in industries.

Keywords: Deep learning, Steel belts, Magnetic sensor, Fault detection

*Corresponding author

1. Introduction

Tires are essential components of modern transportation systems, ensuring vehicle stability, traction, and safety [1]. The steel belt, embedded within the tire's structure, is a critical component that provides reinforcement and load-bearing capacity. Defects in the steel belt may lead to catastrophic tire failures, posing significant risks to vehicle occupants and other road users. Early and accurate detection of these defects is crucial for preventing accidents and ensuring road safety [2]. There are frequent traffic accidents today and when we investigate the causes of these accidents, some of them are driver errors and the other large part is the damage to the car as a result of the vehicle not being inspected on time. One of these damages is the damage to the tires. There may be malfunctions such as wear and tear on the tires or a flat tire. One of these malfunctions is the damage to the steel belts inside the tire. The problem is that this damage is noticed late. Not detecting the damage to the steel belts early can also indirectly damage your vehicle. For example, if there is a break in the wires of the steel belts on your vehicle's tire and you drive your vehicle without noticing it, you will notice the following symptoms in your vehicle in the future [3]. These symptoms from the steering wheel shaking and if the damage is on the left tire, the vehicle pulls to the left, if the malfunction is on the right tire, the vehicle pulls to the right. Figure 1 represents a view of a steel belt in a tire.

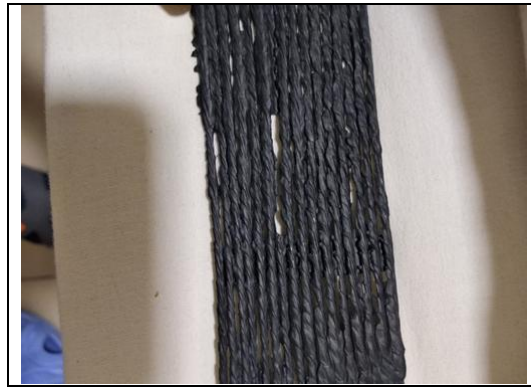


Figure 1. An example of the steel belt of a tire

Traditional methods for inspecting steel belts, such as visual inspection and X-ray radiography, are time-consuming, labor-intensive, and often unable to detect hidden flaws. Current methods for inspecting tires are destructive because they require disassembly, making them impractical for in-service checks. Therefore, non-destructive and efficient techniques for detecting faults in steel belts are urgently needed [4]. Magnetic sensors offer a promising solution for this purpose by identifying changes in magnetic field patterns caused by defects like cracks, delaminations, and corrosion. Defects can be found and identified by analyzing these magnetic field fingerprints [5]. Deep learning is a potent tool for interpreting complicated data; it is well-known for its effectiveness in image and signal processing. Its capacity to identify high-level characteristics from unprocessed data makes it a potent contender for steel belt failure diagnosis. Using data from magnetic sensors and deep learning algorithms, reliable and precise defect detection models may be created. While several components have been the subject of flaw detection research, the use of deep learning and magnetic sensors to steel belt inspection is still mostly unexplored. The literature on reliable and efficient defect detection systems that make use of this mix of technologies is noticeably lacking. By assessing the viability and effectiveness of several deep learning models for using magnetic sensor data to identify flaws in steel belts, this paper aims to bridge that gap.

The primary objectives of this study are:

- To develop a magnetic image scanner to investigate the characteristics and potential of magnetic image sensors (MISs) for non-invasive detection of steel belt damage in tires.
- To investigate the performance of various deep learning models for this application.

- To evaluate the effectiveness of different feature extraction techniques for enhancing fault detection accuracy.
- To optimize the proposed system for real-world implementation, considering factors such as computational efficiency and robustness.

The remainder of this paper is organized as follows. Section 2 presents a literature review. Section 3 presents system implementation including magnetic image sensor design and the fault detection methodology. Section 4 presents the experimental results, including performance evaluation metrics and comparative analysis of different models. Section 5 discusses the performance of the results in brief. Finally, Section 6 summarizes the key findings, contributions, and potential future research directions.

2. Literature Review

Zhang et al. (2017) presented a research on the identification of tire flaws in multitextural radiography pictures [6]. They addressed the tire defect characterization problem using local regularity analysis and scale characteristic. A defect edge measurement model was used to identify the optimal scale and threshold parameters for defect edge detection. This framework separated faults from background textures. Finally, a novel approach for detecting tire problems was suggested using wavelet multiscale analysis. In order to effectively diagnose tire flaws, Zheng et al. (2021) presented a novel deep learning model called DCScNet [7]. This model offered advantages over regular CNNs, such as removing the requirement for labeled training data and lowering subjectivity in manually generated features, by substituting sparse coding for classic convolutional kernels. As a result, DCScNet performed better in categorization. Liu et al. (2022) combined the analysis of video and static image data to present a unique approach for diagnosing belt damage [8]. They created a deep learning framework for processing video data captured during on-site monitoring in order to detect damage from beginning to conclusion. While temporal convolutional networks (TCNs) extract dynamic information from consecutive video frames, improving detection accuracy by mitigating the effects of lighting conditions and shadows, an improved attention mechanism aids the model in focusing on relevant image regions despite complex backgrounds. Xie et al. (2021) developed an intelligent system combining deep learning for autonomous defect detection in order to automate the process of defect identification [9]. In order to overcome the shortcomings of conventional CNNs with sample-based data, they unveiled a new architecture known as Fusion Feature CNN (FFCNN), which is intended to extract and integrate pertinent features from sample inputs for accurate classification. Martínez-Parrales and Téllez-Anguiano (2022) developed an IoT-enabled malfunction detection system for conveyor belts [10]. The technology precisely calculated important characteristics such as stroke, direction, and frequency by measuring acceleration force at six vital spots on the machine using two-axis wireless accelerometers. By comparing these numbers to preset reference points, the system generated real-time visual warnings on the machine's state, both on-site and remotely. The system's efficacy was carefully tested by testing on an actual conveyor prototype. Lin (2023) described a revolutionary deep learning-based strategy for reliably detecting tire problems [2]. The suggested technology outperforms typical ShuffleNet architecture in terms of recognizing tire debris faults. When compared to other top models like GoogLeNet, VGGNet, ResNet, and the original ShuffleNet, the enhanced ShuffleNet obtains an impressive detection rate of 94.7%. This innovative solution benefits both drivers and tire producers by lowering labor costs and considerably speeding up the tire problem identification process. Zhang et al. (2023) introduced IDD-Net, a pioneering deep learning model created expressly to address the issues involved with industrial defect detection [3]. IDD-Net used a novel local-global backbone feature network (LGB-Net) to successfully resolve flaws with various degrees of similarity and diversity. Furthermore, the suggested Three-Layer Feature Aggregation network (TFLA-Net) efficiently addresses the issue of large scale changes in faults. TFLA-Net used a revolutionary three-layer descending approach to smoothly incorporate semantic and fine-grained information. To solve the issue of object loss deviation at different scales, a new IoU loss function, Defect-IoU loss, was proposed. This novel loss function adjusts the loss amount according to the area difference between objects of different sizes, resulting in a more balanced optimization process. Sedaghat et al. (2021) introduced a new strategy for identifying tire flaws in X-ray pictures based on an entropy filter, patch texture attributes extraction by Local Binary Pattern, and defect classification via Support Vector Machine (SVM) [11]. The suggested technique begins by applying an entropy filter to

the input. The patch classifier identified the candidate areas, which were picked from the picture and had distinct patterns. All flaws were found and categorized, and the algorithm's efficiency was evaluated. Şener et al. (2022) presented a ground-breaking method for increasing car safety: a vision-based seat belt detector that changes the seat height without the driver or passenger's interaction [12]. The device assisted in preventing potentially catastrophic neck injuries caused by inappropriate seat belt positioning by properly recognizing the position of the seat belt relative to the driver's or passenger's neck. DenseNet121, GoogLeNet (Inception-v3), and ResNet50 were used in a comprehensive benchmarking procedure to assess the performance of several deep learning architectures. The models were evaluated according to their sensitivity, specificity, precision, false-positive rate, false-negative rate, F1 score, and accuracy. Furthermore, training and validation loss curves, as well as accuracy curves, were produced for each model to offer a thorough study of its performance. A noise reduction technique was introduced by Sun et al. (2024) to reduce metal slag interference in steel cord conveyor belt damage signals [13]. Wavelet thresholding and Empirical Mode Decomposition (EMD) were combined in this approach. Wavelet thresholding attenuates high-frequency sounds while retaining crucial low-frequency information in the intrinsic mode functions (IMFs) created by EMD's breakdown of the original signal into IMFs. This allowed for the separation of high-frequency noise components associated with metal slag.

3. System Implementation

In this section, the magnetic image scanner design of the study was made and the methodology for fault detection of steel belts was presented.

3.1. Designing of magnetic image scanner

Hall effect sensors were used in series and turned into a circuit to detect faults in steel belts in tires. As an application to understand the operation of the circuit and its logic, scanning of steel wires inside vehicle tires and highlighting damaged areas and showing them to the user were performed. As a result of the research, the control of whether the structure inside vehicle tires is undamaged/faultless is evaluated as successful or unsuccessful only by scanning the tire with X-ray logic at the stage before the tire is put on sale in the factory where it is produced and visualizing it on the computer and reading and interpreting the image by technical staff. The output and working principle of the MIS have been investigated. In this direction, a simple magnetic image scanner has been designed. Using this scanner, it is aimed to visualize and detect the damages in the steel belts inside the vehicle tires in a computer environment without any physical intervention. Figure 2 shows the magnetic sensors soldered onto designed printed circuit board.

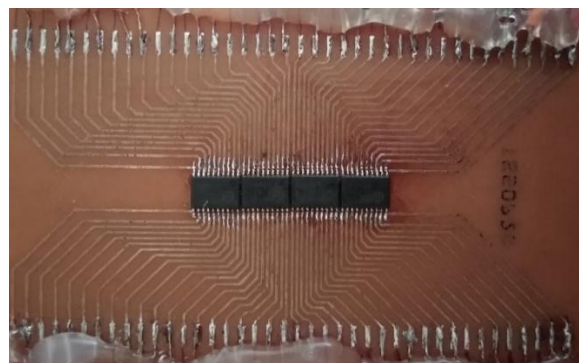


Figure 2. Magnetic sensors soldered onto printed circuit board

The scanner utilizes X-ray logic to evaluate the structural integrity of the steel belts, providing visual representation and interpretation for technical staff.

Hardware Implementation:

Sensor Selection: Four IC-ML sensors, each containing four Hall effect sensors, were chosen for their sensitivity and reliability.

Circuit Design: A custom-designed printed circuit board (PCB) was fabricated to accommodate the sensors and their connections.

Sensor Placement: The sensors were arranged in a specific configuration to ensure accurate detection of anomalies in the steel belts.

Interfacing with Microcontroller: A multiplexer was used to interface the analog outputs from the sensors with the Arduino Uno microcontroller.

Data Transmission: Node.js and Arduino IDE were employed for real-time data transfer and visualization.

Software Implementation:

Data Acquisition: The microcontroller collected sensor data at a specified sampling rate.

Data Processing: Algorithms were developed to analyze the sensor data and identify patterns indicative of faults. **Visualization:** A user interface was created to display the detected faults visually, allowing for easy interpretation.

Challenges and Solutions:

During the implementation process, it was discovered that one of the IC-ML sensors was malfunctioning. This issue was addressed by excluding the faulty sensor and proceeding with the remaining 12 sensors.

The magnetic image scanner successfully demonstrated its ability to detect faults in steel belts within vehicle tires. The design incorporates a series of Hall effect sensors, a custom PCB, and a software interface for data acquisition, processing, and visualization. By addressing challenges encountered during development, the final system provides a reliable and effective solution for quality control in tire manufacturing. It was realized by using a piece consisting of a series of steel wires carefully removed from the tire in an industrial environment. For the hardware part of the application, 4 IC-ML sensors were placed side by side. Since there was no ready PCB for this process, a printed circuit board was designed from scratch. The sensors were placed side by side in a 17.6 x 2 millimeter area and their integrated legs were extended to the edges of the board. In order to ensure that the sensors were not affected by the cables and the microcontroller, the board we prepared was placed on another plate and the cables soldered to the leg ends were passed through the holes opened in this plate and transmitted to the intermediate side. The transmitted cables were separated according to the pin configuration. Since there were 4 Hall effect sensors in each IC-ML sensor, there were a total of 16 analog outputs and 6 analog inputs in the Arduino Uno. To eliminate this incompatibility, 1 16x1 multiplexer circuit was used. The analog outputs from the sensor were given as inputs to the multiplexer and the output of the multiplexer was connected to the A0 pin of the Arduino circuit. After assembling all the parts on the large plate, the visualization process was started in the software section. In order to perform live data transfer and visualization at the same time, the commands written with javascript technologies which are Node.js and Arduino IDE were communicated with 9600 baudrate. The fact that the software used achieved this job smoothly and flawlessly increased the success rate of the application. During the implementation process of the application, a problem was encountered such that one of the IC-ML sensors used could not provide the expected results and this sensor had to be canceled. As a result, the magnetic image sensor design was realized with 12 Hall effect sensors instead of 16 and the scanning - visualization process was achieved. The results and the images related to the final state of the product are shown in Figures 3 and 4.

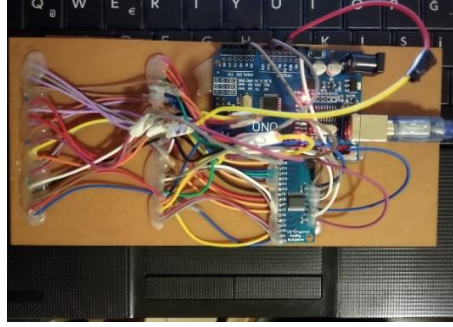


Figure 3. Back side of the card prepared for the study



Figure 4. Front side of the card prepared for study

The design of the card was carried out in this way so that the sensors are not affected by the magnetic field created by the wiring and the microcontroller.

3.2. Fault detection methodology

The experimental methodology involved the following steps [3]:

Assumptions:

- The steel belt is a linear magnetic material.
- Magnetic field perturbations due to defects are small.
- The tire and steel belt can be represented as a 2D or 3D structure.

The magnetic field intensity, H , in a material is related to the magnetic flux density, B , by the permeability, μ , is computed as in Equation 1.

$$B = \mu H \quad (1)$$

For a linear material, μ is a constant. However, in the presence of defects, μ becomes a function of position is presented as in Equation 2.

$$B(r) = \mu(r)H(r) \quad (2)$$

Magnetic field perturbation is calculated as in Equation 3.

$$\Delta B(r) = [\mu(r) - \mu_0]H(r) \quad (3)$$

where μ_0 is permeability of defect-free material. Additionally, magnetic sensor output is computed as in Equation 4.

$$V_{sensor} = f(\Delta B(r)) \quad (4)$$

Equation 5 illustrates the widespread application of the categorical cross-entropy loss function in classification issues.

$$Loss = -\sum (y_{true} * \log(y_{pred})) \quad (5)$$

where y_{true} is the true label (0 for no defect, 1 for defect), y_{pred} is the predicted probability of the defect. The model is trained using backpropagation through time (BPTT) to compute gradients. An Adam optimizer is used to update the model parameters. The model is trained on a dataset of labeled tire samples. Once the model is trained, it can be used to classify new, unseen tire data. If the model predicts a high probability of a defect, an alert can be generated. By combining this mathematical model with a well-structured deep learning network, this approach effectively detects faults in steel belts using magnetic sensor data.

4. Experimental Results and Discussion

The study utilized a Windows 10 computer with an Intel Core i7-8650U CPU installed and 16 GB of RAM. Python 3.8.5 served as the primary programming language for all implemented methods. Code development was facilitated by PyCharm IDE, while Jupyter Notebook was used for step-by-step execution.

4.1. Collected data analysis

In this study, a total of 480 magnetic images were collected for None, Crack and Delamination, each in equal numbers. using the MIS designed for the dataset. 80% of them were reserved for training and the rest for testing. The collected magnetic sensor data from the MIS design, was subjected to rigorous analysis to extract meaningful features indicative of steel belt defects. Figure 5 shows the defect types, including crack and delamination defects of the tires.



Figure 5. Defect types. a) crack defect b) Delamination defect [2]

Table 1 presents the data structure obtained from the magnetic images. Signal processing techniques, fourier transform has been employed to characterize the magnetic field signatures. The dataset consists of multiple records, each representing a measurement taken from a specific point on a tire. TireID: A unique identifier for each tire. SensorID: A unique identifier for each sensor. X_coordinate: The x-coordinate of the sensor's position on the tire. Y_coordinate: The y-coordinate of the sensor's position on the tire. Z_coordinate: The z-coordinate of the sensor's position on the tire. MagneticFieldX: The x-component of the magnetic field measured by the sensor. MagneticFieldY: The y-component of the magnetic field measured by the sensor. MagneticFieldZ: The z-component of the magnetic field measured by the sensor. DefectType: The type of defect presents in the tire (if any), e.g., crack, delamination, corrosion, or none. DefectSize: The size of the defect. DefectLocation: The location of

the defect. Given that the dataset consists of numerical data from magnetic sensors rather than images, the labeling process involved analyzing the sensor readings to identify patterns indicative of defects. For each record in the dataset, it was compared the magnetic field measurements to established baseline values and thresholds. Deviations from these norms were then classified as potential defects, with their type, size, and location determined based on the specific patterns observed in the sensor data. This approach allowed us to effectively label instances within the dataset, providing a solid foundation for the subsequent machine learning tasks.

Table 1. Data structure

TireID	SensorID	X,Y,Z coordinate	MagneticFieldX,Y,Z	DefectType	DefectSize	DefectLocation
T1	S1	10,20,5	123,-45,78	None	-	-
T1	S2	15,20,5	132,-51,82	Crack	5mm	Outer
T2	S3	5,15,4	118,-39,75	Delamination	8mm	Inner

The magnetic image scanner was tested on actual vehicle tires in a controlled industrial environment. We faced several challenges during the data collection phase, including:

Tire Variability: Tires can vary significantly in terms of their construction, materials, and manufacturing processes. This introduced variability into the data and required careful consideration when developing the fault detection algorithm.

Environmental Factors: Factors such as temperature, humidity, and vibrations can influence the performance of the sensors and the accuracy of the measurements. We implemented measures to minimize the impact of these environmental factors.

Noise Reduction: The sensor signals were subject to noise, which could interfere with the detection of faults. Noise reduction techniques were employed to improve the signal-to-noise ratio and enhance the accuracy of the system.

By addressing these challenges and conducting experiments in a real-world setting, we were able to validate the effectiveness of our magnetic image scanner for detecting faults in steel belts within vehicle tires.

The dataset used in this study was specifically curated to address the research objectives. While it may not be as extensive as larger datasets, its size was carefully considered to balance data quality, representativeness, and computational feasibility. Given the nature of the data collected from magnetic sensors and the specific focus of this research, the dataset's size was deemed adequate to provide robust insights and conclusions. Since it was obtained with real magnetic circuits, only 480 pieces of data could be obtained. This study, while aligning with the general framework of previous research in the field of tire defect detection using magnetic sensors, offers several distinctive contributions that enhance the understanding and application of this technology. The dataset was meticulously collected in a real-world setting, ensuring that the sensor readings accurately reflect the conditions encountered in actual tire usage. This contrasts with some studies that may rely on simulated or controlled environments, potentially limiting the generalizability of their findings. A strategic sensor placement approach was employed, considering factors tire geometry. This optimization maximizes the sensitivity of our system to detect a wide range of defects, including those that might be overlooked by less carefully planned sensor arrangements. The sampling rate of our microcontroller was carefully chosen to capture the dynamic nature of tire defects. This study leverages state-of-the-art algorithms for data analysis and feature extraction, such as machine learning techniques and signal processing methods. These advanced approaches enable us to identify complex patterns and relationships within the sensor data that may not be apparent through simpler analysis techniques. We did indeed employ feature engineering techniques to extract relevant features from the raw sensor data. These features included not only the six coordinate information (X, Y, Z, MagneticFieldX, MagneticFieldY, MagneticFieldZ) but also additional derived features such as the rate of change of the magnetic field, standard deviation, and variance. By carefully

selecting and combining these features, we aimed to enhance the informativeness of our dataset and improve the performance of our machine learning and deep learning models.

4.2. Performance evaluation

The experimental results demonstrated the effectiveness of magnetic sensors in detecting faults in tire steel belts. The extracted features showed distinct patterns for different defect types, indicating the potential for accurate classification. Note that the performance of the fault detection system influences by factors such as sensor placement, magnetization strength, defect size, and location.

Figure 6 represents an output from a magnetic image sensor. The numerical values within the grid likely correspond to sensor readings or pixel intensities. The consistent value of 127 across most of the image suggests a baseline or reference reading, indicating a uniform magnetic field and the absence of any significant magnetic anomalies. The values might be normalized to a specific range (0-255) for processing and display purposes. The sensor has limited sensitivity and resolution, resulting in a uniform output in the absence of strong magnetic signals. Therefore, it is understood from Figure 6 that no fault was detected in the steel belts.

Figure 7 presents the output of a magnetic image sensor, used for inspecting steel belts in tires. The grid-like structure displays numerical values, representing the sensor readings at different positions. The presence of anomalous values, deviating from the background value of 127, suggests potential defects in the steel belt. The image indicates a potential anomaly or defect in the steel belt within the region covered by sensors S5 and S6. The values of 20 and 27 in these sensors deviate significantly from the background value of 127, suggesting a change in magnetic properties within that area. This change could be attributed to a defect in the steel belt, such as a crack or delamination. That is, based on the anomalous sensor readings from S5 and S6, a fault exists in the corresponding region of the steel belt.

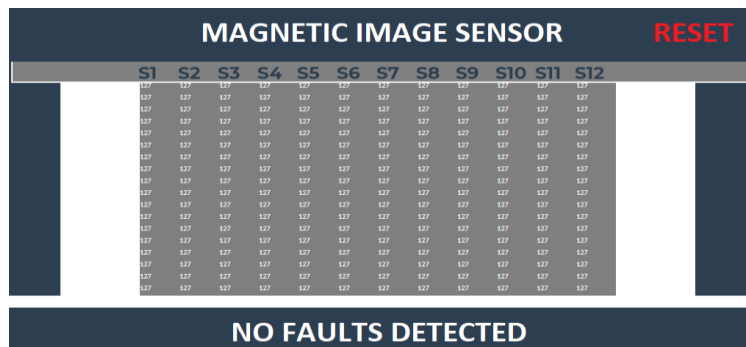


Figure 6. No faults detected in steel belts by magnetic image sensors

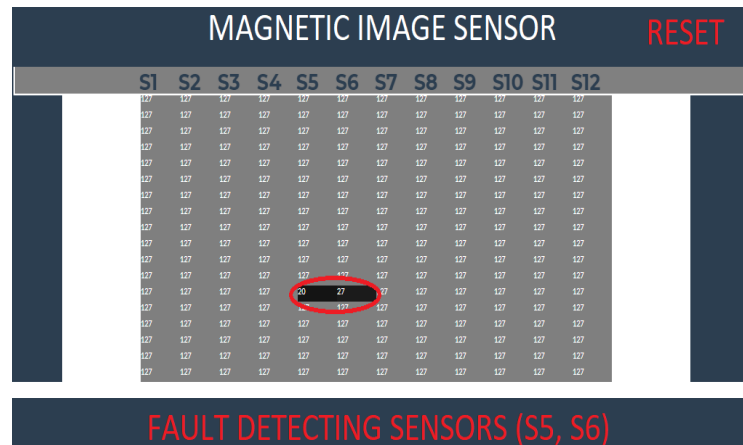


Figure 7. Detection of faults in steel belts from magnetic image 5th and 6th sensors

K-fold cross-validation is an effective strategy for testing model performance, especially with smaller datasets as in our study. This strategy efficiently uses all available data for training and assessment, resulting in a more accurate performance prediction than a standard train-test split. This strategy, which is widely used in machine learning, divides the dataset into K equal-sized subsets or "folds". During each cycle, K-1 subsets are utilized for model training, while the remaining subset confirms the model's performance. This method is repeated K times, each time with a new subset for validation. This produces K performance measurements, allowing for an averaged total performance estimation. To reduce overfitting, we randomly divided the dataset into five subsets (K = 5) as suggested by Hamdi et al. [14]. Table 2 shows the K-fold cross-validation steps performed on the five prior models. The fundamental advantage of K-fold cross-validation is that it essentially expands the database size, resulting in K times more performance measurements, which is especially useful for smaller datasets like ours. As a result, using this strategy effectively increases the effective size of our database by five.

Table 2. The operation steps of the K=5-fold cross-validation

Model No	K=5-Fold 1	K=5-Fold 2	K=5-Fold 3	K=5-Fold 4	K=5-Fold 5
	Data Processing Type				
1	Testing	Training	Training	Training	Training
2	Training	Testing	Training	Training	Training
3	Training	Training	Testing	Training	Training
4	Training	Training	Training	Testing	Training
5	Training	Training	Training	Training	Testing

Table 3 shows the performance of the different pre-trained models, which are the SVM, CNN, LSTM, GRU, BiLSTM, Transformer, Attention-based LSTM, CNN-LSTM Hybrid, ResNeXt, DenseNet, according to the average results of the K=5-fold cross-validations. The details of these models used in the study are available in the studies in references [15-20]. In the performance comparison of the models, accuracy, precision, recall, F1-score, FPR, FNR, AUC score and computational cost analyses, which are frequently used in deep learning studies, were performed.

Table 3. The performance of the different models in terms of average results of the K=5-fold cross-validations

Model	Accuracy (%)	Precision (%)	Recall			AUC-ROC	Computational Cost (s)	
			(TPR) (%)	F1-Score	FPR			FNR
SVM	92.35	90.22	91.46	0.918	0.082	0.093	0.957	0.22
CNN	94.31	92.43	93.65	0.933	0.063	0.074	0.964	14
LSTM	95.18	93.74	94.44	0.946	0.054	0.062	0.977	24
GRU	94.82	93.18	94.14	0.937	0.064	0.066	0.972	21
BiLSTM	95.54	94.16	94.77	0.949	0.042	0.054	0.985	28
Transformer	96.12	94.75	95.11	0.952	0.041	0.053	0.983	37
Attention-based LSTM	95.29	94.16	94.29	0.945	0.054	0.064	0.975	26
CNN-LSTM Hybrid	95.76	94.48	94.88	0.944	0.046	0.057	0.984	33
ResNeXt	95.65	94.28	94.72	0.944	0.047	0.052	0.983	43
DenseNet	95.39	94.20	94.37	0.943	0.053	0.066	0.978	41

Transformer and ResNeXt consistently outperform other models across most metrics, indicating their superior ability to capture complex patterns in the data. LSTM and GRU also demonstrate strong performance, especially in terms of recall, suggesting their effectiveness in handling sequential data. CNN and CNN-LSTM Hybrid models show good accuracy and F1-scores, indicating their ability to extract relevant features. SVM generally has lower performance across most metrics, likely due to its simpler linear decision boundary. Transformer and ResNeXt achieve the highest accuracy, indicating their ability to correctly classify a higher percentage of samples. All models exhibit high precision, suggesting a low rate of false positives. Transformer, ResNeXt, and BiLSTM demonstrate higher recall,

indicating better ability to identify all actual defects. Consistent with accuracy, precision, and recall, Transformer and ResNeXt show the best F1-scores, indicating a good balance between precision and recall. Lower FPR and FNR values for Transformer, ResNeXt, and BiLSTM indicate fewer false alarms and missed defects. Transformer and ResNeXt achieve the highest AUC-ROC scores, suggesting their ability to discriminate between classes across different classification thresholds. There's a trade-off between performance and computational resources. Transformer and ResNeXt demand higher computational costs due to their complexity. In this means, the Transformer model consistently outperformed the other models, achieving the highest scores in accuracy (96.12%), precision (94.75%), recall (95.11%), F1-score (0.952), and AUC-ROC (0.983). LSTM-based models, including BiLSTM and Attention-based LSTM, also demonstrated strong performance, indicating their effectiveness for sequential data. CNN and SVM models offered a balance between performance and computational efficiency. Overall, the choice of the best model depends on the specific requirements of the application, considering factors such as computational resources and the importance of accuracy, precision, and recall.

Following the achievement of peak performance, a confusion matrix was produced and the Transformer model was used to the fault type classification process. This matrix is shown in Figure 8, which provides a graphic representation of the model's performance in classifying steel belt faults into three categories: none, crack, and delamination. The number of predicted instances for each class (column) compared to the actual class (row) is displayed in the matrix's cells. For the "None" category, a diagonal value of 149 denotes good accuracy in recognizing samples free of defects. Similar to this, a value of 151 for the "Crack" category indicates that crack flaws may be classified with some degree of precision, but a value of 155 for the "Delamination" category indicates that delamination defects can be detected with high accuracy. Off-diagonal values are used to indicate misclassifications. For example, five samples from the "None" class might be mistakenly classed as "Crack." An unbalanced dataset may have an effect on how well the model performs. Strong performance is demonstrated by the Transformer model, especially for the "Delamination" class; nonetheless, examining misclassified data might reveal potential biases and places for development.

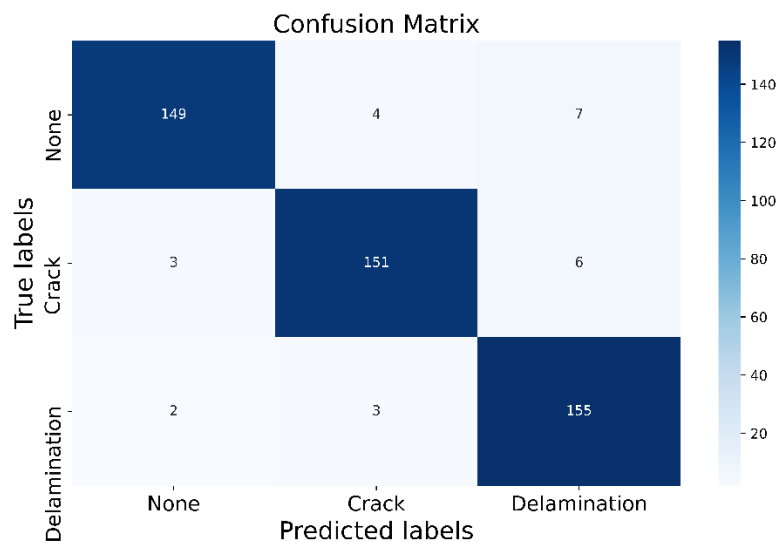


Figure 8. Confusion matrix for the fault classification using Transformer model

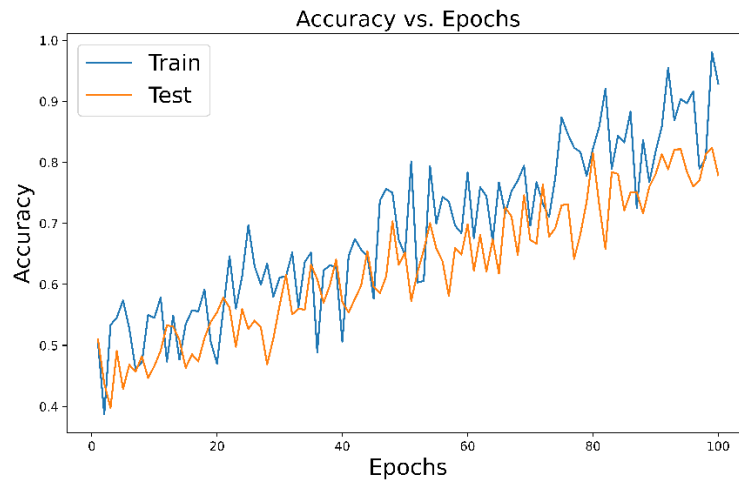


Figure 9. Accuracy results of the Transformer model

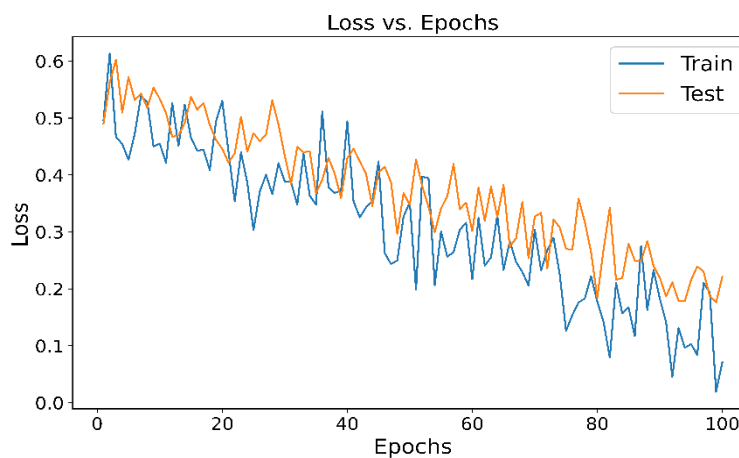


Figure 10. Loss results of the Transformer model

The Transformer model's training and test accuracy across 100 epochs is shown in Figure 9. The y-axis displays accuracy, while the x-axis displays the total number of epochs. Significant fluctuations in the training accuracy curve point to potential overfitting or susceptibility to noise in the training set. In spite of these variations, training accuracy is often trending increasing, suggesting learning. After around 40 epochs, there is a discernible difference between the training and test accuracy curves, indicating that the model is becoming overly specialized to the training set and is struggling to generalize to new data. The test accuracy curve reaches a plateau approximately around the 80th epoch, suggesting that the model's capacity for generalization has peaked. The Transformer model's training and validation loss across 100 epochs is shown in Figure 10. This plot provides information on the model's learning process as well as possible areas for development. In the early epochs, training and validation losses both drop very quickly, suggesting efficient learning. Around epoch 40, a discrepancy between the training and validation loss curves manifests themselves, indicating overfitting. The model is not generalizing effectively to previously unknown data and is growing overly specialized to the training set. The training process's intrinsic randomness or intricate patterns in the data might be the cause of the fluctuations in both curves. The validation loss curve levels off at 0.25, suggesting that the model may be operating at maximum efficiency.

5. Discussion

The performance of various learning models has been discussed, including their accuracy, precision, recall, F1-score, and other relevant metrics. The comparison of different models is conducted to identify the most effective approach for tire defect detection. The importance of different features in the models is analyzed using techniques such as feature permutation importance or SHAP values. This analysis helps to understand which features contribute most significantly to the model's predictions. A comparison of the researcher's

results with those reported in previous studies on tire defect detection is conducted. This comparison allows for the assessment of the novelty and significance of the findings and the identification of areas where the researcher's work contributes to the advancement of the field. The limitations of the study, such as the size of the dataset, the specific types of defects considered, and the potential generalizability of the findings, are acknowledged. Potential future research directions, including the collection of larger datasets, the exploration of additional sensor modalities, and the development of more advanced machine learning and deep learning techniques, are discussed. The potential implications of the findings for the field of tire safety and maintenance are discussed. The study demonstrates the feasibility of using magnetic sensors and machine learning techniques for accurate and timely detection of tire defects. This has significant implications for improving tire safety, reducing maintenance costs, and preventing tire failures that could lead to accidents.

6. Conclusions and Future Direction

This study effectively demonstrated the potential of using deep learning in conjunction with magnetic sensors to identify tire steel belt defects. The device detects two types of flaws with great accuracy by detecting small differences in magnetic field patterns. Studies comparing various deep learning models revealed that the Transformer model consistently surpassed the other models, achieving the highest scores in accuracy of 96.12%, precision of 94.75%, recall of 95.11%, F1-score of 0.952, and AUC-ROC of 0.983. LSTM-based models, including BiLSTM and Attention-based LSTM, also exhibited strong performance, suggesting their effectiveness for sequential data. The drawbacks of conventional techniques are addressed by the integration of deep learning with magnetic sensors, which offers a feasible alternative for non-destructive tire examination. The technology that has been created has the potential to greatly improve tire safety by facilitating the early identification of serious faults.

Potential avenues for future research might involve expanding the dataset to include a greater range of fault kinds and severities. Furthermore, investigating more complex deep learning strategies like attention processes and transfer learning may help the system function even better. It is possible to fully exploit the promise of this technology to revolutionize tire care and inspection by continually improving the model and integrating real-world data.

This research highlights the potential of deep learning in addressing difficult engineering difficulties and enhances defect identification in the tire business.

7. Author Contribution Statement

In this study, Author contributed to the development of the method, obtaining experimental results, and preparation of the paper.

8. Ethics Committee Approval and Conflict of Interest

“There is no conflict of interest with any person/institution in the prepared article”

9. References

- [1] Y. Zhang, D. Lefebvre, and Q. Li, "Automatic detection of defects in tire radiographic images," *IEEE Trans. Autom. Sci. Eng.*, vol. 14, no. 3, pp. 1378–1386, Jul. 2017.
- [2] S. L. Lin, "Research on tire crack detection using image deep learning method," *Sci. Rep.*, vol. 13, p. 8027, 2023.
- [3] Z. Zhang, M. Zhou, H. Wan, M. Li, G. Li, and D. Han, "IDD-Net: Industrial defect detection method based on deep learning," *Eng. Appl. Artif. Intell.*, vol. 123, pt. B, p. 106390, 2023.
- [4] B. Wang, D. Dou, and N. Shen, "An intelligent belt wear fault diagnosis method based on deep learning," *Int. J. Coal Prep. Util.*, vol. 43, no. 4, pp. 708–725, 2022.
- [5] S. Brol and J. Warczek, "Utilization of magnetic signature of automotive tire for exploitative wear assessment," *Diagnostyka*, vol. 23, no. 4, p. 2022412, 2022.
- [6] Y. Zhang, D. Lefebvre, Q. Li, "Automatic Detection of Defects in Tire Radiographic Images," in *IEEE Trans. Autom. Sci. Eng.*, vol. 14, no. 3, pp. 1378–1386, July 2017.
- [7] Z. Zheng, J. Shen, Y. Shao, J. Zhang, C. Tian, B. Yu, and Y. Zhang, "Tire defect classification using a deep convolutional sparse-coding network," *Meas. Sci. Technol.*, vol. 32, no. 5, p. 055401, 2021.
- [8] M. Liu, Q. Zhu, Y. Yin, Y. Fan, Z. Su, and S. Zhang, "Damage detection method of mining conveyor belt based on deep learning," *IEEE Sens. J.*, vol. 22, no. 11, pp. 10870–10879, Jun. 2022.
- [9] L. Xie, X. Xiang, H. Xu, L. Wang, L. Lin, and G. Yin, "FFCNN: A deep neural network for surface defect detection of magnetic tile," *IEEE Trans. Ind. Electron.*, vol. 68, no. 4, pp. 3506–3516, Apr. 2021.
- [10] R. Martínez-Parralles and A. C. Téllez-Anguiano, "Vibration-based fault detection system with IoT capabilities for a conveyor machine," *Acta Polytech. Hung.*, vol. 19, no. 9, pp. 7–24, 2022.
- [11] Y. Sedaghat, N. Parhizgar, and A. Keshavarz, "Automatic defects detection using neighborhood windows features in tire X-ray images," *Int. J. Nonlinear Anal. Appl.*, vol. 12, spec. iss., pp. 2493–2508, 2021.
- [12] A. Ş. Şener, I. F. Ince, H. B. Baydargil, I. Garip, and O. Ozturk, "Deep learning-based automatic vertical height adjustment of incorrectly fastened seat belts for driver and passenger safety in fleet vehicles," *Proc. Inst. Mech. Eng., Part D: J. Automob. Eng.*, vol. 236, no. 4, pp. 639–654, 2022.
- [13] G. Sun, R. Zhang, Z. Liu, L. Wu, Q. Yu, and X. Tan, "EMD-based noise reduction study of steel-cored conveyor belt containing slag signal," *Alexandria Eng. J.*, vol. 98, pp. 56–67, 2024.
- [14] A. Hamdi, Y. F. Yapan, A. Uysal, and H. Abderazek, "Multi-objective analysis and optimization of energy aspects during dry and MQL turning of unreinforced polypropylene (PP): An approach based on ANOVA, ANN, MOWCA, and MOALO," *Int. J. Adv. Manuf. Technol.*, vol. 128, no. 11, pp. 4933–4950, 2023.
- [15] T. Nguyen-Da, P. Nguyen-Thanh, and M.-Y. Cho, "Real-time AIoT anomaly detection for industrial diesel generator based on efficient deep learning CNN-LSTM in Industry 4.0," *Internet Things*, vol. 27, p. 101280, 2024.
- [16] P. N. Thanh and M.-Y. Cho, "Advanced AIoT for failure classification of industrial diesel generators based on hybrid deep learning CNN-BiLSTM algorithm," *Adv. Eng. Inf.*, vol. 62, pt. A, p. 102644, 2024.
- [17] Y. Tian, G. Wang, H. Li, Y. Huang, F. Zhao, Y. Guo, J. Gao, J. Lai, "A novel deep learning method based on 2-D CNNs and GRUs for permeability prediction of tight sandstone," *Geoenergy Sci. Eng.*, vol. 238, p. 212851, 2024.
- [18] X. Qin, W. Zhu, Q. Hu, Z. Zhou, Y. Ding, X. Gao, R. Gu, "DenseNet-Transformer: A deep learning method for spatial-temporal traffic prediction in optical fronthaul network," *Comput. Netw.*, p. 110674, 2024.
- [19] V. V. N. S. Kumar, G. H. Reddy, and M. N. GiriPrasad, "A novel glaucoma detection model using Unet++-based segmentation and ResNet with GRU-based optimized deep learning," *Biomed. Signal Process. Control*, vol. 86, pt. A, p. 105069, 2023.
- [20] E. Ozbay and F. A. Ozbay, "Derin öğrenme ve sınıflandırma yaklaşımları ile BT görüntülerinden Covid-19 tespiti," *Dicle Univ. Muhendislik Fak. Muhendislik Derg.*, vol. 12, no. 2, pp. 211–219, 2021.



İnsansız Araç Navigasyonunun Optimize Edilmesi: Verimli Rota Planlaması için Hibrit PSO-GWO Algoritması

Gökhan ALTUN¹ , İlhan AYDIN^{2*} 

¹Tatvan Meslek Yüksekokulu, Bitlis Eren Üniversitesi, Bitlis, Türkiye.

²Bilgisayar Mühendisliği, Mühendislik Fakültesi, Fırat Üniversite, Elazığ, Türkiye.

¹altungokhann@gmail.com, ²aydin@firat.edu.tr

Geliş Tarihi: 14.06.2024
Kabul Tarihi: 16.09.2024

Düzeltilme Tarihi: 10.09.2024

doi: <https://doi.org/10.62520/fujece.1501508>
Araştırma Makalesi

Alıntı: G. Altun ve İ. Aydın, “İnsansız araç navigasyonunun optimize edilmesi: verimli rota planlaması için hibrit pso-gwo algoritması”, Fırat Üni. Deny. ve Hes. Müh. Derg., vol. 4, no 1, pp. 100-114, Şubat 2025.

Öz

Bu çalışma, insansız araçların kullanımında önemli bir yere sahip olan otonom sistemler için rota planlama problemini ele almayı amaçlamaktadır. Belirtilen problemin çözümünde kullanılacak olan meta-sezgisel algoritma yaklaşımlarının performansını artırmak amacıyla hibrit bir algoritma önerilmiştir. Önerilen hibrit algoritmada, Parçacık Sürü Optimizasyonu (PSO) algoritmasının basit kullanımı ve güçlü küresel arama yetenekleri, Gri Kurt Optimizasyonu (GKO) algoritmasının güçlü keşif ve yerel minimumdan kaçınma özellikleriyle birleştirilmiştir. Önerilen hibrit yaklaşım, hem hesaplama doğruluğunu hem de işlem süresinde verimliliği sağlamayı hedeflemektedir. Hibrit yaklaşım kullanılarak, bilinmeyen bir ortamda sensörler yardımıyla rotalar hesaplanmıştır. Hibrit algoritmanın performansı, bireysel PSO ve GKO algoritmaları ile karşılaştırılmıştır. Karşılaştırma sırasında algoritmalar; optimum rotayı bulma süreleri, hesaplanan rota uzunluğu, gerekli iterasyon sayısı ve yerel minimumdan kaçınma yetenekleri açısından değerlendirilmiştir. Sonuçlar, özel olarak geliştirilmiş bir arayüz kullanılarak simüle edilmiş ve rota hesaplama süresi açısından önemli bir avantaj sağlandığı gözlemlenmiştir. Ayrıca, PSO yaklaşımında mevcut olan yerel minimum problemi başarılı bir şekilde ortadan kaldırılmış ve GKO yaklaşımına kıyasla iterasyon sayısı ile işlem süresi iyileştirilmiştir. Bu yaklaşımın, özellikle afet yönetimi senaryolarında fayda sağlaması beklenmektedir. Çünkü otonom insansız araçlar, arama, kurtarma ve kaynak dağıtımı için bilinmeyen veya engelli ortamlarda verimli rota planlaması yapılmasına yardımcı olabilir.

Anahtar kelimeler: Parçacık sürü optimizasyonu, Gri kurt optimizasyonu, Rota planlama, İnsansız hava aracı, Hibrit algoritma.

*Yazışılan yazar

İntihal Kontrol: Evet – Turnitin

Şikayet: fujece@firat.edu.tr

Telif Hakkı ve Lisans: Dergide yayın yapan yazarlar, CC BY-NC 4.0 kapsamında lisanslanan çalışmalarının telif hakkını saklı tutar.



Optimizing Unmanned Vehicle Navigation: A Hybrid PSO-GWO Algorithm for Efficient Route Planning

Gökhan ALTUN¹ , İlhan AYDIN^{2*} 

¹Tatvan Vocational School, Bitlis Eren University, 13200, Bitlis, Türkiye.

²Computer Engineering Department, Faculty of Engineering, Firat University, 23119, Elazığ, Türkiye.

¹altungokhann@gmail.com, ²iydin@firat.edu.tr

Received: 14.06.2024

Accepted: 16.09.2024

Revision: 10.09.2024

doi: <https://doi.org/10.62520/fujece.1501508>
Research Article

Citation: G. Altun and İ. Aydın, "Optimizing unmanned vehicle navigation: a hybrid pso-gwo algorithm for efficient route planning", *Firat Univ. Jour. of Exper. and Comp. Eng.*, vol. 4, no 1, pp. 100-114, February 2025.

Abstract

This study aims to address the route-planning problem for autonomous systems, which plays a significant role in the operation of unmanned vehicles. A hybrid algorithm has been proposed to enhance the performance of metaheuristic algorithm approaches used to solve the specified problem. In the hybrid algorithm, the simplicity and powerful global search capabilities of the Particle Swarm Optimization (PSO) algorithm are combined with the strong exploration and local minimum avoidance features of the Grey Wolf Optimization (GWO) algorithm. The proposed hybrid approach seeks to achieve both computational accuracy and efficiency in processing time. Using the hybrid approach, routes were calculated in an unknown environment with the help of sensors. The performance of the hybrid algorithm was compared with that of the standalone PSO and GWO algorithms. The comparison evaluated the algorithms based on their execution time for finding the optimal route, the length of the calculated route, the required number of iterations, and their ability to escape local minima. The results were simulated using a custom-built interface, demonstrating a significant advantage in terms of route calculation time. Furthermore, the local minimum problem inherent in the PSO approach was successfully mitigated, while the iteration count and processing time were improved compared to the GWO approach. This approach can be particularly beneficial in disaster management scenarios, where autonomous unmanned vehicles can assist in efficiently planning routes for search, rescue, and resource delivery in unknown or obstructed environments.

Keywords: Particle swarm optimization, Grey wolf optimization, Route planning, Unmanned aerial vehicle, Hybrid algorithm

*Corresponding author

1. Introduction

Advancements in hardware and software technology have created a growing need for automating tasks in various fields. As a result, we observe significant developments in industrial, agricultural, military, and daily life applications. Route planning plays a crucial role in enabling unmanned vehicles to operate autonomously. This problem has been a topic of interest for researchers for a long time, with the earliest studies tracing back to the Traveling Salesman Problem (TSP) introduced by William Hamilton [1]. However, as technology has advanced and the application areas of the TSP have expanded, new constraints and parameters have emerged, increasing the complexity of the problem. Initially, solutions relied on non-intuitive methods, but these approaches often came with significant computational costs and resource usage. The growing constraints and problem complexity have driven the search for more efficient and practical solutions. Consequently, heuristic, meta-heuristic, and deep learning methods have been developed as alternatives to traditional approaches.

For the route-planning problem, the environment is categorized into two types: known and unknown. In a known environment, route planning for unmanned vehicles is performed using approaches such as heuristic, meta-heuristic, and reinforcement learning algorithms. Additionally, strategies like Grid-Based Search, Random Search, Virtual Line-Based Search, and Line-Based Search have been developed to adapt these algorithms to the problem. By employing these methods, route information is preloaded into the unmanned vehicle, enabling its movement along the calculated path. In contrast, in an unknown environment, the unmanned vehicle must process real-time data using additional hardware components such as sensors and cameras. The data collected is used to calculate the direction and the longest possible movement by running the algorithm over the maximum area detectable by the sensors or cameras.

To address the routing problem in the unknown environment defined in this study, algorithms that are efficient in both processing time and resource consumption are essential. Since computational operations will be performed on UAVs, the algorithms must deliver fast responses while consuming minimal resources. Based on the literature review, PSO was chosen due to its simplicity, ease of implementation, and speed. However, PSO has notable limitations, including a tendency to get stuck in local minima and weak exploration capabilities. Şenel et al. [2] proposed a hybrid approach combining GWO and PSO algorithms for classical optimization problems. To prevent PSO from getting stuck in local minima, the GWO algorithm was run with a low population size and a limited number of iterations. Successful particles were then transferred to PSO to improve the solution. Kamboj [3] introduced a hybrid approach that combines GWO and PSO algorithms. In their study, the PSO algorithm was executed first, and the three best results were assigned as alpha, beta, and delta wolves for the GWO algorithm. This method was applied to optimize the timeline for coordinating energy production facilities. Mahapatra et al. [4] developed hybrid optimization methods to minimize total energy loss and reactive power loss in power planning. They proposed three hybrid techniques: linear weight declining PSO, constant inertia weight PSO, and a GWO-PSO hybrid approach. In the PSO-GWO hybrid approach, particles generated by GWO were transferred to PSO, which prevented PSO from getting stuck in local minima and led to an optimal solution. Singh and Singh [5] proposed the hybrid Particle Swarm Optimization and Grey Wolf Optimizer (HPSOGWO), which integrates the efficient exploitation of PSO with the robust exploration capabilities of GWO to improve convergence performance and address limitations such as PSO's susceptibility to local minima and GWO's weaker exploitation. Nguyen et al. [6] focused on speed control for a non-linear DC motor system. Their work involved optimizing parameters for a PID-type fuzzy logic controller using PSO, GWO, Cuckoo-GWO hybrid, and PSO-GWO hybrid algorithms. Negi et al. [7] proposed a PSO-GWO hybrid approach to address the reliability allocation and optimization problem for complex bridge systems and life-support systems in space capsules. Thobiani et al. [8] conducted a study to detect vertical and horizontal cracks in plates. GWO and PSO-GWO hybrid methods were used to tune the parameters of artificial neural networks. Gul et al. [9] proposed a PSO-GWO hybrid algorithm for solving the path planning problem required by autonomous guided robots. Their method aimed to improve performance in route planning by leveraging metaheuristic approaches. Liu and Wang [10] employed the Quantum Particle Swarm Optimization (QPSO) algorithm for dynamic route planning of UAVs. They used the rounding timed active area control method to avoid local minima. Chen et al. [11] utilized the advanced artificial potential field-based path planning algorithm for route planning of UAVs in dynamic environments. Their approach addressed the local minimum problem and conducted route planning

in a 2D environment. Zhang et al. [12] solved the path planning problem for mobile robots using the advanced localized PSO algorithm. By modifying inertia weights, acceleration factors, and localization, they aimed to overcome the local minimum problem in the PSO algorithm. Xu et al. [13] used the Gravity Search Algorithm (GSA) for UAV route planning. Due to the low performance of the standalone approach, they explored a hybrid method. However, the hybrid solution increased the cost, and the problem was addressed by controlling the convergence rate on the gravitational threshold parameter for GSA. Tang et al. [14] performed dynamic route planning for multiple robots in unknown terrain using the GWO algorithm. Their approach enabled the robots to reach fixed and moving targets without hitting obstacles, relying on sensors to control specific areas in unknown environments. He et al. [15] addressed UAV route planning using a deep reinforcement learning method. Their study simulated obstacle-filled environments using AirSim, where sensors on the UAVs guided route planning. Garip et al. [16] proposed a hybrid approach for mobile robot route planning. The outputs of the cuckoo search, PSO, and firefly algorithms were utilized as inputs for other algorithms to enhance route planning performance. Yılmaz and Aydoğmuş [17] tackled the route planning problem for an unmanned vehicle in a 3D environment. They utilized the CoppeliaSim simulator to implement the deep deterministic policy gradient algorithm. Their study reported up to 80% success but noted shortcomings in environmental perception. Sun et al. [18] developed a hybrid algorithm to solve the route planning problem in environments with fixed obstacles. Their hybrid approach combined the ant swarm algorithm and the intelligent water drop algorithm. Routes were evaluated based on path length and the ability to avoid restricted areas. Wan et al. [19] applied the Advanced Whale Optimization Algorithm (AWOA) and the Dynamic Artificial Potential Field (DAPF) method for route planning in dynamic environments. AWOA was used for global path planning, while DAPF helped avoid moving obstacles.

This paper presents a novel hybrid PSO-GWO algorithm for route planning in the autonomous navigation of unmanned vehicles. By leveraging the strengths of hybrid approaches, the proposed algorithm combines the simplicity and speed of PSO with the robust exploration and local minimum avoidance capabilities of GWO. The study aims to solve the route-planning problem with improved computational efficiency and accuracy, providing innovative solutions for dynamic, obstacle-filled, and unknown environments. Comprehensive performance evaluations demonstrate that the proposed algorithm offers significant advantages over existing methods in terms of computation time, route length, and the number of iterations required.

2. The Proposed Hybrid PSO-GWO Algorithm for Route Planning

One of the key challenges in enabling autonomous functionality for UAVs and other unmanned vehicles is route planning. Route planning can be classified into two categories: static and dynamic. Static route planning involves calculating a path to the target within a known field before movement begins, ensuring that the vehicle avoids obstacles and prohibited zones. In this case, the computational cost increases logarithmically with the number of obstacles in the field. Dynamic route planning, on the other hand, involves creating a route in a previously unknown field using sensors or cameras to scan a limited range around the vehicle. Since the field structure and obstacle locations are not known in advance, the algorithm must calculate the shortest route while minimizing computation time, often relying on random movements to navigate the environment. For unmanned vehicles, the route must be as short as possible. However, when the environment is unknown and the route is generated dynamically, the importance of computation time increases significantly. Any delay in calculation directly impacts the total time required to reach the target, which in turn increases fuel consumption. In dynamic route planning, both total travel time and route length are critical factors for reducing fuel consumption and avoiding issues related to fuel shortages. Metaheuristic algorithm approaches are widely used in route planning due to their efficiency and adaptability. Various metaheuristic algorithms have been developed, many of which have successfully solved a wide range of problems. However, each algorithm has its own strengths and weaknesses. Among the most widely used metaheuristic methods in recent years are the PSO and GWO algorithms. PSO is known for its simplicity, ease of implementation, and swarm-based approach [20]. One significant drawback, however, is its tendency to become trapped in local minima, which can impede its search for the optimal solution. In contrast, the GWO algorithm excels in exploration and has demonstrated strong performance in avoiding local minima [21]. However, GWO's balance between exploration and exploitation is somewhat limited and dependent on specific conditions [22]. In this study, the exploration capability of the PSO algorithm is combined with the exploitation strength of the GWO algorithm. In the problem-solving process, PSO begins by assigning a

random position to each particle in the swarm. The solution search continues until either a predefined iteration limit or a termination criterion is reached. During this process, the global best solution ($gbest^*$) represents the optimal result obtained by the entire swarm, while the personal best solution ($pbest^*$) denotes the best result discovered by each individual particle. Each particle's velocity is updated based on these best solutions, as illustrated in (1), and its position is then updated using the newly computed velocity vector, as given in (2).

$$v_{i+1} = w * v_i + c_1 * rand_1 * (pbest - x_i) + c_2 * rand_2 * (gbest - x_i) \quad (1)$$

$$X_{i+1} = x_i + v_{i+1} \quad (2)$$

In (1), the values of c_1 and c_2 are fixed constants randomly selected between 0 and 2. Similarly, $rand_1$ and $rand_2$ are randomly generated values between 0 and 1, while w represents the inertia constant, selected within the range of 0 to 2.

The GWO algorithm is a nature-inspired metaheuristic method that replicates the leadership hierarchy and hunting strategies of grey wolves in their natural environment. It models the hunting process through three key phases: encircling the prey, attacking the prey (exploitation), and searching for the prey (exploration). These phases enable the algorithm to maintain a balance between global exploration and local exploitation, thereby achieving efficient optimization. During the hunt, grey wolves exhibit encircling behavior around their prey. This behavior is mathematically represented using (3)-(4).

$$D = |C \cdot X_{p(t)} - X_{(t)}| \quad (3)$$

$$X_{t+1} = |X_{p(t)} - A \cdot D| \quad (4)$$

In (3)-(4), t represents the current iteration. The parameters A and C denote the coefficient vectors, while X and X_p represent the position vectors of the grey wolf and the prey, respectively. A and C values are calculated by using (5) and (6).

$$A = |2ar_1 - a| \quad (5)$$

$$C = |2r_2| \quad (6)$$

The r_1 and r_2 values used in (5)-(6) are randomly generated values between 0 and 1. The value of a is shown with a linearly decreasing value from 2 to 0 by using (7).

$$a = 2 \cdot (1 - i/iteration) \quad (7)$$

In the algorithm, after the prey is encircled, the hunting phase begins. The positions of the wolves in the herd are updated using Equations (8) to (14), which build upon the containment formulas (3) and (4). These updates are guided by the positions of the alpha, beta, and delta wolves, which are the closest to the current position of the prey.

$$D_\alpha = |C \cdot X_\alpha - X_{(t)}| \quad (8)$$

$$D_\beta = |C \cdot X_\beta - X_{(t)}| \quad (9)$$

$$D_{\delta} = |C.X_{\delta} - X_{(t)}| \quad (10)$$

$$X_1 = |X_{\alpha} - A.D_{\alpha}| \quad (11)$$

$$X_2 = |X_{\alpha} - A.D_{\beta}| \quad (12)$$

$$X_3 = |X_{\alpha} - A.D_{\delta}| \quad (13)$$

$$X_{t+1} = \frac{(X_1 + X_2 + X_3)}{3} \quad (14)$$

As the value of a approaches zero during the optimization, the hunt transitions into the attack phase, where coefficient vector A takes random values within the range of $[-1,1]$. This progression allows the steps of encircling the prey, hunting, and attacking to be executed sequentially. In this study, a hybrid approach is proposed by integrating the strong exploration capabilities of the GWO with the efficient exploitation strengths of the PSO. The flowchart of the hybrid algorithm is shown in Figure 1.

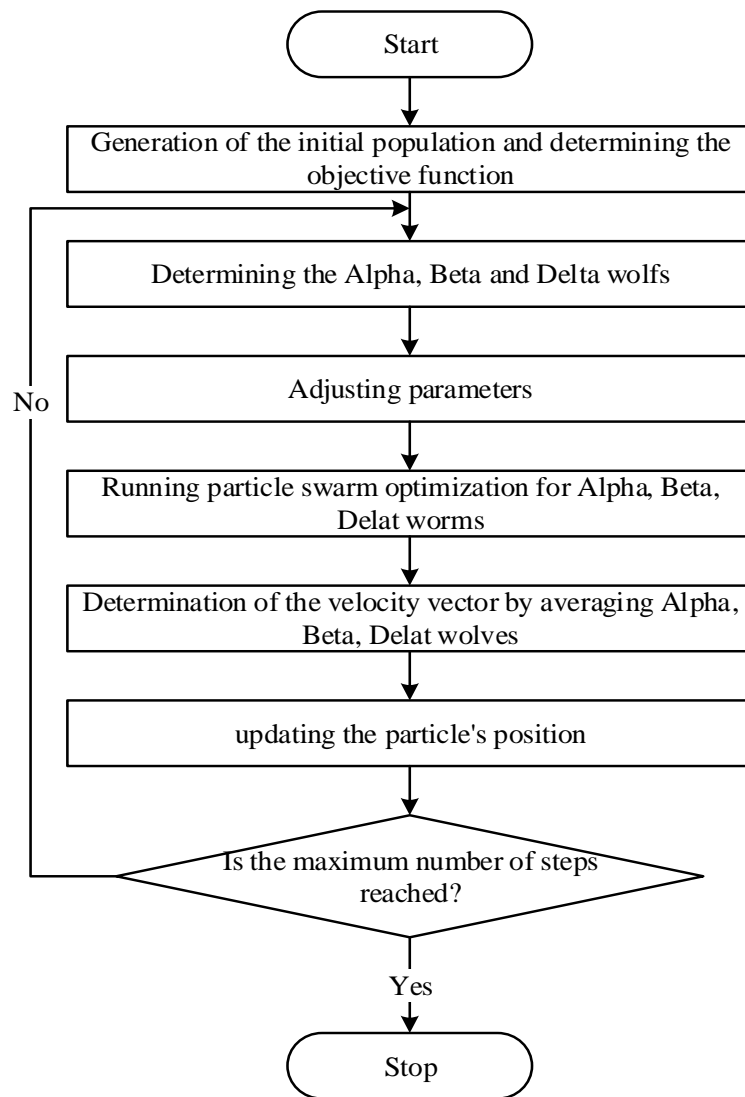


Figure 1. Flowchart Diagram of Hybrid Algoritm

The formula for calculating the parameter a in the GWO algorithm has been adapted to the constant w to regulate the oscillation of the velocity vector during calculations as shown in (15). The coefficient c_1 used in the velocity vector calculation is determined using (16).

$$w = 1 - i/iteration \quad (15)$$

$$c_1 = 4 - (2 * w * random(0,1)) \quad (16)$$

With the proposed approach, the influence of the velocity vector decreases as the number of iterations increases, keeping oscillation under control. In the hybrid approach, the exploration capability of GWO and the exploitation features of PSO are combined. In the GWO algorithm, the velocity updates for the alpha, beta, and delta wolves are performed using (17) to (19). Subsequently, the overall velocity is calculated as mean values of three wolves using (20), and the position of each particle is updated based on (21).

$$v_{i\alpha}^{t+1} = w \cdot v_i^t + r_1 \cdot c_1 \cdot (x_\alpha - x_i^t) \quad (17)$$

$$v_{i\beta}^{t+1} = w \cdot v_i^t + r_1 \cdot c_1 \cdot (x_\beta - x_i^t) \quad (18)$$

$$v_{i\delta}^{t+1} = w \cdot v_i^t + r_1 \cdot c_1 \cdot (x_\delta - x_i^t) \quad (19)$$

$$v_i^{t+1} = \frac{(v_{i\alpha}^{t+1} + v_{i\beta}^{t+1} + v_{i\delta}^{t+1})}{3} \quad (20)$$

$$x_i^{t+1} = x_i^t + v_i^{t+1} \quad (21)$$

A balanced exploration capability is achieved by using the best three particles in the population and averaging the three newly obtained velocity vectors. To evaluate the efficiency of the proposed hybrid algorithm, the route planning problem for UAVs is addressed. The route planning is performed in an unknown environment, where UAV relies on sensors to explore the area and execute the routing process. The maximum area detectable by the sensor is assumed to have a diameter of 20 units. This means the UAV can identify obstacles within a 20-unit detection range. The direction and movement distance are calculated based on the available information. If the calculated movement exceeds the sensor's maximum detectable range, the movement is adjusted by taking the modulus of the calculated value. The maximum value is avoided because the proximity of obstacles outside the detection range is unknown. The goal is to avoid restricting the mobility of unmanned vehicles. In the route planning problem for UAVs, the search strategy used alongside the selected algorithm is crucial. The chosen search strategy must be compatible with the algorithm and applicable to the field structure being studied. The selected search algorithm and strategy play a significant role in route planning, influencing computation time, result performance, and the accuracy of algorithm. In this study, a random search strategy is combined with a metaheuristic algorithm for operation in an unknown environment. In the random search strategy, the step length is determined first. From the UAV's current position, random points are generated within the maximum step length using Euclidean calculations. For these points to be valid, the UAV must not collide with obstacles or pass through restricted areas between its current position and the new position. Figure 2 illustrates the Random Search Strategy for an UAV navigating an environment with obstacles.

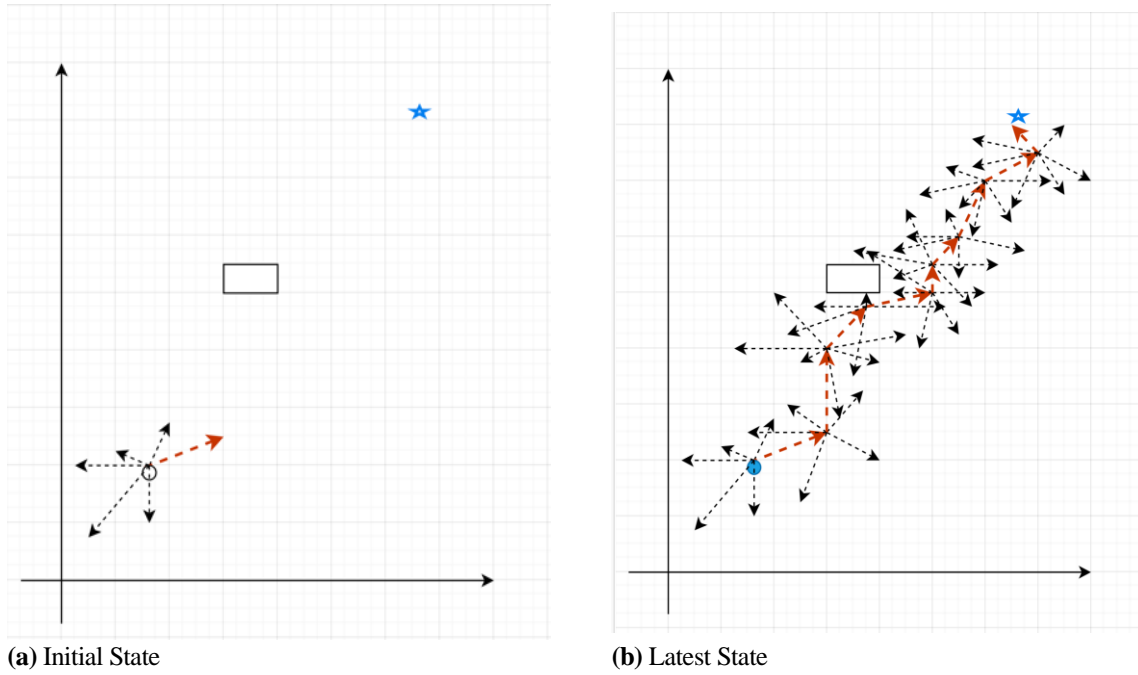


Figure 2. Random Search Strategy

In Figure 2(a), the UAV starts at its initial position and generates random points (indicated by arrows), selecting the point closest to the target (blue star) based on Euclidean distance. In Figure 2(b), the UAV progresses toward the target by iteratively updating its position while avoiding collisions with obstacles (rectangles). The selected path is shown in red, demonstrating how the UAV dynamically moves closer to the target without crossing restricted areas.

3. Application Results

The fundamental working principle of the proposed hybrid algorithm is based on the velocity update mechanism of the PSO algorithm, combined with the selection of the top three wolves in the GWO algorithm, and an iteration-based weight reduction mechanism approaching zero. To assess the effectiveness and superiority of this method, the task of discovering a randomly generated point within a 1000x1000-scale space was evaluated based on iteration count, computation time, and distance. The evaluation was conducted by comparing the proposed hybrid algorithm with standalone PSO and GWO algorithms. In the existing literature, iteration count and distance are commonly used as performance metrics. However, since computation time is critical for real-world applications such as the dynamic routing problem in UAVs, it was included as an additional evaluation criterion. To ensure a fair comparison, all experiments were performed with the same population size. Each test function was executed independently 15 times for each algorithm. The population size was fixed at 20, and the maximum number of iterations was limited to 200. The evaluation criteria included the minimum values of computation time and distance, with success defined as the step at which the iteration value fell below one unit. In the results, red markers denote local minima, while bold values indicate successful outcomes for the corresponding tests. The results are summarized in Table 1.

Table 1. Result of Testing

Processing time			Distance			Number of iterations		
PSO	GWO	Hybrid	PSO	GWO	Hybrid	PSO	GWO	Hybrid
325	513	391	0.528660654	0.05543581	0.00036105	138	194	7
276	505	386	0.000478167	0.04297425	3.8913E-05	40	192	11
275	462	416	1.719389262	0.31649431	2.3391E-06	31	192	13
697	493	400	10.73632129	0.16824665	1.4392E-06	93	182	12
282	497	414	7.3996E-06	0.19867104	4.384E-07	23	196	12
284	478	385	0.000419992	0.3027555	1.2511E-05	45	194	15
287	461	400	11.58451303	0.16900177	0.00012228	14	165	10
289	481	383	8.357593682	0.01555127	0.00137818	34	112	12
294	478	409	5.152039051	0.40561707	0.00173228	61	191	10
249	465	372	5.68434E-14	0.05788538	0.00029738	10	91	10
277	489	371	0.199539361	0.21778345	0.00135569	106	78	8
283	494	402	0.397384449	0.17952916	0.00048415	46	184	4
277	493	365	0.001096472	0.4388497	0.02923901	68	190	11
290	473	412	2.44817E-08	0.2689691	0.09687925	25	180	8
280	487	414	0.102694885	0.16521049	0.00785485	60	188	12

As shown in Table 1, PSO exhibits a local minimization problem, while GWO is computationally expensive in terms of computation time. The proposed hybrid algorithm, however, demonstrates successful outcomes in terms of both exploitation and iteration. In this study, two different field structures (regular and irregular) and varying numbers of obstacles were considered as part of a real-world problem. The fields for simulation were created using the C# programming language and the drawing library. The simulated field was scaled to a 600x600 unit structure, resulting in a total field area of 360,000 units². The first field structure is an irregular layout containing 20 nested obstacles of varying sizes. These nested obstacles were designed to test the algorithms' ability to handle local minimum problems during the route computation process. The second field structure is a regular layout, consisting of 48 obstacles of uniform size arranged in six rows, with eight obstacles per row. The obstacles in each row were offset to fill the gaps between obstacles in the preceding row. The visual representations of the field structures created for both scenarios are provided in Figure 3.

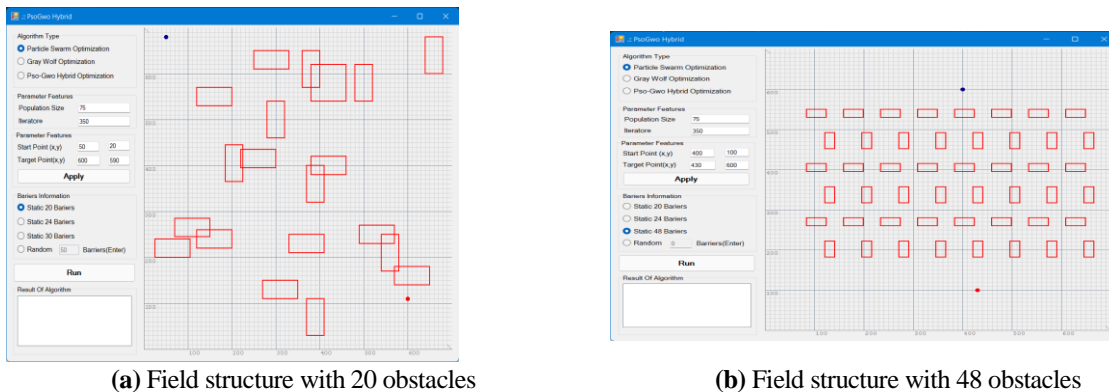


Figure 3. Field structure

The algorithms will be evaluated based on criteria such as avoiding local minima, finding the global optimal route, and determining the route in the shortest possible time in environments with fixed obstacles. In real-

world scenarios, unmanned vehicles often lack prior knowledge of the area they are navigating. Instead, they rely on integrated cameras and sensors to generate routes and make movement decisions. These systems analyze the area within a specified radius before taking action. To avoid collisions with obstacles during movement, the route creation process must be instantaneous and highly efficient. In this study, a UAV is tasked with generating a route in a previously unknown field structure by processing data received from its sensors. The sensors are assumed to detect obstacles within a maximum range of 20 units. The hybrid algorithm will be used to determine both the direction of movement and the step size until the next sensor query. The initial field structure consists of 20 obstacles, some of which are nested, with a Euclidean distance of 790 units between the starting and ending points. The population size for the algorithms is set at 75, and the iteration count is limited to 500. To ensure a fair comparison, all algorithms were executed 15 times with identical population parameters under the specified criteria. The results, including the processing time for each test step, are visualized in Figure 4.

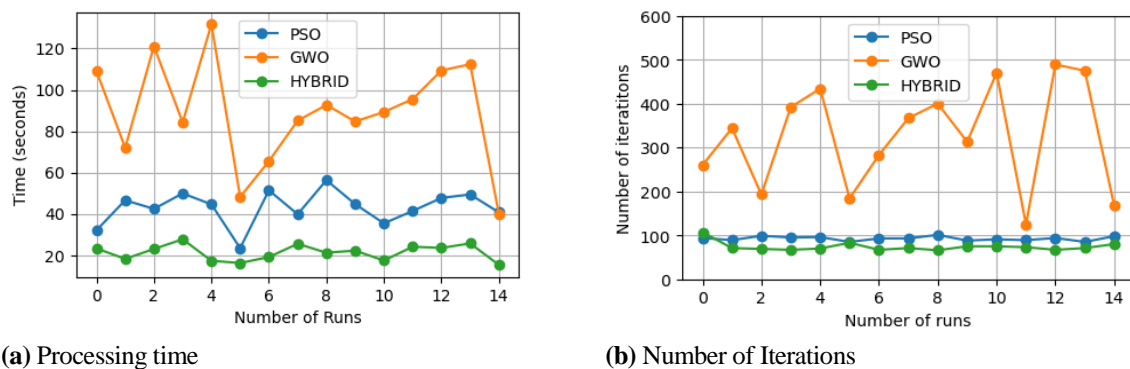


Figure 4. Performance comparisons of three algorithms for twenty obstacles

As illustrated in Figure 4, the proposed hybrid algorithm outperforms the other algorithms in terms of runtime and the number of iterations. The hybrid algorithm demonstrates a shorter runtime compared to PSO and converges more quickly to the optimal solution. Figure 5 provides a visual representation of the routes identified by each algorithm.

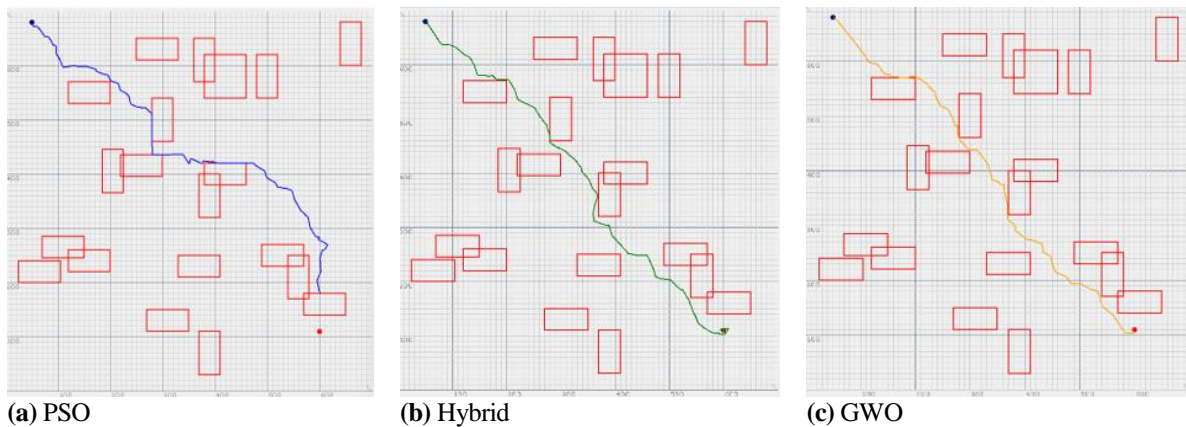


Figure 5. Route of each algorithm for twenty obstacles

In Figure 5, it can be observed that the PSO algorithm becomes trapped in local minima due to the nested obstacles in the field structure. In contrast, the proposed hybrid approach not only provides an advantage in terms of processing time but also successfully avoids local minima. Although the GWO algorithm excels in exploration and exploitation, it is more costly in terms of computation time and iterations compared to the hybrid approach. The second field structure comprises 48 obstacles, with a Euclidean distance of 538 units between the starting and ending points. This structure consists of 6 rows of 8 obstacles arranged side by side, designed such that the gaps between obstacles in one row align with the

obstacles in the adjacent row. The population size for this scenario was set to 75, and the iteration count was defined as 800. To ensure a fair comparison, all algorithms were executed 10 times using the same population parameters under the specified criteria. The processing time and number of iterations are given in Figure 6 for 10 execution.

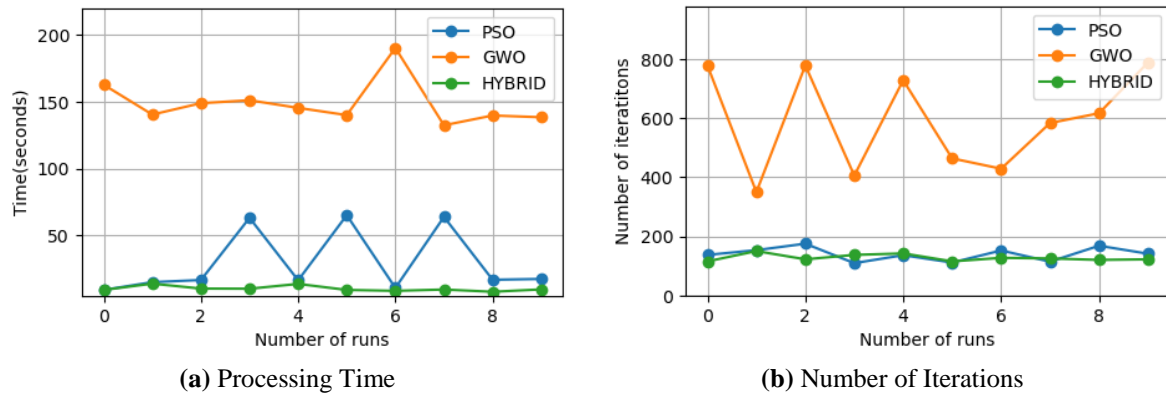


Figure 6. Performance comparisons of three algorithms for forty-eight obstacles

Figure 6 (a) demonstrates that the hybrid algorithm outperforms the other algorithms in terms of runtime, consistently achieving faster execution. For the PSO algorithm, the runtime was significantly higher in three of the runs, primarily due to its tendency to become trapped in local minima. In Figure 6 (b), the hybrid algorithm and PSO show comparable performance in terms of the number of iterations. However, PSO converged to a local minimum in three out of ten runs, highlighting its limitations in complex scenarios. Figure 7 illustrates the routes generated by the three algorithms when navigating through the 48-obstacle field.

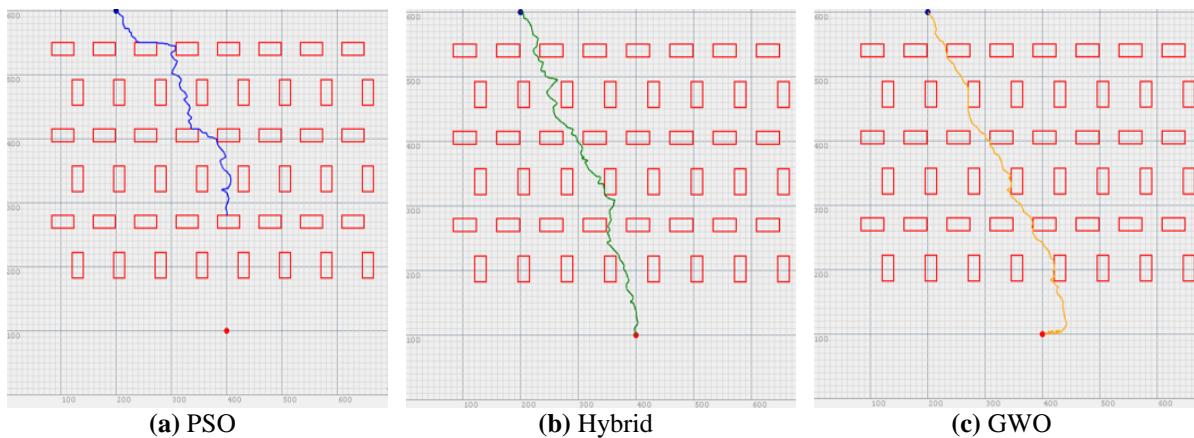


Figure 7. Route of each algorithm for twenty obstacles

In Figure 7, the PSO algorithm reached a local minimum in 3 out of 10 runs. When the time spent on local minimization is excluded from the average runtime table, a corrected value of 14.7 seconds is obtained. Even with this adjustment, the hybrid approach remains advantageous. Compared to the GWO

algorithm, the hybrid approach demonstrates superiority not only in time performance but also in path distance optimization. Figure 8 presents the path distance results.

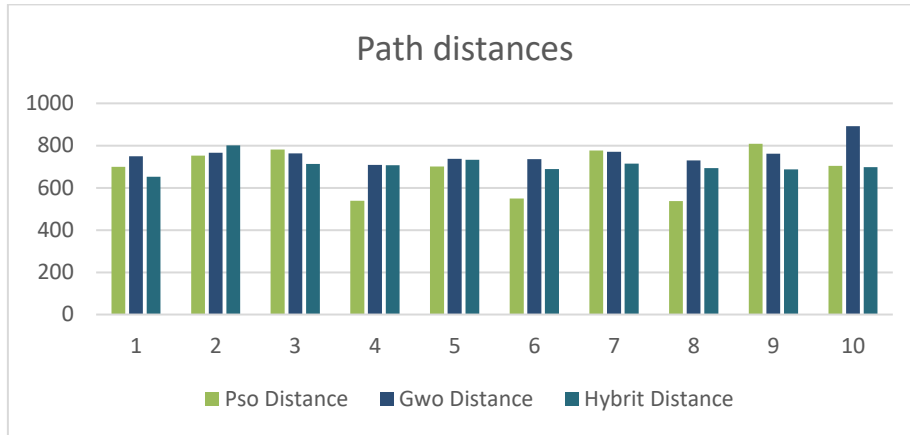


Figure 8. 48 road distances measured during tests in an obstacle field

In Figure 8, the hybrid approach demonstrated a clear advantage in path distance, achieving superior results in 7 out of 10 tests. The test results obtained in the 2D environment were further validated in a 3D simulation environment to ensure their accuracy in real-world applications. The simulations were conducted using the Gazebo application as the simulation platform. Data from the virtual environment created in Gazebo was collected using a LiDAR sensor, which was managed through ROS (Robot Operating System) software. In the simulation environment designed for UAV testing, 20 walls (dimensions: 7x5x0.2 meters) were added. The Euclidean distance between the starting point and the target point was set at 102 meters. Both 2D and 3D visualizations of the simulation environment are shown in Figure 9.

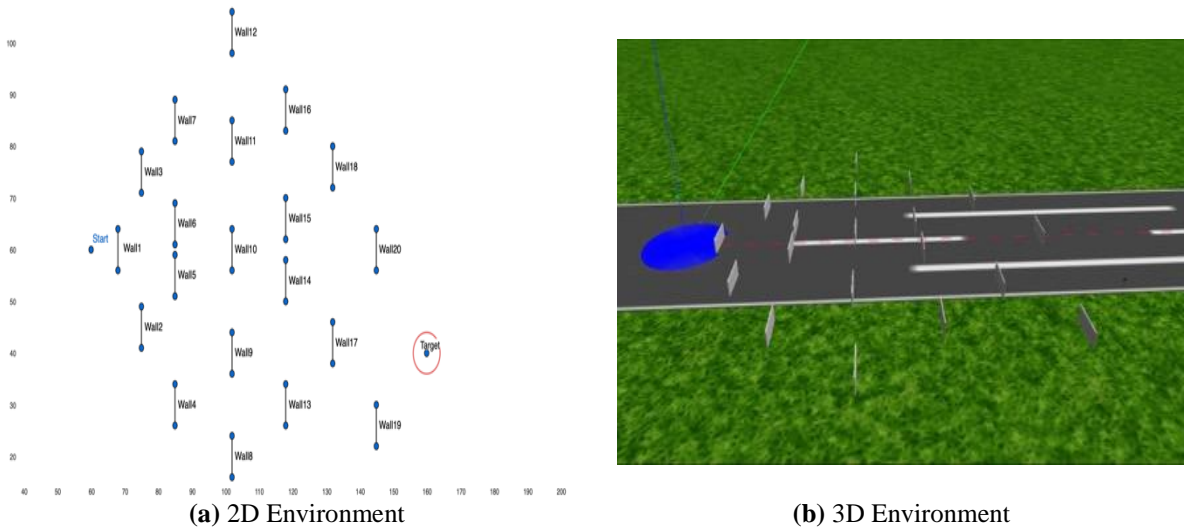


Figure 9. Gazebo Simulation Environment

After the drone takes off, the hybrid algorithm determines the direction and magnitude of movement based on data received from the LiDAR sensor, which has a measurement range of 10 meters. The 2D route plan for the autonomous flight, managed by the hybrid algorithm, is presented in Figure 10.

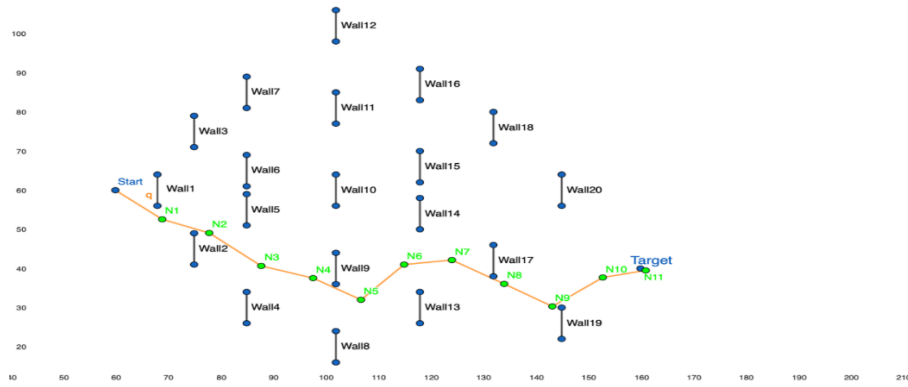


Figure 10. Autonomous flying

The route of the UAV, as depicted in the Figure 10, demonstrates the efficiency of the hybrid algorithm in navigating a complex environment with multiple obstacles. Starting from the initial position, the UAV successfully maneuvers around 20 walls while maintaining an optimized path toward the target. The numbered nodes illustrate key decision points where the algorithm determined the UAV's next direction and step size based on LiDAR sensor data. The trajectory is smooth and avoids unnecessary detours, highlighting the algorithm's ability to balance exploration and exploitation effectively. The UAV's ability to reach the target within a proximity of 0.23 meters and a total route length of 130 meters further validates the precision and adaptability of the hybrid approach in a constrained environment.

4. Conclusions

The test results from this study highlight the significant advantages of the proposed hybrid algorithm. Its structure leverages the simplicity, proven robustness, and exploitation capabilities of PSO, combined with the exploration strength and local minimum avoidance properties of GWO. This combination makes the hybrid algorithm particularly effective in computations where processing time is critical. For route planning—an essential aspect of unmanned vehicle operations—this approach proves valuable due to its efficiency in navigating complex field structures, minimizing processing time, and avoiding local minima. To further validate its real-world applicability, the algorithm was tested in a three-dimensional Gazebo simulation environment for autonomous UAV flight, yielding successful results. The proposed approach demonstrates readiness for real-world implementation. Future studies aim to extend its application to complex and irregular environments, such as disaster zones and conflict areas, to further enhance the efficiency and utility of unmanned aerial vehicles in challenging scenarios.

5. Acknowledgements

This study was supported by the Scientific and Technological Research Council of Turkey (TUBITAK) under Project No. 123E669.

6. Author Contribution Statement

G. Altun was responsible for the conceptualization, methodology, software development, and writing of the original draft. I. Aydın contributed to the conceptualization, methodology, writing of the original draft, and the review and editing of the manuscript.

7. Ethics Committee Approval and Conflict of Interest

No ethics committee approval was required for this study and there is no conflict of interest between the authors.

8. References

- [1] N. L. Biggs, E. K. Lloyd, and R. J. Wilson, *Graph Theory*, 1736-1936, 1986.
- [2] F. A. Şenel, F. Gökçe, A. S. Yüksel, and T. Yiğit, "A Novel Hybrid PSO–GWO Algorithm for Optimization Problems," *Engineering with Computers*, vol. 35, no. 4, pp. 1359–1373, Dec. 2018.
- [3] V. K. Kamboj, "A Novel Hybrid PSO–GWO Approach for Unit Commitment Problem," *Neural Computing and Applications*, vol. 27, no. 6, pp. 1643–1655, Jun. 2015.
- [4] S. Mahapatra, M. Badi, and S. Raj, "Implementation of PSO, it's variants and Hybrid GWOPSO for improving Reactive Power Planning," in *2019 Global Conference for Advancement in Technology (GCAT)*, pp. 1–6.
- [5] N. Singh and S. B. Singh, "Hybrid Algorithm of Particle Swarm Optimization and Grey Wolf Optimizer for Improving Convergence Performance," *Journal of Applied Mathematics*, vol. 2017, p. e2030489, Nov. 2017.
- [6] D.-T. Nguyen, J.-R. Ho, P.-C. Tung, and C.-K. Lin, "A Hybrid PSO–GWO Fuzzy Logic Controller with a New Fuzzy Tuner," *International Journal of Fuzzy Systems*, vol. 24, no. 3, pp. 1586–1604, Nov. 2021.
- [7] G. Negi, A. Kumar, S. Pant, and M. Ram, "Optimization of Complex System Reliability Using Hybrid Grey Wolf Optimizer," *Decision Making: Applications in Management and Engineering*, vol. 4, no. 2, pp. 241–256, Oct. 2021.
- [8] A. Thobiani, S. Khatir, B. Benaissa, E. Ghandourah, S. Mirjalili, and A. Wahab, "A hybrid PSO and Grey Wolf Optimization algorithm for static and dynamic crack identification," *Theoretical and Applied Fracture Mechanics*, vol. 118, p. 103213, 2022.
- [9] F. Gul, W. Rahiman, S. S. N. Alhady, A. Ali, I. Mir, and A. Jalil, "Meta-heuristic Approach for Solving multi-objective Path Planning for Autonomous Guided Robot Using PSO–GWO Optimization Algorithm with Evolutionary Programming," *Journal of Ambient Intelligence and Humanized Computing*, vol. 12, no. 7, pp. 7873–7890, Sep. 2020.
- [10] B. Liu and X. Wang, "UAV Route Planning Based on QPSO Algorithm under Rolling Time Domain Control," in *2019 2nd World Conference on Mechanical Engineering and Intelligent Manufacturing (WCMEIM)*, pp. 612–617.
- [11] S. Chen, Z. Yang, Z. Liu, and H. Jin, "An improved artificial potential field based path planning algorithm for unmanned aerial vehicle in dynamic environments," in *2017 International Conference on Security, Pattern Analysis, and Cybernetics (SPAC)*, pp. 591–596.
- [12] L. Zhang, Y. Zhang, and Y. Li, "Mobile Robot Path Planning Based on Improved Localized Particle Swarm Optimization," *IEEE Sensors Journal*, vol. 21, no. 5, pp. 6962–6972, 2021.
- [13] H. Xu, S. Jiang, and A. Zhang, "Path Planning for Unmanned Aerial Vehicle Using a MixStrategyBased Gravitational Search Algorithm," *IEEE Access*, vol. 9, pp. 57033–57045, 2021.
- [14] H. Tang, W. Sun, A. Lin, M. Xue, and X. Zhang, "A GWO based multirobot cooperation method for target searching in unknown environments," *Expert Systems with Applications*, vol. 186, p. 115795, 2021.
- [15] L. He, N. Aouf, and B. Song, "Explainable Deep Reinforcement Learning for UAV autonomous path planning," *Aerospace Science and Technology*, vol. 118, p. 107052, 2021.
- [16] Z. Garip, D. Karayel, and M. Erhan Çimen, "A Study on Path Planning Optimization of Mobile Robots Based on Hybrid Algorithm," *Concurrency and Computation: Practice and Experience*, vol. 34, no. 5, Nov. 2021.
- [17] T. Yılmaz and Ö. Aydoğmus, "Deep Deterministic Policy Gradient Reinforcement Learning for collision-free Navigation of Mobile Robots in Unknown Environments," *Firat University Journal of Experimental and Computational Engineering*, vol. 2, no. 2, pp. 87–96, Jan. 2023.
- [18] X. Sun, S. Pan, N. Bao, and N. Liu, "Hybrid Ant Colony and Intelligent Water Drop Algorithm for Route Planning of Unmanned Aerial Vehicles," *Computers & Electrical Engineering*, vol. 111, pp. 108957–108957, Nov. 2023.
- [19] R. Wan, X. Wang, and Z. Ma, "UAV route planning based on improved whale optimization algorithm and dynamic artificial potential field method," in *2023 6th International Symposium on Autonomous Systems (ISAS)*, pp. 1–8.

- [20] R. Eberhart and J. Kennedy, "A new optimizer using particle swarm theory," in MHS'95. Proceedings of the Sixth International Symposium on Micro Machine and Human Science, pp. 39–43.
- [21] S. Mirjalili, Seyed Mohammad Mirjalili, and A. Lewis, "Grey Wolf Optimizer," *Advances in Engineering Software*, vol. 69, pp. 46–61, 2014.
- [22] B. N. Gohil and D. R. Patel, "A hybrid GWOPSO Algorithm for Load Balancing in Cloud Computing Environment," in 2018 Second International Conference on Green Computing and Internet of Things (ICGCIoT), pp. 185–191.



Farklı Geometrik Konfigürasyonlara Sahip Silindir Oluklu Sandviç Yapıların Basma Mukavemetlerinin ve Enerji Emiliminin İncelenmesi

Ilyas Bozkurt^{1*}

¹Makine Mühendisliği, Mühendislik ve Mimarlık Fakültesi, Muş Alparslan Üniversitesi, Muş, Türkiye.
i.bozkurt@alparslan.edu.tr

Geliş Tarihi: 16.07.2024
Kabul Tarihi: 07.10.2024

Düzeltilme Tarihi: 27.09.2024

doi: <https://doi.org/10.62520/fujece.1516879>
Araştırma Makalesi

Alıntı: İ. Bozkurt, "Farklı geometrik konfigürasyonlara sahip silindir oluklu sandviç yapıların basma mukavemetlerinin ve enerji emiliminin incelenmesi", Fırat Üni. Deny. ve Hes. Müh. Derg., vol. 4, no 1, pp. 115-135, Şubat 2025.

Öz

Bu çalışmanın amacı beş farklı geometrik konfigürasyona sahip CFRP kompozit silindir sandviç yapıların basma mukavemetlerini ve enerji absorberlerini sayısal olarak incelemek ve birbirleri ile mukayese etmektir. Çalışmada farklı çekirdek yapıları için kompozit sandviçlerin ezilme performansları (Maksimum ezilme kuvveti (PCF), ortalama ezilme kuvveti (MCF), Ezilme kuvveti verimliliği (CFE), enerji emilimi (EA) ve spesifik enerji emilimi (SEA)) ve meydana gelen hasar türleri belirlenmiştir. Basma analizleri *LS DYNA* sonlu elemanlar programında *MAT-54* malzeme modeli kullanılarak *Hashin hasar kriteri*, *Kohezif Bölge Modeli (CZM)* ve *Bilinear traction-separation* yasaının kombinasyonuna dayalı ilerlemeli hasar analizi ile gerçekleştirilmiştir. Çalışmada beş farklı numune arasında PCF değeri en yüksek eksenel oluklu çekirdek yapı Trapezoidal olurken en düşük ise dairesel oluklu çekirdek yapı Arc shaped olmuştur. Eksenel arc shaped SEA değeri en yüksek sandviç yapı olurken, dairesel sinusoidal oluklu çekirdek ise SEA değeri en düşük sandviç yapı olmuştur. Eksenel ve dairesel oluklu çekirdek arasında sinusoidal yapının CFE değeri en yüksek olarak belirlenmiştir. Sandviç yapıların deformasyon davranışlarına çekirdek yapısının etkisinin yüksek olduğu görülmüştür.

Anahtar kelimeler: Dairesel sandviç kompozit, Basma testi, Ezilme dayanımı, İlerlemeli hasar analizi, Sonlu elemanlar yöntemi

*Yazışılan yazar

İntihal Kontrol: Evet – Turnitin
Şikayet: fujece@firat.edu.tr

Telif Hakkı ve Lisans: Dergide yayın yapan yazarlar, CC BY-NC 4.0 kapsamında lisanslanan çalışmalarının telif hakkını saklı tutar.



Investigation of Compressive Strength and Energy Absorption of Cylinder Corrugated Sandwich Structures with Different Geometric Configurations

Ilyas Bozkurt¹ *

¹Department of Mechanical Engineering, Architecture and Engineering Faculty, Mus Alparslan University, Muş, Türkiye.
i.bozkurt@alparslan.edu.tr

Received: 16.07.2024
Accepted: 07.10.2024

Revision: 27.09.2024

doi: <https://doi.org/10.62520/fujece.1516879>
Research Article

Citation: İ. Bozkurt, "Investigation of compressive strength and energy absorption of cylinder corrugated sandwich structures with different geometric configurations", *Firat Univ Jour. of Exp. and Comp. Eng.*, vol. 4, no 1, pp. 115-135, February 2025.

Abstract

The aim of this study is to numerically investigate and compare the compressive strength and energy absorption of CFRP composite cylinder sandwich structures with five different geometric configurations. The crushing performances (Peak crushing force (PCF), Mean crushing force (MCF), Crushing force efficiency (CFE), energy absorption (EA) and specific energy absorption (SEA)) of the composite cylinder for different core configurations and the failure types were determined. Compression analyses were performed in *LS DYNA* finite element program using MAT-54 material model with progressive failure analysis based on the combination of Hashin failure criterion, Cohesive Zone Model (CZM) and Bilinear traction-separation law. Among the five different specimens in the study, the highest PCF value was Trapezoidal with axial corrugated core while the lowest was Arc shaped with circular core. Axial arc shaped core was the sandwich structure with the highest SEA value, while circular sinusoidal corrugated core was the sandwich structure with the lowest SEA value. Between axial core and circular core, the CFE value of the sinusoidal core specimen was determined to be the highest. It was observed that the effect of core structure on the deformation behavior of sandwich structures was high.

Keywords: Circular sandwich composite, Compression test, Crashworthiness, Progressive failure analysis, Finite element method

*Corresponding author

1. Introduction

Sandwich composite structures with high strength/weight and high energy absorption capacity are actively used in many sectors, especially in the aerospace industry [1]. Sandwich structures are indispensable structures for engineers, especially in components and sections with high energy absorption requirements. Sandwich structures are generally composed of a part called core, which is placed between the upper and lower facesheets [2]. Although the facesheets are usually in the form of plates, different configurations are used in the core structure. Especially with the development of manufacturing technology and production techniques, many different core structures have been produced and their strength values have been studied by researchers. Different types of adhesives such as epoxy or Araldite are used to join the facesheets to the core [3, 4]. Sandwich structures can be produced as flat plates or cylinders depending on the area of use [5]. There is a great need especially in areas where cylindrical structures are used, such as airplane parts, wing sections and bicycle bodies, where lightness and high strength come to the fore.

The main purpose of using corrugated structures in sandwich structures is to reduce the total mass. Even if they are not as light as thin lattice structures, these structures with high strength values can have the strength values required by engineers. If instead of using a corrugated structure, only a hollow and shapeless body was used, it would not be preferred much due to its high weight. It is also known that weight has a great impact on fuel consumption. By using lighter structures, environmental failure can also be minimized. However, since the strength effect also changes with the change of core type, it is an area that can be intervened and controlled for researchers [6-8]. In addition, the effects of strength values of different composite types (such as glass fiber, carbon fiber, kevlar) or alloy types (such as aluminum, steel) can be examined [9].

Many studies have been conducted to improve the strength performance of corrugated sandwich composite structures [2, 10-17]. Zhang et al. [18] investigated the compression performance and failure modes of square honeycomb core sandwich cylinders by experimental measurement, analytical modeling and numerical simulation. Wu et al. [19] investigated four possible failure modes (Euler buckling, axisymmetric buckling, local buckling and face panel crushing of the sandwich cylinders) and their corresponding strength values under compression loading of low density pyramid lattice core sandwich cylinders made of plain woven carbon fiber fabrics. Ge et al. [20] experimentally and numerically investigated the compression behavior and failure modes of a new sandwich structure with bidirectional corrugated cores produced by 3D printing. The study shows that corrugated buckling and fracture are the main failure modes in flat compression. However, the front panels mostly support the loading in the edge direction and no significant deformation is observed. Zhu et al. [21] experimentally, numerically and analytically investigated the axial compression behavior of trapezoidal staggered corrugated truss, bidirectional corrugated truss and hexagonal honeycomb core sandwich plates. Zhu et al. [22] experimentally and numerically investigated the axial and lateral compression behaviors and failure modes of inner square tube, corrugated core and outer square tube produced by hot pressing method. Chen et al. [23] experimentally and numerically performed compression tests to determine the failure modes of the number and core configurations (regular, perpendicular and symmetrical) of multilayer corrugated sandwich panels produced by hot pressing. Han et al. [24] investigated the compression behavior of honeycomb corrugated hybrid core aluminum sandwich structures both experimentally and theoretically.

In this study, unlike the literature, compressive strength values (Peak crushing force (PCF), Mean crushing force (MCF), Crushing force efficiency (CFE), energy absorption (EA) and specific energy absorption (SEA)) and failures of five different cylindrical corrugated sandwich carbon composite structures (Trapezoidal, Rectangular, Arc-shaped, Triangular and Sinusoidal) were determined numerically and compared with each other. Compression simulations were performed in *LS DYNA* finite element program using MAT-54 material model based on *Hashin failure criterion, Cohesive Zone Model (CZM) and Bilinear traction-separation laws*.

2. Numerical Study

2.1. Finite element model

The compression behavior of carbon fiber cylindrical composite sandwich structures with different core configurations was investigated using the *LS DYNA* finite element program [25]. The solution methodology of the program includes material cards that provide failure models based on the continuous failure mechanism (CDM) [26]. By using models based on CDM, it is possible to see structural failure in a progressive manner. When creating the numerical model, it is important that all specimens are under the same limit and under the same standards. Because in this study, no experimental study was taken as a reference, only the compression behaviors were compared with each other. Therefore, it is important that all specimens are under the same conditions.

In order to determine and compare the compressive strength and energy absorption capabilities of sandwich composite structures, it is necessary to determine crashworthiness parameters. These parameters are calculated from force-displacement curves. Figure 1 shows an example force-displacement curve obtained from a compression test. During the crushing behavior of cylindrical sandwich structures, there are three distinct stages. First stage, plateau stage and densification stage. In the first stage, the crushing force increases rapidly with the crushing distance until it reaches the initial peak force (PCF). This is followed by the plateau stage, characterized by the development of folds in the tubes, causing fluctuations in the crushing force. This fluctuation is caused by the buckling, bending and collapse of the cell walls. Finally, in the densification stage, the crushing force experiences a significant increase due to densification.

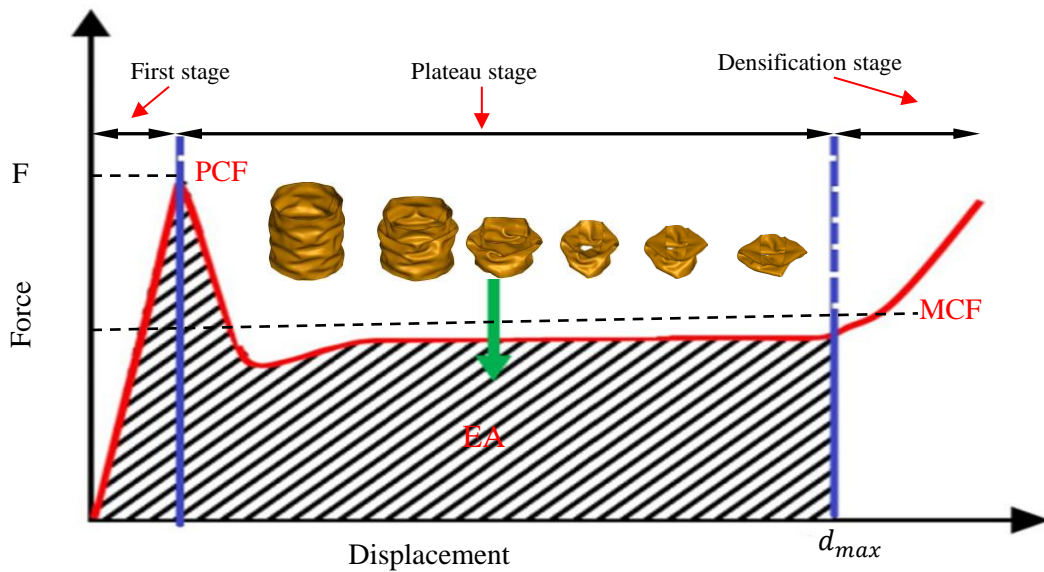


Figure 1. Example force-displacement curve obtained from compression testing

Here, the area under the graph gives the absorption energy (*EA*) or total inner energy (*TIE*) (1).

$$EA(dx) = \int_0^{d_x} F(x) dx \quad (1)$$

where d_x is the crush distance and $F(x)$ is the crush force as a function of the crush distance of x .

$$SEA = \frac{EA}{m} \quad (2)$$

Energy per unit of mass is denoted by SEA, where m is mass.

Crushing force efficiency (CFE) represents the ratio of mean crushing force (F mean) to peak crushing force (PCF) and is defined as:

$$CFE = \frac{MCF}{PCF} \quad (3)$$

Peak breaking force (PCF) is the maximum force value of the system. Mean crushing force (MCF) is considered as the average force.

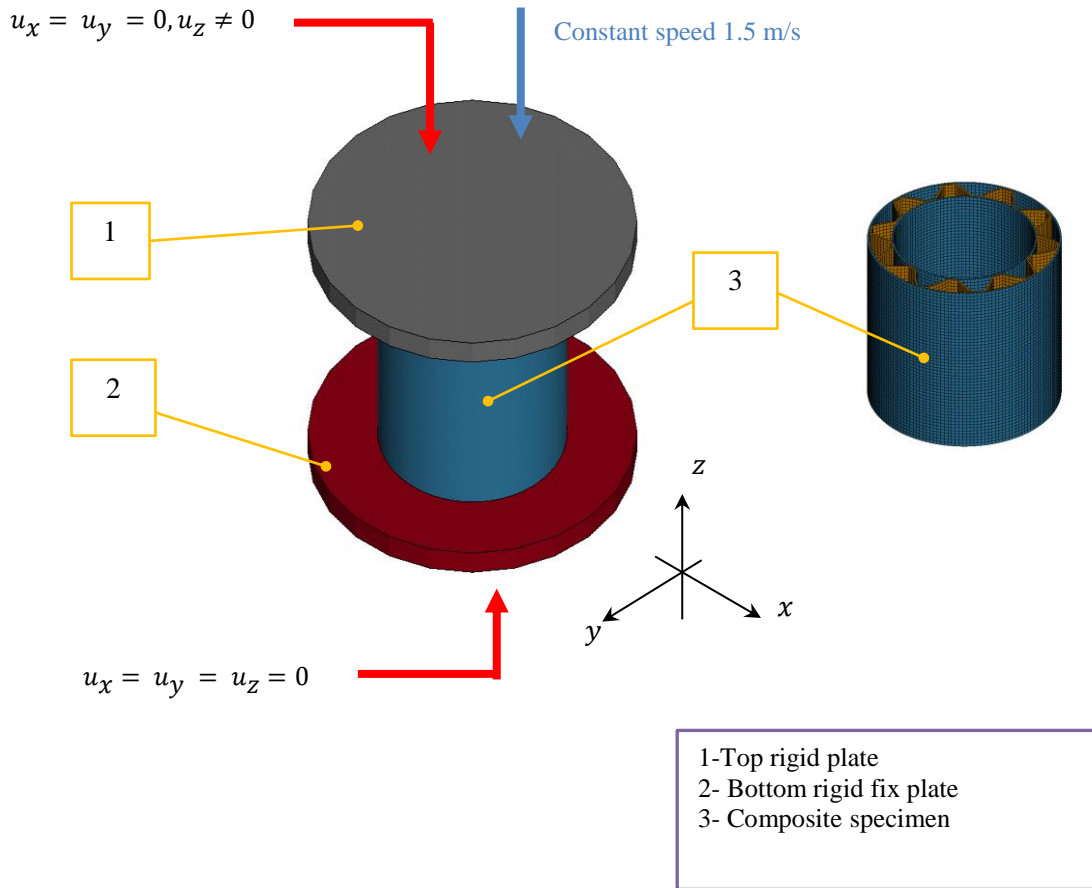


Figure 2. FEM model

In the study, the element mesh size was taken as 2 mm x 2 mm considering the analysis time, efficiency, specimen thickness and 8-node brick solid element (*ELFORM1*) was used as the element type. It is the most commonly used element type as a solid model in the literature [27]. Figure 2 shows the compression test finite element model of cylindrical sandwich composites. The specimens are placed between the upper and lower rigid plates. The lower plate motions were kept constant in the *x*, *y* and *z* directions, while the upper plate was allowed to move freely in the *z* direction. The compression speed of the top plate was set as 1.5 m/s considering the processing time and efficiency. "CONTACT_AUTOMATIC_SURFACE_TO_SURFACE" contact card was defined between the top plate and the composite. 'CONTACT_AUTOMATIC_SINGLE_SURFACE' contact card was used to prevent interference between the elements in the composite specimens.

Both dynamic and static friction coefficients were defined as 0.2 [27]. For the quasi-static compression test of the composite specimens, the upper plate was moved in the z direction using the BOUNDARY_PRESCRIBED_MOTION_SET card. The bottom plate was assigned as fixed. To avoid dynamic effect, the initial speed was increased linearly starting from 0 up to 1.5 m/s and then kept constant. Different core structures shown in Figure 3 were used in the study. The diameter x length dimensions of the axial corrugated core specimens are 100 mm x 100 mm while the circular core specimens are 115 mm x 140 mm. The unit cell dimensions and weights of these core structures are given in Table 1. Cell widths and cell heights are the same. In order to make their weights the same, it was tried to equalize their weights by reducing the material thickness and entering their densities in the finite element program. The maximum difference between the weights is 1.65%. Therefore, a healthy comparison can be made under the same boundary conditions by considering the cell width, cell height and weights equal. From each figure given in Table 1, two different corrugated core structures, axial and circular, were formed by bending. It is shown in Figure 4 in stages. The specimens used in the study and the pictures of the core structures are given in Table 2.

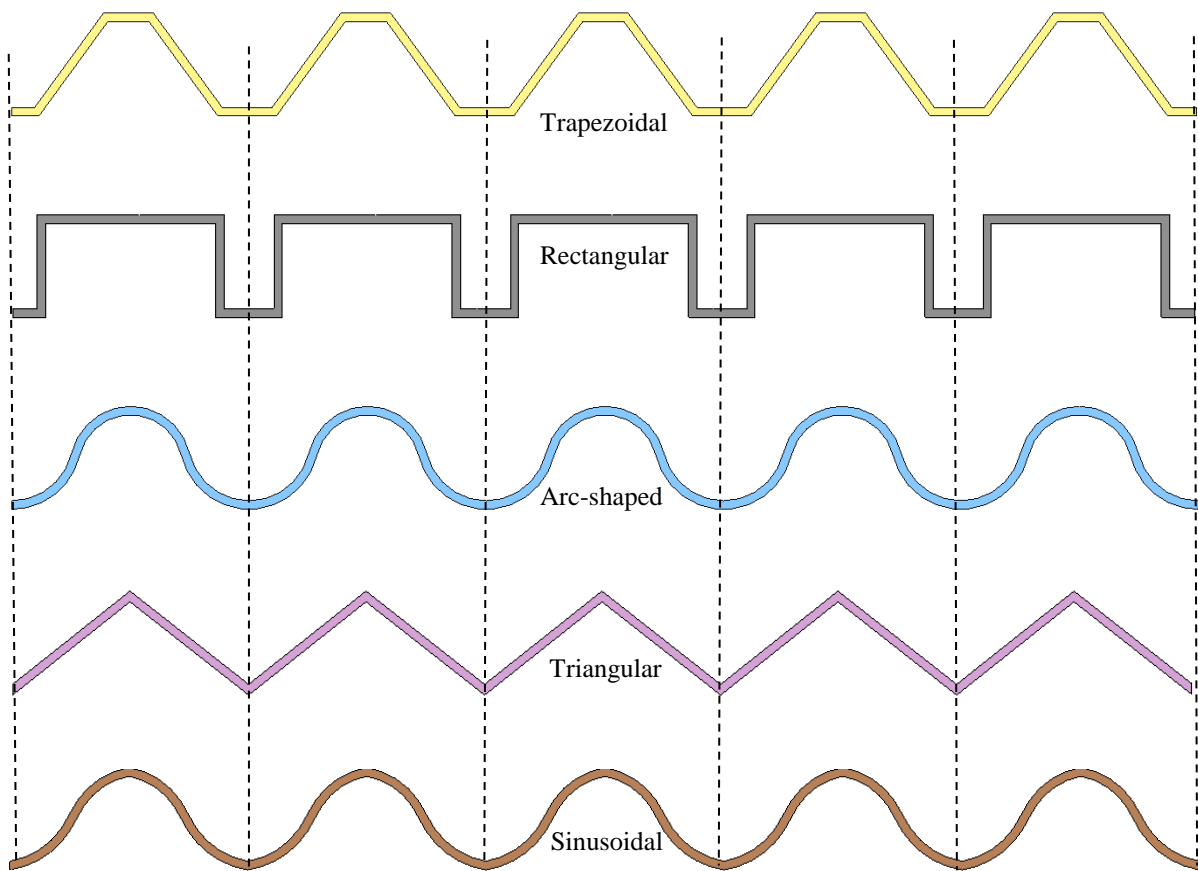


Figure 3. Different corrugated core structures used in the research

Table 1. Dimensions and masses of corrugated core structures

Cell name	Cell Shape	Axial Mass (gr)	Circular Mass(gr)
Trapezoidal		145.778	231.931
Rectangular		145.879	220.000
Arc-shaped		144.997	230.559
Triangular		146.666	223.775
Sinusoidal		147.394	223.775

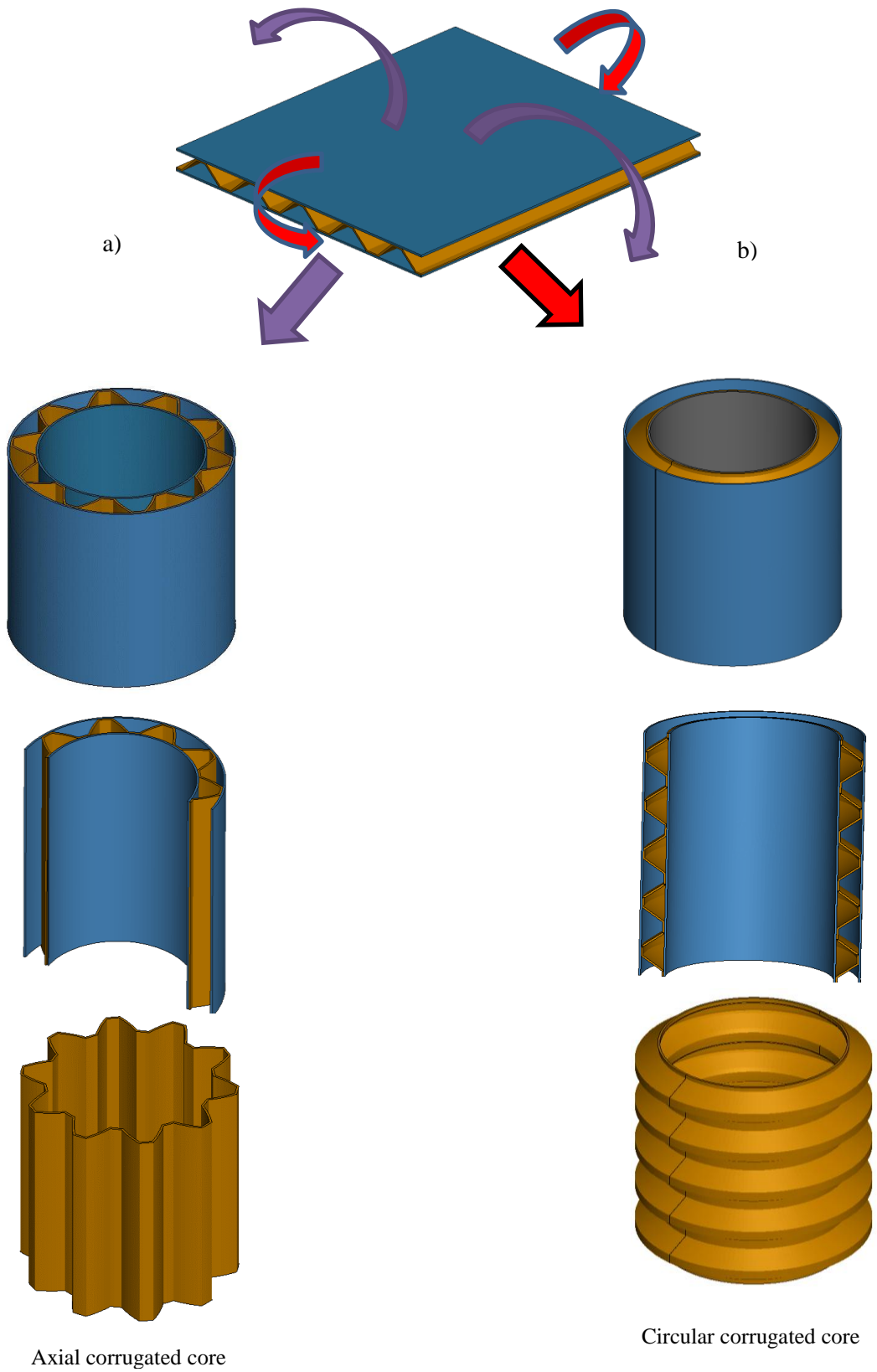
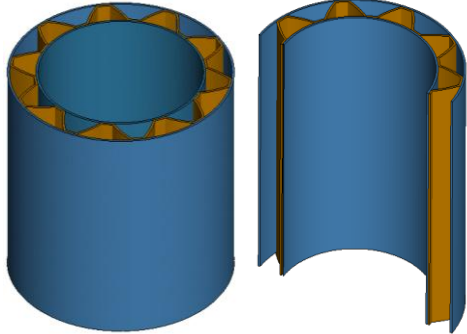
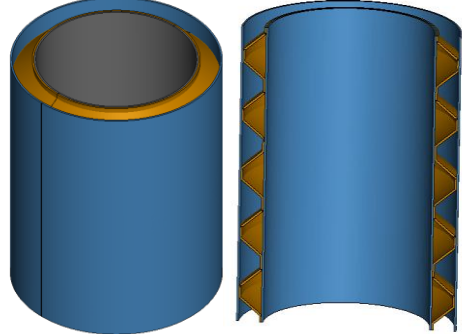
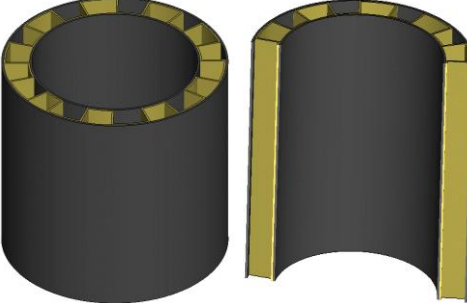
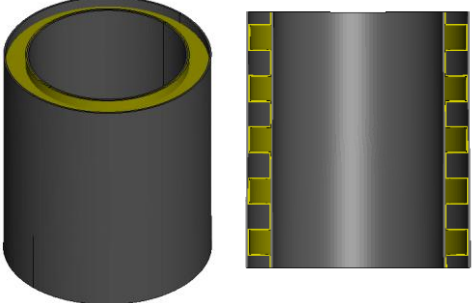
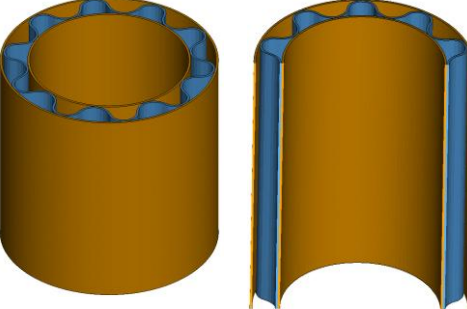
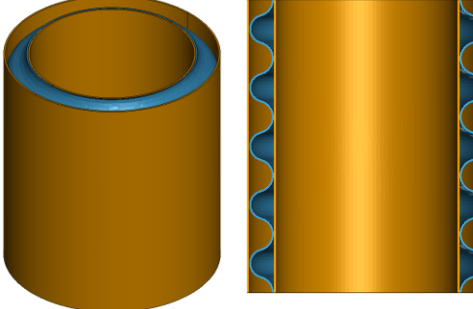
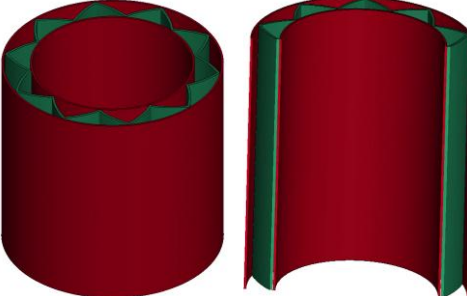
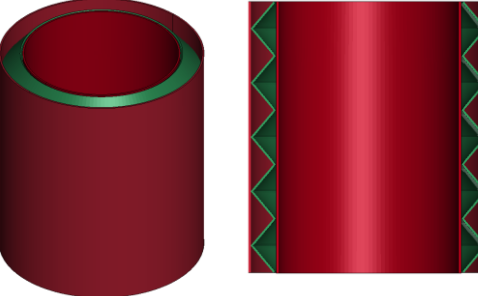
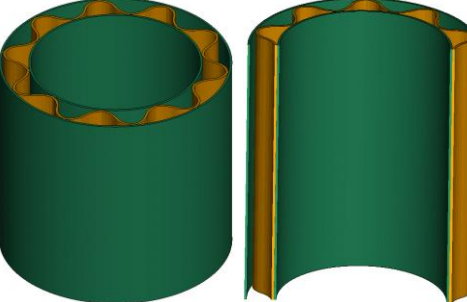
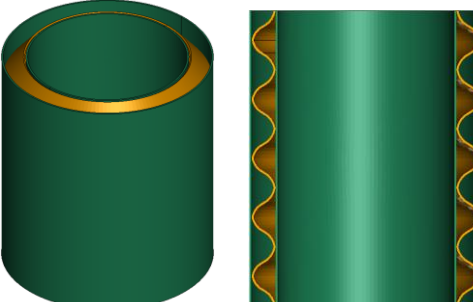


Figure 4. Specimens (a) axial corrugated core, (b) circular corrugated core

Table 2. Compression specimens

Specimens	Axial corrugated core	Circular corrugated core
Trapezoidal		
Rectangular		
Arc-shaped		
Triangular		
Sinusoidal		

2.2. Material models

It is very important to determine the material model in *LS DYNA* finite elements. Because the strength values and failure deformations in the structure exposed to load are realized according to the determined criterion. There are many material models to define the composite structure in *LS DYNA*. Among these, the most widely used material models by researchers are *MAT 22*, *MAT 54/55*, *MAT 58*, *MAT 59* and *MAT 162*. The main difference between these material models is the failure criterion and material behavior as a result of loading. Strength parameters (transverse compressive strength, longitudinal compressive strength, transverse tensile strength and shear strength) are used to determine the failure to the material. is needed. Among these material models, the *MAT-22* material model based on the Hashin failure criterion, which is the most widely used in the literature, was used in the study. When defining the *MAT54* material model, 25 input values are needed. Of these, 15 parameters are material constants given in Table 3. The remaining 10 numerical parameters (shown in Table 4) are obtained by calibrating through finite elements [28].

Table 3. Mechanical parameters of the CFRP composite [27]

Symbol	Property	Value	Unit
ρ	Density	1500	kg/m ³
E_a, E_b	Young modulus <i>a</i> and <i>b</i> direction	43.7	GPa
E_c	Young modulus in <i>c</i> direction	15	GPa
ν_{ab}	Poisson's ratio in <i>ab</i> plane	0.21	-
ν_{bc}	Poisson's ratio in <i>bc</i> plane	0.21	-
ν_{ca}	Poisson's ratio in <i>ca</i> plane	0.21	-
G_{ab}	Shear modulus in <i>ab</i> plane	14.18	GPa
G_{bc}	Shear modulus in <i>bc</i> plane	14.65	GPa
G_{ca}	Shear modulus in <i>ca</i> plane	14.65	GPa
S_{aT}	Tensile strength <i>a</i> direction	0.589	GPa
S_{aC}	Compressive strength <i>a</i> direction	0.1096	GPa
S_{bT}	Tensile strength <i>b</i> direction	0.589	GPa
S_{bC}	Compressive strength <i>b</i> direction	0.1096	GPa
S_{ab}	Shear strength in <i>ab</i> plane	0.1082	GPa

Table 4. Failure parameters of the CFRP composite.

Symbol	Description	Unit
<i>DFAILM</i>	Transverse matrix failure strain experimental	0.0
<i>DFAILS</i>	Shear failure strain experimental	0.0
<i>DFAILT</i>	Tensile fiber failure strain experimental	0.0
<i>DFAILC</i>	Compressive fiber failure strain experimental	0.0
<i>TFAIL</i>	Timestep for element deletion computational	0.16
<i>Alpha</i>	Shear stress parameter failure dependent	0.0
<i>Soft</i>	Strength reduction factor failure dependent	0.7
<i>FBRT</i>	Reduction factor for X_t failure dependent	1
<i>YCFAC</i>	Reduction factor for X_c failure dependent	3
<i>EFS</i>	Efective failure strain computational	0.90

2.3. Modeling of adhesive layer

In sandwich structures, the core structure and the upper and lower facesheets structures need to be bonded to each other. Different types of adhesives such as resin or Araldite 55 are used to ensure this bonding. These adhesives are applied to the contact points of the core and facesheet structures and adhesion is achieved by waiting for a certain period of time at room temperature. This adhesion is of great importance in absorbing the force coming to the upper facesheet in case of impact and distributing it homogeneously to other areas. Therefore, this adhesion and separation due to impact is based on some mechanical principles. In the literature, it is characterized as CZM with a bilinear traction-separation law. This law is based on the application of 3 independent parameters. The traction t_0 , between the layers when the force is applied, the separation distance δ_0 when the failure starts and the G_c under this curve. After the impact occurs, the separation between the layers occurs according to this principle (Figure 5).

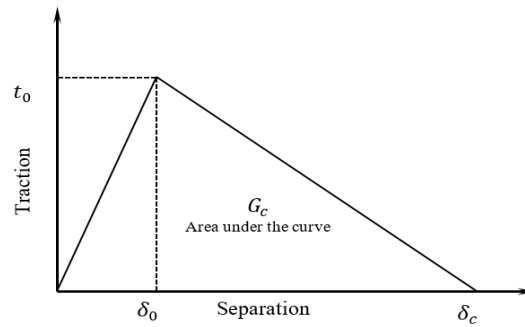


Figure 5. Bilinear traction-separation law

The connection between the core and the facesheet can be achieved in two ways in FEM. First, it can be achieved by assigning a thin film material here. Or instead, this adhesion can be achieved by providing a connection between the surfaces. Dogan et al [29] determined that this method is effective instead of using intermediate material. In this study, The CONTACT_AUTOMATIC SURFACE TO SURFACE TIEBREAK contact card was used to bond the top and bottom cover to the core material in between. While adhesion is achieved here, separations occur based on the Bilinear traction-separation law. With this contact card, the nodes making contact in the beginning connect with each other according to the following criterion.

$$\left(\frac{|\sigma_n|}{NFLS}\right)^2 + \left(\frac{|\sigma_s|}{SFLS}\right)^2 \geq 1 \quad (5)$$

Here, while σ_n and σ_s are the current normal and shear stresses, *NFLS* and *SFLS* are respectively the interface and shear strength. When the condition of Equation (5) is met, interface node stress is decreased to zero and the connection between the nodes is released. The contact parameters for Araldite 2015, which was used as the adhesive material in this research, are provided in Table 5.

Table 5. Cohesive parameters between core and face sheets interfaces [30]

Contact Tiebreak Variable	Description	Value	Units
<i>NFLS</i>	Peak traction in normal direction	21.63x10 ⁹	Pa
<i>SFLS</i>	Peak traction in tangential direction	17.9x10 ⁹	Pa
<i>PARAM</i>	Exponent of mixed-mode criteria	1	-
<i>ERATEN</i>	Energy release rate for Mode I	430	N/m
<i>ERATES</i>	Energy release rate for Mode II	4700	N/m
<i>CT2CN</i>	Ratio of tangential stiffness to normal stiffness	1	-
<i>CN</i>	Normal stiffness	8080	Pa/m

2.4. MAT_54-55: Enhanced composite failure model

It is the most widely used material model in the analysis of composite structures. In the material model, it is assumed that the material is orthotropic and linear elastic in the absence of any failure. In this model, *MAT 54* failure criterion was proposed by *Chang* and *MAT 55* failure criterion was proposed by *Tsai-Wu*. The operating principle of this material model is the same as that of *MAT 22*, but additionally includes a compression failure mode. The *Chang–Chang criterion (MAT -54)* is given below [27];
 Tensile fibre ($\sigma_{11} > 0$).

$$\left(\frac{\sigma_{11}}{S_1}\right)^2 + \bar{\tau} = 1 \quad (6)$$

All moduli and Poisson's ratios are set to zero when the tensile fibre failure criteria are met, that is $E_1 = E_2 = G_{12} = \nu_{12} = \nu_{21} = 0$. All the stresses in the elements are reduced to zero, and the element layer has failed.

Failure mode for compressive fibre ($\sigma_{11} > 0$),

$$\left(\frac{\sigma_{11}}{S_{12}}\right)^2 = 1 \quad (7)$$

Failure mode for tensile matrix ($\sigma_{11} > 0$),

$$\left(\frac{\sigma_{22}}{S_2}\right)^2 + \bar{\tau} = 1 \quad (8)$$

Failure mode for compressive matrix

$$\left(\frac{\sigma_{22}}{2S_{12}}\right)^2 + \left[\left(\frac{C_2}{2S_{12}}\right) - 1\right] \frac{\sigma_{22}}{C_2} + \bar{\tau} = 1 \quad (9)$$

Where E_1 and E_2 are the longitudinal and transverse elastic moduli, respectively, G_{12} is the shear modulus, ν_{12} and ν_{21} are the in-plane Poisson's ratios.

3. Results and Discussion

The force-displacement plots of axial corrugated core and circular corrugated core cylindrical sandwich composite structures under axial load are shown in Figure 6a and 6b respectively. Figure 6a shows the graphs of five different axial corrugated core structures as well as the without core specimen after compression test. The PCF value for the without core specimen is 24.5 kN while the MCF value is 4.22 kN. Core was added to this without core specimen in five different configurations and compression simulations were performed again. The aim here is to increase the crashworthiness performance without increasing the weight too much. When the graphs are analyzed, the load for all specimens increased to the maximum point and then decreased [27]. It is seen that the specimen with the highest PCF value is the specimen with Trapezoidal core.

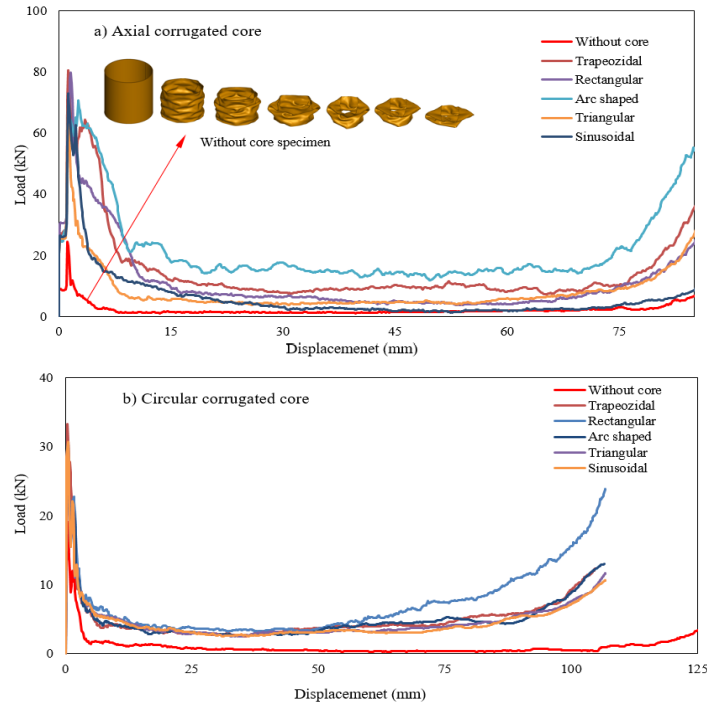


Figure 6. Force-displacement results for a) Axial corrugated core and

It was observed for all specimens that the force value increased to the maximum point, the force decreased slightly and then increased again. The reason for this is that fluctuations occur on the structure due to the load. After the load drop, the force value continued at a certain value until the end of the crushing test [31]. This value is obtained in parallel with the MCF value. According to this, it is seen that the MCF value of the specimen with Arc shaped core structure is higher than the others. This is because these force values are averaged when determining the average force value. Since densification occurred in the material structure due to the effect of crushing force in the last section, the load value increased [32].

Figure 6b shows the graphs of five different circular corrugated core structures and without core specimen after compression test. The PCF value for the without core specimen is 19.11 kN while the MCF value is 1 kN. When the graph is analyzed, it is seen that the force reached the maximum point and then the force value decreased sharply. Then, it was observed that crushing occurred at an average force value. In the last section, it was determined that an increase in the load value occurred due to the densification situation. It is noticed that the last part of the Without core specimen has a later densification effect unlike the other specimens. The reason for this is the absence of core structure and the amount of material for densification is less than the other specimens.

Figure 7 shows the PCF and EA results for sandwich composites with axial and circular corrugated core structure after compression test. When the PCF values are examined in Figure 7a, the maximum peak load value was obtained in the axial corrugated core Trapezoidal specimen with 80.53 kN. The minimum was 26.69 kN for the Arc shaped specimen. Accordingly, the PCF value for the axial corrugated core increased by a maximum of 2.28 times compared to the without core specimen. When the maximum PCF value obtained from the circular corrugated core specimen is compared with the without core specimen, an increase of 0.74 times is observed. When the EA values are analyzed in Figure 7b, the maximum EA value among all specimens was obtained as 1626.2 J for the axial corrugated Arc shaped core specimen. The minimum value occurred in the circular sinusoidal specimen with 452 J. When the energy absorption values of with core and without core specimens are compared, the maximum value is increased 3.82 times for axial core structures and 5.71 times for circular core.

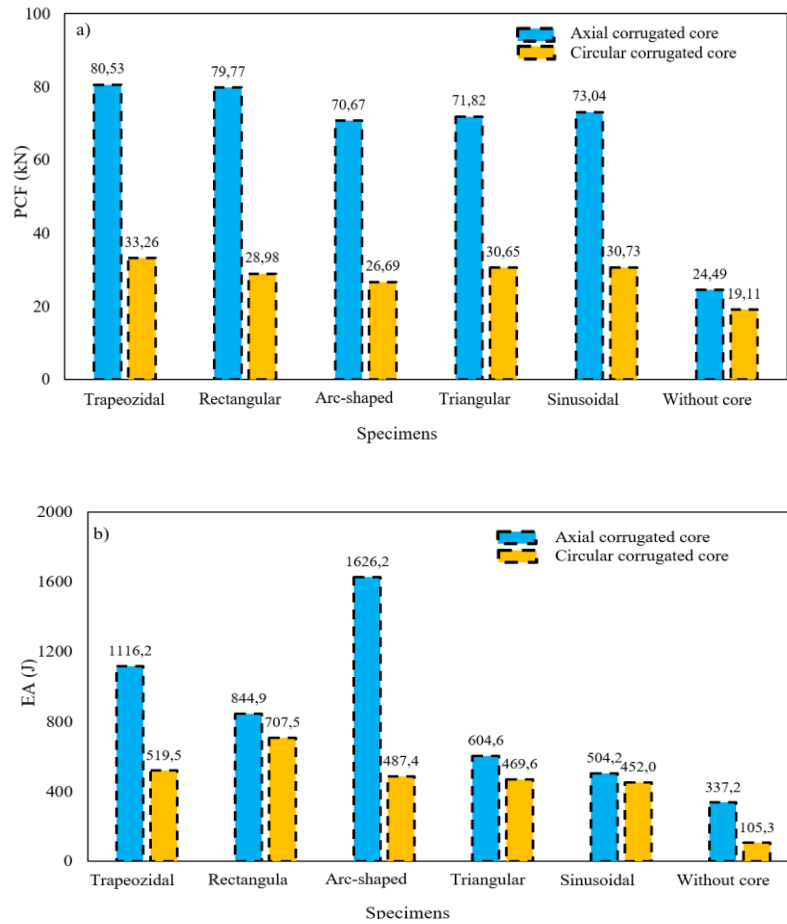


Figure 7. a) PCF and b) EA results

Although the EA value increases by using circular core, the maximum value remains low when compared to axial core. But what is important here is the SEA value. That is, the energy absorbed per weight. The results regarding this will be given in the following section.

At the end of the compression test, many results are obtained about the mechanical structure and strength of the material. These results provide vital information about the structure and provide researchers with important information about the behavior of the structure under load and its strength limits [33]. The PCF value is an important parameter for assessing crashworthiness [6]. But the most important parameter affecting the energy absorption capacity is MCF. Because the energy absorption value is calculated from the area under the MCF. In some cases, the PCF value may be too high while the MCF value may be too low. Therefore, the higher the MCF value, the higher the energy absorption capacity. Here the CFE value expresses the efficiency between these two. It should be as high as possible to control the energy absorption efficiency without any failure during an accident [34]. Figure 8a-c shows the SEA, MCF and CFE results of the specimens at the end of the compression simulation. When the SEA results in Figure 8a are examined, the axial corrugated arc shaped core specimen is the sandwich structure with the highest SEA value with 11.2 J/g, while the circular sinusoidal corrugated core with 2.02 J/g is the lowest sandwich structure. By using axial corrugated core structure, the maximum SEA value increased by 65% compared to without core structure. By using circular corrugated core structure, the maximum SEA value increased by 136.7% compared to without core structure. When the MCF results are analyzed in Figure 8b, the MCF value of the axial corrugated arc shaped core specimen is the highest with 20.33 kN, while the circular sinusoidal specimen has the lowest value with 4.3 kN. Already in Figure 6, these results are clearly seen in the graphs. Figure 8c shows the crushing force efficiency (CFE) results. Here, the highest CFE value means that the higher the energy absorption capacity in case of accident or loading. In other words, the

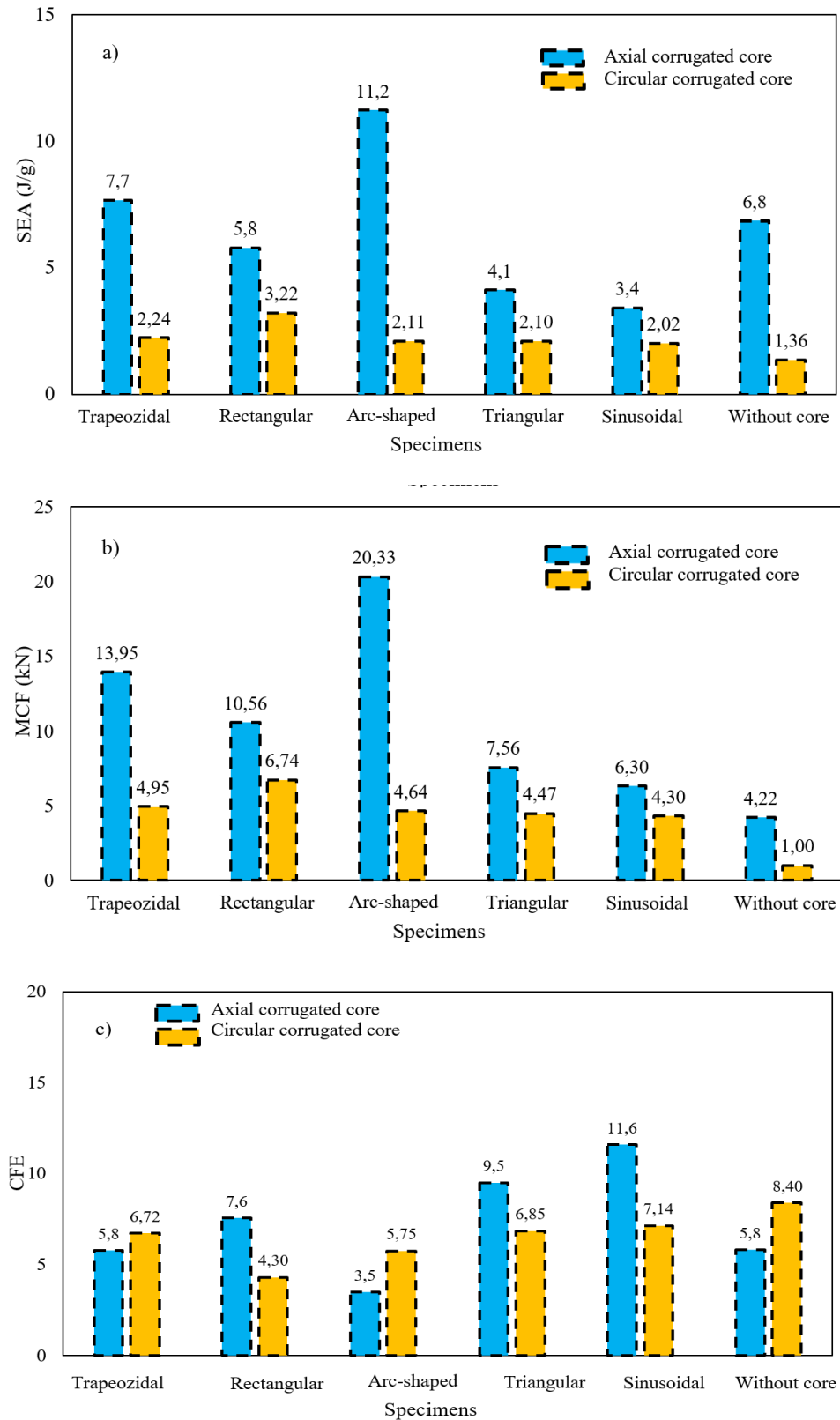


Figure 8. a) SEA and b) MCF and c) CFE results

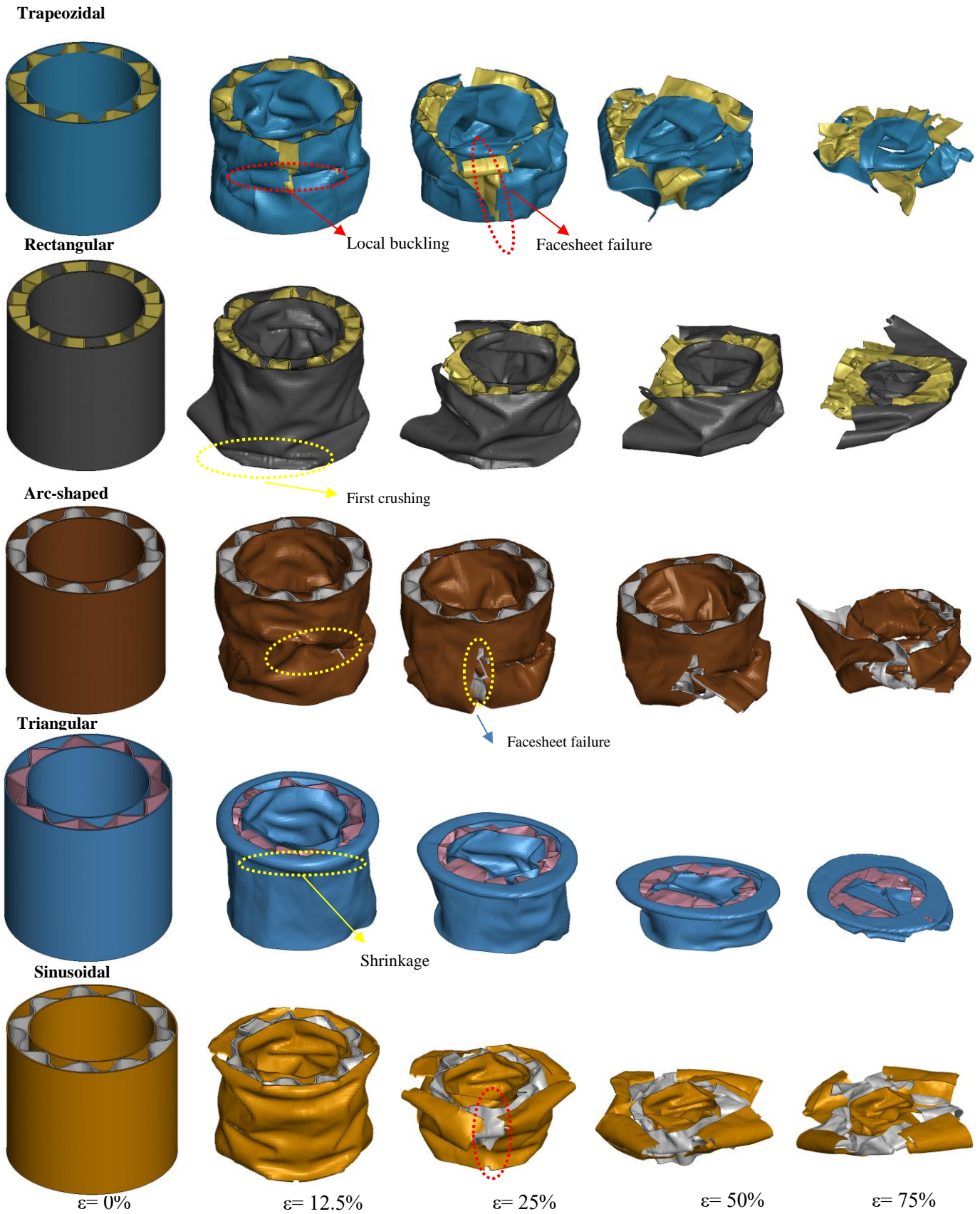


Figure 9. Deformations after compression test for axial corrugated core

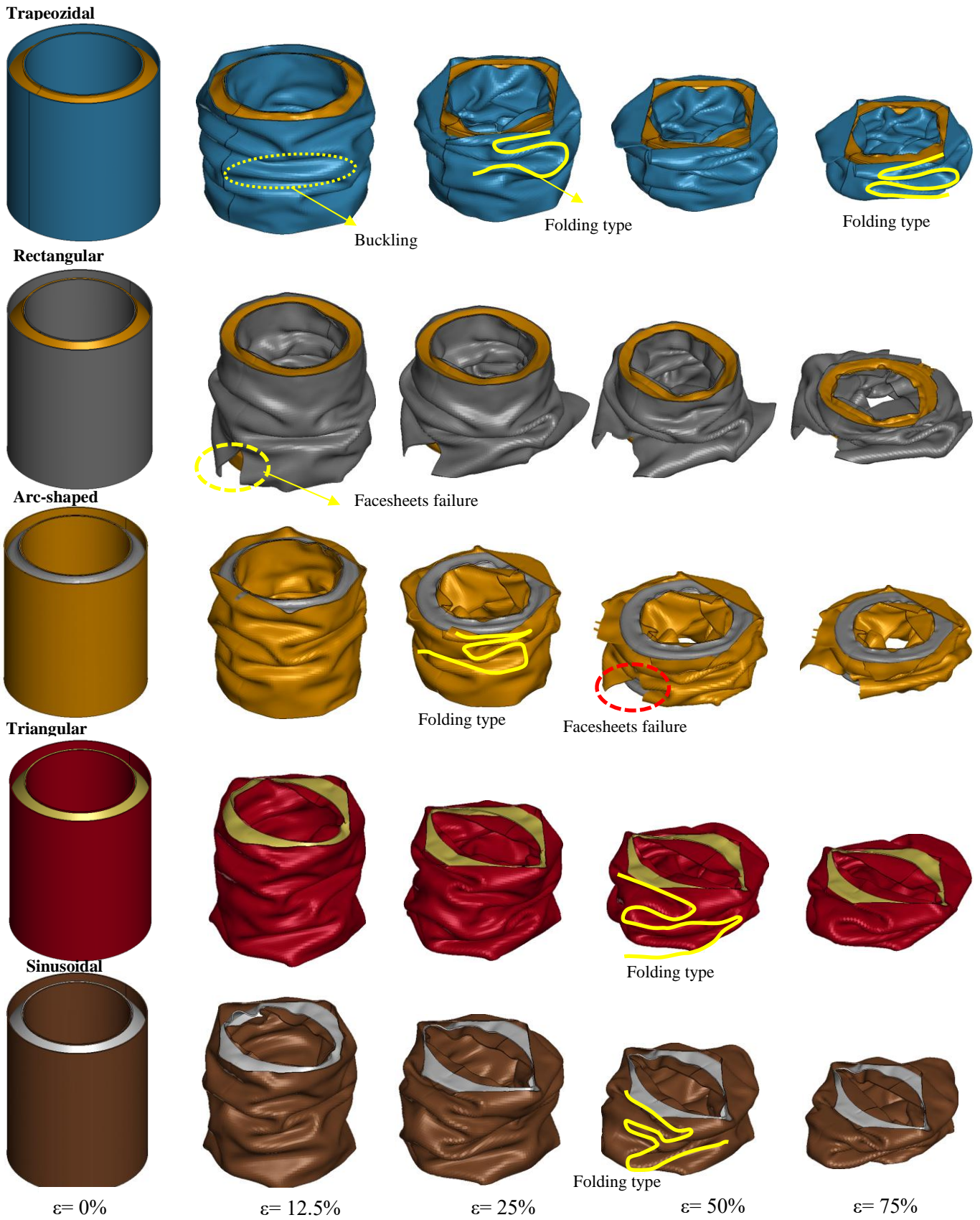


Figure 10. Deformations after compression test for circular corrugated core

CFE value is always the highest value, which is a desired result for researchers working in this field. Among the axial core and circular core specimens, the CFE value of the sinusoidal core specimen was the highest. The lowest was Arc-shaped for Axial core and rectangular core for circular core.

The deformations of axial and circular corrugated sandwich composite structures are given in Figure 9 and Figure 10 respectively. After the load is applied to the sandwich structure, it gradually increases with displacement and no significant deviation in linear behavior is observed until the peak [18]. Here, the structure can resist up to a point while the load increases [35]. Then a sharp drop in load occurs. This is the scenario that generally occurs when any specimen is tested in compression [36]. Depending on the type of specimen used, the peak crushing force value and the average load amount with sudden load drop may vary.

Figure 9 shows the deformations of axial core sandwich structures. Due to the difference in the structural configuration of the five different specimens, the failure types or initial failures are different from each other. In the trapezoidal specimen, buckling failure and facesheet failure were observed in the center of the specimen due to loading. In Rectangular, the first failure started at the base of the specimen, while both buckling and facesheet failure were observed in the arc shaped specimen. In the triangular specimen, the specimen was folded with shrinkage failure, while in the sinusoidal specimen, large deformation occurred in the failure. Figure 10 shows the deformation pictures of circular core sandwich structures. When the post-compression deformations of all specimens were examined, it was seen that the deformation rate was higher in axial core structures. As the compression rate increased, the folding rate also increased. While some specimens showed face sheet failure (rectangular and arc-shaped), most of them were deformed by folding.

4. Conclusions

In this study, the crushing performance of sandwich composite structures with different core configurations (Trapezoidal, Rectangular, Arc-shaped, Triangular and Sinusoidal) under quasi-static compression loading was determined using the finite element method. The numerical model was applied by performing *progressive failure analysis* with *MAT-54* material model in *LS DYNA* finite element model. In the study, the performances (Peak force (PF), Mean crushing force (MCF), Crushing force efficiency (CFE) and specific energy absorption (SAE)) and failure types for different core structures and core orientations (axial-circular) were determined. Based on the data obtained at the end of the study, the results can be summarized as follows:

- Among the five different specimens, the Trapezoidal specimen with axial corrugated core has the highest PCF value while the Arc shaped specimen with circular core has the lowest PCF value. Accordingly, the PCF value for the axial corrugated core increased by a maximum of 2.28 times compared to the without core specimen. The maximum PCF value obtained from the circular corrugated core specimen increased by 0.74 times compared to the without core specimen.
- When the EA values were analyzed, the maximum EA value among all specimens was the axial corrugated Arc shaped specimen, while the minimum value was the circular sinusoidal specimen. When the energy absorption values of with core and without core specimens are compared, the maximum energy absorption value for axial core structures increased by 3.82 times and 5.71 times for circular core.
- Using the axial corrugated core, the energy absorption value increased by a maximum of 3.82 times, while with the circular corrugated core, the energy absorption value increased by a maximum of 5.72 times.
- Axial corrugated arc shaped core specimen was the sandwich structure with the highest SEA value, while circular sinusoidal corrugated core was the sandwich structure with the lowest SEA value. By using the axial corrugated core structure, the maximum SEA value increased by 65% compared to the without core structure. By using circular corrugated core structure, the maximum SEA value increased by 136.7% compared to without core structure.
- The MCF value of the axial corrugated arc shaped core specimen was the highest while the circular sinusoidal specimen had the lowest value. Among the axial core and circular core specimens, the

CFE value of the sinusoidal core specimen was the highest. The lowest value was Arc-shaped for axial core and rectangular core for circular core.

- The deformation behavior of corrugated sandwich structures mainly depends on the core type. Folding shape, bending type, facesheets failure differ according to the core type.
- This numerical research has the potential to make a great contribution to the literature by being supported experimentally in future studies.

Nomenclature

CFE: Crushing force efficiency

CZM: Cohesive Zone Model

EA: Energy absorption

MCF: Mean crushing force

PCF: Peak-crushing force

SEA: Specific energy absorption

5. Author Contribution Declaration

In the study carried out, Author contributed to the formation of the idea, design and literature review, evaluation of the results, procurement of the materials used and examination of the results, and checking the article in terms of spelling and content.

6. Ethics Committee Approval and Conflict of Interest Declaration

There is no need to obtain ethics committee permission for the article prepared. There is no conflict of interest with any person/institution in the prepared article.

7. References

- [1] B. Kiyak, and M. O. Kaman, "Mechanical properties of new-manufactured sandwich composite having carbon fiber core," *J. Compos. Mater.*, vol. 53, no. 22, pp. 3093-3109, 2019.
- [2] M. O. Kaman, M. Y. Solmaz, and K. Turan, "Experimental and numerical analysis of critical buckling load of honeycomb sandwich panels," *J. Compos. Mater.*, vol. 44, no. 24, pp. 2819-2831, 2010.
- [3] M. Albayrak, M. O. Kaman, and I. Bozkurt, "Experimental and Numerical Investigation of the Geometrical Effect on Low Velocity Impact Behavior for Curved Composites with a Rubber Interlayer," *Appl. Compos. Mater.*, vol. 30, no. 2, pp. 507-538, 2023.
- [4] M. Albayrak, M. O. Kaman, and I. Bozkurt, "The effect of lamina configuration on low-velocity impact behaviour for glass fiber/rubber curved composites," *J. Compos. Mater.*, vol. 57, no. 11, pp. 1875-1908.
- [5] Q. Zheng, D. Jiang, C. Huang, X. Shang, and S. Ju, "Analysis of failure loads and optimal design of composite lattice cylinder under axial compression," *Compos. Struct.*, vol. 131, pp. 885-894, Nov. 2015.
- [6] S. Hou, S. Zhao, L. Ren, X. Han, and Q. Li, "Crashworthiness optimization of corrugated sandwich panels," *Mater. Des.*, vol. 51, pp. 1071-1084, 2013.
- [7] Y. Hu, W. Li, X. An, and H. Fan, "Fabrication and mechanical behaviors of corrugated lattice truss composite sandwich panels," *Compos. Sci. Technol.*, vol. 125, pp. 114-122, 2016.
- [8] W. He, J. Liu, S. Wang, and D. Xie, "Low-velocity impact response and post-impact flexural behaviour of composite sandwich structures with corrugated cores," *Compos. Struct.*, vol. 189, pp. 37-53, Apr. 2018.
- [9] J. Liu, W. He, D. Xie, and B. Tao, "The effect of impactor shape on the low-velocity impact behavior of hybrid corrugated core sandwich structures," *Compos. B Eng.*, vol. 111, pp. 315-331, 2017.
- [10] J. Xiong, R. Ghosh, L. Ma, A. Vaziri, Y. Wang, and L. Wu, "Sandwich-walled cylindrical shells with lightweight metallic lattice truss cores and carbon fiber-reinforced composite face sheets," *Compos. Part A Appl. Sci. Manuf.*, vol. 56, pp. 226-238, Jan. 2014.
- [11] T. Zhao et al., "An experimental investigation on low-velocity impact response of a novel corrugated sandwiched composite structure," *Compos. Struct.*, vol. 252, no. June, p. 112676, 2020.
- [12] V. Crupi, E. Kara, G. Epasto, E. Guglielmino, and H. Aykul, "Prediction model for the impact response of glass fibre reinforced aluminium foam sandwiches," *Int. J. Impact Eng.*, vol. 77, pp. 97-107, 2015.
- [13] R. Mohammed, F. Zhang, B. Sun, and B. Gu, "Finite element analyses of low-velocity impact failure of foam sandwiched composites with different ply angles face sheets," *Mater. Des.*, vol. 47, pp. 189-199, 2013.
- [14] P. B. Su et al., "Axial compressive collapse of ultralight corrugated sandwich cylindrical shells," *Mater. Des.*, vol. 160, pp. 325-337, Dec. 2018.
- [15] J. Xiong, A. Vaziri, R. Ghosh, H. Hu, L. Ma, and L. Wu, "Compression behavior and energy absorption of carbon fiber reinforced composite sandwich panels made of three-dimensional honeycomb grid cores," *Extreme Mech. Lett.*, vol. 7, pp. 114-120, 2016.
- [16] L. Yan, P. Su, Y. Han, and B. Han, "Effects of Aluminum Foam Filling on Compressive Strength and Energy Absorption of Metallic Y-Shape Cored Sandwich Panel," *Metals*, vol. 10, no. 12, p. 1670.
- [17] H. Fan, L. Yang, F. Sun, and D. Fang, "Compression and bending performances of carbon fiber reinforced lattice-core sandwich composites," *Compos. Part A Appl. Sci. Manuf.*, vol. 52, pp. 118-125, 2013.
- [18] Z. Jia Zhang et al., "Mechanical behaviors and failure modes of sandwich cylinders with square honeycomb cores under axial compression," *Thin-Walled Struct.*, vol. 172, p. 108868, Mar. 2022.
- [19] Q. Wu et al., "Failure of carbon fiber composite sandwich cylinders with a lattice core under axial compressive loading," *Compos. Part A Appl. Sci. Manuf.*, vol. 155, p. 106812, Apr. 2022.
- [20] L. Ge, H. Zheng, H. Li, B. Liu, H. Su, and D. Fang, "Compression behavior of a novel sandwich structure with bi-directional corrugated core," *Thin-Walled Struct.*, vol. 161, p. 107413.

- [21] X. Zhu et al., "Experimental study and modeling analysis of planar compression of composite corrugated, lattice and honeycomb sandwich plates," *Compos. Struct.*, vol. 308, p. 116690, Mar. 2023.
- [22] X. Zhu et al., "Compression responses of composite corrugated sandwich square tube: Experimental and numerical investigation," *Thin-Walled Struct.*, vol. 169, p. 108440, Dec. 2021.
- [23] L. Chen et al., "Compressive response of multi-layered thermoplastic composite corrugated sandwich panels: Modelling and experiments," *Compos. B Eng.*, vol. 189, p. 107899, May 2020.
- [24] B. Han, K. Qin, B. Yu, B. Wang, Q. Zhang, and T. J. Lu, "Honeycomb–corrugation hybrid as a novel sandwich core for significantly enhanced compressive performance," *Mater. Des.*, vol. 93, pp. 271-282, Mar. 2016.
- [25] H. JO., *LS-DYNA Keyword User's Manual Volume II Material Models, Version 971*. Livermore Software Technology Corporation, 2017.
- [26] S. Murakami, *Continuum failure mechanics: a continuum mechanics approach to the analysis of failure and fracture*.
- [27] I. Bozkurt, M. O. Kaman, and M. Albayrak, "Low-velocity impact behaviours of sandwiches manufactured from fully carbon fiber composite for different cell types and compression behaviours for different core types," *Mater. Prüfung/Materials Testing*, vol. 65, no. 9, pp. 1349-1372, 2023.
- [28] P. Feraboli, B. Wade, F. Deleo, M. Rassaian, M. Higgins, and A. Byar, "LS-DYNA MAT54 modeling of the axial crushing of a composite tape sinusoidal specimen," *Compos. Part A Appl. Sci. Manuf.*, vol. 42, no. 11, pp. 1809-1825, Nov. 2011.
- [29] F. Dogan, H. Hadavinia, T. Donchev, and P. S. Bhonge, "Delamination of impacted composite structures by cohesive zone interface elements and tiebreak contact," *Cent. Eur. J. Eng.*, vol. 2, no. 4, pp. 612-626, 2012.
- [30] I. Bozkurt, M. O. Kaman, and M. Albayrak, "Experimental and numerical impact behavior of fully carbon fiber sandwiches for different core types," *J. Braz. Soc. Mech. Sci. Eng.*, vol. 46, no. 5, p. 318, May 2024.
- [31] W. Liu, S. Wang, J. Bu, and X. Ding, "An analytical model for the progressive failure prediction of reinforced thermoplastic pipes under axial compression," *Polym. Compos.*, vol. 42, no. 6, pp. 3011-3024, Jun. 2021.
- [32] H. Zhu, P. Wang, D. Wei, J. Si, and Y. Wu, "Energy absorption of diamond lattice cylindrical shells under axial compression loading," *Thin-Walled Struct.*, vol. 181, p. 110131, Dec. 2022.
- [33] I. Bozkurt, "Effect of geometric configurations and curvature angle of corrugated sandwich structures on impact behavior," *Polym. Compos.*, pp. 1-24, 2024.
- [34] E. Demirci and A. R. Yıldız, "An experimental and numerical investigation of the effects of geometry and spot welds on the crashworthiness of vehicle thin-walled structures," vol. 60, no. 6, pp. 553-561, 2018.
- [35] İ. Bozkurt, "Numerical Investigation of the Effects of Impactor Geometry on Impact Behavior of Sandwich Structures," *Bitlis Eren Univ. J. Sci. Tech.*, Sep. 2024.
- [36] F. Taheri-Behrooz, R. A. Esmael, and F. Taheri, "Response of perforated composite tubes subjected to axial compressive loading," *Thin-Walled Struct.*, vol. 50, no. 1, pp. 174-181, Jan. 2012.



Bitlis Yöresindeki Bazalt ve Kireçtaşı Agregalarının Parçalanma ve Aşınma Direncinin Araştırılması ve MgSO₄ ile Yassılık İndeksi Değerleri Arasındaki İlişkinin İncelenmesi

Alev AKILLI EL ^{1*}

¹İnşaat Bölümü, Teknik Bilimler Meslek Yüksekokulu, Bitlis Eren Üniversitesi, Bitlis, Türkiye.
aakilli@beu.edu.tr

Geliş Tarihi: 22.04.2024
Kabul Tarihi: 20.10.2024

Düzeltilme Tarihi: 21.07.2024

doi: <https://doi.org/10.62520/fujece.1472097>
Araştırma Makalesi

Alıntı: A. A. El, “Bitlis yöresindeki bazalt ve kireçtaşı agregalarının parçalanma ve aşınma direncinin araştırılması ve MgSO₄ ile yassılık indeksi değerleri arasındaki ilişkinin incelenmesi”, Fırat Üni. Deny. ve Hes. Müh. Derg., vol. 4, no 1, pp. 136-150, Şubat 2025.

Öz

Agregaların mekanik özellikleri asfalt karışımların performansını doğrudan etkilemektedir. Yol yapımında kullanılacak agregaların bazı önemli özelliklere sahip olması gerekir; temiz, sert, dayanıklı, aşınmaya karşı dirençli, homojen nitelikte ve zararlı maddelerden arındırılmış olmalıdır. Aşınmaya karşı direnç, agregaların kullanımını içeren mühendislik alanlarında oldukça önemli bir özelliktir. Agregaların aşınma ve parçalanma performans özelliklerini belirlemek için yapılan en yaygın mekanik deneyler Los Angeles parçalanma ve Mikro-Deval aşınma deneyidir. Bu çalışmada bazalt ve kalker agregası kullanılarak her iki agreganın aşınma ve parçalanmaya karşı dirençleri yassılık indeksi ve dona karşı dayanımları ile aralarındaki ilişkileri analiz edilmiştir. Ayrıca Los Angeles ve Mikro-deval deney prosürlerindeki parametreler değerlendirilmiştir. Deney sonuçlarına göre Mikro-Deval deneyi ile agregaların diğer fiziksel ve dayanım özellikleri ile aralarındaki ilişkinin daha tutarlı olduğu ve Mikro deval aşınma deneyinin agregaların parçalanma direncinin belirlenmesinde daha gerçekçi değerler sunduğu belirlenmiştir. Ayrıca Los Angeles deneyinde kullanılan çelik bilyelerin agregaların iç özelliklerinin parçalanma süreci üzerindeki gerçek etkisini yansıtmadığı kanısına varılmıştır.

Anahtar kelimeler: Yol agregaları, Bazalt, Kalker, Los angeles, Mikro-deval

* Yazışılan yazar



Investigation of Fragmentation and Abrasion Resistance of Basalt and Limestone Aggregates in Bitlis Region and the Relationship between $MgSO_4$ and Flatness Index Values

Alev AKILLI EL ^{1*} 

¹Civil Department, Technical Sciences Vocational School, Bitlis Eren University, Bitlis, Türkiye.
aakilli@beu.edu.tr

Received: 22.04.2024
Accepted: 20.10.2024

Revision: 21.07.2024

doi: <https://doi.org/10.62520/fujece.1472097>
Research Article

Citation: A. A. El, "Investigation of fragmentation and abrasion resistance of basalt and limestone aggregates in bitlis region and the relationship between $Mgso_4$ and flatness index values", Firat Univ. Jour. of Exper. and Comp. Eng., vol. 4, no 1, pp. 136-150, February 2025.

Abstract

The mechanical characteristics of aggregates have a direct impact on the performance of asphalt mixtures. The aggregates used in road construction must possess certain essential qualities; they should be clean, hard, durable, resistant to abrasion, of uniform quality, and free from harmful substances. Resistance to abrasion is a very important property in engineering fields involving the use of aggregates. The Los Angeles fragmentation and Micro-Deval abrasion tests are among the most commonly used mechanical tests to assess the performance characteristics of aggregates in terms of abrasion and fragmentation. This study examined the abrasion and fragmentation resistance, flatness index, and frost resistance of both basalt and limestone aggregates. The study also evaluated parameters within the Los Angeles and Micro-Deval test processes. Based on the test results, it was concluded that the Micro-Deval abrasion test exhibited a more consistent relationship with other physical and strength properties of the aggregates. Moreover, the Micro-Deval test provided more realistic values for assessing the fragmentation resistance of the aggregates. Additionally, it was concluded that the steel balls employed in the Los Angeles test did not accurately represent the true impact of the internal properties of the aggregates on the disintegration process.

Keywords: Road aggregates, Basalt, Limestone, Los angeles, Mikro-deval

*Corresponding author

1. Introduction

The demand for crushed stone aggregates is increasing rapidly with the expansion of many areas such as highways, dams, asphalt, and concrete production. With the decrease in naturally occurring aggregate resources, the need for crushed stone aggregates has become more widespread.

It is crucial to determine the properties of aggregates to assess their suitability for the intended engineering purposes. In terms of their application areas, aggregates must possess resistance to abrasion to avoid crushing, fragmentation, and deterioration when subjected to stacking, compression, feeding from an asphalt plant, laying with a paver, and most importantly, exposure to traffic loads. Aggregates with inadequate wear resistance cannot deliver sufficient efficiency in usage, as their performance properties will degrade under such conditions of use [1]. Aggregates serve as the foundational material in construction and are thus subjected to diverse physical and chemical influences depending on their application. Consequently, they must exhibit high levels of hardness and durability. Additionally, they should possess smoothness, cleanliness, and strong resistance to abrasion and fragmentation [2, 3].

Determining the mechanical properties of aggregates allows for the prediction of their behavior under various loads. Moreover, it plays a crucial role in assessing both the physical and mechanical characteristics of aggregates and in evaluating the strength of asphalt mixture and concrete mixtures [4, 5, 6]. The mechanical properties of aggregates hold significant importance in asphalt mixture roads, particularly because coarse aggregates endure high contact stresses without the support provided by fine aggregates. Additionally, aggregates with low abrasion resistance may experience premature structural failure. Consequently, aggregates lacking in abrasion resistance can lead to severe environmental issues during the production of bituminous hot mix roads [3].

There are test methods developed to determine the mechanical properties of materials used in superstructure. When the studies are examined, many test methods are available to evaluate the toughness and wear resistance of aggregates. When we look at the commonly used test methods, Los Angeles fragmentation resistance (LA), aggregate impact value and Micro-Deval abrasion (M_{DE}) test are at the top [7].

The size distribution of aggregate particles examined through various mechanical test methods can help interpret the type of degradation occurring, whether fragmentation or abrasion resistance. A well-graded distribution comprising particles with a broad range of grain sizes suggests fragmentation, whereas a poorly graded distribution curve containing particles with a limited range of grain sizes indicates aggregate wear. [8].

The Los Angeles experiment is the most widely used method for measuring the resistance of aggregates to fragmentation. In this experiment, aggregate particles are abraded between steel spheres; to measure their resistance to fragmentation and crushing. [9]. The Micro-Deval test is a straightforward and rapid procedure, typically taking only a few hours to complete. Its smaller equipment size, reduced sample size, and simpler procedure make it more convenient and cost-effective compared to alternative experiments [7].

While there are similarities in determining abrasion and fragmentation resistance, including the preparation of aggregates and experimental procedures, examination of the procedures reveals that the processes in the degradation of aggregates differ due to various mechanical interactions. The Micro-Deval experiment assesses the abrasion resistance of only the outer layer of aggregate grains under the influence of water and steel balls. On the other hand, the Los Angeles experiment evaluates both the wear resulting from the interaction between aggregates and the resistance to deterioration caused by the impact and crushing action of steel balls. [4]. Gökalp et al. stated that conducting the Micro-Deval abrasion experimental with water is more effective than the Los Angeles fragmentation experimental because it reflects the field conditions better [7]. In their study, Fladvad and Ulvik found that the use of the tested aggregate in limited sizes brought different disadvantages. A wide range of aggregate sizes are not used in Micro-Deval and Los Angeles experimentals. Therefore, there are limited parameters in determining the differences of aggregates during the design period of the experiments [10]. Li et al. determined that the Los Angeles experimental, which involved failure of steel balls due to impacts or the crushing effect of aggregate, could not adequately simulate

actual compaction or field conditions. For this reason, they determined that the disintegration test could not provide accurate results. They also observed that the internal properties of the material significantly affect the fragmentation [11].

Additional tests are needed to evaluate the long-term durability of aggregates rather than the applied test methods. In their study, Czinder et al. exposed aggregates to wear for a longer period in the Micro-Deval experiment. They determined that the total wear, which is a function of the number of revolutions, has an exponential character and used a new parameter related to wear that explains long-term aggregate durability [12].

Erichsen conducted research during the Los Angeles experiment that demonstrated the linearity of the analysis of the fragmentation process. The experiment was carried out with the Los Angeles drum rotating at up to 900 rpm. As a result of the experiment, he recommends a more comprehensive study to understand the behavior of the aggregates over a longer period of time [13]. In their study, Tunç and Alyamaç tested the degree of disintegration of ground aggregate material in the Los Angeles drum with different amounts of steel balls and different rotation numbers of the drum. In the study, they determined that the number of steel balls and drum rotations had a significant effect on LA (Los Angeles fragmentation loss) in the Los Angeles experiment. They found that with the variability of the LA (Los Angeles fragmentation loss) coefficient, the number of rotations and the increase of steel balls, the values of material loss due to wear increased up to 100% [14].

Disintegration and classification are the main basic processes that allow the production of aggregates with the desired grain size. Therefore, its effects on the aggregate production process is an important issue that needs to be examined. Miskovsky et al. stated that the strength parameters of aggregates are affected by Microcracks and mineral content. Therefore, they found that an inappropriate production process causes the destruction of the aggregate and, as a result, a decrease in its wear and chipping resistance [15].

The initial stage in verifying the usability of aggregates involves examining the composition, structure, and susceptibility to physical and chemical weathering of the rock material. Prior to use, all materials must undergo testing to assess their physical, mechanical, and geometric properties [16]. Abad et al. asserted that a quality aggregate must comprise particles possessing adequate strength and anticipated engineering characteristics, while also demonstrating resistance to the environmental conditions to which it is subjected. [2]. Fournari and Loannou determined that knowing various aggregate properties can help predict the wear resistance of the aggregate [17].

The dimensions of the aggregate to be used in construction works are also very important in terms of its strength properties. Geometric properties of aggregates are closely related to their strength values. An example of this is that the higher the content of flat and longitudinal grains in aggregates, the higher the wear value [18].

Numerous researchers have examined wear and fragmentation processes employing the Los Angeles and Micro-Deval machines. Through their studies, these researchers have noted alterations in both the size and surface roughness of aggregate grains. Their findings indicate that during the initial stage of wear and disintegration processes, aggregate grains exhibit sharp edges and tips. However, as the testing advances, these edges become flattened, and the volume of the grains decreases [19-23].

The qualitative evaluation of aggregates should be based on the analysis of various aggregate properties. Comparison of these properties should also be made between various aggregate types with various geological characteristics.

The main objective of this study is to inform the relevant institutions and organizations that basalt and limestone aggregates of volcanic origin, which constitute a significant deficiency in terms of mineral resources in Bitlis region, can be used more effectively in the construction sector. In addition, considering that the abrasion and fragmentation resistance of aggregates used in road construction under traffic loads is of great importance, the factors affecting the performance of both aggregates were investigated in detail.

In this study, Los Angeles and Micro-Deval tests were conducted to assess the fragmentation and abrasion resistance of basalt and limestone aggregates. The results were evaluated to understand the impact of these aggregates on their resistance properties, considering factors such as the flatness index and $MgSO_4$ frost resistance. According to the study's results, the physical and mechanical properties of both aggregate types in the Bitlis region were presented comparatively, and it was determined that this analysis would make a significant contribution to the literature.

2. Material Method

Within the scope of the study, basalt of volcanic origin and limestone crushed stone aggregate of sedimentary origin were used. Basalt aggregate was supplied from Baysan basalt quarry, which has been operating in Bitlis region since 1992, and limestone aggregate was supplied from Mermer limestone quarry, which is also located in the same region and has been operating since 2010 (Figure 1).

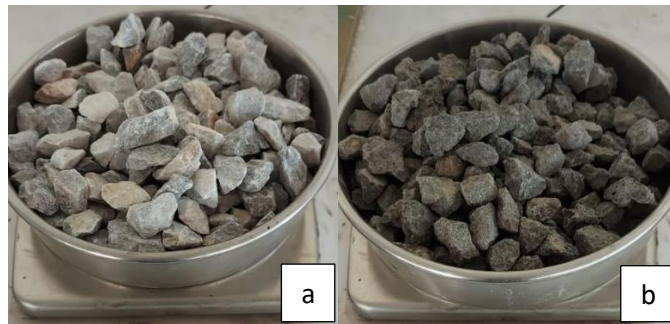


Figure 1. Used in the experiment (a) limestone, (b) basalt

XRF (X-Ray Fluorence Spectrometter) chemical analyses were performed on the aggregates to be used in Los Angeles and Micro Deval tests using the glass tablet method using the fusion method. The samples obtained as glass tablets for chemical analysis are given in Figure 2.

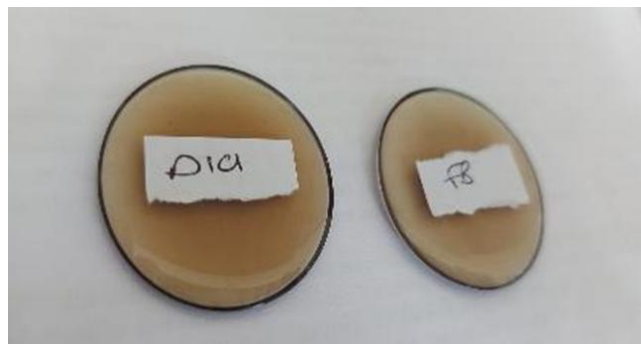


Figure 2. Fusing aggregates into glass tablets by fusion method

The chemical analysis of the basalt and limestone aggregates to be used in the experiment are given in Table 1 and Table 2.

Table 1. Chemical Analysis of Basalt Aggregate Results

The Compound	The values (%)
Bao	0.04
SiO ₂	55.43
Al ₂ O ₃	16.84
Fe ₂ O ₃	8.49
CaO	4.77
MgO	1.97
Na ₂ O	4.61
TiO ₂	1.66
Others	6.19
Ignition Loss (%)	2.91

Table 2. Chemical Analysis of Limestone Aggregate Results

The Compound	The values (%)
Bao	0.01
SiO ₂	1.93
Al ₂ O ₃	0.15
Fe ₂ O ₃	0.14
CaO	52.74
MgO	1.38
Na ₂ O	0.06
TiO ₂	0
Others	43.73
Ignition Loss (%)	43.33

The results of the tests carried out to determine the gradation values and physical properties of the aggregates used in the study are given in Table 3.

Table 3. Gradation limits and physical properties of aggregates

Sieve Size (mm)	Gradation values	Flatness index values		Water Absorption (%)		Bulk Specific Gravity (gr/cm ³)		Apparent Specific Gravity (gr/cm ³)		MgSO ₄ Missing (%)	
		Limestone	Basalt	Limestone	Basalt	Limestone	Basalt	Limestone	Basalt	Limestone	Basalt
25	100	-	-	-	-	-	-	-	-		
19	95-100	19.2	16.1	-	-	-	-	-	-		
12.5	90-100	11.6	19.6	0.50	1.25	2.75	2.78	-	-	%8	%4.5
9.5	63-77	19.7	10.9	0.20	1.25	2.72	2.74	-	-		
4.75	11-35	19.6	19.6	0.68	1.48	2.70	2.74	-	-		
2	10-20	-	-	1.16	1.99	-	-	2.60	2.73		
0.180	5-10	-	-	1.66	1.43	-	-	2.62	2.71		
0.075	3-7	-	-	1.77	1.56	-	-	2.76	2.58		

2.1. Los angeles (fragmentation) experiment

The Los Angeles fragmentation resistance experiment performed within the scope of the study was carried out according to TS-EN 1097-2:2010 standard [24]. The aggregates to be used within the scope of the experiment were first dried in an oven at a temperature of 110±5 °C. The samples taken out of the oven were kept at room temperature before the experiment was performed. First, 5000 g of aggregate samples with a diameter of 10-14 mm were taken and placed in the Los Angeles test device. To apply load on the aggregates, 11 steel balls with a diameter of 45-49 mm and a weight of 400 g-445 g were placed. Then, the lid of the machine was closed and it was subjected to 500 cycles at a constant speed of 31-33 rpm. In the Los Angeles experiment, as the drum rotates, a rack plate picks up the sample and steel balls and transports them until they fall on the opposite side of the drum, causing an impact crushing effect [3]. The Los Angeles device, aggregates and steel balls used in the experiment are shown in Figure 3.

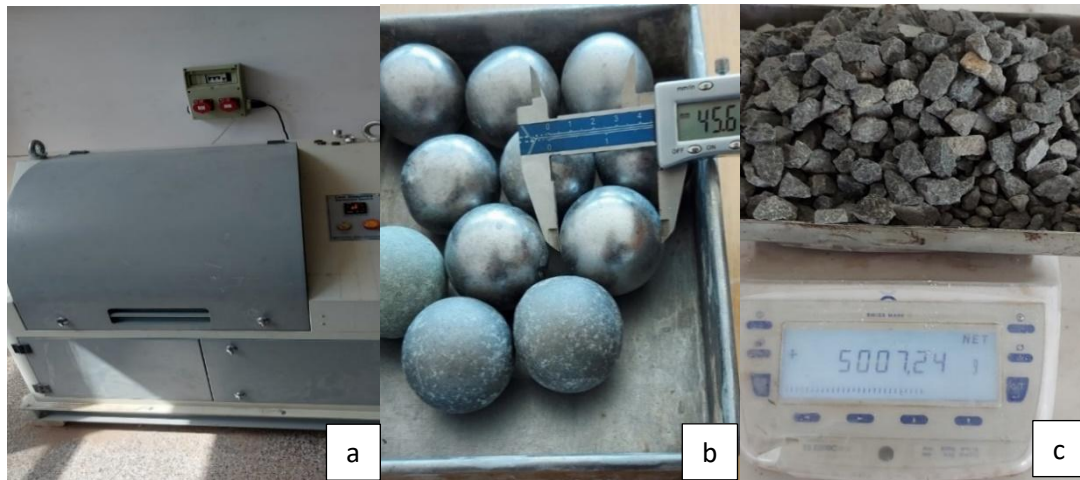


Figure 3. (a) Los Angeles Experiment Device, (b) Steel Balls and (c) Basalt aggregate

After the determined number of revolutions, the samples and steel balls are discharged from the drum into a steel tray. While discharging material from the drum, care should be taken to keep material loss to a minimum. After the cycle is completed, the drum is emptied and the aggregate is separated from the steel balls and sieved through a sieve with a 1.6 mm mesh opening and weighed (Figure 4).

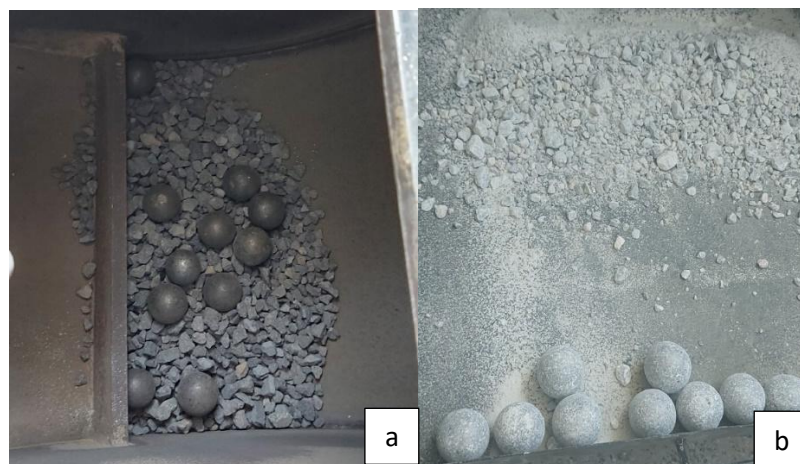


Figure 4. Aggregate and Steel balls (a) Before the cycle (b) After the cycle

Experiments were conducted twice for basalt and limestone aggregate and the average was taken. The experiment was carried out as a dry method. After the experiment, the Los Angeles coefficient of the aggregates was obtained using the formula below.

$$LA = (5000 - m)/50 \quad [1]$$

In this equation;

LA: Los Angeles Coefficient

m: Weight of dry aggregate remaining on 1.6 mm sieve (g)

Los Angeles fragmentation loss, reflects properties such as the hardness and brittleness of the minerals that make up the aggregate, the interlocking of the grains, porosity, the effect of mineral fractionation and the strength of the intergranular bond [25].

The Los Angeles fragmentation loss varies within the same rock type due to certain characteristics. Rocks exhibiting good and robust features such as strong texture, high density, grain interlocking, rough grain surfaces, sturdy intergranular bonding, and low porosity are less prone to degradation compared to rocks with looser textures. In igneous rocks, the Los Angeles fragmentation loss correlates with grain size and porosity. Fine-grained igneous rocks tend to be more resistant to fragmentation than coarse-grained counterparts with similar levels of porosity [26].

Table 4 shows the Los Angeles Fragmentation resistance specification values of the coarse aggregates to be used in the road layers specified in the Highways Technical Specifications [27].

Table 4. Limit values of fragmentation resistance of aggregates used in road construction layers in highway technical specifications

Layers	Fragmentation Resistance (Los Angeles) %	Experiment Standard
Subbase	≤45 (LA ₄₅)	TS EN 1097-2
Base	≤ 35 (LA ₃₅)	TS EN 1097-2
Bituminous chip seal	≤ 30 (LA ₃₀)	TS EN 1097-2
Macadam chip seal	≤ 30 (LA ₃₀)	TS EN 1097-2
Bituminous base	≤ 30 (LA ₃₀)	TS EN 1097-2
Wearing Course	≤ 27 (LA ₂₇)	TS EN 1097-2
Binder Course	≤ 30 (LA ₃₀)	TS EN 1097-2
Stone Mastic Asphalt	≤ 25 (LA ₂₅)	TS EN 1097-2
Porous Asphalt	≤ 25 (LA ₂₅)	TS EN 1097-2

2.2. Micro deval (abrasion) experiment

The experiment was carried out according to TS EN-1097-1 standard [28]. The Micro-Deval test is an experiment carried out with aggregate and 2.5 liters of water in cylindrical steel drums. 500 g of material from aggregate samples with a diameter of 9.5 mm is weighed and water is added with 5000 g of spherical steel balls into a hollow drum with an inner diameter of 200 mm (Figure 5).



Figure 5. Micro-Deval Device, Micro-Deval drum, aggregate, steel shot and water mixture

The steel drum was rotated 12000 revolutions at a rotation speed of 100 ± 5 revolutions per minute. Experiments were performed twice for each aggregate sample and averaged. After the cycle is completed, the drums are removed from the device and their covers are carefully opened. The drum is emptied onto a 1.6 mm sieve without causing sample loss, thus steel balls, water and aggregate are separated. Steel balls are separated from the aggregate samples with the help of a magnet.

The aggregate samples separated from the steel balls are washed on the sieve, the remaining sample is weighed and the Micro-Deval coefficient is calculated by measuring the average mass loss.

The Micro-Deval coefficient (M_{DE}) is calculated by the formula below.

$$M_{DE} = (500 - m)/5 \quad [2]$$

In this equation;

M_{DE} : Micro-Deval Coefficient

m: Total amount of aggregate remaining in the 1.6 mm sieve (g)

Table 5 shows the Micro Deval Abrasion resistance specification values of the coarse aggregates to be used in the road layers specified in the Highways technical specifications [27].

Table 5. Limit values of abrasion resistance of aggregates used in road construction layers in highway technical specificatione

Layers	Abrasion Resistance (Micro Deval) %	Experiment Standard
Subbase	-	TS EN 1097-1
Base	-	TS EN 1097-1
Bituminous chip seal	$\leq 25 (M_{DE}25)$	TS EN 1097-1
Macadam chip seal	$\leq 25 (M_{DE}25)$	TS EN 1097-1
Bituminous base	$\leq 25 (M_{DE}25)$	TS EN 1097-1
Wearing Course	$\leq 20 (M_{DE}20)$	TS EN 1097-1
Binder Course	$\leq 25 M_{DE}25)$	TS EN 1097-1
Stone Mastic Asphalt	$\leq 20 (M_{DE}20)$	TS EN 1097-1
Porous Asphalt	$\leq 20 (M_{DE}20)$	TS EN 1097-1

4. Results and Discussion

In the micro-deval test, the surface texture, grain corners and sharp edges of the aggregates are abraded, while in the Los Angeles test, the entire aggregate disintegrates. Aggregates with long, straight and sharp edges generally show weaker resistance to continuous fragmentation and abrasion. However, the frequency of the tests and the deformation behavior also depend on the duration of the test. To understand the wear development of aggregate grains, the use of 3D (three-dimensional) analysis instead of 2D (two-dimensional analysis) in conjunction with numerical simulations is shown to be an effective method to study the morphological behavior of aggregates before and after impact [21, 29].

Increasing the standard cycle level in the micro deval test causes changes in the wear properties of the aggregates [23]. However, in the Los Angeles experiment, increasing cycle numbers could significantly reduce the steepest peak of the aggregates and negatively affect their interlocking properties. The reason for this can be explained by the presence of larger, rounder and stronger corners, which increase the resistance to fragmentation [30].

As a result of the studies, Los Angeles and Micro-Deval tests were performed separately on basalt and limestone aggregates. The experiments were performed twice on each aggregate and average values were obtained. The results of Los Angeles and Micro-Deval tests of the aggregates are given in Figure 6-Figure 9 in comparison with the flatness index and $MgSO_4$ loss values.

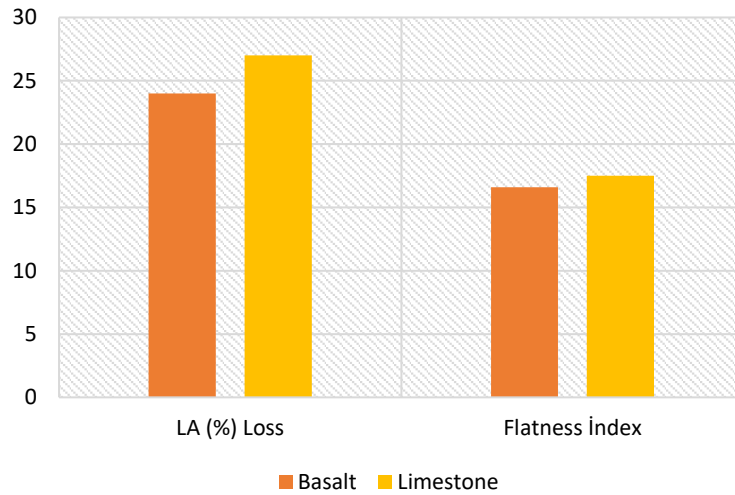


Figure 6. Relationship between LA (%) loss values of aggregates and Flatness index values

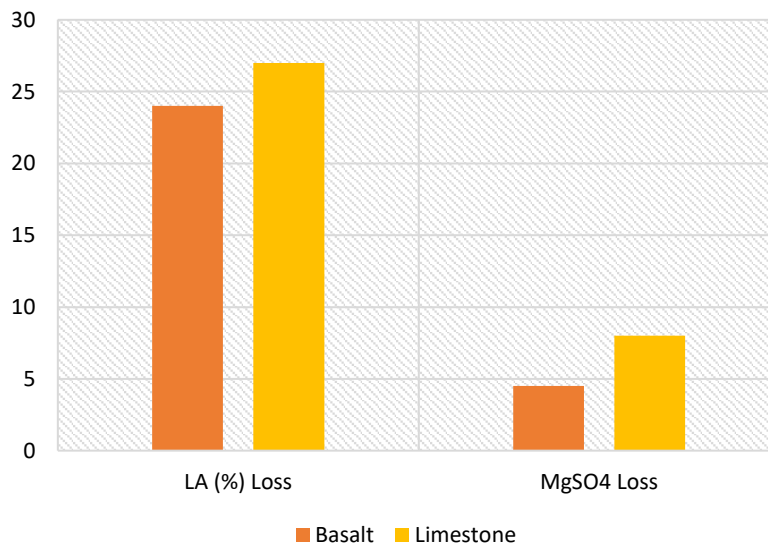


Figure 7. Relationship between LA (%) loss values of aggregates and MgSO₄ loss values

In the Los Angeles test, the aggregate is subjected to the effects of fragmentation and impact. In general, Los Angeles fragmentation values are affected by different geological and crushing properties of aggregates. When the Los Angeles test results with basalt and limestone aggregates were analyzed, Los Angeles loss for limestone aggregate was 27%, while Los Angeles loss for basalt aggregate was 24%. When the test results were evaluated, similar findings were reported in the literature. Pang et al. found the Los Angeles fragmentation value for limestone aggregate to be 25% and suggested that LA performance might be influenced by the calcite mineral content of the aggregate [31].

Considering the Los Angeles fragmentation resistance values specified in the Highways Technical Specification for road layers constructed on highways, both aggregate types generally meet these limit values. According to the test results shown in Figure 6, when examining the relationship between Los Angeles particle loss strength and the aggregate flatness index values, the flatness index for basalt aggregate is 16.6%, while for limestone aggregate it is 17%. Both types of aggregates are generally quite angular in structure and have many sharp edges due to their crushed stone composition. Basalt aggregate generally has greater strength than limestone aggregate in terms of its physical and mechanical properties. For this reason, the fragmentation loss value should be lower than the limestone aggregate, but since the angularity and flatness

of the aggregate are close to the limestone aggregate, it has experienced approximately the same loss in terms of fragmentation as the limestone aggregate.

The gradual loss of aggregate corners in the Los Angeles test depends on the rate of flaking and elongation index of the aggregates. Therefore, it was determined that aggregates with high mass loss have a high rate of flaking and elongation index and become more susceptible to fracture under fragmentation test [32].

When the relationship between the Los Angeles particle loss value and the $MgSO_4$ loss value is examined in Figure 7, the loss in basalt was 4.5%, while this loss in limestone aggregate was 8%. Aggregates exposed to the freeze-thaw cycle crumble and decrease in size due to the effect of the solution inside. The freeze-thaw loss value of basalt aggregate shows that it is approximately 2 times more durable than limestone aggregate. Despite this, the fact that the fragmentation loss value was obtained at approximately the same value as the limestone aggregate appears as an experiment that should be discussed regarding how accurate the results of the Los Angeles fragmentation test are.

When examining the M_{DE} (Micro-Deval) loss values obtained from the Micro-Deval test for basalt and limestone aggregates, it was found to be 17% for basalt aggregate and 19% for limestone aggregate. According to the highway technical specifications, the M_{DE} loss limit values for aggregates used in road construction layers fall within the maximum range of 20%-25%. Based on these limit values, it has been determined that both types of aggregates can be utilized in road construction based on their abrasion loss values.

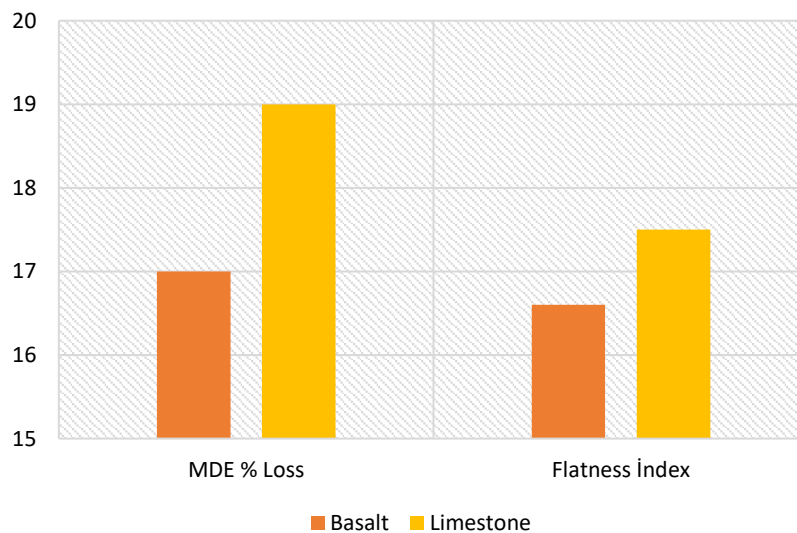


Figure 8. Relationship between M_{DE} (%) loss values of aggregates and Flatness index values

Examination of figure 8 reveals that increasing angularity of the aggregates accelerates wear. This is primarily due to the interaction between the aggregate surfaces and the steel balls used in the test, as well as the internal hard surfaces of the steel cylinder molds employed in the Micro-Deval test. The extent of degradation of morphological properties, as determined by the Micro-Deval test, varies depending on other mineralogical properties of the aggregates, such as the Mohs mineral hardness value. Aggregates with a high Mohs hardness value experience less abrasion [33].

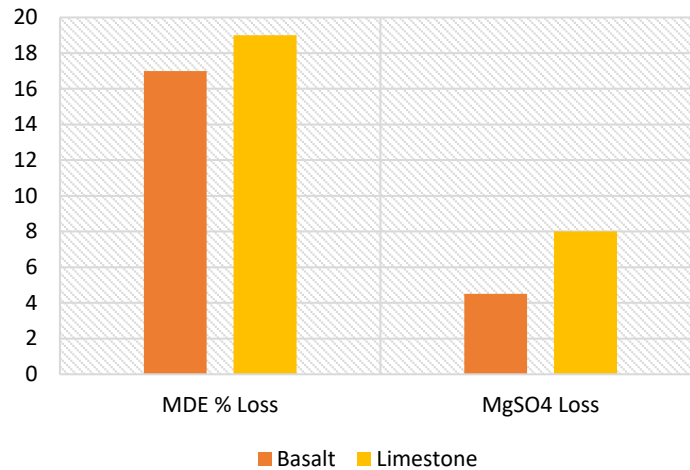


Figure 9. Relationship between M_{DE} (%) loss values of aggregates and $MgSO_4$ loss values

Figure 9 shows a clear relationship between the flatness index of basalt and limestone aggregates and their $MgSO_4$ loss values as well as abrasion loss values. The abrasion loss value of basalt aggregate, with a flatness index of 16.6%, was determined as 17%, while the abrasion loss value of limestone aggregate, with a flatness index of 17.5%, was determined as 19%. It's observed that the abrasion loss of basalt aggregate, with a lower flatness index value, is lower, whereas the abrasion loss of limestone aggregate, with a higher flatness index value, is higher. Therefore, there exists a close relationship between the flatness index values of the aggregates and their abrasion values.

When examining the relationship between abrasion loss values and $MgSO_4$ loss values, a result similar to the relationship between flatness index value and abrasion loss value was observed. In basic, it has been found that the abrasion resistance value of basalt aggregate, which is stronger and exhibits a lower value in terms of frost resistance, is low, while the abrasion loss value of limestone aggregate, with a % loss value higher than that of basalt aggregate due to frost resistance, is high. The experimental results obtained from the study are presented collectively in Table 6.

Table 6. Experiment results

Aggregate/Experiment Results	M_{DE} (%) Loss	LA (%) Loss	Flatness Indeks	$MgSO_4$ Loss (%)
Basalt	17	24	16.6	4.5
Limestone	19	27	17.5	8

There are similarities in the procedures for testing aggregates to determine abrasion and fragmentation resistance. Both methods reveal different aspects of aggregate degradation due to mechanical interactions. While the Micro-Deval test assesses the resistance of only the outer layer of aggregate grains to abrasion caused by steel balls, the Los Angeles fragmentation test evaluates the aggregate's resistance against both fragmentation resulting from aggregate-to-aggregate interaction and deterioration caused by the impact and crushing movement induced by the steel balls [4]. In a study comparing both methods, it was concluded that the Micro-Deval abrasion test was more effective than the Los Angeles fragmentation test because it more accurately reflected field conditions [7].

According to these results, the Micro-Deval test used for abrasion loss resistance of aggregates gives better results than the Los Angeles test used for disintegration loss resistance, more consistent results are obtained when compared to other physical properties of aggregates, and it reflects field conditions better. It was concluded that more clear results would be obtained by using the Micro-Deval experiment to determine the value.

As a result of the research and experiments, there are many factors that affect the abrasion and fragmentation of aggregates. For this reason, more extensive studies on the Los Angeles and Micro Deval tests should be carried out to select the most appropriate test method, extensive analyzes should be made indicating that the tested aggregates should be made in a wider grain size range, and the effect of the aggregates on the physical and mechanical properties of the crushers in the production process should be examined in more detail should be investigated accordingly. In addition, both experiments should be carried out under the same conditions and larger studies should be conducted focusing on the geological properties of the aggregates.

5. Conclusion

In this study, methods for determining the behavior of aggregates in abrasion and fragmentation resistance tests for different aggregate types are described and also proposes further research steps aimed at developing test procedures that take into account the existing conditions.

The results presented in this paper indicate that:

- In light of the results presented in the study, variations are observed in the disintegration values of aggregates depending on the application of both test methods, the type of materials, classification size, and the experiments conducted under different conditions.
- Aggregates tested for abrasion and fragmentation should be analyzed over a wider size range and the most appropriate test method should be selected accordingly.
- It was concluded that the fragmentation and abrasion tests conducted on aggregates were inadequate for drawing a comprehensive conclusion regarding aggregate performance solely based on a single textural factor.
- A comprehensive examination of how the production process affects the physical and mechanical characteristics of aggregates is necessary.
- In addition to scrutinizing the physical and mechanical attributes of aggregates, it is imperative to conduct a comprehensive analysis of their geometric parameters and the interrelations among them, with particular emphasis on the geological properties of the aggregates.
- Furthermore, there is a need for further exploration into the correlation between micro-cracks, mineral distribution, and mineral shape of aggregates within the context of Los Angeles and Micro-Deval tests.

6. Author Contribution Statement

Author 1 contributed to the idea, design and literature review, evaluation of the results obtained, procurement of the materials used and examination of the results, spell check and content control of the manuscript.

7. Ethics Committee Approval and Conflict of Interest Statement

"There is no need to obtain ethics committee permission for the prepared article"

8. References

- [1] A. Teymen, "Estimation of Los Angeles abrasion resistance of igneous rocks from mechanical aggregate properties," *Bull. Eng. Geol. Environ.*, vol. 78, no. 2, pp. 837–846, 2019.
- [2] N. K. A. Seyed Vahid Alavi, M. Yilmaz, D. J. Armaghani, and A. Tugrul, "Prediction of the durability of limestone aggregates using computational techniques," *Neural Comput. Appl.*, vol. 29, pp. 423–433, 2018.
- [3] T. Umar, E. Charles, and S. Messaoud, "A modified method for Los Angeles abrasion test," *Iran. J. Sci. Technol.*, vol. 44, pp. 941–947, 2020.
- [4] M. Palassi and D. Akbar, "Relationships between abrasion/degradation of aggregate evaluated from various tests and the effect of saturation," *Rock Mech. Rock Eng.*, vol. 49, pp. 2937–2943, 2016.
- [5] E. T. Tunc and K. E. Alyamac, "Determination of the relationship between the Los Angeles abrasion values of aggregates and concrete strength using the Response Surface Methodology," *Constr. Build. Mater.*, vol. 260, p. 119850, 2020.
- [6] W. Sun, Y. Liu, D. S. Lane, H. Nair, and L. Wang, "Experimental investigation of the relationship between mineral content and aggregate morphological characteristics using the improved FTI system and XRD method," *Constr. Build. Mater.*, vol. 155, pp. 981–991, 2017.
- [7] İ. Gökalp, V. E. Uz, and M. Saltan, "Testing the abrasion resistance of aggregates including by-products by using Micro Deval apparatus with different standard test methods," *Constr. Build. Mater.*, vol. 123, pp. 1–7, 2016.
- [8] E. Erichsen, A. Ulvik, and K. Sævik, "Mechanical degradation of aggregate by the Los Angeles-, the Micro-Deval- and the Nordic test methods," *Rock Mech. Rock Eng.*, vol. 44, pp. 333–337, 2011.
- [9] S. Kahraman and M. Fener, "Predicting the Los Angeles abrasion loss of rock aggregates from the uniaxial compressive strength," *Mater. Lett.*, vol. 61, pp. 4861–4865, 2007.
- [10] M. Fladvad and A. Ulvik, "Large-size aggregates for road construction—a review of standard specifications and test methods," *Bull. Eng. Geol. Environ.*, vol. 80, pp. 8847–8859, 2019.
- [11] C. Li, J. C. Ashlock, D. J. White, C. T. Jahren, and B. Cetin, "Gyratory abrasion with 2D image analysis test method for evaluation of mechanical degradation and changes in morphology and shear strength of compacted granular materials," *Constr. Build. Mater.*, vol. 152, pp. 547–557, 2017.
- [12] B. Czinder, B. Vásárhelyi, and Á. Török, "Long-term abrasion of rocks assessed by micro-Deval tests and estimation of the abrasion process of rock types based on strength parameters," *Eng. Geol.*, vol. 282, p. 105996, 2021.
- [13] E. Erichsen, "Plotting aggregate degradation results from the Los Angeles test on a triangular diagram: proposal of a new quality ranking for aggregates," *Bull. Eng. Geol. Environ.*, vol. 74, pp. 667–671, 2014.
- [14] E. T. Tunc and K. E. Alyamac, "A preliminary estimation method of Los Angeles abrasion value of concrete aggregates," *Constr. Build. Mater.*, vol. 222, pp. 437–446, 2019.
- [15] K. Miskovsky, M. T. Duarte, S. Q. Kou, and P. A. Lindqvist, "Influence of the mineralogical composition and textural properties on the quality of coarse aggregates," *J. Mater. Eng. Perform.*, vol. 13, pp. 144–150, 2004.
- [16] I. Rigopoulos, B. Tsikouras, P. Pomonis, and K. Hatzipanagiotou, "Determination of the interrelations between the engineering parameters of construction aggregates from ophiolite complexes of Greece using factor analysis," *Constr. Build. Mater.*, vol. 49, pp. 747–757, 2013.
- [17] R. Fournari and L. Loannou, "Correlations between the properties of crushed fine aggregates," *Minerals*, vol. 9, p. 86, 2019.
- [18] C. S. Cook, B. F. Tanyu, and A. Yavuz, "Effect of particle shape on durability and performance of unbound aggregate base," *J. Mater. Civ. Eng.*, vol. 29, p. 04016221, 2017.
- [19] M. Bulevičius, K. Petkevičius, and S. Čirba, "The influence of geometric parameters on strength properties of the aggregates used to produce asphalt mixtures," *J. Civ. Eng. Manag.*, vol. 19, pp. 894–902, 2013.
- [20] Y. Qian, H. Boler, M. Moaveni, E. Tutumluer, Y. M. A. Hashash, and J. Ghaboussi, "Characterizing ballast degradation through Los Angeles abrasion test and image analysis," *Transp. Res. Rec.*, vol. 2448, pp. 142–151, 2014.

- [21] I. D. Quintanilla, G. Combe, F. Emeriault, C. Voivret, and J. F. Ferellec, "X-ray CT analysis of the evolution of ballast grain morphology along a Micro-Deval test: key role of the asperity scale," *Granular Matter*, vol. 21, p. 30, 2019.
- [22] H. Ge, A. Sha, Z. Han, and X. Xiong, "Three-dimensional characterization of morphology and abrasion decay laws for coarse aggregates," *Constr. Build. Mater.*, vol. 188, pp. 58–67, 2018.
- [23] D. Wang, H. Wang, Y. Bu, C. Schulze, and M. Oeser, "Evaluation of aggregate resistance to wear with Micro-Deval test in combination with aggregate imaging techniques," *Wear*, vol. 338-339, pp. 288–296, 2015.
- [24] T. E. 1097-2, "Agregaların mekanik ve fiziksel özellikleri için deneyler bölüm 2: Parçalanma direncinin tayini için metotlar," *Türk Standartları Enstitüsü*, Ankara, 2010.
- [25] R. Ajalloeian and M. Kamani, "An investigation of the relationship between Los Angeles abrasion loss and rock texture for carbonate aggregates," *Bull. Eng. Geol. Environ.*, vol. 78, pp. 1555–1563, 2017.
- [26] H. Haraldsson, "Relations between petrography and the aggregate properties of Icelandic rocks," *Bull. Eng. Geol. Environ.*, vol. 30, 1984.
- [27] KGM, *Karayolları Teknik Şartnamesi*, Ankara: Karayolları Genel Müdürlüğü, 2013.
- [28] T. E. 1097-1, "Agregaların mekanik ve fiziksel özellikleri için deneyler Bölüm 1: Aşınma Direncinin tayini (Mikro-Deval)," *Türk Standartları Enstitüsü*, Ankara, 2011.
- [29] J. Wu, L. Wang, Y. Hou, Z. Qian, L. Meng, and Q. Zhao, "Simulation on the Micro-Deval test for the aggregate wear properties measurement," *Constr. Build. Mater.*, vol. 180, pp. 445–454, 2018.
- [30] I. D. Quintanilla, D. Deiros, F. Emeriault, J. B. Toni, C. Voivret, and J. F. Ferellec, "Wear of sharp aggregates in a rotating drum," in *EPJ Web Conf.*, France, 2017.
- [31] L. Pang, S. Wu, J. Zhu, and L. Wan, "Relationship between retrographical and physical properties of aggregates," *J. Wuhan Univ. Technol.-Mater. Sci. Ed.*, vol. 25, no. 4, pp. 678–681, 2010.
- [32] S. Adomako, C. J. Engelsen, R. T. Thorstensen, and D. M. Barbieri, "Review of the relationship between aggregates geology and Los Angeles and micro-Deval tests," *Bull. Eng. Geol. Environ.*, vol. 80, pp. 1963–1980, 2021.
- [33] H. Wang, D. Wang, P. Liu, J. Hu, C. Schulze, and M. Oeser, "Development of morphological properties of road surfacing aggregates during the polishing process," *Int. J. Pavement Eng.*, vol. 18, pp. 367–380, 2017.



Derin Öğrenme ile Kısa Vadeli Rüzgar Hız Tahmini

Fatih KARAASLAN¹ , Zeynep Mine ALÇİN² , Muzaffer ASLAN^{3*} 

¹Yenilenebilir Enerji Sistemleri, Fen Bilimleri Enstitüsü, Bingöl, Türkiye.

²Elektronik, Battalgazi İlçe Milli Eğitim Müdürlüğü, Malatya, Türkiye.

³Elektrik-Elektronik Mühendisliği, Mühendislik ve Mimarlık, Bingöl, Türkiye.

¹fkaraslan23@gmail.com, ²zmozkan@gmail.com, ³muzafferaskan@bingol.edu.tr

Geliş Tarihi: 17.07.2024

Kabul Tarihi: 25.10.2024

Düzeltilme Tarihi: 02.10.2024

doi: <https://doi.org/10.62520/fujece.1517615>

Araştırma Makalesi

Alıntı: F. Karaslan, Z. M. Alçin ve M. Aslan, "Derin öğrenme ile kısa vadeli rüzgar hız tahmini", Fırat Üni. Deny. ve Hes. Müh. Derg., vol. 4, no 1, pp. 151-162, Şubat 2025.

Öz

Rüzgar hızı, yenilenebilir rüzgar enerjisine yatırım yapılması ve planlanmasında rüzgar hızının tahmin edilmesi hayati önem taşımaktadır. Ayrıca mevcut rüzgar santrallerinin üretimi ve iletim hatlarının kapasitelerinin artırılmasında da rüzgar hızının tahmin edilmesi oldukça önem arz etmektedir. Fakat rüzgar hızının aralıklı ve stokastik dalgalanmaları, yüksek kaliteli rüzgar hızı tahmini için önemli bir sorun oluşturmaktadır. Bu çalışmada, rüzgar santrallerinin planlanması ve uygulanabilirlik çalışmaları için rüzgar hız tahminini daha kolay sağlayabilecek derin öğrenme temelli bir yaklaşım önerilmiştir. Bu yaklaşımda öncelikle rüzgar hız zaman verileri sürekli dalgacık dönüşümü ile renkli görüntüye dönüştürüldü. Elde edilen görüntüler, önceden eğitilmiş AlexNet CNN modeline uygulanarak rüzgar hız tahmini gerçekleştirilmektedir. Çalışma, Elazığ meteoroloji bölge müdürlüğünden alınan 2018-2019 yılları arasındaki saatlik hız verileri kullanılmıştır. Yapılan deneysel çalışmalarda, 1-saat, 2-saat ve 3-saat olmak üzere üç farklı ileri ufuk tahmini yapılmıştır. Önerilen tahmin modelinin modelin performans değerlendirilmesi için ortalama mutlak hata (MAE), ortalama karekök hatası (RMSE) ve korelasyon katsayısı (R) metrikleri kullanılmıştır. Deneysel çalışmalarda, tüm veri seti görüntüleri transfer öğrenimi için rastgele bir şekilde sırasıyla %70, %10 ve %20 oranlarında eğitim, doğrulama ve test olmak üzere üç bölüme ayrılmıştır. 1-saat ileri tahminde RMSE, MAE ve R metrikleri için sırasıyla 0,0335, 0,0275 ve 0,9517 deneysel sonuçlar ile en iyi rüzgar hız tahmini gerçekleştirilmiştir. Bu bakımdan önerilen AlexNet modelinde, 1 saat ileri tahmininde, daha güvenilir ve doğru tahmin gerçekleştirdiğinden rüzgar hız tahmininde etkili bir model olduğunu göstermektedir.

Anahtar kelimeler: Rüzgar hız tahmini, Sürekli dalgacık dönüşümü, Evrişimli sinir ağları, Derin öğrenme

*Yazışılan yazar

İntihal Kontrol: Evet – Turnitin

Şikayet: fujece@firat.edu.tr

Telif Hakkı ve Lisans: Dergide yayın yapan yazarlar, CC BY-NC 4.0 kapsamında lisanslanan çalışmalarının telif hakkını saklı tutar.



Short-Term Wind Speed Forecasting With Deep Learning

Fatih KARAASLAN¹ , Zeynep Mine ALÇİN² , Muzaffer ASLAN^{*3} 

¹ Renewable Energy Systems, Institute of Science and Technology, Bingöl, Türkiye.

² Electrical-Electronics, Battalgazi District Directorate of National Education, Malatya, Türkiye.

³Electrical-Electronics Engineering, Engineering and Architecture, Bingöl, Bingöl, Türkiye.

¹fkaraslan23@gmail.com, ²zmozkan@gmail.com, ³muzafferaskan@bingol.edu.tr

Received: 17.07.2024

Accepted: 25.10.2024

Revision: 02.10.2024

doi: <https://doi.org/10.62520/fujece.1517615>

Research Article

Citation: F. Karaslan, Z. M. Alçin ve M. Aslan, "Short-term wind speed forecasting with deep learning", *Firat Univ. Jour. of Exper. and Comp. Eng.*, vol. 4, no 1, pp. 151-162, February 2025.

Abstract

Wind speed forecasting is crucial for planning and investing in renewable wind energy. In addition, Wind speed forecasting is essential for planning renewable wind energy, optimizing wind power production, and enhancing transmission line capacities. However, intermittent and stochastic fluctuations of wind speed pose a significant problem for high quality wind speed forecasting. In this study, a deep learning-based approach is proposed for wind power plant planning and feasibility studies that can provide wind speed prediction more easily. In this approach, firstly, wind speed time data were converted into color images using continuous wavelet transform. The obtained images were applied to the pre-trained AlexNet CNN model and wind speed prediction was performed. In the study, hourly speed data from the Elazığ meteorology regional directorate between 2018-2019 were used. In the experimental studies, three different horizon forecasts were made: 1-hour, 2-hour and 3-hour. Metrics like correlation coefficient (R), mean absolute error (MAE), and root means square error (RMSE) were utilized to assess the proposed forecasting models performance. In the experimental studies, the whole dataset images were randomly divided into three parts as training, validation and test at the rates of 70%, 10% and 20% respectively for transfer learning. In the 1-hour horizon forecast, the best wind speed prediction was achieved with experimental results of 0.0335, 0.0275 and 0.9517 for RMSE, MAE and R metrics, respectively. In this respect, the proposed AlexNet model shows that it is an effective model in wind speed forecast since the 1-hour horizon forecast is more reliable and accurate.

Keywords: Wind speed forecasting, Continuous wavelet transform, Convolutional neural networks, Deep learning

*Corresponding author

1. Introduction

Global energy consumption is rising significantly due to population growth and technological and economic developments. With the increase in energy demands and the overuse of existing fossil resources, serious environmental problems such as global warming and climate change have been searched for new energy sources [1].

Electrical energy is the most used type of energy in daily life. Among low-carbon generation technologies, wind energy is one of the most important Renewable Energy Sources (RES) in many countries [2]. In this environment, the installed capacity of wind energy is growing annually on a global scale, reaching 650 GW in 2019 [3]. However, wind speed represents a significant variable in the reliability of the electricity grid [4]. Accurate and efficient forecasting of wind energy is of great importance in ensuring the safe and efficient operation of the electricity grid.

Many approaches to wind energy forecasting have been suggested and applied, initially traditional statistical models, physical models and more recently machine learning based models [5]. In wind energy forecasting with physical models, atmospheric flow is simulated using numerical weather forecasts for several locations in each geographical region. Despite the high computational cost, this model demonstrates satisfactory performance in medium- period and long-period wind forecasting. In contrast, traditional-statistical models refer to the data matching among the historical-data and the output of the wind farm. It is a time series approach where traditional statistical models are generally effective in short-term forecasting.

Advances in computer technology has facilitated the wider adoption of machine learning-based methods in the field of wind forecasting [6]. In the literature, there are many works using various deep learning approaches for wind forecasting.

Yildiz et al. [5] improved an enhanced residual-based convolutional neural network for the prediction of wind energy. Although the developed network is less complex and requires less computational resources, it is important to note that some features in the data may be lost due to the residual connection approach. Azimi et al. [7] proposed an approach for feature extraction that combines discrete wavelet transform, harmonic time series analysis, and k-means. For feature extraction, they adopted the decomposition of historical air temperature, wind speed and power data. They then trained a Multi-layer Perceptron Neural Network (MLN) with these extracted features to perform wind forecasting.

Jaseena and Koor [8], empirical model decomposition (EMD), ensemble-EMD, wavelet transform (WT) and empirical wavelet transform (EWT) methods combined the features obtained in data decomposition. They then applied these features to a Bidirectional Long-Sort Time Memory (Bi-LSTM) deep learning model for wind speed forecasting. They tested the performance evaluation of the proposed hybrid model with the Dhanushkodi and Melamandai dataset. The experimental results demonstrated that it outperforms other data decomposed-based models in terms of accuracy and stability. Li et al. [9] examined the effect of time resolution in wind energy forecasting. To minimize these effects, they proposed an artificial neural network (ANN)-based wind forecasting model.

Noman et al. [10] proposed the use of multivariate exogenous input variables to improve model performance in wind forecasting. Using the suggested approach features, eight transfer learning techniques, and four neural networks, they were able to predict the wind. They conducted experimental studies with two years of wind speed data averaging over 10-minute intervals. Experimental outcomes showed that the nonlinear autoregressive exogenous model is more performant than other methods. Zameer et al. [11] developed a genetic programming-based ANN model for short-term wind power forecasting. This developed model was tested with data from five different wind farms. They showed that the model has higher performance than some artificial intelligence-based models. Altan et al. [12] developed a non-linear hybrid model based on gray wolf optimizer decomposition and LSTM deep learning for more accurate and reliable wind speed prediction. With this model, the features obtained from the combination of parsing and LSTM model were combined. They then improved the performance of the wind speed prediction model by optimizing the weighted coefficients of the intrinsic mode function output with gray wolf optimization. Emeksiz and Tan [13]

proposed a method based on combining deep learning and mode separation approaches for wind speed estimation. In the proposed model, the signals obtained from adaptive noise reduction and EMD methods are converted into images by continuous wavelet transform in the pre-processing of the data. These images have been applied to various CNN models for effective wind speed forecasting. A multistep wind speed prediction model based on a transformer is proposed, and the multistep wind speed prediction problem is recognized as a sequence-to-sequence mapping problem [14].

In this work, a two-stage transfer learning-based model is proposed for wind speed prediction. In the first stage, hourly wind speed data were converted into images with Continuous Wavelet Transform (CWT). Then, these images were applied to the pre-trained AlexNet model and wind speed prediction was performed. Experimental studies were carried out with hourly wind speed data of Elazig center for the years 2018-2019. The study's contributions are assessed in the manner listed below.

- To overcome the stochastic and unstable features of wind data and reach higher accuracy capacity, RGB color space image sensitive to CWT changes of wind data is provided,
- With the color images derived from wind speed data, the training reliability of the pre-trained convolutional neural network (CNN) improved, and wind forecasting performance is increased.

2. Material and Methods

In this study, a CNN-based model for wind speed forecasting was proposed, and its structure is shown in Figure 1. First, in the suggested model, hourly wind speed data were converted into a two-dimensional image by CWT transformation and then colored and converted into a 3D image. Then, the image size was resized for the input of the AlexNet model. In the final stage, the classification layer of the pre-trained ESA model AlexNet was replaced with a regression layer to predict deep features, enabling automatic wind speed forecasting.

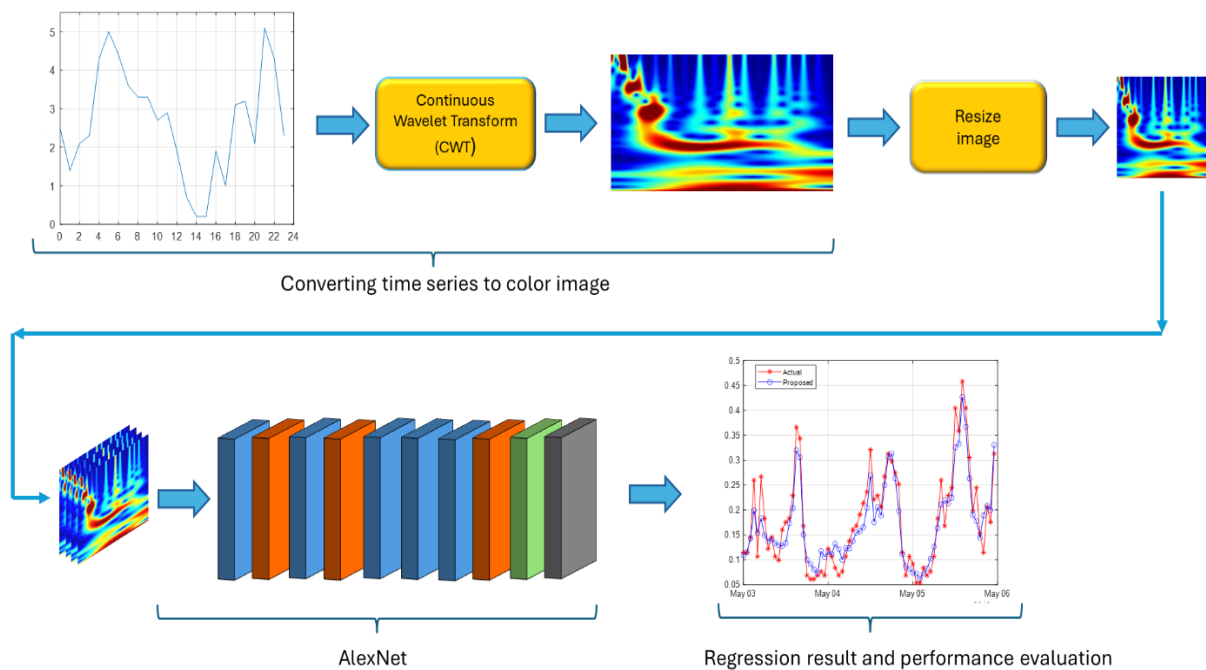


Figure 1. Proposed model chart

2.1. Dataset

The experimental studies used hourly wind direction and speed data (2018–2019) from the Meteorology Directorate's Central/Elazig station (No. 17201). The details of the dataset used in the experimental studies are presented in Figure 2. As seen in figure 2, the columns show the hourly time changes, and the rows show the changes in wind speeds (m/s) against the hourly changes during the day. There is a total of 17448 hours of wind data in the dataset for two years.

Date	0:00:00	1:00:00	2:00:00	3:00:00	4:00:00	5:00:00	6:00:00	7:00:00	8:00:00	9:00:00	10:00:00
January 1, 2018	2.5	1.4	2.1	2.3	4.3	5.0	4.4	3.6	3.3	3.3	2.7
January 2, 2018	0.7	0.3	0.7	0.9	0.7	1.4	0.8	1.5	4.0	5.2	5.2
January 3, 2018	1.8	1.9	1.8	1.8	1.5	1.3	0.9	1.0	1.8	2.2	2.0
January 4, 2018	5.5	4.2	3.8	4.4	4.6	4.0	4.4	6.0	6.0	6.9	5.2
January 5, 2018	5.4	4.9	5.6	5.7	6.3	5.2	4.5	5.0	6.1	5.0	3.0
January 6, 2018	1.8	1.8	1.6	1.6	1.8	1.7	1.2	0.5	1.6	1.8	2.3
January 7, 2018	2.3	1.8	0.9	1.5	2.4	2.0	0.6	0.9	0.7	1.5	2.3
January 8, 2018	1.8	1.6	2.0	1.6	1.5	1.5	0.8	0.4	1.3	2.0	1.7
January 9, 2018	1.7	0.1	1.5	0.8	1.3	1.2	0.7	0.7	1.6	2.2	1.9
January 10, 2018	2.6	2.7	2.8	2.0	2.2	1.6	1.3	0.6	0.6	2.1	2.2
January 11, 2018	0.2	0.2	0.2	0.2	0.5	1.0	0.7	0.5	1.8	1.9	1.6
January 12, 2018	1.4	0.8	0.3	1.0	0.9	1.3	1.3	1.0	0.8	2.3	2.4
January 13, 2018	0.8	0.7	1.5	1.0	0.5	0.8	0.3	1.6	1.1	1.6	2.0
January 14, 2018	0.9	2.5	1.5	1.6	3.8	1.0	1.6	3.2	4.0	5.0	4.4
January 15, 2018	0.5	0.6	1.8	1.9	2.0	2.0	2.0	1.9	1.2	1.3	1.5

Figure 2. Dataset details

2.2. Continuous wavelets transform

The Continuous Wavelet Transform (CWT) is one of the most advanced signal processing techniques available for analyzing time-series data due to its ability to handle non-stationary signals, which are common in real-world applications such as weather patterns, financial data, and physiological signals [13]. CWT allows for the simultaneous analysis of both time and frequency content of a signal, which is particularly important for non-stationary time series where the frequency characteristics change over time. In contrast, traditional methods like the Fourier Transform provide only frequency information and fail to capture the temporal variations within the signal [13-15] Furthermore, CWT enables the signal to be analyzed at multiple scales, providing insights into different frequency components at various time points. This multi-scale analysis offers significant advantages in detecting patterns such as peaks, trends, or anomalies at different resolutions [14, 15].

The basic principle of CWT is based on decomposing a continuous-time function into a set of wavelet functions. The wavelets are derived by applying a shift and scaling operation to the mother wavelet function. Accordingly, CWT can be defined by Equation 1.

$$CWT_f(a, \tau) = [f(t), \psi_{a,\tau}(t)] = \frac{1}{\sqrt{a}} \int f(t) \psi^* \left(\frac{t - \tau}{a} \right) dt, a > 0 \quad (1)$$

Where, ψ is the main wavelet function, a is the scale factor of the wavelet and expands the wavelet length and frequency, τ is the delay factor and controls the delay position on the time axis, and ψ^* is the complex conjugate of the wavelet master function. a should be chosen small for the high-frequency features of the signal in the given time series, and a should be chosen large for the low-frequency features of the signal.

Scalograms, which visualize the output of the wavelet transform, show the intensity of different frequencies over time. When displayed in grayscale, it can be difficult to perceive important details [16,17]. Therefore, gray images are often converted to color images to enhance clarity. The choice of color mapping in these images is critical, as it influences how well human observers can detect important patterns, anomalies, or features. For instance, a heat map-style color scheme with a gradient from cool to warm colors (blue to red), such as the "jet" color map, can clearly distinguish between low- and high-energy regions. This clear contrast between low- and high-energy areas makes it easier to identify significant features in the data, such as spikes or frequency shifts [18].

2.3. AlexNet

The AlexNet CNN model was introduced by Alex Krizhevsky et al. in the ImageNet Large-Scale Visual Recognition Challenge (ILSVRC) competition to contribute to image classification problems [19]. This CNN model broke new ground in computer vision applications, surpassing all previous techniques [20]. AlexNet is a complex neural network consisting of 60 million parameters and trained with more than 1.2 million high-resolution images to classify 1000 different objects, and unlike previous models, it uses the ReLU activation function [21, 22]. As can be seen in the architecture in Figure 3, it consists of 5 convolution layers (Conv), three pooling layers (Max pool) and three fully connected layers (FC). There is also a ReLU activation layer after each convolution layer [23]. In the experimental studies, AlexNet was preferred due to its lighter weights compared to other popular CNN models such as GoogLeNet, VGG, and ResNet.

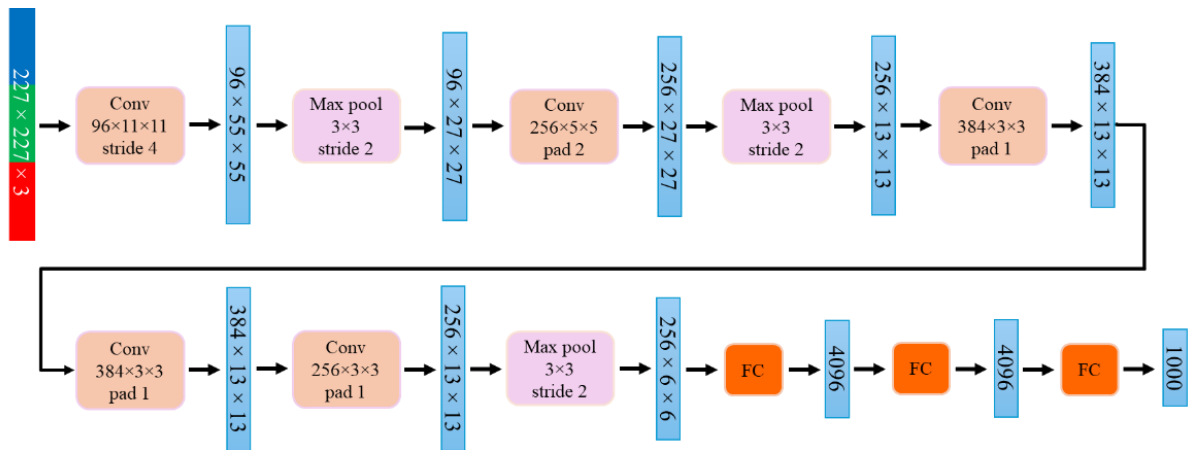


Figure 3. AlexNet architecture

Transfer learning is the reuse of any pre-trained machine learning model with different data with some fine-tuning [24]. The fine-tuning approach is based on optimizing certain parameters of a pre-trained model with a small subset of target data. Its widespread use by researchers is due to its advantages such as simplicity, ease of implementation and efficient use of computational resources [25].

In addition to exploiting prior knowledge in the source domain, this approach allows for more adaptive results by making localized adjustments for target domain-specific tasks. The main aim of transfer learning is to save training time and provide better performance without requiring too much data [26]. AlexNet transfer learning, which will be used in experimental studies, is shown in Figure 4. In experimental studies, the classifier layer connected to the last FC layer of the AlexNet model, details of which are given in Figure 3, was replaced with a regression layer.

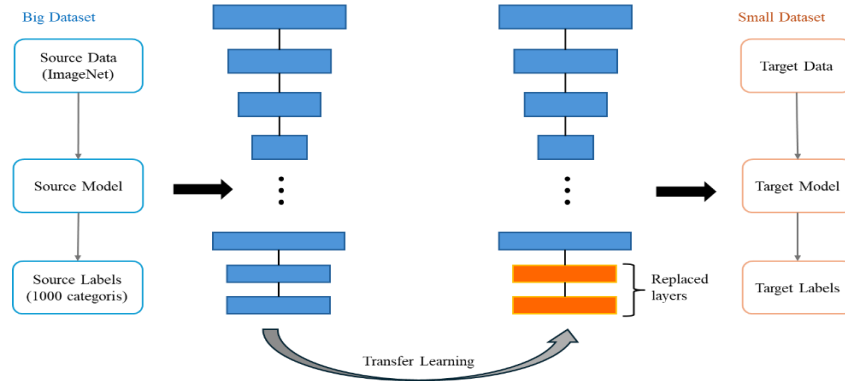


Figure 4. The schematic of AlexNet with transfer learning

2.4. Performance evaluation metrics

Three quantitative evaluation criteria were selected to assess the performance of the proposed method. These are the correlation coefficient (R), the mean absolute error (MAE), and the root mean square error (RMSE).

- RMSE indicates the amount of error between the values predicted by a model and the observed results. A smaller RMSE indicates better performance of the prediction model.
- MAE is a widely used measure for assessing the accuracy of a forecasted model. It is particularly used in regression analysis and determines the average magnitude of errors in predictions. A smaller MAE means higher prediction accuracy.
- R is a measure of the relationship between inputs and outputs [6].

Equations (2-4) of these metrics are given below [27].

$$RMSE = \sqrt{\frac{1}{n} \sum_{k=1}^n (y_k - x_k)^2} \quad (2)$$

$$MAE = \frac{1}{n} \sum_{k=1}^n |y_k - x_k| \quad (3)$$

$$R = \frac{\sum_{k=1}^n (x_k - \bar{x}_k)(y_k - \bar{y}_k)}{\sqrt{\sum_{i=1}^n (y_k - \bar{y}_k)^2 \sum_{k=1}^n (x_k - \bar{x}_k)^2}} \quad (4)$$

Where n is the total number of test data, x_k is the actual data values, y_k represent the anticipated data values and \bar{y}_k , \bar{x}_k are the mean values of the data.

3. Experimental Studies and Results

This section presents a concise overview of the experimental setup, and the results obtained in the prediction of wind speed. The experimental studies were conducted on a computer with the following specifications: MATLAB (2021b) installed, quad-core Intel i7 processor, NVIDIA GTX 850M GPU, and 16GB memory.

In the first stage of the experimental studies, time series were converted into images with CWT. For this purpose, the time series signals containing hourly wind speeds between 2018-2019 were first converted into a grey image with dimensions of 168×360 as shown in Figure 5. Subsequently, the changes in pixel brightness and contrast values within the grey image were assigned a jet128 color map of uniform distribution, resulting in a 168×360×3 color scalogram image. This image was then resized to 227×227×3 in accordance with the proposed AlexNet model input. All images were also normalized by mean subtraction.

In the first stage of the experimental studies, the whole dataset was randomly divided into three parts, namely training, validation and test, with 70%, 10% and 20% of the images, respectively, for transfer learning. The training dataset was used in the learning process of the proposed model, while the validation dataset was used as a part of the training set to build the model. The model parameters were also modified using the validation dataset. The performance evaluation was conducted using the test dataset.

The experiments were repeated several times to determine the best parameters of the model during the AlexNet training process. In the initial stages of the training process, the learning rate was adjusted to 0.0001, the mini-batch size was adjusted to 32, and the maximum number of epochs was adjusted to 40, with a drop factor of 0.5 applied every 10 epochs. Moreover, the adaptive moment prediction (Adam) algorithm was used to optimize the whole cost function for the AlexNet model to eliminate convolutional kernels during the back-propagation phase.

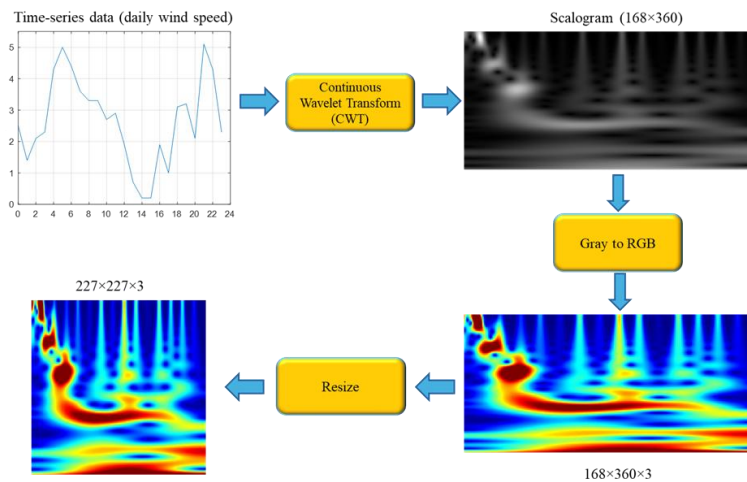


Figure 5. Convert to scalogram images from time series

The experiments were grouped by different forecast horizons to assess the proposed methods precision. The R, MAE and RMSE values for the one-hour, two-hour, and three-hour horizon forecasts of the suggested AlexNet model are presented in Table 1.

Table 1. Performance metrics of 1-hour, 2-hour and 3-hour horizon forecasting for AlexNet

Method	Horizon	Metrics		
		RMSE	MAE	R
AlexNet	1-hour	0.0335	0.0275	0.9517
	2-hour	0.0443	0.0357	0.8908
	3-hour	0.0505	0.0346	0.8365

The proposed AlexNet model has R, MAE and RMSE values of 0.0335, 0.0275 and 0.9517 for 1-hour horizon forecasts, respectively. Similarly, RMSE, MAE and R values for 2-hour horizon forecasts are 0.0443, 0.0357 and 0.8908, respectively. For 3-hour horizon forecasts, RMSE is 0.0505, MAE is 0.0346 and R is 0.8365.

The proposed model performs best for one-hour horizon wind speed forecasting. Therefore, in the proposed The AlexNet model, when utilized in conjunction with a one-hour forecast, can be regarded as a highly effective tool for the generation of more reliable and accurate forecast responses.

In addition, the visualization of certain time intervals to show the validity of the actual and normalized results of the one-hour, two-hour and three-hour horizon forecasts are shown in Figure 6 respectively. As can be seen from the graphs in Figure 6, the wind speed is better predicted in the actual and normalized curves of the 1-hour forecast.

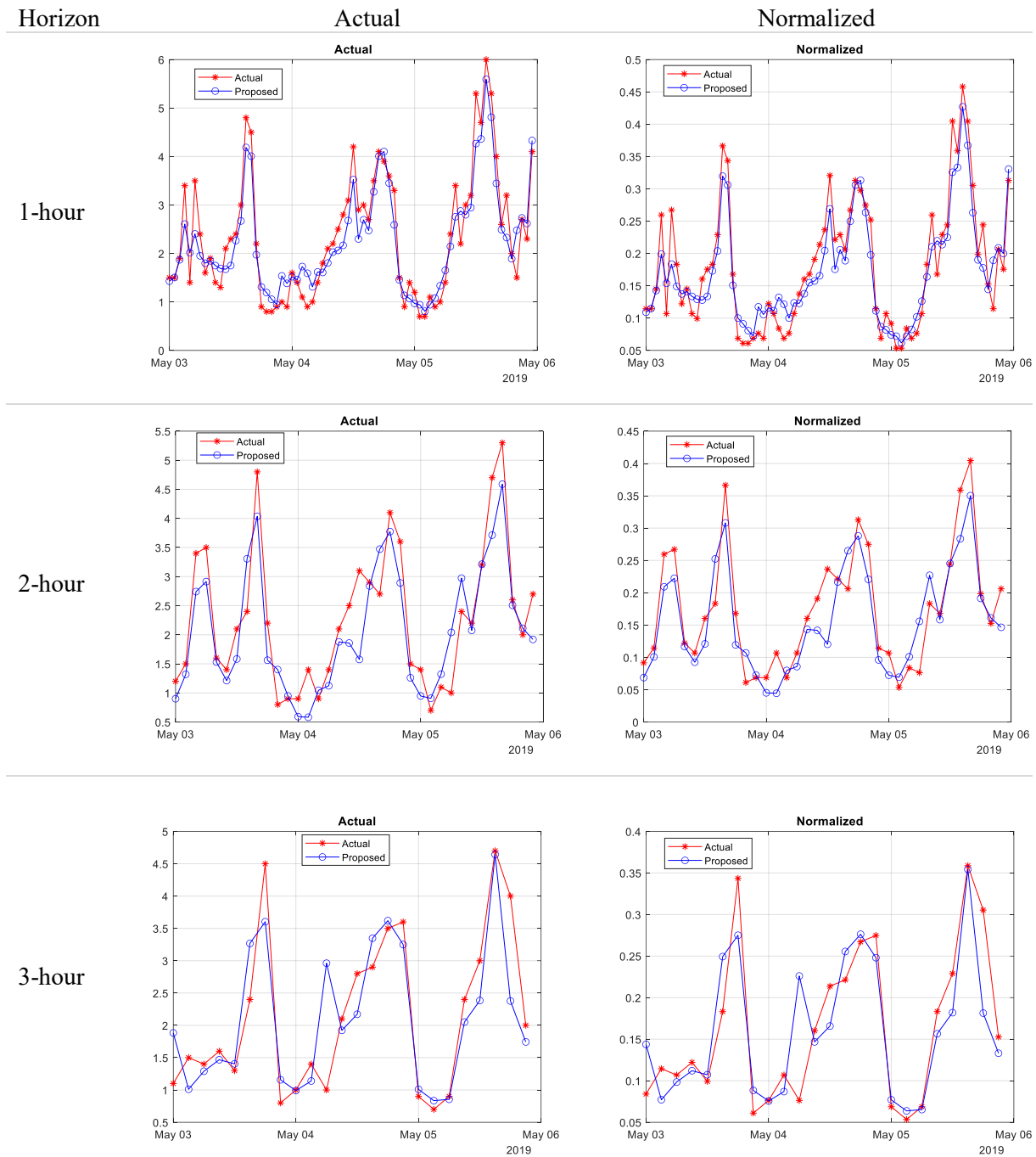


Figure 6. Wind speed forecasting results for 1-hour, 2-hour and 3-hour horizon

4. Conclusions

This study aims to develop a wind speed forecast model based on deep learning. This method involves first converting the wind speed data into scalogram images, which are then used to extract features from the AlexNet convolutional neural network model based on transfer learning to predict wind speed.

The results demonstrate that the proposed AlexNet model performs exceptionally well for shorter forecast periods. Specifically, the RMSE, MAE and R values for 3-hour horizon forecasts have performance values of 0.0505, 0.0346 and 0.8365, respectively. The 2-hour horizon forecasts show a slight increase in performance with RMSE, MAE and R values of 0.0443, 0.0357 and 0.8908, respectively. For the 1-hour

horizon forecasts, the model reaches RMSE, MAE and R values of 0.0335, 0.0275 and 0.9517, respectively, and it is observed that its performance is further improved, and it has a high level of accuracy and reliability.

The experimental results show that the 1-hour horizon forecast is the most effective and reliable for wind speed forecasting. Similarly, the actual and normalized speed forecast plots also support this conclusion. For the 1-hour horizon forecast, the actual and normalized results closely match the observed data, reinforcing the effectiveness of the model in short-term wind speed forecasting.

In future studies, the researchers will investigate the effects on CNN models by converting time-dependent wind speed data into images with different approaches to further improve short-term wind speed prediction accuracy.

5. Acknowledgment

We would like to thank Elazig Regional Directorate of Metrology for their support during the creation of the dataset.

6. Author Contribution Statement

Author 1: Provided a contribution to the literature review, conducted experimental studies, and prepared the article. Author 2: Contributed to experimental studies and evaluated the results obtained. Author 3: Contributed to the formation of the idea, the design of the study, and was responsible for spell check and content control of the manuscript.

7. Ethics Committee Approval and Conflict of Interest

Ethics committee permission is not required for this study. Additionally, there is no conflict of interest with any person or institution.

8. Reference

- [1] S. H. Yoon, S. Y. Kim, G. H. Park, Y. K. Kim, C. H. Cho, and B. H. Park, "Multiple power-based building energy management system for efficient management of building energy," *Sustain. Cities Soc.*, vol. 42, pp. 462–470, August 2018.
- [2] J. Zhang, C. Cheng, and S. Yu, "Recognizing the mapping relationship between wind power output and meteorological information at a province level by coupling GIS and CNN technologies," *Appl. Energy*, vol. 360, p. 122791, April 2024.
- [3] H. Wang, Z. Tan, Y. Liang, F. Li, Z. Zhang, and L. Ju, "A novel multi-layer stacking ensemble wind power prediction model under Tensorflow deep learning framework considering feature enhancement and data hierarchy processing," *Energy*, vol. 286, 2024.
- [4] D. Niu, M. Yu, L. Sun, T. Gao, and K. Wang, "Short-term multi-energy load forecasting for integrated energy systems based on CNN-BiGRU optimized by attention mechanism," *Appl. Energy*, vol. 313, 2022.
- [5] C. Yildiz, H. Acikgoz, D. Korkmaz, and U. Budak, "An improved residual-based convolutional neural network for very short-term wind power forecasting," *Energy Convers. Manag.*, vol. 228, 2021.
- [6] F. Demir, and B. Taşcı, "Predicting the power of a wind turbine with machine learning-based approaches from wind direction and speed data," in *2021 International Conference on Technology and Policy in Energy and Electric Power (ICT-PEP)*, pp. 37–40, 2021.
- [7] R. Azimi, M. Ghofrani, and M. Ghayekhloo, "A hybrid wind power forecasting model based on data mining and wavelets analysis," *Energy Convers. Manag.*, vol. 127, pp. 208–225, 2016.
- [8] K. U. Jaseena and B. C. Kovoov, "Decomposition-based hybrid wind speed forecasting model using deep bidirectional LSTM networks," *Energy Convers. Manag.*, vol. 234, 2021.
- [9] L. Li, Y. Li, B. Zhou, Q. Wu, X. Shen, H. Liu, Z. Gong, "An adaptive time-resolution method for ultra-short-term wind power prediction," *Int. J. Electr. Power Energy Syst.*, vol. 118, 2020.
- [10] F. Noman, G. Alkaws, A. A. Alkahtani, A. Q. Al-Shetwi, S. K. Tiong, N. Alalwan, J. Ekanayake, A. I. Alzahrani, "Multistep short-term wind speed prediction using nonlinear auto-regressive neural network with exogenous variable selection," *Alexandria Eng. J.*, vol. 60, no. 1, pp. 1221–1229, 2021.
- [11] A. Zameer, J. Arshad, A. Khan, and M. A. Z. Raja, "Intelligent and robust prediction of short-term wind power using genetic programming based ensemble of neural networks," *Energy Convers. Manag.*, vol. 134, pp. 361–372, 2017.
- [12] A. Altan, S. Karasu, and E. Zio, "A new hybrid model for wind speed forecasting combining long short-term memory neural network, decomposition methods and grey wolf optimizer," *Appl. Soft Comput.*, vol. 100, 2021.
- [13] C. Emeksiz and M. Tan, "Wind speed estimation using novelty hybrid adaptive estimation model based on decomposition and deep learning methods (ICEEMDAN-CNN)," *Energy*, vol. 249, 2022.
- [14] M. A. Gabry, A. Gharieb, M. Y. Soliman, I. Eltaleb, S. M. Farouq-Ali, and C. Cipolla, "Advanced Deep Learning for microseismic events prediction for hydraulic fracture treatment via Continuous Wavelet Transform," *Geoenergy Sci. Eng.*, vol. 239, 2024.
- [15] Q. Yu et al., "Cement pavement void detection algorithm based on GPR signal and continuous wavelet transform method," *Sci. Rep.*, vol. 13, no. 1, 2023.
- [16] M. Aslan, "CNN based efficient approach for emotion recognition," *J. King Saud Univ. - Comput. Inf. Sci.*, vol. 34, no. 9, pp. 7335–7346, 2022.
- [17] M. S. Jrad, A. E. Oueslati, and Z. Lachiri, "Image segmentation based thresholding technique: Application to DNA sequence scalograms," in *2016 2nd International Conference on Advanced Technologies for Signal and Image Processing (ATSIP)*, pp. 319–324, 2016.
- [18] B. Ari et al., "Wavelet ELM-AE based data augmentation and deep learning for efficient emotion recognition using EEG recordings," *IEEE Access*, vol. 10, pp. 72171–72181, 2022.
- [19] R. S. Salles et al., "Visualization of quality performance parameters using wavelet scalograms images for power systems," in *Congresso Brasileiro de Automática-CBA*, vol. 2, no. 1, 2020.
- [20] A. Krizhevsky, I. Sutskever, and G. E. Hinton, "ImageNet classification with deep convolutional neural networks," in *Advances in Neural Information Processing Systems*, pp. 1097–1105, 2012.

- [21] A. S. Nandhini, R. M. Aiyer, V. P. Kumar, and E. M. R. Nithin, "Pancreases segmentation and classification based on RCNN and AlexNet," in *EAI/Springer Innovations in Communication and Computing*, pp. 457–466, 2022.
- [22] H. C. Shin et al., "Deep convolutional neural networks for computer-aided detection: CNN architectures, dataset characteristics and transfer learning," *IEEE Trans. Med. Imaging*, vol. 35, no. 5, pp. 1285–1298, 2016.
- [23] N. V. Sridharan, S. Vaithyanathan, and M. Aghaei, "Voting based ensemble for detecting visual faults in photovoltaic modules using AlexNet features," *Energy Reports*, vol. 11, pp. 3889–3901, 2024.
- [24] T. Lu, B. Han, and F. Yu, "Detection and classification of marine mammal sounds using AlexNet with transfer learning," *Ecol. Inform.*, vol. 62, 2021.
- [25] X. Chen, T. Sun, X. Lai, Y. Zheng, and X. Han, "Transfer learning strategies for lithium-ion battery capacity estimation under domain shift differences," *J. Energy Storage*, vol. 90, 2024.
- [26] E. N. Zurel, Z. M. Alçin, and M. Aslan, "Konutlardaki elektrikli cihazların evrişimli sinir ağı ile otomatik sınıflandırılması," *Gazi Üniversitesi Fen Bilim. Derg. Part C Tasarım ve Teknol.*, vol. 10, no. 4, pp. 940–952, 2022.
- [27] E. S. Olivas, J. D. M. Guerrero, M. Martinez Sober, J. R. Magdalena Benedito, and A. J. Serrano López, *Handbook of research on machine learning applications and trends: Algorithms, methods, and techniques*, 2009, pp. 1–703.
- [28] H. Acikgoz, U. Budak, D. Korkmaz, and C. Yildiz, "WSFNet: An efficient wind speed forecasting model using channel attention-based densely connected convolutional neural network," *Energy*, vol. 233, 2021.



Hava Kirliliği Dinamikleri ve Kalitesine İlişkin İlgörüler: Türkiye'deki Akademik Araştırmaların Kapsamlı Bir Analizi

Saliha Çelikcan BİLGİN^{1*} , Turgay Tugay BİLGİN² 

¹Enerji Sistemleri Mühendisliği, Lisansüstü Eğitim Enstitüsü, Bursa Teknik Üniversitesi, Bursa, Türkiye.

²Bilgisayar Mühendisliği, Mühendislik ve Doğa Bilimleri Fakültesi, Bursa Teknik Üniversitesi, Bursa, Türkiye.

¹saliha.celikcanbilgin@gmail.com, ²turgay.bilgin@btu.edu.tr

Geliş Tarihi: 18.07.2024

Kabul Tarihi: 30.10.2024

Düzelme Tarihi: 11.09.2024

doi: <https://doi.org/10.62520/fujece.1518347>

Derleme Makalesi

Alıntı: S. Ç. Bilgin ve T.T. Bilgin, "Hava kirliliği dinamikleri ve kalitesine ilişkin ilgörüler: Türkiye'deki akademik araştırmaların kapsamlı bir analizi", Fırat Üni. Deny. ve Hes. Müh. Derg., vol. 4, no 1, pp. 163-181, Şubat 2025.

Öz

Hava kirliliği, insan sağlığı, sürdürülebilir çevre ve sosyo-ekonomik refah için uzun vadeli sonuçları olan ciddi bir küresel sorundur. Bu kapsamlı analiz, Türkiye'de 2022 ve 2023 yılları arasında DergiPark platformunda yayınlanan makalelerden elde edilen en son araştırma bulgularını birleştirerek hava kirliliğinin ve kalitesinin çok yönlü doğasına yer vermektedir. Çalışmamız, araştırma konularına göre makaleleri kategorize etmektedir. Temel bulgular, hava koşulları, şehirleşme, sanayinin hava kirliliği ve hava kalitesi üzerinde etkili olduğunu göstermektedir. Ayrıca, COVID-19 pandemisinin hava kalitesi dinamikleri ile etkileşime girdiği belirlenmiştir. Araştırmacılar, tahmin, değerlendirme ve modelleme için bir dizi yöntem kullanmışlardır. Bu konuda yenilikçi yaklaşımlarla üzerinde durulması gereken zorluklar devam etmektedir. Hava kirliliğini iklim değişikliği, kentsel gelişme ve ulaşım ile ilişkilendiren neden-sonuç yollarını araştırmak, sorunu daha iyi anlamamıza yardımcı olacaktır. Hava kirliliği ve kalitesinin insan sağlığı üzerindeki etkilerine ilişkin deneysel çalışma, bilinçli politika kararları almak özellikle savunmasız gruplar için önemlidir. Mevcut düzenlemelerin etkinliğini değerlendirmek ve yeni yaklaşımlar oluşturmak, etkili hava kalitesi yönetimine rehberlik edebilir. Sonuç olarak, bu makale, hava kalitesi ve kirliliği hakkında akademik araştırmaları derleyerek konunun yaygın etkisine dair kapsamlı bir inceleme sunmaktadır.

Anahtar kelimeler: Hava kirliliği, Hava kalitesi, COVID-19, İnsan sağlığı

*Yazışılan Yazar

İntihal Kontrol: Evet – Turnitin

Şikayet: fujece@firat.edu.tr

Telif Hakkı ve Lisans: Dergide yayın yapan yazarlar, CC BY-NC 4.0 kapsamında lisanslanan çalışmalarının telif hakkını saklı tutar.



Insights Into Air Pollution Dynamics and Quality: A Comprehensive Analysis Of Scholarly Research In Türkiye

Saliha Çelikcan BİLGİN^{1*} , Turgay Tugay BİLGİN² 

¹Energy System Engineering, Graduate School, Bursa Technical University, Bursa, Türkiye.

²Faculty of Engineering and Natural Sciences, Computer Engineering, Bursa Technical University, Bursa, Türkiye.

lsaliha.celikcanbilgin@gmail.com, 2turgay.bilgin@btu.edu.tr

Received: 18.07.2024

Revision: 11.09.2024

doi: <https://doi.org/10.62520/fujece.1518347>

Accepted: 30.10.2024

Review Article

Citation: S. Ç. Bilgin ve T.T. Bilgin, "Insights into air pollution dynamics and quality: A comprehensive analysis of scholarly research in Türkiye", *Firat Univ. Jour. of Exper. and Comp. Eng.*, vol. 4, no 1, pp. 163-181, February 2025.

Abstract

Air pollution affects human health, the environment, and the economy worldwide. This comprehensive analysis elucidates the intricate characteristics of air pollution and its quality by amalgamating the latest study outcomes derived from papers published on the DergiPark platform in Türkiye throughout the period spanning from 2022 to 2023. The papers in our study are classified according to their research themes. The main findings suggest that weather, urbanization, industry, and wildfires affect air pollution and quality. Additionally, the COVID-19 pandemic has affected air quality dynamics, requiring further study. Scientists have used various methods to forecast, evaluate, and simulate, but challenges remain that require new approaches. Investigating the causal pathways linking air pollution to climate change, urban development, and transportation will help us better understand the problem. Empirical study into the effects of air pollution and quality on human health is essential for making informed policy decisions, especially for vulnerable groups. Evaluating the efficacy of current regulations and establishing new approaches can help guide effective air quality. This paper is a comprehensive synthesis of scholarly studies pertaining to air quality and pollution, providing a comprehensive overview of the extensive ramifications associated with this subject matter.

Keywords: Air pollution, Air quality, COVID-19, Human health

*Corresponding author

1. Introduction

Air pollution has become one of the most pressing global issues due to its significant impact on both environmental sustainability and public health. Defined by the World Health Organization (WHO) as the contamination of indoor or outdoor environments by any chemical, physical, or biological agent that modifies the natural characteristics of the atmosphere, air pollution remains a multidimensional challenge [1]. It stems from a variety of sources, including industrial processes, transportation, residential energy use, and agriculture. Some pollutants are directly emitted from combustion sources as primary pollutants, with elemental carbon being the main constituent of particulate matter (PM). Others are formed in the atmosphere as secondary pollutants, such as nitrates, sulfates, and organic carbon, through complex physicochemical processes involving gaseous precursors from combustion sources, agriculture (ammonia), various anthropogenic activities, and natural processes like biogenic emissions [2]. The most concerning pollutants, such as particulate matter (PM_{2.5} and PM₁₀), sulfur dioxide (SO₂), nitrogen dioxide (NO₂), carbon monoxide (CO), and ozone (O₃), have been linked to severe health outcomes, including respiratory and cardiovascular diseases [3], neurological damage [4], and even premature death [5]. The detrimental effects of poor air quality also extend to ecosystems, leading to biodiversity loss and harm to wildlife [6, 7]. In addition to other pollutants, exposure to volatile organic compounds (VOCs), which are widely found in gaseous form, has also been shown to be linked to serious health effects such as cancer, obesity and diabetes, and cardiovascular issues [8-10].

National and international authorities, such as the WHO, have implemented guidelines and regulations to mitigate air pollution and protect public health. These efforts have led to the establishment of air quality standards for key pollutants and the promotion of measures to reduce emissions. For instance, the World Health Organization's air quality guidelines have set threshold levels for pollutants including PM_{2.5}, PM₁₀, NO₂, SO₂, CO, and O₃. The 2021 guidelines specify an annual limit of 5 µg/m³ for PM_{2.5}, 15 µg/m³ for PM₁₀, and 10 µg/m³ for NO₂. Additionally, the guidelines establish an 8-hour limit of 100 µg/m³ for O₃, a 24-hour limit of 40 µg/m³ for SO₂, and 4 µg/m³ for CO, demonstrating the continuous updates made in response to new scientific evidence [11]. Exceeding these threshold levels can lead to serious health issues, environmental damage, and deterioration of air quality.

Clean air is a human right and fundamental to many of the United Nations' sustainable development goals, including good health, climate action, sustainable cities, clean energy, and the protection of life on land and in the sea [12]. In line with global efforts, Türkiye has incorporated air quality targets into its commitment to the United Nations Sustainable Development Goals (SDGs), aiming to reduce air pollution-related deaths and diseases by 2030 [13]. Achieving these goals will rely heavily on scientific research contributions.

The increasing urgency to address air quality has drawn attention from a wide range of disciplines, including chemistry, biology, environmental engineering, meteorology, public health, and economics. This multidisciplinary focus has resulted in a surge of studies on pollution sources, the spatial and temporal variations of air quality, interactions between pollutants and environmental parameters, and their impacts on human health and ecosystems. For example, in a study by Chen et al., there has been a marked increase in the number of publications on air pollution control over the past two decades, with a particularly rapid rise since 2018, demonstrating the continuous growth in academic interest in this field, as shown in Figure 1 [14].

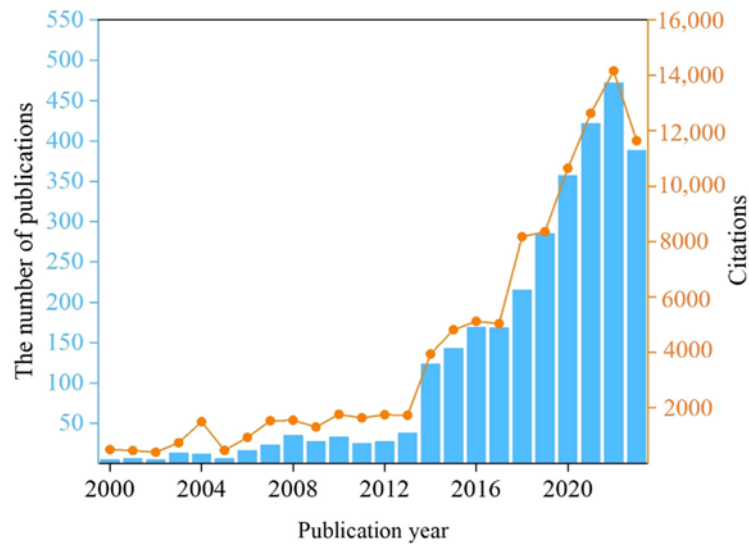


Figure 1. The annual number of publications on air pollution control [14]

In Türkiye, the understanding of the causes and consequences of air pollution, as well as the development of new technologies to prevent pollutant emissions, has become a focal point of scientific research. This review aims to present a compilation of the scientific contributions made by Turkish researchers between 2022 and 2023. By summarizing these works, the review provides insights into the latest developments in air pollution research in Türkiye, highlights the challenges and progress in this field, and aims to create a forecast for future studies.

This study specifically examines articles published on the DergiPark platform, hosted by TÜBİTAK ULAKBİM (The Scientific and Technological Research Council of Türkiye, Informatics and Information Security Advanced Technologies Research Center), which provides editorial management services for electronically published academic journals. We analyzed 50 articles addressing various aspects of air pollution, categorizing them by their topics and examining them under main headings. These articles offer a comprehensive perspective on air pollution, highlighting the complexity of the subject through discussions of various factors. Furthermore, examples from significant studies conducted in different regions of Türkiye are included to illustrate the broader context of air pollution research.

2. Methodology

This article constitutes a review encompassing significant studies identified through a search conducted on articles published in DergiPark between 2022 and 2023. The search criteria included articles with key terms "air pollution" or "air quality." Additionally, variations of these terms such as "Outdoor Air Quality," "Air Quality Index," "Daily Air Quality Index," "Urban Air Quality," and "Perception of Air Pollution" were included in the review. In some instances, articles were selected based on the combination of two of these keywords, as specified by the authors. Figure 2 illustrates the distribution of articles according to the selected keywords.

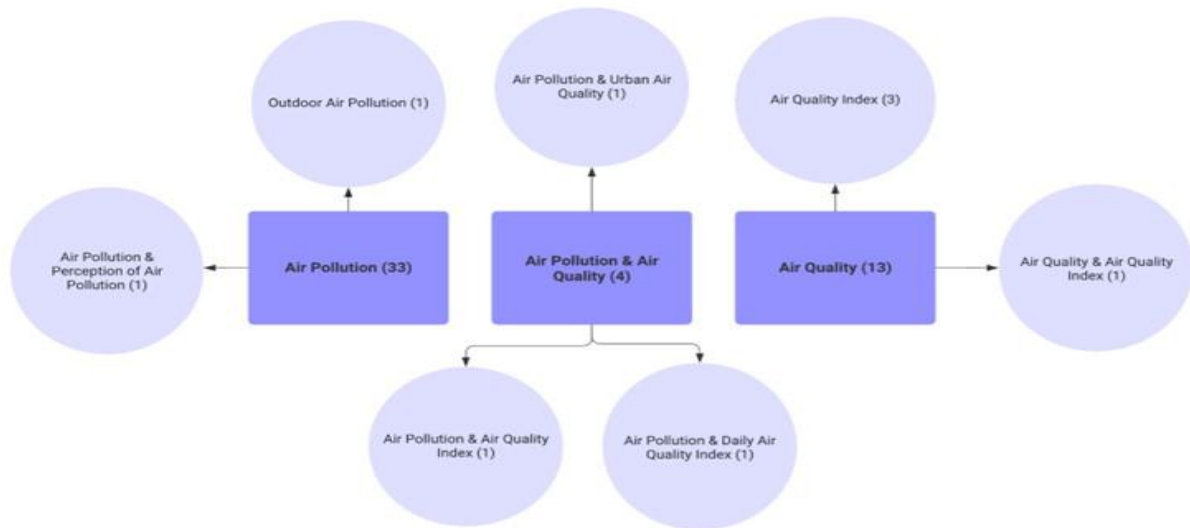


Figure 2. The distribution of articles classified by the selected keywords

Figure 3 illustrates the link between the articles' major phrases. Only terms that were unique to the relationship analysis file were removed to show the density of relationships between keywords. The visual depiction shows the additional keyword selections made by authors who chose 'Air Pollution' and 'Air Quality' for their publications.

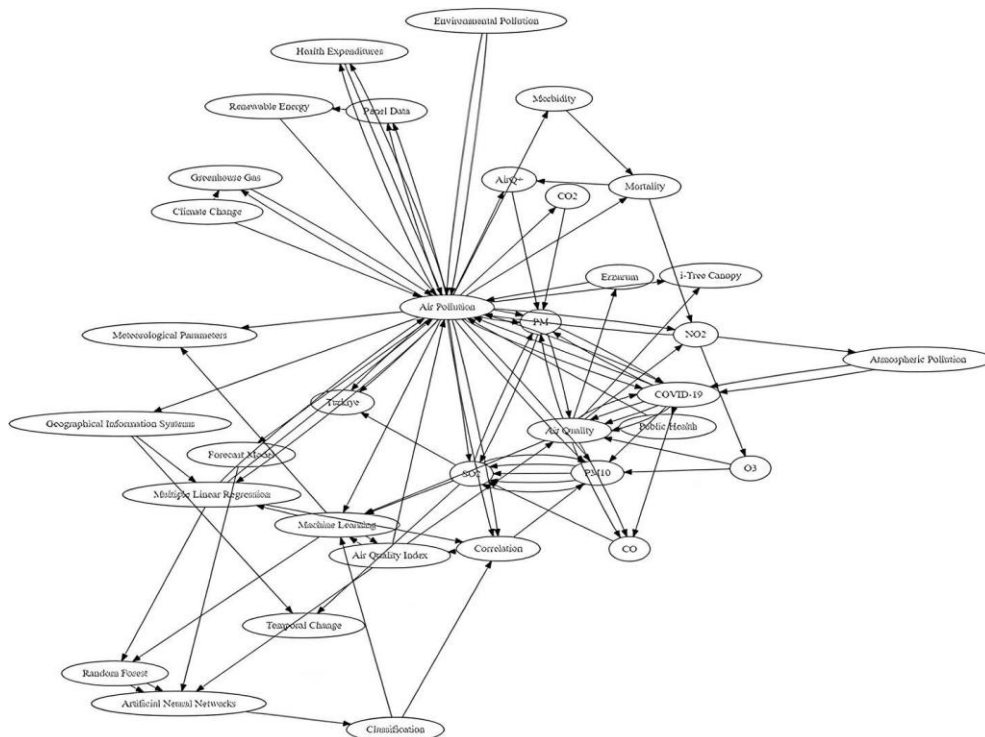


Figure 3. The keywords graph displays extra keywords chosen by authors who selected the 'Air Pollution' and 'Air Quality' keywords

Air pollution is an interdisciplinary topic that enables academics from numerous fields to collaborate. Interdisciplinary collaboration is critical for improving a complete understanding of air pollution challenges and contributing to the development of long-term remedies. The departments reported by the authors as affiliations in the analyzed publications were also investigated in this context. Figure 4 shows a graphic depiction of the reviewed articles that involved transdisciplinary studies.

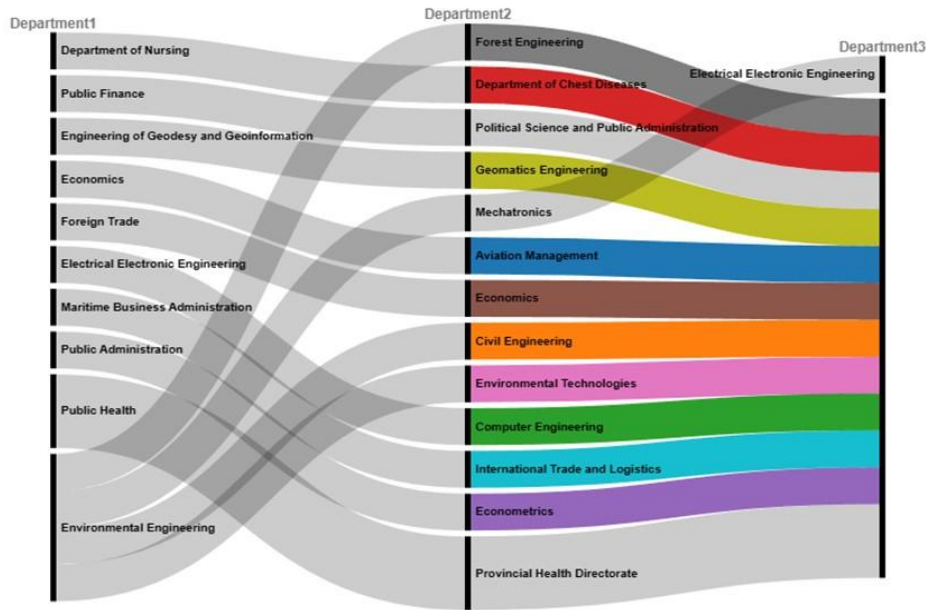


Figure 4. The distribution of studied articles across author affiliations in multidisciplinary air pollution articles

As depicted in Figure 4, researchers from the departments of Environmental Engineering, Mechatronics, and Electrical-Electronics Engineering have collaboratively contributed to studies on air pollution/quality. Following all these preliminary assessments, all articles have been organized under six distinct headings: Temporal/spatial variations in air quality, the relationship between various parameters and air quality, air pollution/quality prediction, the relationship between air quality and health, COVID-19, and other studies and review articles.

2.1. Temporal and spatial analysis of air quality

An analysis was conducted on the temporal and spatial variations of air pollution in different provinces of Türkiye, using eight articles obtained from DergiPark. The study areas, pollutants examined, and meteorological parameters used are presented in Table 1. Meteorological parameters are of paramount importance in the field of air pollution research. Consequently, Table 1 presents studies that make use of meteorological data.

Table 1. Provinces where temporal and spatial changes in air quality are analyzed with pollutant and meteorological data

Location	Pollutants	Meteorological Data	Reference
Kocaeli	SO ₂ , CO, O ₃ , HCHO, NO _x , PM ₁₀ , Aerosol Index	-	[15]
Muş	PM ₁₀ , SO ₂	-	[16]
Mardin	PM ₁₀ , SO ₂	-	[17]
Bayburt	NO _x , NO, NO ₂ , O ₃ , SO ₂ , PM ₁₀	wind direction, wind speed, pressure, relative humidity, temperature	[18]
Karabük	SO ₂ , CH ₄ , CO, CO ₂ , NO _x , O ₃ , PM _{2.5} , PM ₁₀ , VOC	temperature, humidity, atmospheric pressure	[19]
Kütahya	PM (0.3, 0.5, 1, 2, 5, 10 µm), CO ₂	-	[20]
Kocaeli	PM ₁₀ , SO ₂	-	[21]
Erzurum	PM ₁₀ , SO ₂	average temperature, wind speed, wind direction, relative humidity, precipitation	[22]

The initial study conducted in Kocaeli aimed to investigate the spatial distribution of pollutants released into the atmosphere and approximate elevation levels they reach. Utilizing Sentinel-5P satellite data and local station data, the research identified regions with significant air pollution, particularly along the coast of the Gulf of Izmit and specific districts. Moreover, it was revealed that pollutants concentrate within the range of 0-500 meters in elevation [15].

In another study focusing on Muş, researchers observed that between 2012 and 2021, the values of PM₁₀ and SO₂ frequently exceeded the annual average values specified in the Air Quality Assessment and Management Regulation [16]. Another study focusing on pollution levels in Mardin between 2010 and 2021 revealed that both PM₁₀ and SO₂ levels significantly exceeded the regulatory limits specified in both WHO and Turkish regulations during the specified period. This was proved by statistical analyses using Analysis of Variance (ANOVA) and multiple comparison (TUKEY) tests. The high levels of pollutant parameters in the summer and fall seasons compared to other seasons in the province were found to be related to the movement of desert dust [17]. Furthermore, the research by Hirca et al. in Bayburt city center employed statistical methods to analyze the temporal variations of air pollutants, their interactions with local meteorological parameters, and trends. According to the results of the Mann-Whitney U test, the averages of pollutant concentrations during the cold season were statistically significantly dissimilar to the averages during the warm season. Additionally, the Kruskal-Wallis test indicated a statistically significant difference in pollutant concentration averages across the years. Post-Hoc/Tamhane's T2 analysis was performed to identify the years that were significantly different. Furthermore, Spearman's rho (ρ) correlation analysis results demonstrated a statistically significant relationship between air pollutants and meteorological parameters. Using the Innovative Trend Analysis (ITA) method, a decrease in PM₁₀ levels and an increase in other pollutants were observed in Bayburt [18]. Karabük province used a new air pollution measurement device designed to simultaneously measure numerous atmospheric parameters along with SO₂, CH₄, CO₂, CO, NO_x, O₃, PM_{2.5}, and Volatile Organic Compounds (VOC) pollutant parameters. The study demonstrated high concentrations exceeding the standards for SO₂, CO, NO_x, and PM_{2.5}. Additionally, the impact of seasonal variations and atmospheric parameters on pollution levels has been emphasized [19]. In his article on Kütahya, İşinkaralar identified high levels of pollution in the province, primarily caused by heating, fuel types, industrial activities, and transportation [20].

Kotan and Erener conducted a study examining temporal and spatial changes in air pollution using PM₁₀ and SO₂ data in Kocaeli. Seasonal pollution maps created for the years 2008, 2014, and 2019 were subjected to overlay analysis, a Geographic Information Systems technique, revealing seasonal variations in pollutant concentrations across the province. Despite a decrease in concentration values from 2008 to 2019 throughout the province, localized areas exceeding the pollutant concentration limit values set by the European Union and national regulations were identified in 2019 [21]. A study examining the air quality in the city atmosphere of Erzurum from the winter of 1978-1979 to the period of 2018-2019 with SO₂ and PM₁₀ parameters found that the use of natural gas led to a significant structural change in air quality in 2006 and 2009 [22].

2.2. The relationship between various parameters and air quality

Air quality can be influenced by various factors, including meteorological conditions [23], urbanization [24], transportation [25], industrialization [26], wildfires [27], vegetation [28], and many other parameters, all of which can contribute to or affect the formation or magnitude of air pollution. A detailed analysis of the air pollution parameters and their influencing factors is presented in Table 2, based on studies published in DergiPark.

Table 2. Comparative study of air quality indicators and their determinants

Location	Pollutants	Parameters	Findings	Ref.
Marmara	PM _{2.5} , PM ₁₀ , SO ₂ , O ₃ , CO, NO _x	Spatial, meteorological, anthropogenic data	NO _x and O ₃ are influenced by anthropogenic factors, while PM is affected by meteorological and spatial factors.	[29]
Bolu	PM ₁₀ , SO ₂ , NO, NO ₂ , NO _x , CO	Temperature, pressure, wind direction/speed, humidity	Moderate correlation with temperature, pressure, and wind direction; low correlation with speed and humidity.	[30]
Muş	PM ₁₀ , SO ₂	Temperature, wind speed/direction, pressure, humidity	PM ₁₀ is influenced by pressure (positive) temperature and wind speed (negative); SO ₂ by temperature (negative) and humidity (positive).	[31]
Çanakkale	O ₃	Temperature, wind speed/direction, solar radiation, humidity, total precipitation	Ozone levels have a positive correlation with temperature and solar radiation, and a negative correlation with relative humidity.	[32]
Balıkesir	SO ₂ , PM ₁₀	Temperature, wind speed, humidity, pressure and mixing heights	PM ₁₀ levels are negatively correlated with wind speed and temperature, while SO ₂ levels correlate negatively with temperature and mixing height.	[33]
Erzurum	SO ₂ , PM ₁₀ , CO, NO _x , NO, NO ₂ , O ₃	Pressure, altitude, wind, temperature, natural gas/coal consumption, Sky View Factor	Fuel consumption is identified as the primary factor affecting air pollution, while secondary parameters include wind speed and street orientations.	[34]
Konya	CO	Urban Heat Island (UHI)	The amount of heat in the city is directly proportional to the increase in CO.	[35]
Adıyaman	SO ₂ , PM ₁₀	Solar power plants daily electric energy values	There is a notable correlation between air pollution levels and solar energy efficiency.	[36]
Antalya	PM ₁₀ , PM _{2.5} , SO ₂ , CO, O ₃	Wildfires data	The 2021 wildfires had no significant effect on air quality.	[37]
İstanbul	CO, NO ₂ , NO _x , O ₃ , SO ₂ , PM ₁₀ , PM _{2.5}	Traffic sensor data.	Increased vehicle numbers and traffic congestion raise AQI levels.	[38]
General Study	-	Information collected from various sources	Restrictions on ship speed will reduce CO ₂ , black carbon, nitrogen oxides, and nitrous oxide emissions.	[39]
Zonguldak	eCO ₂	Types of vehicles, distances traveled, amounts of waste	Inspection station location affects carbon emissions.	[40]
Altınpark Ankara	O ₃ , NO ₂ , PM _{2.5} , SO ₂ , CO	Land/canopy cover data	Tree/shrub cover and species diversity significantly improve air quality.	[41]
Kuzguncuk İstanbul	CO ₂ , CO, NO ₂ , O ₃ , SO ₂ , PM _{2.5} , PM ₁₀	Land/canopy cover data	Tree/shrub cover helps remove pollutants and contributes economically.	[42]
APEC Countries	-	Economic and environmental indicators	A long-term relationship has been found between the welfare cost of premature deaths caused by ambient particulate matter, real Gross Domestic Product (GDP), trade openness, and renewable energy supply.	[43]
Türkiye	per capita PM	Economic growth, environmental patents, regulations	Economic growth increases pollution, while patents and regulations help reduce it.	[44]
General Study	PM ₁₀	Health expenditure, GDP, population, information communication technologies data	The findings show that air pollution and mobile phone subscriptions have no effect on health expenditures, while internet subscriptions and index variables negatively impact health spending.	[45]

For instance, in a study investigating the impact of spatial, meteorological, and anthropogenic factors on air quality in the Marmara Region, it is emphasized that anthropogenic variables predominantly influence NO_x among the pollutants examined, while meteorological and spatial factors affect particulate matter levels [29]. During their study examining the impact of meteorological parameters on air pollution in Bolu province between 2017 and 2020, Ünal and Özel discovered that contaminants had a moderate association with temperature, air pressure, and wind direction, but a low relationship with wind speed and relative humidity [30]. Another study on the relationship between and air pollution and meteorological parameters was conducted for the province of Muş, revealing that temperature and wind speed (negative), pressure (positive), significantly influence the variations in PM₁₀ levels, while for the SO₂ parameter, temperature (negative) and humidity (positive) were identified as the most influential variables [31]. A study in Çanakkale province examined how meteorological characteristics like temperature, wind speed, and relative humidity affect O₃. The study revealed that the most significant factors influencing ozone concentration levels in the province

are meteorological parameters and pollutants released into the atmosphere from anthropogenic sources (such as vehicles, industrial emissions, solvents, and volatile organic compounds (VOCs) emitted by industries) transported over long distances [32]. In another study focusing on the city center of Balıkesir as the study area, it was demonstrated that among meteorological parameters, wind speed and temperature exhibited the highest correlation coefficients concerning the variations in SO₂ and PM₁₀ levels [33].

In a study conducted in Erzurum, various residential structures were examined in terms of emission rates and geographical variables triggering air pollution (pressure, altitude, wind, temperature) and physical variables (natural gas consumption, coal consumption and Sky View Factor), and recommendations related to residential structures were shared to mitigate pollution [34]. According to the results of the study examining the relationship between urban heat island and carbon monoxide concentration in three central districts of Konya, the urban heat island effect in the city has a positive correlation with carbon monoxide levels [35]. Investigating the influence of solar power plants on air pollution in Adıyaman province, researchers observed a notable correlation between air pollution levels and the energy efficiency derived from solar energy facilities [36].

Analyzing the impact of wildfires on air quality, researchers focused on Antalya, the most heavily affected province by wildfires in Türkiye in 2021. Comparing air quality data before and after the fire, the study concluded that the 2021 forest fire did not have a detrimental effect on air quality in Antalya and its vicinity [37].

Researchers examining the relationship between air quality and traffic through large-scale geographic data analysis have found that an increase in the number of vehicles passing through a point and a decrease in vehicle speeds due to traffic congestion result in an increase in Air Quality Index (AQI) value [44]. In another study, the European Green Deal has been evaluated in terms of air pollution caused by maritime transportation [38].

Ören and Kocabaş investigated the effect of vehicle inspection station location selection on carbon emissions in Zonguldak [39]. A research in Altınpark in Ankara found that tree and shrub canopy cover, as well as the variety and number of tree species present, significantly improves air quality [40]. A comparable study was undertaken for the Kuzguncuk Neighborhood of Istanbul, evaluating the quantity of removal of various air pollutants by tree-shrub cover and the economic contribution made by the removal of these pollutants [41]. There are certain factors influenced by air pollution. Many scholars are interested in the economic and social implications of pollution. Çetin and Bakırtaş examined the long-term effects of increased renewable energy supply on the welfare costs of air pollution-related premature deaths in Asia-Pacific Economic Cooperation (APEC) countries from 1990 to 2016 in their study. They found that the increase in renewable energy sources supply reduces the welfare costs of air pollution [42]. A research comparing the impacts of economic growth and environmental regulations on air pollution in Türkiye found that economic growth has a positive influence on air pollution, whilst the number of patents linked to environmental technologies has a negative effect on air pollution. The study also emphasizes the major influence of environmental rules on lowering air pollution in the short and medium term [43]. In their study, Özgür and Demirtaş stated that they could not find any significant effect of social capital on air pollution [45].

2.3. Air pollution and air quality prediction

The increasing data processing capacity of computers, combined with the integration of artificial intelligence technologies alongside statistical methods, has enabled faster and more accurate results with multidimensional data. A review study focusing on articles published worldwide from 1990 to 2021, which include keywords related to air pollution and machine learning, has been conducted. This study shows that research on air pollution using machine learning has drastically surged since 2017, as depicted in Figure 5. Furthermore, as reported in the same research, Türkiye is ranked 8th for the number of publications, placing it just behind the United Kingdom [46].

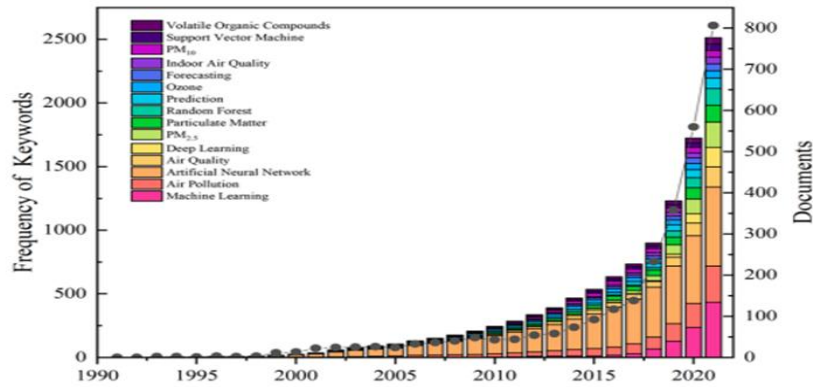


Figure 5. Trends in research on air pollution utilizing machine learning methods from 1990 to 2021 [46]

Between 2022 and 2023, 7 out of every 50 articles published on the DergiPark platform are on air pollution prediction or air quality indicators. One of the selected research regions is from another country, while the others are in Türkiye. Table 3 includes the study locations, pollutant characteristics utilized in the forecasts, projected pollutant information, meteorological data used in the predictions, and forecasting methodologies (Lognormal (LogD), Weibull (WD), and Gamma Distribution (GD), Multiple Linear Regression (MLR), Naive Bayes (NB), Decision Tree (DT), Deep Learning (DL), k-NN, Random Forest (RF), Artificial Neural Network (ANN), Support Vector Machines (SVM), k-NN, Logistic Regression (LR), Bagging, ANN, Multilayer Perceptron (MLPNN), Extreme Learning Machines (ELM)).

Table 3. Location-based analysis of pollutants, methodologies, and success criteria

Location	Pollutants	Other Data	Methods	Success Criteria	Ref.
Van	PM ₁₀	-	LogD, WD, GD	GD R ² : 0.9893	[47]
Ardahan, Kars, Erzurum, Iğdır	AQI	Meteorological data	MLR, NB, DT, DL, RF, k-NN	Accuracy Rates: MLR: 41.8%, NB: 68.91%, DT: 70.29%, DL: 73.05% k-NN: 73.35%, RF: 74.89%	[48]
Kocaeli	Seasonal PM ₁₀ , SO ₂	Urbanization, industrialization, topography meteorological, and demographic data	MLR, ANN	For PM ₁₀ Best Model: ANN MAPE 4.91%-Spring For SO ₂ Best Model: ANN MAPE: 21.76% Winter	[49]
USA	PM _{2.5} , PM ₁₀ , NO ₂ , O ₃ , CO, SO ₂ , AQI	Urbanization, transportation data	SVM, k-NN, NB, LR, RF, DT, Bagging, ANN	Best Model: 3-class models RF: 86.69% 5-class models RF: 81.61%	[50]
Başakşehir İstanbul	PM ₁₀ , CO, SO ₂ , NO ₂ , NO _x , O ₃	Meteorological data	MLR, k-NN, SVM, RF, DT, MLPNN	Best Method: For PM ₁₀ , CO, SO ₂ , O ₃ RF (MAPE: 0.28, 0.2, 0.418, 0.169 respectively) For NO ₂ MLR (MAPE: 0.016)	[51]
Sıhhiye Ankara	PM ₁₀ , SO ₂ , CO, AQI	Meteorological data	ELM, ANN	AQI Classification Prediction Success Rate: ELM: 85.71% ANN: 71.43%	[52]
Beşiktaş İstanbul	PM _{2.5} , PM ₁₀ , NO _x , SO ₂	Traffic density, and meteorological data	ANN, MLR, SVM, RF	Best Model: RF R ² : 0.675	[53]

The first paper on air pollution prediction chose Van province as its study region. The study focuses on Van province in Eastern Anatolia, Türkiye, and models PM₁₀ levels, a crucial air pollutant, using lognormal,

Weibull, and Gamma distributions. The study also predicts PM₁₀ concentrations that exceed legal limits, indicating that the Gamma distribution beat the other two in effectively modeling and predicting province-wide exceedances [47]. Akgün and Barlık examined several linear regression and machine learning algorithms (Deep Learning, K-Nearest Neighbors (k-NN), Naive Bayes, Decision Tree, Random Forest) to forecast air quality index in Ardahan, Kars, Erzurum, and Iğdır provinces. The Random Forest technique produced the highest accuracy in forecasting the Air Quality Index (AQI) [48]. In another study, artificial neural network and multiple linear regression approaches were used to forecast seasonal averages of PM₁₀ and SO₂ levels in Kocaeli. The models drew on meteorological, pollution, urbanization, industrialization, topography, and demographic data. The study discovered that artificial neural networks beat multiple regression analysis in terms of performance [49]. Another study addressed the air quality classification problem by taking into account factors such as population, the quantity of concrete structures, green spaces, and transportation utilization ratios. Class assignments were based on the impact ratios of Air Quality Index (AQI) values on human health, which were divided into three categories (Good, Unhealthy, and Hazardous) and five categories (Good, Moderate, Unhealthy, Very Unhealthy, and Hazardous). The study used eight different classification algorithms (Bagging, Artificial Neural Networks Decision Trees, Logistic Regression, K-Nearest Neighbors (k-NN), Gauss Naive Bayes, Support Vector Machines and Random Forest) and found that the Random Forest algorithm produced the highest classification accuracy [50]. The Başakşehir area of Istanbul was used to forecast concentrations of NO₂, SO₂, CO, PM₁₀, and O₃ pollutants using Support Vector Machines, Multiple Linear Regression, K-Nearest Neighbors (k-NN), Random Forest, Multilayer Perceptron, and Decision Trees techniques. Notably, the Random Forest technique performed better in forecasting CO, SO₂, O₃, and PM₁₀ concentrations than Multiple Linear Regression in predicting NO₂ [51]. A study used Artificial Neural Networks (ANN) and Extreme Learning Machines (ELM) algorithms to forecast the Air Quality Index (AQI) in Sıhhiye/Ankara. The results showed that the ELM algorithm outperformed the ANN algorithm in making more accurate predictions [52]. PM_{2.5} concentrations in Beşiktaş, Istanbul, were forecasted using various machine learning methods. While Random Forest achieved the highest accuracy on average, Multiple Linear Regression performed the worst [53].

2.4. Health implications of air pollution

Air pollution poses a significant threat to human health, with numerous studies linking exposure to harmful pollutants to a wide range of adverse health outcomes. Exposure to air pollutants such as PM_{2.5}, PM₁₀, SO₂, NO_x, CO, and heavy metals has been linked to significant health risks, including respiratory issues [54], [55] and cognitive decline [56]. PM_{2.5}, in particular, has been associated with increased hypertension risk [57], adverse cardiovascular outcomes [58], and heightened cancer risk [54], [59] due to the presence of heavy metals. Airborne pollutants induce oxidative stress and inflammation, exacerbating conditions like asthma and contributing to chronic diseases that affect multiple organs [60]. Studies have also shown a connection between air pollution and increased mortality from respiratory and cardiovascular diseases [61].

Numerous research has been undertaken in Türkiye to investigate the relationship between air pollution and health, documenting the effects on major health indicators such as respiratory disorders, cardiovascular diseases, and mortality risk. During the research period, DergiPark published 7 research articles in Table 4 on the effects of air pollution on human health, the pollution-mortality relationship, and the cost of pollution-related health problems.

Table 4. Health impacts and health-related expenditures due to air pollution in Turkish cities and nationwide

Location	Pollutant	Findings	Ref.
Samsun	PM ₁₀	Hospital admissions and hospitalizations increased by 1-3% for every 10 µg/m ³ rise in PM ₁₀ levels.	[62]
Konya	PM _{2.5}	The study results show that premature deaths during the 3-year period could have been prevented if PM _{2.5} levels had stayed below 10 µg/m ³ .	[63]
Sakarya	NO ₂	Increase in annual NO ₂ concentrations in 2018 and 2019 led to a rise in mortality attributable to NO ₂ for the age group of 30 and older.	[64]
Ankara	PM _{2.5} , PM ₁₀	Calculations with PM _{2.5} and PM ₁₀ did not show an effect of particulate air pollution on infant deaths in the first week.	[65]
Türkiye	SO ₂ , NO ₂ , PM _{2.5} , PM ₁₀ , CO, non-methane volatile organic compound (VOC)	The health costs arising from air pollution in Türkiye are estimated to be at least 25,845 million TL and up to 52,492 million TL.	[66]
Türkiye	PM ₁₀	An increase of 1% in economic growth boosts healthcare spending by 2.018%, while a 1% rise in transportation-related air pollution increases costs by 0.266%.	[67]
Türkiye	PM ₁₀	Results indicate that air pollution and mobile subscriptions do not affect healthcare spending, while internet subscriptions and index variables negatively impact costs.	[68]

A study conducted in Samsun Province found that a 10 µg/m³ increase in PM₁₀ levels resulted in a 3% rise in respiratory system diseases, a 2% rise in cardiovascular diseases, a 1% rise in neurological and psychiatric diseases, and a 2% rise in respiratory system hospitalizations [62]. Two additional studies focusing on Konya and Sakarya revealed that air pollution increases mortality [63, 64]. Another study examined the association between particle air pollution and newborn mortality [65].

There are three studies looking at the health costs of air pollution from diverse angles. One study estimated that the health cost of air pollution in Türkiye ranged from 25.845 million TL to 52.492 million TL [66]. Another study discovered that a 1% increase in air pollution from mobility resulted in an increase in health expenses ranging from 0.266% to 0.381% [67]. In a study of the impact of Information and Communication Technologies (ICT) on health expenditures related to air pollution, it was demonstrated that air pollution and the number of mobile phone subscribers had no significant impact on health expenditures, whereas the number of internet subscribers and index variables had a negative impact on health expenditures [68].

2.5. COVID-19 pandemic and its influence on air quality

The COVID-19 epidemic, which has swept the planet since 2020, has provided new opportunities for researchers to evaluate the regional and global influence of human activities on air quality. The pandemic's restrictions on outdoor activities have resulted in major changes in pollution levels in the atmosphere. Numerous studies have been undertaken to assess the improvement in air quality when human intervention is reduced [69], [70]. Following numerous studies conducted worldwide on the effects of COVID-19, many studies have also been carried out in Türkiye during this period, and the findings summarized in Table 5 highlight the significant impacts of the pandemic on air pollutants in various regions.

Table 5. Impact of COVID-19 on Air Pollutants in Türkiye

Location	Pollutant	Findings	Ref.
Adana, Ankara, Antalya, Denizli, Edirne, Erzurum, Istanbul, Izmir, Kayseri, Kocaeli, Trabzon, Zonguldak	PM ₁₀ , NO ₂ , SO ₂ , CO, O ₃	PM ₁₀ , NO ₂ , and SO ₂ levels dropped by up to 75-80%, while CO and O ₃ concentrations increased in many cities.	[71]
78 provinces including Ankara, Istanbul, Izmir	PM ₁₀ , SO ₂	Based on population density, 87.6% and 70.2% of Türkiye's population benefited from reductions in PM ₁₀ and SO ₂ levels, respectively.	[72]
31 Turkish provinces	PM ₁₀ , O ₃ , NO ₂ , SO ₂	There was no significant change in SO ₂ , limited improvement in PM ₁₀ , a general decrease in O ₃ , and an overall increase in NO ₂ levels.	[73]
Adana	SO ₂ , CO, NO _x , NO, NO ₂ , O ₃	The COVID-19 measures led to decreases of 0.35% in PM ₁₀ , 23.6% in SO ₂ , 84% in CO, 46.5% in NO _x , 34.5% in NO, 63.1% in NO ₂ , and 68.4% in O ₃ concentrations.	[74]
Şile Istanbul	PM ₁₀	PM ₁₀ concentrations in Şile increased by approximately 16.90%	[75]
Adana, Mersin	NO ₂	Industrial and commercial areas have the highest NO ₂ concentrations, with Adana generally showing higher levels than Mersin, and significant decreases in NO ₂ during COVID-19 lockdowns were observed across both cities.	[76]
Marmara Region	NO ₂	Tropospheric NO ₂ in the Marmara Region was analyzed using Sentinel-5P images, confirming its effectiveness in monitoring air pollution with a high correlation (r=0.85) to ground data.	[77]

Significant reductions in PM₁₀, NO₂, and SO₂ concentrations were recorded in an article that covered cities such as Adana, Ankara, Antalya, Denizli, Edirne, Erzurum, Istanbul, Izmir, Kayseri, Kocaeli, Trabzon, and Zonguldak. However, the same study discovered an increase in O₃ and CO concentrations in some cities, which was linked to meteorological conditions impacting secondary air pollutants formed by the oxidation of primary pollutants [71]. A study of 78 provinces, including Ankara, Istanbul, and Izmir, assessed the favorable impact of lower PM₁₀ and SO₂ levels during the epidemic as a proportion of Türkiye's entire population. The computed ratios for the population in areas positively affected by the reduction are 87.6% for PM₁₀ and 70.2% for SO₂ [72]. Yıkıcı and Ünal found that COVID-related actions improved air quality in 31 Turkish provinces [73]. A research done for the province of Adana also yielded similar results [74]. During the pandemic-related restrictions, the rise in PM₁₀ concentrations in the Şile (Istanbul) district was linked to traffic and human movement driven by migration from neighboring areas [75]. Another study used satellite images from the COVID-19 period to investigate the association between air quality and pandemic measures in the cities of Adana and Mersin. In particular, higher tropospheric NO₂ concentrations were found in industrial and commercial areas [76]. An analysis of Sentinel-5P satellite images from the Marmara Region during Türkiye's COVID-19 pandemic emergency measures revealed that a decrease in NO₂ concentrations was associated with reduced fossil fuel use [77].

2.6. Other studies and review articles

The various studies and review articles on air pollution in Türkiye, summarized in Table 6, highlight significant findings and contributions to the understanding of this critical issue.

Tablo 6. Other studies and review articles on air pollution in Türkiye

Article Type	Topic	Details	Ref.
Research Article	Air Pollution Survey	Investigated university students' perceptions of air pollution in Eastern Anatolia; significant effects from study field, father's education/profession, and monthly expenditure on health opinions.	[78]
Review Article	Impact of Air Pollution on Health in Türkiye	Examines national studies on air pollution's health impact and changes during the COVID-19 pandemic.	[79]
Review Article	Municipal Approaches to Climate and Air Quality	The evolving roles of municipalities in Türkiye, particularly in Bursa, emphasize the necessity for enhanced funding and strategies to combat climate change and air pollution.	[80]
Review Article	Link Between Air Pollution and COVID-19	The review highlights the potential roles of particulate matter (PM) in COVID-19 transmission, inflammation, and oxidative stress, alongside the impacts of air pollutants like NO ₂ and O ₃ , and the effects of lockdown measures on air quality.	[81]

In addition to articles organized by topic, one article reports on the findings of an air pollution survey. The survey was undertaken with university students studying in the Eastern Anatolia Region to investigate their perceptions of air pollution. Researchers discovered that students' primary field of study, father's educational level/profession, and monthly expenditure all had a statistically significant effect on their opinion of air pollution's negative impact on health [78].

Three publications were screened as review articles for DergiPark. The first review article examines many national studies on the impact of air pollution on health in Türkiye. Furthermore, the publication includes studies that assess the changes and impacts of outdoor air pollution during the COVID-19 pandemic [79]. Another review article explores the changing roles and new responsibilities of municipalities in Türkiye from the Republic period to the present, examining environmental protection and climate change reduction, adaptation, and waste goals within the budgets of municipalities, with a specific focus on the Bursa Metropolitan Municipality from 2018 to 2022 [80]. In the final paper, the authors synthesize research from multiple sources without regard to year, investigating the link between air pollution and COVID-19 [81].

3. Conclusions

This comprehensive review of recent air pollution and air quality research in Türkiye, spanning 2022 to 2023, reveals significant progress in understanding the complexities of air pollution dynamics while highlighting persistent challenges and areas requiring further investigation.

The synthesis of studies from various regions of Türkiye provides a multifaceted perspective on air quality issues, encompassing temporal and spatial variations, influential parameters, prediction models, health impacts, and the unprecedented effects of the COVID-19 pandemic. This body of research underscores the intricate interplay between air pollution and factors such as meteorology, urbanization, industrial activities, and natural phenomena like wildfires.

Several key findings emerge from this analysis. Persistent exceedances of regulatory limits for various pollutants, particularly PM₁₀ and SO₂, in multiple Turkish cities indicate an ongoing public health concern. The significant influence of meteorological conditions, seasonal variations, and local topography on pollutant concentrations and dispersion patterns is evident. There is a growing application of advanced statistical methods, machine learning algorithms, and remote sensing techniques in air quality assessment and prediction. The complex relationship between air pollution and human health is becoming clearer, with emerging evidence linking poor air quality to various health outcomes. The temporary improvement in air quality during COVID-19 lockdowns provided valuable insights into the potential for rapid air quality changes under reduced anthropogenic activities.

However, this review also illuminates critical gaps in current research and areas requiring further attention. Long-term epidemiological studies investigating the chronic health effects of air pollution exposure, particularly on vulnerable populations, are needed. Comprehensive assessments of the effectiveness of current air quality regulations and policy interventions are essential. In-depth exploration of the intricate

relationships between air pollution, climate change, and urban development is crucial. The development of more accurate, high-resolution air quality prediction models integrating multiple data sources and advanced AI techniques should be prioritized. Investigation of innovative pollution control technologies and sustainable urban planning strategies to mitigate air pollution in rapidly growing cities is necessary. Expansion of air quality monitoring networks to cover a broader range of pollutants, including emerging contaminants of concern, would provide more comprehensive data.

As Türkiye continues to grapple with air quality challenges while striving to meet its commitments to the United Nations Sustainable Development Goals, the role of rigorous scientific research becomes increasingly crucial. This review underscores the need for sustained, interdisciplinary research efforts to inform evidence-based policies, enhance public awareness, and ultimately improve air quality and public health across the nation.

Future research should focus on addressing these identified gaps, fostering collaborations between academic institutions, government agencies, and international partners. Moreover, efforts should be made to translate research findings into actionable policies and public health interventions. By building on the foundation of knowledge synthesized in this review, researchers and policymakers can work towards a future where clean air is a reality for all citizens of Türkiye, contributing to improved public health, environmental sustainability, and overall quality of life.

4. Acknowledgments

The authors would like to thank TUBITAK ULAKBİM for providing access to valuable research articles on air pollution and air quality, which significantly contributed to the completion of this review.

5. Author contribution statement

Author 1 contributed to the writing of the original draft, methodology, visualization. Author 2, conceptualized the study and was involved in writing, reviewing and editing.

6. Ethics Committee Approval and Conflict of Interest

There is no conflict of interest with any person/institution in the prepared article.

7. References

- [1] “Air pollution.” Accessed: Jan. 16, 2024. [Online]. Available: <https://www.who.int/health-topics/air-pollution>
- [2] “WHO global air quality guidelines: particulate matter (PM_{2.5} and PM₁₀), ozone, nitrogen dioxide, sulfur dioxide and carbon monoxide.” Accessed: Sep. 26, 2024. [Online]. Available: <https://www.who.int/publications/i/item/9789240034228>
- [3] E. K. Witkowska et al., “Air pollution - a factor of the cardiovascular system diseases,” Polish Journal of Public Health. Accessed: Sep. 23, 2024. [Online]. Available: <https://openurl.ebsco.com/contentitem>
- [4] R. Roy and A. D’Angiulli, “Air pollution and neurological diseases: Current state highlights,” *Front. Neurosci.*, vol. 18, Mar. 2024.
- [5] A. Yang, Q. Tan, C. Rajapakshe, M. Chin, and H. Yu, “Global premature mortality by dust and pollution PM_{2.5} estimated from aerosol reanalysis of the modern-era retrospective analysis for research and applications, version 2,” *Front. Environ. Sci.*, vol. 10, Sep. 2022.
- [6] M. A. Bhuiyan, H. U. R. Khan, K. Zaman, and S. S. Hishan, “Measuring the impact of global tropospheric ozone, carbon dioxide and sulfur dioxide concentrations on biodiversity loss,” *Environ. Res.*, vol. 160, pp. 398–411, Jan. 2018.
- [7] G. Usman et al., “Effects of environmental pollution on wildlife and human health and novel mitigation strategies,” *World J. Adv. Res. Rev.*, vol. 19, no. 2, pp. 1239–1251, Aug. 2023.
- [8] B. Huang, C. Lei, C. Wei, and G. Zeng, “Chlorinated volatile organic compounds (Cl-VOCs) in the environment—sources, potential human health impacts, and current remediation technologies,” *Environ. Int.*, vol. 71, pp. 118–138, Oct. 2014.
- [9] I. Lee et al., “Exposure to polycyclic aromatic hydrocarbons and volatile organic compounds is associated with a risk of obesity and diabetes mellitus among Korean adults: Korean National Environmental Health Survey (KoNEHS) 2015–2017.” *International Journal of Hygiene and Environmental Health*, vol. 240, p. 113886, Mar. 2022.
- [10] K. E. McGraw et al., “Exposure to volatile organic compounds – acrolein, 1,3-butadiene, and crotonaldehyde – is associated with vascular dysfunction,” *Environ. Res.*, vol. 196, p. 110903, May 2021.
- [11] “What are the WHO Air Quality Guidelines?” Accessed: Sep. 19, 2024. [Online]. Available: <https://www.who.int/news-room/feature-stories/detail/what-are-the-who-air-quality-guidelines>
- [12] J. Lelieveld, “Reducing air pollution: Avoidable health burden,” in *Health of People, Health of Planet and Our Responsibility: Climate Change, Air Pollution and Health*, W. K. Al-Delaimy, V. Ramanathan, and M. Sánchez Sorondo, Eds. Cham: Springer Int. Publ., 2020, pp. 105–117.
- [13] “Sürdürülebilir Kalkınma Amaçları Değerlendirme Raporu.” Accessed: Sep. 19, 2024. [Online]. Available: https://www.sbb.gov.tr/wp-content/uploads/2020/03/Surdurulebilir-Kalkinma-Amaclari-Degerlendirme-Raporu_13_12_2019-WEB.pdf
- [14] J. Chen, Q. Chen, L. Hu, T. Yang, C. Yi, and Y. Zhou, “Unveiling trends and hotspots in air pollution control: A bibliometric analysis,” *Atmosphere*, vol. 15, no. 6, Art. no. 6, Jun. 2024.
- [15] M. Coşkun, H. Şahiner, S. K. M. Abujayyab, and O. Canbulat, “Kocaeli ilinde uydu verileri ve yer istasyonu ölçümlerine bağlı olarak hava kalitesinin değerlendirilmesi,” *Türk Coğrafya Derg.*, no. 81, pp. 53–68, 2022.
- [16] Z. Yılmaz, M. B. Karagözoğlu, B. Köker, and S. F. Selçuk, “Kirlenici parametrelerin atmosferdeki yoğunluklarına dair sınır değerler: Örnek çalışma Muş ilinin hava kirliliği,” *Kırklareli Univ. Mühendislik ve Fen Bilimleri Derg.*, vol. 8, no. 1, pp. 69–87, Jun. 2022.
- [17] Z. Yılmaz and M. B. Karagözoğlu, “Hava kirliliğinin (PM₁₀ ve SO₂) ANOVA yöntemiyle değerlendirilmesi – Mardin (Türkiye) ili örneği,” *KLUJES*, vol. 8, no. 2, Art. no. 2, Dec. 2022.
- [18] T. Hirca, G. E. Türkkan, and H. Bayraktar, “Analysis of air pollution in Bayburt province with statistical methods,” *DUBİTED*, vol. 10, no. 2, Art. no. 2, Apr. 2022.
- [19] A. Can and H. Özsoy, “A different perspective on air pollution measurements,” *Politeknik Derg.*, vol. 26, no. 1, Art. no. 1, Mar. 2023.
- [20] K. Işınkaralar, “Kütahya kent merkezinde hava kalitesinin zamansal ve mekansal değişimi,” *Mühendislik Bilimleri ve Tasarım Derg.*, vol. 10, no. 1, pp. 152–160, Mar. 2022.

- [21] B. Kotan and A. Erener, "Sanayi kenti Kocaeli ilinde meteorolojik koşullara bağlı olarak ana hava kirleticilerinin ve konsantrasyonlarının mekânsal ve zamansal değişimi," *Coğrafya Derg.*, no. 46, Art. no. 46, May 2023.
- [22] Z. Eren, F. Y. Tatoğlu, and T. Akarsu, "Isınma amaçlı doğal gaz kullanımının Erzurum ili hava kalitesine etkisinin SO₂ ve PM₁₀ parametreleri üzerinden istatistiksel bir değerlendirmesi," *Pamukkale Univ. Mühendislik Bilimleri Derg.*, vol. 28, no. 6, Art. no. 6, Nov. 2022.
- [23] I. A. Pérez, M. Á. García, M. L. Sánchez, N. Pardo, and B. Fernández-Duque, "Key points in air pollution meteorology," *Int. J. Environ. Res. Public Health*, vol. 17, no. 22, Art. no. 22, Jan. 2020.
- [24] G. Qi, J. Che, and Z. Wang, "Differential effects of urbanization on air pollution: Evidences from six air pollutants in mainland China," *Ecol. Indic.*, vol. 146, p. 109924, Feb. 2023.
- [25] "Estimating the relationship between traffic and air pollution - ProQuest." Accessed: Sep. 23, 2024. [Online]. Available: <https://www.proquest.com/openview/eb96a36f75771637683f06cbbf338445/1?pq-origsite=gscholar&cbl=33298>
- [26] N. Thanvisitthpon, K. Kallawicha, and H. J. Chao, "Chapter 10 - Effects of urbanization and industrialization on air quality," in *Health and Environmental Effects of Ambient Air Pollution*, M. H. Dehghani, R. R. Karri, T. Vera, and S. K. M. Hassan, Eds. Academic Press, 2024, pp. 231–255.
- [27] W. Knorr, F. Dentener, J.-F. Lamarque, L. Jiang, and A. Arneeth, "Wildfire air pollution hazard during the 21st century," *Atmos. Chem. Phys.*, vol. 17, no. 14, pp. 9223–9236, Jul. 2017.
- [28] J. Lindén, M. Gustafsson, J. Uddling, Å. Watne, and H. Pleijel, "Air pollution removal through deposition on urban vegetation: The importance of vegetation characteristics," *Urban For. Urban Green.*, vol. 81, p. 127843, Mar. 2023.
- [29] İ. Yener and K. O. Demirarslan, "Determining the factors affecting air quality in Marmara, Turkey, and assessing it using air quality indices," *J. Nat. Haz. Environ.*, vol. 8, no. 2, pp. 383–395, Jul. 2022.
- [30] C. Ünal and G. Özel, "Bolu ili hava kirletici maddeler ile meteorolojik faktörler arasındaki ilişkilerin incelenmesi," *Karaelmas Fen Mühendislik Derg.*, vol. 12, no. 2, Art. no. 2, Dec. 2022.
- [31] Z. Yılmaz, "Meteorolojik parametrelerin hava kirliliğine etkisinin istatistiksel analizi – Muş ili (2021)," *MBTD*, vol. 10, no. 4, Art. no. 4, Dec. 2022.
- [32] H. Arslan, "Impacts of meteorological parameters on tropospheric ozone concentrations in Çanakkale," *JEPS*, vol. 35, no. 1, Art. no. 1, Mar. 2023.
- [33] İ. Çildir and A. Mutlu, "Balıkesir şehir merkezinde hava kirliliği seviyelerinin zamansal ve mekansal analizleri," *JARNAS*, vol. 8, no. 2, Art. no. 2, Jun. 2022.
- [34] E. N. Sari and S. Yılmaz, "Farklı konut dokularının hava kirliliği yoğunluğu üzerindeki etkisi: Erzurum örneği," *ADÜ Ziraat Derg.*, vol. 20, no. 1, Art. no. 1, Jun. 2023.
- [35] D. Arikan and F. Yıldız, "Investigation of urban heat island and carbon monoxide change using Google Earth Engine in Konya," *NÖHÜ Müh. Bilim. Derg.*, vol. 12, no. 4, Art. no. 4, Oct. 2023.
- [36] Z. A. Çevik, A. Özbeyaz, and Y. Demirci, "Makine öğrenme algoritması kullanarak yenilenebilir enerji ile hava kirliliği arasındaki ilişkinin incelenmesi," 2022.
- [37] İ. Bolat, "Orman yangınlarının hava kalitesine etkisi: Antalya örneği," *Bartın Orman Fakültesi Derg.*, vol. 24, no. 3, pp. 651–666, Dec. 2022.
- [38] H. Y. Keser and G. Ç. Ceyhun, "Avrupa Yeşil Mutabakatının denizyolu taşımacılığı kökenli hava kirliliği yönünden incelenmesi," *TESAM Akad. Derg.*, vol. 10, no. 1, Art. no. 1, Jan. 2023.
- [39] S. Ören and S. Kocabaş, "Karbon emisyonuna dayalı araç muayene istasyonu yer seçimi: Zonguldak örneği," *KFBD*, vol. 13, no. 3, Art. no. 3, Sep. 2023.
- [40] P. Ş. Körmeçli, "Kent parklarının hava kalitesini iyileştirme üzerine etkisinin değerlendirilmesi: Ankara Altınpark örneği," **AÇÜOFD**, vol. 24, no. 2, pp. 23–30, Oct. 2023.
- [41] T. Ü. Topal and Ö. Demirel, "Measuring air quality impacts of green areas and ecosystem services (ESS) using web-based I-Tree Canopy tool: A case study in Istanbul," **Turk J. For. Sci.**, vol. 7, no. 2, Art. no. 2, Oct. 2023.
- [42] M. A. Çetin and İ. Bakırtaş, "The mitigating role of renewable energy sources on the welfare cost of air pollution in APEC countries," *ASBİ*, vol. 22, no. 1, Art. no. 1, Mar. 2022.
- [43] M. A. Polat and S. Ergün, "Türkiye'de çevresel düzenlemeler ve ekonomik büyümenin hava kirliliği üzerindeki etkileri: Ampirik bir uygulama," *Verimlilik Derg.*, pp. 113–126, Jan. 2023.

- [44] A. Ç. Aydınoglu, R. Bovkir, and M. Bulut, "Akıllı şehirlerde büyük coğrafi veri yönetimi ve analizi: Hava kalitesi örneği," *Geomatik*, vol. 7, no. 3, Art. no. 3, Dec. 2022.
- [45] M. I. Özgür and C. Demirtaş, "Social capital and air pollution: Evidence from Turkey," *MAKU IIBFD*, vol. 9, no. 2, Art. no. 2, Jul. 2022.
- [46] Y. Li, Z. Sha, A. Tang, K. Goulding, and X. Liu, "The application of machine learning to air pollution research: A bibliometric analysis," *Ecotoxicol. Environ. Saf.*, vol. 257, p. 114911, Jun. 2023.
- [47] K. Bağcı, "Application of statistical distributions to PM10 concentrations: Van, Türkiye," *Yüzüncü Yıl Univ. Sos. Bilim. Enst. Derg.*, no. 60, Art. no. 60, Jun. 2023.
- [48] M. Akgün and N. Barlık, "Makine öğrenmesi algoritmaları kullanılarak hava kalitesi indeksinin tahmini," *EJOSAT*, no. 51, Art. no. 51, Aug. 2023.
- [49] B. Kotan and A. Erener, "PM10, SO2 hava kirleticilerinin çoklu doğrusal regresyon ve yapay sinir ağları ile sezonsal tahmini," *Geomatik*, vol. 8, no. 2, Art. no. 2, Aug. 2023.
- [50] M. Öklü and P. Canbay, "Makine öğrenmesi yöntemleri ile şehirlerin hava kalitesi tahmini," *JEPS*, vol. 35, no. 1, Art. no. 1, Mar. 2023.
- [51] S. Ünaldi and N. Yalçın, "Hava kirliliğinin makine öğrenmesi tabanlı tahmini: Başakşehir örneği," *BJESR*, vol. 4, no. 1, Art. no. 1, Apr. 2022.
- [52] B. Baran, "Sihhiye bölgesi hava kalitesi indeksinin aşırı öğrenme makineleri ve yapay sinir ağları ile tahmini," *Researcher*, vol. 2, no. 1, Art. no. 1, Jul. 2022.
- [53] E. Ç. Yağmur, "Atmosferik partikül maddelerin makine öğrenmesi ile tahmini: Beşiktaş, İstanbul örneği," *KONJES*, vol. 10, no. 4, Art. no. 4, Dec. 2022.
- [54] "Airborne particulate matter and associated heavy metals: A review - Maring - 2023 - Macromolecular Symposia - Wiley Online Library." Accessed: Sep. 18, 2024. [Online]. Available: <https://onlinelibrary.wiley.com>.
- [55] X. Huang, "The impact of PM10 and other airborne particulate matter on the cardiopulmonary and respiratory systems of sports personnel under atmospheric exposure," *Atmosphere*, vol. 14, no. 11, Art. no. 11, Nov. 2023.
- [56] S. A. Meo, N. Shaikh, M. Alotaibi, A. A. AlWabel, and H. Alqumaidi, "Effect of air pollutants particulate matter (PM2.5, PM10), sulfur dioxide (SO2) and ozone (O3) on cognitive health," *Sci. Rep.*, vol. 14, no. 1, p. 19616, Aug. 2024.
- [57] L. Fu et al., "Effects of long-term exposure to ambient fine particulate matter and its specific components on blood pressure and hypertension incidence," *Environ. Int.*, vol. 184, p. 108464, Feb. 2024.
- [58] D. Kahe et al., "Effect of PM2.5 exposure on adhesion molecules and systemic nitric oxide in healthy adults: The role of metals, PAHs, and oxidative potential," *Chemosphere*, vol. 354, p. 141631, Apr. 2024.
- [59] Q. Yang et al., "Atmospheric emissions of particulate matter-bound heavy metals from industrial sources," *Sci. Total Environ.*, vol. 947, p. 174467, Oct. 2024.
- [60] H. Chen et al., "Effects of air pollution on human health – Mechanistic evidence suggested by in vitro and in vivo modelling," *Environ. Res.*, vol. 212, p. 113378, Sep. 2022.
- [61] M. Saini, M. Joon, and S. K. Saini, "Human health effects of particulate matter," in *Airborne Particulate Matter: Source, Chemistry and Health*, S. Sonwani and A. Shukla, Eds. Singapore: Springer Nature, pp. 195–228, 2022.
- [62] F. N. T. Yenerçag and A. T. Sünter, "Effects of air pollution on mortality and morbidity in Samsun Province of Turkey," *Mid. Black Sea J. Health Sci.*, vol. 8, no. 4, Art. no. 4, Nov. 2022.
- [63] E. Filiz, "Investigation of the effect of long-term exposure to outdoor air pollution on deaths in Konya with AirQ+ software," *Urban Acad.*, vol. 16, no. 2, Art. no. 2, Jun. 2023.
- [64] K. Ulutaş, "Prediction of mortality attributed to NO2 air pollutant in Sakarya by using AIRQ+ software for 2018 and 2019," *ESTUDAM Public Health J.*, vol. 7, no. 2, Art. no. 2, Jun. 2022.
- [65] H. Kasim, T. Bekar, Y. E. Bulut, and B. Piyal, "The effect of particulate air pollution on infant mortality in the short term: The case of Ankara Province in 2018–2020," *TJFMPC*, vol. 17, no. 3, Art. no. 3, Sep. 2023.
- [66] Ş. Güzel and P. Özer, "Türkiye’de hava kirliliği ve sağlık harcamaları," *SARAD*, vol. 4, no. 2, Art. no. 2, Jul. 2022.

- [67] M. A. Polat and C. S. Özkök, "Ulaşımın kaynaklanan hava kirliliği ve ekonomik büyümenin sağlık harcamaları üzerine etkileri: Türkiye analizi," *Ekonomik ve Sosyal Araştırmalar Derg.*, vol. 18, no. 1, Art. no. 1, Jun. 2022.
- [68] C. Demirtaş and M. I. Özgür, "The effect of information-communication technologies (ICT) and air pollution on health expenditures," *Sosyoekonomi*, vol. 30, no. 51, Art. no. 51, Jan. 2022.
- [69] S. Gope, S. Dawn, and S. S. Das, "Effect of COVID-19 pandemic on air quality: A study based on air quality index," *Environ. Sci. Pollut. Res.*, vol. 28, no. 27, pp. 35564–35583, Jul. 2021.
- [70] K. Mehmood et al., "The impact of COVID-19 pandemic on air pollution: A global research framework, challenges, and future perspectives," *Environ. Sci. Pollut. Res.*, vol. 29, no. 35, pp. 52618–52634, Jul. 2022.
- [71] S. G. Durak, "Impact of COVID-19 lockdown precautions on air pollutants in Turkey," *UUJFE*, vol. 27, no. 3, Art. no. 3, Dec. 2022.
- [72] Z. Yılmaz and M. B. Karagözoğlu, "Temporal variation of air pollution variables in different regions of Turkey during the COVID-19 restrictions," *NOHU J. Eng. Sci.*, vol. 11, no. 4, Art. no. 4, Oct. 2022.
- [73] A. Yıkıcı and H. Ünal, "Türkiye’de hava kalitesinin COVID-19 bağlamında değerlendirilmesi," *KTÜSBD*, vol. 12, no. 23, Art. no. 23, Jun. 2022.
- [74] B. Mete, O. Acar, C. Kanat, and E. Doğan, "The effect of measures taken during the COVID-19 pandemic on air pollution: A East Mediterranean example from Turkey," *TJPH*, vol. 20, no. 1, Art. no. 1, Apr. 2022.
- [75] U. Özveren and H. Yakişik, "The impact of the COVID-19 pandemic on the air quality (PM10) in Şile district of İstanbul, Turkey," *JEPS*, vol. 34, no. 2, Art. no. 2, Jun. 2022.
- [76] M. Ü. Çilek, "Troposferik nitrojen dioksit (NO₂) COVID-19 pandemisinde mekânsal ve zamansal analizi: Adana-Mersin bölgesi," *YYUFBED*, vol. 27, no. 3, Art. no. 3, Dec. 2022.
- [77] M. Sünsüli and K. Kalkan, "Sentinel-5p uydu görüntüleri ile azot dioksit (NO₂) kirliliğinin izlenmesi," *TUZAL*, vol. 4, no. 1, Art. no. 1, Jun. 2022.
- [78] E. Ö. Osmanoğlu and H. Eygü, "Öğrencilerin hava kirliliği algı düzeyinin araştırılması: Doğu Anadolu bölgesi örneği," *Trend Bus Econ*, vol. 36, no. 2, Art. no. 2, Apr. 2022.
- [79] P. Bostan and S. S. Olcay, "Dünden bugüne ülkemizde yapılan dış ortam hava kirliliği sağlık etkileri araştırmaları," *TSAD*, vol. 3, no. 3, Art. no. 3, Dec. 2022.
- [80] A. Yılmaztürk and Ş. Öner, "Cumhuriyetten günümüze belediyelerin değişen rolleri ve yeni görevi: İklim değişikliği ve hava kirliliğiyle mücadele," *Kent Akademisi*, vol. 16, Türkiye Cumhuriyetinin 100. Yılı Özel Sayısı, Art. no. Türkiye Cumhuriyetinin 100. Yılı Özel Sayısı, Oct. 2023.
- [81] C. Fidan and R. Akdur, "Hava kirliliği ve COVID-19," **ESTÜDAM Halk Sağlığı Dergisi*, vol. 7, no. 2, Art. no. 2, Jun. 2022.



Tam Denetimli Kavşaklarda Şerit Kapasitesinin İncelenmesi

Nihat Can KARABULUT^{1*}, Murat ÖZEN², Oruç ALTINAŞI³

¹İnşaat Mühendisliği Bölümü, İnşaat Mühendisliği Fakültesi, Yıldız Teknik Üniversitesi, İstanbul, Türkiye.

²İnşaat Mühendisliği Bölümü, Mühendislik Fakültesi, Mersin Üniversitesi, Mersin, Türkiye.

³İnşaat Mühendisliği Bölümü, Mühendislik ve Mimarlık Fakültesi, İzmir Kâtip Çelebi Üniversitesi, İzmir, Türkiye.

¹can.karabulut@std.yildiz.edu.tr, ²ozen.murat@mersin.edu.tr, ³oruc.altintasi@ikcu.edu.tr

Geliş Tarihi: 09.03.2024

Kabul Tarihi: 11.11.2024

Düzeltilme Tarihi: 13.05.2024

doi: <https://doi.org/10.62520/fujece.1449990>

Araştırma Makalesi

Alıntı: N. C. Karabulut, M. Özen ve O. Altınaşı "Tam denetimli kavşaklarda şerit kapasitesinin incelenmesi", Fırat Üni. Deny. ve Hes. Müh. Derg., vol. 4, no 1, pp. 182-191, Şubat 2025.

Öz

Bu çalışma, Mersin'deki tam denetimli sinyal kontrol sistemiyle yönetilen bir kavşakta şerit kapasitesine etki eden faktörler incelenmektedir. Kapasite yönetimi, trafik akışındaki gecikmeleri azaltarak ve trafik sıklığını hafifleterek önemli avantajlar sağlar. Bu durum, emisyonların azaltılması ve kentsel hava kalitesinin iyileştirilmesi gibi çevresel sürdürülebilirlik hedeflerine katkıda bulunabilir. Çalışmada, kuyruk uzunluğu, ağır vasıtaların yüzdesi ve boşaltım oranı gibi faktörlerin şerit kapasitesi üzerindeki etkileri detaylı olarak incelenmiştir. Analiz için ağırlıklı en küçük kareler tekniği kullanılmıştır, bu da verilerin istatistiksel olarak değerlendirilmesine ve sonuçların doğrulanmasına olanak sağlamıştır. Çalışmanın temel bulguları şunlardır: Ağır vasıtaların varlığı şerit kapasitesini azaltır. Kuyruk uzunluğunun artması şerit kapasitesinin artmasını sağlar. Boşaltım oranının artmasıyla, şerit kapasitesinin artma eğilimi vardır. Bu bulgular, kentsel ulaşım stratejilerini geliştirmek isteyen karar vericilere önemli bilgiler sunmaktadır. Özellikle trafik yönetiminde ve sürdürülebilir ulaşım politikalarının oluşturulmasında, bu tür analizlerin ve sonuçların dikkate alınması büyük önem taşımaktadır.

Anahtar kelimeler: Şerit kapasitesi, Doygun akım oranı, Ağırlıklandırılmış en küçük kareler, Hekzagonal histogram, Kentsel trafik

*Yazışılan Yazar

İntihal Kontrol: Evet – Turnitin

Şikayet: fujece@firat.edu.tr

Telif Hakkı ve Lisans: Dergide yayın yapan yazarlar, CC BY-NC 4.0 kapsamında lisanslanan çalışmalarının telif hakkını saklı tutar.



Examination of Lane Capacity at Fully Actuated Intersections

Nihat Can KARABULUT^{1*} , Murat OZEN² , Oruc ALTINTASI³ 

¹Department of Civil Engineering, Faculty of Civil Engineering, Yıldız Technical University, Istanbul, Türkiye.

²Department of Civil Engineering, Faculty of Engineering, Mersin University, Mersin, Türkiye.

³Department of Civil Engineering, Faculty of Engineering and Architecture, Izmir Kâtip Celebi University, Izmir, Türkiye.

¹can.karabulut@std.yildiz.edu.tr, ²ozen.murat@mersin.edu.tr, ³oruc.altintasi@ikcu.edu.tr

Received: 09.03.2024

Accepted: 11.11.2024

Revision: 13.05.2024

doi: <https://doi.org/10.62520/fujece.1449990>

Review Article

Citation: N. C. Karabulut, M. Özen and O. Altınası, "Examination of lane capacity at fully actuated intersections", *Firat Univ. Jour. of Exper. and Comp. Eng.*, vol. 4, no 1, pp. 182-191, February 2025.

Abstract

This study investigates factors influencing lane capacity at a fully actuated intersection in Mersin. This study examines the factors affecting lane capacity at an intersection in Mersin managed by a fully actuated signal control system. Capacity management provides significant advantages by reducing delays in traffic flow and alleviating traffic congestion. This can contribute to environmental sustainability goals such as reducing emissions and improving urban air quality. The study thoroughly investigates the impact of factors such as queue length, the percentage of heavy vehicles, and discharge flow rate on lane capacity. The Weighted Least Squares (WLS) technique was used for the analysis, allowing for the statistical evaluation of the data and verification of the results. The key findings of the study are as follows: The presence of heavy vehicles reduces lane capacity. An increase in queue length leads to an increase in lane capacity. There is a tendency for lane capacity to increase with a higher discharge flow rate. These findings provide important insights for decision-makers looking to develop urban transportation strategies. It is important to take such analyses and results into consideration, especially in traffic management and the creation of sustainable transportation policies.

Keywords: Lane capacity, Saturation flow rate, Weighted least squares, Hexagonal histogram, Urban traffic

*Corresponding author

1. Introduction

Signalized intersections are a fundamental element of urban transportation, essential for creating livable cities, enhancing traffic safety, and improving service levels [1-3]. Well-designed signal control systems, which regulate traffic flow from various approaches, can reduce delays and increase capacity, thereby maximizing the efficiency of the transportation network [4-5].

Today, urban transportation widely utilizes many signal control systems. Fixed-time signal control systems manage intersections based on predetermined signal timings, assuming constant traffic flow throughout the day [6]. However, these signal plans need to be updated and optimized considering instant traffic demand; fixed plans account for approximately 5-10% of traffic congestion and delays [7]. In such cases, real-time signal control systems, which adjust signal timings based on real-time traffic flow, are more suitable. Examples include fully actuated and adaptive signal control systems, which are widely preferred by transportation engineers. Adaptive systems are effective over larger areas with optimization potential, while fully actuated systems are ideal for managing specific traffic demands at the local level. Both systems are designed to improve traffic flow and provide a more efficient journey for drivers.

This study focuses on capacity analysis of saturated cycles at intersections managed by fully actuated signal control systems. Fully actuated intersections dynamically adjust signal timings based on real-time traffic demands, distributing the total intersection capacity to approach lanes according to traffic demand. Consequently, the capacity of the approach lanes varies from cycle to cycle. This variability will be modeled as a parameter called "lane capacity" within the scope of this study.

Lane capacity refers to the variable capacity offered to an approach lane during the green time defined by the signal system. The study examines the impact of traffic composition and flow parameters on lane capacity. The aim is to provide a comprehensive model for traffic engineering by linking traffic flow and composition parameters. The model evaluates capacity management at intersections controlled by fully actuated signal systems, aiming to reduce congestion and delays, thereby decreasing emissions and improving air quality in urban areas. Effective capacity management not only enhances intersection performance but also supports sustainable traffic management goals. This study seeks to demonstrate how traffic management practices intersect with sustainability goals, contributing to the development of holistic urban transportation planning approaches that prioritize both efficiency and environmental responsibility.

The article is organized as follows: The second section presents the literature review. The third section covers the data collection process. The fourth section details the methodology. The fifth section provides the descriptive evaluation and model results. The last section offers conclusions and discussions.

2. Literature

To achieve the operational capacity of an urban transportation network, achieving a thorough examination of signalized intersections is essential [5]. Signalized intersections can cause delays in traffic flow, increased fuel consumption, and higher emissions [8]. Consequently, researchers have extensively evaluated the performance of these intersections. These studies have demonstrated that the saturation flow rate is a crucial concept in assessing the capacity of signalized intersections [9].

The saturation flow rate plays a vital role in geometric design, signal control, and level of service evaluations at signalized intersections [10]. Numerous studies have investigated the factors affecting the saturation flow rate. These factors include turning vehicles (left and right) [11], the slope of the approach lane [12], lane width and markings [13-14], vehicle composition [15], pedestrian and bicycle activity [16], and signal characteristics [17].

The concept of discharge flow rate represents another parameter closely linked to intersection capacity. Researchers have analyzed the effects of green time and queue lengths on the discharge flow rate [16, 18-19]. Stanić et al. [20] noted that the discharge flow rate of the first four vehicles in the queue is significantly lower compared to other vehicles in the queue. Similarly, Karabulut et al. [19] reported that the discharge

flow rate increases by approximately 30% after the first four vehicles. This is attributed to the significant initial lost times experienced by the first four vehicles in the queue. Chaudhry and Ranjitkar [18] observed a decrease in the discharge flow rate for vehicles at the end of the queue, a result supported by other studies as well [11, 21]. Researchers further observed that the discharge flow rate decreases as green time increases [19, 22]. Khosla and Williams [23] reported a similar trend; however, the decrease in discharge flow rate was not found to be statistically significant after the sixtieth second of the green phase.

3. Data

This study used traffic flow data from a fully actuated signal-controlled urban intersection in Mersin (Figure 1), namely Mall Intersection. The roundabout has four approach lanes, each with three lanes varying in width from 3.0 to 3.6 meters and a slight gradient of 2%. The intersection experiences mixed traffic and limited pedestrian activity. Traffic video recordings of the approach lanes were obtained from the Mersin Metropolitan Municipality during the morning peak hours of 7:30-9:30 under prevailing weather conditions for analysis.



Figure 1. Locations of Mall intersection

4. Methodology

Figure 2 illustrates the methodology. Figure 2 visually represents the methodological process. Traffic flow videos were analyzed using MATLAB® to determine time headways between vehicles. HCM [24] recommends a minimum of eight vehicles in a standing queue to achieve saturation flow. Therefore, only green periods with at least eight vehicles in the queue were considered. As a result, the analysis included 178 green periods (125 for the west approach and 53 for the east approach) (see Table 1).

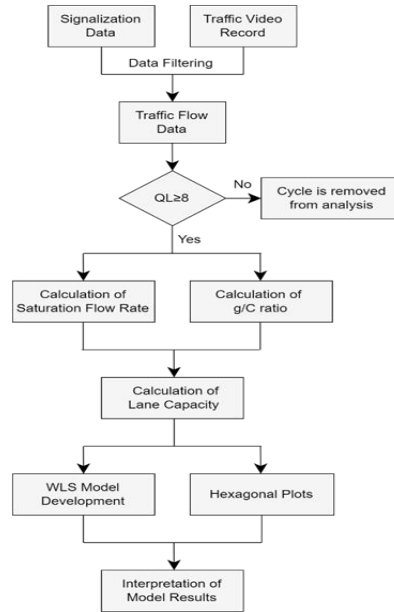


Figure 2. Flow chart of the proposed methodology

Table 1. Detail of West and East approach leg cycles

Approach Leg		West	East
Number of green periods		125	53
Green time (sec)	Min.	31	19
	Avg.	56	32
	Max.	72	35
Ratio of effective green time to cycle time	Min.	0.323	0.187
	Avg.	0.516	0.297
	Max.	0.673	0.366
Queue length (veh/cycle/lane)	Min.	8	8
	Max.	25	15
Departure volume (veh/cycle/lane)	Min.	9	8
	Max.	33	15
Discharge flow rate (veh/hour/lane)	Min.	1148	983
	Max.	1926	1815
Traffic composition (%)	PC	94.3	92.2
	HV	5.7	7.8

The capacity of signalized intersections depends on the saturated flow rate, effective green time, and cycle time. The lane capacity was calculated by Eq. 1 [24].

$$c_i = S_i \cdot (g_i / C_i) \quad (1)$$

where c refers to the lane capacity (veh/hour/lane); S refers to the saturation flow rate; g refers to the effective green time (sec); C refers to the cycle time (sec). The saturation flow rate was calculated by Eq. 2 [24].

$$S_i = 1 / h_{si} \quad (2)$$

where S_i refers to the saturation flow rate and h_{si} refers to the saturated headway (hour/veh). The saturated headway was calculated using Eq. 3 [24].

$$h_{si} = \left(\sum_{q=5}^n h_i \right) / (n - 4) \quad (3)$$

where n is the total number of vehicles in a queue; and q is the time headway of qth queued vehicle. Effective green time refers to the green time during which vehicles may proceed at saturation flow rate. The effective green time was calculated by Eq. 4 [24].

$$g_i = G_i + Y + AR - t_{Li} \quad (4)$$

where g_i refers to the effective green time (sec), G refers to the green time (sec), Y refers to the yellow time (sec), AR refers to the all-red time (sec) and t_L refers to the total lost time (sec).

The lane capacity expressed by Eq. 1 was calculated separately for each examined green period. Subsequently, the lane capacity was modeled using the Weighted Least Squares (WLS) method. Table 2 presents the details of the parameters used in the model.

Table 2. Details of parameters used in the lane capacity model

Variable Type	Variable	Notation	Unit
Dependent variable	Lane capacity	CAP	veh/hour/lane
Independent variables	Queue length	QL	veh/cycle/lane
	Percentage of heavy vehicles	HV	%
	Discharge flow rate	DFR	veh/hour/lane

The WLS model is a form of ordinary least squares (OLS) that assigns a weight to each observation by scaling the square of the residual. In OLS, observations are assumed to have constant variance, implying homoscedasticity. However, in many modeling scenarios, the homoscedasticity assumption is not valid. In such cases, the WLS modeling technique may be preferred. If the covariance structure of the data is known, Generalized Least Squares (GLS) can be used [25]. A special case of GLS is WLS, which assumes heteroscedasticity but uncorrelated residuals, meaning there are no cross-covariance terms. The general equation of the WLS model can be expressed as Eq. 5 [25]:

$$y = \beta_0 + \beta_1 x_1 + \beta_2 x_2 \quad (5)$$

where y is the dependent variable, x represents the independent variables, and β is the coefficient of the variables. WLS assigns different weights to each data point based on the variability of residuals associated with that data point. It accomplishes this by assigning larger weights to observations with smaller variances and smaller weights to observations with larger variances [25]. In WLS, each observation may have a different weight, denoted as w_i, where i represents each observation. The weighted sum of squared residuals is minimized as seen in Eq. 6 [25]:

$$\text{minimize} \sum_{i=1}^n w_i (y_i - \beta_0 - \beta_1 x_{1i} - \beta_2 x_{2i})^2 \quad (6)$$

where n is the number of observations. As a result, the impact of heteroscedasticity on model predictions is reduced by minimizing the weights at each data point. Therefore, in situations where heteroscedasticity is present, using WLS can improve model performance and provide more accurate predictions.

5. Results

The foundation of Ordinary Least Squares (OLS) analysis relies on the presupposition that the independent variables integrated into the model exhibit statistical independence. Therefore, assessing whether these variables adhere to this assumption requires conducting a Pearson correlation analysis. Figure 3 depicts the

correlation coefficients among the independent variables, providing insight into their interrelationships. According to the criteria outlined by Hosseinzadeh [26], correlation coefficients exceeding an absolute value of 0.70 signify a substantial correlation between independent variables. The correlation matrix is depicted in Figure 3. QL, HV, and DFR are not highly correlated with each other (see Fig. 3). This implies that all independent variables can be used together.

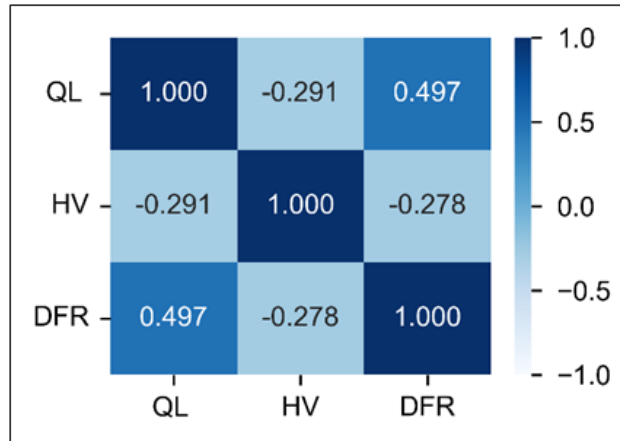


Figure 3. Correlation matrix of independent variables

Table 3 summarizes the results of the Weighted Least Squares (WLS) model. QL and DFR emerged as significant factors positively influencing CAP. On the other hand, HV emerged as a significant factor contributing adversely to CAP. All independent variables in the developed model were found to be statistically significant at the 5% significance level. Additionally, the adjusted R-squared value of this model is 0.927.

Table 3. Result of lane capacity model

Independent Variables	Coeff.	p-value	R ²
Queue length (QL)	25.906	0.000	0.927
Percentages of heavy vehicles (HV)	-10.803	0.000	
Discharge flow rate (DFR)	0.339	0.000	

Hexagonal histograms also visualize the relationship between the dependent and independent variables (see Fig. 4). These plots demonstrate the distribution and density differences between variables. If one variable depends on the other, denser colored areas with more observations will appear on the hexagonal histogram. Additionally, hexagonal histograms help in understanding the effect of the independent variable on the dependent variable and identifying clusters. The relationships observed between the dependent and independent variables in hexagonal histograms can be verified with statistical measurements such as the Pearson correlation coefficient.

Two distinct clusters are observed in the relationship between queue length and lane capacity, centered around queue lengths of 10 and 15 vehicles. The cluster around a queue length of 15 vehicles corresponds to a higher lane capacity (see Fig. 4). A single cluster is observed in the relationship between heavy vehicle percentage and lane capacity. Similarly, a single cluster is also observed in the relationship between discharge flow rate and lane capacity. This cluster indicates that lane capacity increases with an increasing discharge flow rate (see Fig. 4).

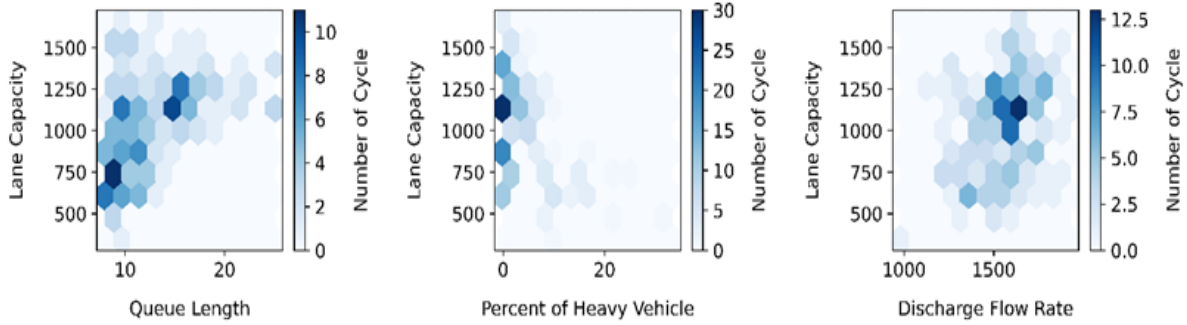


Figure 4. Hexagonal histogram of independent variables with lane capacity

6. Conclusion

This study examines the concept of variable capacity at intersections controlled by fully actuated signal systems. The aim is to determine the impact of factors such as queue length (QL), heavy vehicle percentage (HV), and discharge flow rate (DFR) on capacity at intersections where these systems are used.

Capacity management aims to reduce traffic congestion and delays, thereby decreasing emissions and improving urban air quality. This not only enhances intersection performance but also contributes to sustainable traffic management goals. The model developed in the study can guide decision-makers in sustainable urban transportation strategies and provides a significant tool for evaluating capacity management at intersections using fully actuated signal control systems. The results are summarized below:

- The adverse effect of heavy vehicles on road capacity is notable. These vehicles, being larger and slower, can negatively impact traffic flow and reduce lane capacity. An increasing percentage of heavy vehicles can affect the driving behavior of passenger car drivers, reducing discharge flow rate and average speed, leading to a decrease in lane capacity.
- An increase in queue length results in a significant increase in lane capacity. Long queues facilitate more efficient use of green time, enhancing saturation flow rates and thereby increasing lane capacity. Conversely, short queues can lead to inefficient use of green time, reducing capacity. Therefore, proper planning of traffic signal control systems is critical to maintaining maximum lane capacity.

In conclusion, this study can be considered a crucial step in traffic management and sustainable transportation at intersections managed by fully actuated signal control systems.

7. Author Contribution Statement

Nihat Can KARABULUT: Conceptualization, literature review, data curation, methodology, software and formal analysis, visualization, original draft preparation. Murat OZEN: writing-review and editing. Oruc ALTINTASI: writing-review and editing.

8. Ethics Committee Approval and Conflict of Interest Declaration

“There is no need for an ethics committee approval in the prepared article”

“There is no conflict of interest with any person/institution in the prepared article”

9. References

- [1] A. E. Kitali, and P. T. Sando, "A full Bayesian approach to appraise the safety effects of pedestrian countdown signals to drivers," *Accid. Anal. Prev.*, vol. 106, pp. 327-335.
- [2] S. Mokhtarimousavi, J. C. Anderson, A. Azizinamini, and M. Hadi, "Factors affecting injury severity in vehicle-pedestrian crashes: a day-of-week analysis using random parameter ordered response models and artificial neural networks," *Int. J. Transp. Sci. Technol.*, vol. 9, no. 2, pp. 100-115, Jun. 2020.
- [3] M. Hadi, M. S. Iqbal, T. Wang, Y. Xiao, M. Arafat, and S. Afreen, "Connected vehicle vehicle-to-infrastructure support of active traffic management," May 2019. (Dergi ismi belirtilmedi, eksik olabilir.)
- [4] Y. J. Gong, and J. Zhang, "Real-time traffic signal control for modern roundabouts by using particle swarm optimization-based fuzzy controller," arXiv:1408.0689, 2014.
- [5] A. H. Alomari and T. I. Alhadidi, "A Stochastic Approach for Modeling the Saturation Flow Rate at Traffic Signals in Jordan," *Iran. J. Sci. Technol.*, vol. 1–12, Apr. 2024.
- [6] S. El-Tantawy, B. Abdulhai, and H. Abdelgawad, "Multiagent reinforcement learning for integrated network of adaptive traffic signal controllers (MARLIN-ATSC): Methodology and large-scale application on downtown Toronto," *IEEE Trans. Intell. Transp. Syst.*, vol. 14, no. 3, pp. 1140-1150, Sep. 2013.
- [7] S. M. Chin, O. Franzese, D. L. Greene, H. L. Hwang, and R. Gibson, "Temporary losses of highway capacity and impacts on performance: Phase 2." (Dergi ismi belirtilmemiş, eksik olabilir.)
- [8] M. I. Ashqer, H. I. Ashqar, M. Elhenawy, M. Almanaa, M. A. Aljimal, H. A. Rakha, and M. Bikdash, "Evaluating a signalized intersection performance using unmanned aerial data," *Transp. Lett.*, vol. 16, no. 5, pp. 452-460, Apr. 2024.
- [9] Y. Du, A. Kouvelas, W. ShangGuan, and M. A. Makridis, "Dynamic capacity estimation of mixed traffic flows with application in adaptive traffic signal control," *Physica A*, vol. 606, p. 128065, Nov. 2022.
- [10] X. Liu, J. Yu, and X. Yang, "Diagnostic-oriented and evaluation-driven framework for bus route performance improvement," *J. Transp. Eng., Part A: Syst.*, vol. 147, no. 6, Mar. 2021.
- [11] P. Chen, H. Qi, and J. Sun, "Investigation of saturation flow on shared right-turn lane at signalized intersections," *Transp. Res. Rec.*, vol. 2461, no. 1, pp. 66-75, Jan. 2014.
- [12] C. Q. Shao, J. Rong, and X. M. Liu, "Study on the saturation flow rate and its influence factors at signalized intersections in China," *Procedia Soc. Behav. Sci.*, vol. 16, pp. 504-514, Jun. 2011.
- [13] I. B. Potts, J. F. Ringert, K. M. Bauer, J. D. Zegeer, and D. W. Harwood, "Relationship of lane width to saturation flow rate on urban and suburban signalized intersection approaches," *Transp. Res. Rec.*, vol. 2027, no. 1, pp. 45-51, Jan. 2007.
- [14] Z. Qin, J. Zhao, S. Liang, and J. Yao, "Impact of guideline markings on saturation flow rate at signalized intersections," *J. Adv. Transp.*, vol. 1–13, Apr. 2019.
- [15] S. R. Davoodi, S. Sadeghiyan, and S. F. Faezi, "The analysis the role of motorcycles on saturation flow rates at signalized intersections in Gorgan," *Indian J. Sci. Technol.*, vol. 8, no. 13, pp. 1-6, Jul. 2015.
- [16] Y. Wang, J. Rong, C. Zhou, X. Chang, and S. Liu, "An analysis of the interactions between adjustment factors of saturation flow rates at signalized intersections," *Sustainability*, vol. 12, no. 2, p. 665, Jan. 2020.
- [17] S. Mondal and A. Gupta, "Non-linear evaluation model to analyze saturation flow under weak-lane-disciplined mixed traffic stream," *Transp. Res. Rec.*, vol. 2675, no. 8, pp. 422–431, Mar. 2021.
- [18] M. S. Chaudhry and P. Ranjitkar, "Capacity and signal timing analysis of signalized intersections with increasing saturation flow rate," *Transp. Res. Board*, vol. 13, p. 3396, Jan. 2013.
- [19] N. C. Karabulut, M. Özen, and O. Altınış, "Investigation of the discharge flow rate patterns at real-time traffic signal control intersections," *Turk. J. Eng.*, vol. 7, no. 1, pp. 49-55, Jan. 2023.
- [20] B. Stanić, V. Tubić, and N. Čelar, "Straight lane saturation flow and its rate in Serbian cities," *Transport*, vol. 26, no. 3, pp. 329-334, Oct. 2011.
- [21] H. Li and P. D. Prevedouros, "Detailed observations of saturation headways and start-up lost times," *Transp. Res. Rec.*, vol. 1802, no. 1, pp. 44-53, Jan. 2002.

- [22] R. W. Denney Jr, E. Curtis, and L. Head, "Long green times and cycles at congested traffic signals," *Transp. Res. Rec.*, vol. 2128, no. 1, pp. 1-10, Jan. 2009.
- [23] K. Khosla and J. C. Williams, "Saturation flow at signalized intersections during longer green time," *Transp. Res. Rec.*, vol. 1978, no. 1, pp. 61-67, Jan. 2006.
- [24] *Transp. Res. Board (TRB), Highway Capacity Manual, Transp. Res. Board.*
- [25] T. Strutz, *Data Fitting and Uncertainty: A Practical Introduction to Weighted Least Squares and Beyond*, vol. 1, Wiesbaden: Vieweg+ Teubner, 2011.
- [26] A. Hosseinzadeh, M. Algomaiah, R. Kluger, and Z. Li, "Spatial analysis of shared e-scooter trips," *J. Transp. Geogr.*, vol. 92, p. 103016, Apr. 2021.



Dağıtım Şebekelerinde Teknik Olmayan Kayıpların Makine Öğrenme Yöntemleriyle Tespiti

Mahmut TÜRK¹ , Cem HAYDAROĞLU^{2*} , Heybet KILIÇ³ 

¹Diyarbakır Organize Sanayi Bölgesi Müdürlüğü, Diyarbakır, Türkiye.

²Elektrik-Elektronik Mühendisliği Bölümü, Mühendislik Fakültesi, Dicle Üniversitesi, Diyarbakır, Türkiye.

³Elektrik ve Enerji Bölümü, Teknik Bilimler Meslek Yüksek Okulu, Dicle Üniversitesi, Diyarbakır, Türkiye.

¹mahmut.turk@diyarbakirosb.org.tr, ²cem.haydaroglu@dicle.edu.tr, ³heybet.kilic@dicle.edu.tr

Geliş Tarihi: 17.09.2024
Kabul Tarihi: 07.12.2024

Düzeltilme Tarihi: 28.10.2024

doi: <https://doi.org/10.62520/fujece.1551601>
Araştırma Makalesi

Alıntı: M. Türk, C. Haydaroglu ve H. Kılıç, “Dağıtım şebekelerinde teknik olmayan kayıpların makine öğrenme yöntemleriyle analizi”, Fırat Üni. Deny. ve Hes. Müh. Derg., vol. 4, no 1, pp. 192-205, Şubat 2025.

Öz

Bu çalışma, elektrik şebeke sistemlerinde enerji hırsızlığından kaynaklanan teknik olmayan kayıpların (NTL) oluşturduğu ciddi sürdürülebilirlik ve güvenilirlik sorununa odaklanmaktadır. Bu kayıpları azaltmak amacıyla, farklı kaçak türlerinin (gerilim kaçağı, akım kaçağı ve gerilim-akım kaçağı) tespitinde derin öğrenme mimarilerinden yararlanan yapay zeka tabanlı bir yaklaşım öneriyoruz. Literatürdeki çalışmalardan farklı olarak veri seti iki boyutlu matrislere dönüştürülerek, günümüzün popüler yaklaşımları olan Convolutional Neural Network (CNN) ve Long Short-Term Memory (LSTM) modelleri ile analiz edilmiş; CNN, %97,50 doğruluk oranı ile LSTM'nin %64,17 doğruluk oranını geride bırakmıştır. Ayrıca, klasik yöntemlerden, k-En Yakın Komşu (k-NN) yöntemi ile 67,5 doğruluk oranı ve Destek Vektör Makineleri (SVM) yöntemi ile 62,25 doğruluk oranı elde edilmiştir. Bu gibi geleneksel yöntemlerle yapılan karşılaştırmalar, CNN'in karmaşık kaçak desenlerini belirlemedeki üstünlüğünü ortaya koymuştur. Bulgular, CNN'in akıllı şebeke sistemlerine entegre edilerek gerçek zamanlı hırsızlık tespiti için güvenilir bir araç olarak kullanılma potansiyelini vurgulamaktadır. Gelecekteki araştırmalar, gerçek zamanlı verilerin entegrasyonunu ve hibrit model yaklaşımlarını inceleyerek bu çözümün ölçeklenebilirliğini ve etkinliğini daha da artırmayı hedefleyecektir.

Anahtar kelimeler: Teknik olmayan kayıplar (TOK), Kaçak elektrik tespiti, Derin öğrenme, Konvolüsyonel sinir ağı (CNN), Akıllı şebeke

*Yazışılan Yazar

İntihal Kontrol: Evet – Turnitin

Şikayet: fujece@firat.edu.tr

Telif Hakkı ve Lisans: Dergide yayın yapan yazarlar, CC BY-NC 4.0 kapsamında lisanslanan çalışmalarının telif hakkını saklı tutar.



Machine Learning-Based Detection of Non-Technical Losses in Power Distribution Networks

Mahmut TÜRK¹ , Cem HAYDAROĞLU^{2*} , Heybet KILIÇ³ 

¹Diyarbakir Organized Industrial Zone Directorate, Diyarbakir, Türkiye.

²Department of Electrical and Electronics Engineering, Faculty of Engineering, Dicle University, Diyarbakir, Türkiye.

³Department of Electrical and Energy, Technical Sciences Vocational School, Dicle University, Diyarbakir, Türkiye

¹mahmut.turk@diyarbakirosb.org.tr, ²cem.haydaroglu@dicle.edu.tr, ³heybet.kilic@dicle.edu.tr

Received: 17.09.2024

Accepted: 07.12.2024

Revision: 28.10.2024

doi: <https://doi.org/10.62520/fujece.1551601>

Research Article

Citation: M. Türk, C. Haydaroglu, and H. Kılıç, "Analysis of non-technical losses in distribution networks using machine learning methods", *Firat Univ. Jour.of Exper. and Comp. Eng.*, vol. 4, no 1, pp. 192-205, February 2025.

Abstract

This study focuses on the serious sustainability and reliability problem caused by non-technical losses (NTL) due to energy theft in electrical grid systems. In order to reduce these losses, we propose an artificial intelligence-based approach that utilizes deep learning architectures in the detection of different types of leakage (voltage leakage, current leakage and voltage-current leakage). Unlike the studies in the literature, the data set is converted into two-dimensional matrices and analyzed with today's popular approaches, Convolutional Neural Network (CNN) and Long Short-Term Memory (LSTM) models; CNN surpassed LSTM's 64.17% accuracy rate with 97.50% accuracy rate. In addition, from the classical methods, 67.5 accuracy rate was obtained with the k-Nearest Neighbor (k-NN) method and 62.25 accuracy rate was obtained with the Support Vector Machines (SVM) method. Comparisons with such traditional methods have revealed the superiority of CNN in determining complex leakage patterns. The findings highlight the potential of CNN to be used as a reliable tool for real-time theft detection by integrating it into smart grid systems. Future research will aim to further increase the scalability and effectiveness of this solution by examining the integration of real-time data and hybrid model approaches.

Keywords: Non-technical losses (NTL), Electricity theft detection, Deep learning, Convolutional neural network(CNN),SmartGrid

*Corresponding author

1. Introduction

According to worldwide studies, the cost of illegal energy use causes approximately \$96 billion in lost revenues annually [1]. For example, in the USA and the UK, the loss of revenue due to electricity theft is approximately \$6 billion each year [2-3]. Since high loss rates are reflected in the cost of electricity, honest customers are also affected by the increasing unit prices of electricity [4].

Non-technical losses in distribution networks are considered as non-technical losses that occur when the energy transmitted to the user via the energy transmission line by the supplier is invoiced incompletely or not invoiced at all by third parties or subscribers intervening in the distribution network or measurement system, or when the supplied energy cannot be measured or is measured incompletely due to the supplier company's personnel or incorrect adjustment of the measurement system [5]. Non-technical losses can be listed as illegal electricity use, wiring errors, meter errors, billing errors [6]. Wiring errors, errors made by supplier personnel in facility installations, use of poor quality cables and use of inadequate, low quality measuring devices are among the factors that cause these losses. Failure or incorrect connection of meters, electricity meters are electronic devices used to measure the energy consumed or produced in a circuit. Failure or incorrect connection of these devices causes the consumed energy to be invoiced incompletely or not invoiced at all. Billing errors are equivalent to invoicing the consumed energy in monetary terms, everything included. In this case, it is important to bill the consumed energy in a healthy way. Otherwise, the energy consumed in the wrong case will be reflected as a loss to the supplier. Separating losses and leakages from each other, minimizing the leakages detected by measurements and observations to be made in the distribution networks will increase the energy quality. Reducing leakages will also ensure that the electricity network, which acts as an electricity transmission system, operates healthily and correctly under suitable conditions. There are many studies in the literature as a solution to the problems mentioned above. These studies can be evaluated in two categories. These are: i) Classifications made with traditional methods, ii) Algorithmic and regression-based approaches. Classifications made with traditional methods are summarized below. Ghori et al. used three classifiers to predict electricity theft from a real dataset obtained from a distribution company containing 80,000 monthly consumption records. Fourteen performance evaluation metrics were calculated among the three classifiers. Based on these data, the performance of the classifiers in scenarios to detect electricity theft yielded 99.12% for Random Forest, 99.27% for K-Nearest Neighbors (KNN), and 98.37% for Linear Support Vector Machine (SVM) [7]. Çelikpençe attempted to detect electricity theft using six machine learning-based classification algorithms. For this purpose, five large-scale and real-time system data, including the Customer Information System (CIS), Geographic Information System (GIS), Field Management System (FMS), and two different Automatic Meter Reading Systems (AMRS), were utilized. During the data preprocessing stage, data cleaning was performed using SQL techniques, and data normalization was conducted using min-max scaling methods. In the next step, feature extraction was carried out, and the extracted features were fed into the related classification methods. In the final step, the validation process was performed. Using the GridSearch method, an accuracy rate of 68.6% was achieved. The accuracy, sensitivity, and precision values were obtained as 67.11%, 81.70%, and 69.16%, respectively. Using the same parameters with SVM, the values were found as 66.70%, 83.07%, and 68.97% [8].

Ghori et al. used 15 different machine learning algorithms, including recently developed classifiers such as CatBoost, LGBBoost, and XGBoost, for theft detection. The study showed that the Artificial Neural Network (ANN) outperformed other classifiers in detecting theft, achieving a 77% success rate in detecting electricity theft. Additionally, the study identified the best 14 features out of the 71 generated features [9]. Gerardo Figueroa et al. presented a framework to address the data imbalance problem in supervised classification techniques for detecting non-technical losses in power grids through resampling techniques. Support Vector Machine (SVM) and Artificial Neural Network (ANN) were used as classifiers. Classification accuracies of 89% and 90% were achieved with the SVM and ANN classifiers, respectively [10].

Algorithmic and regression-based approaches are summarized below. Capeletti et al. proposed an end-to-end solution for the detection of non-technical losses (NTL) using supervised classification learning,

specifically through a multilayer perceptron (MLP) model of artificial neural networks (ANN). In this model, data mining concepts were applied to external data (especially ambient temperature) and internal data from energy companies. By correlating these data, improvements were made in the input data of the model, which allows for the identification of consumer units with NTL. The test results indicate a success with an increase of 0.0213 in ROC-AUC and a recall rate of 6.26% [11]. Žarković et al. utilized various artificial intelligence (AI) algorithms, including artificial neural networks (ANN), adaptive neuro-fuzzy inference systems (ANFIS), autoencoder neural networks, and K-means clustering, to detect losses in distribution networks. The artificial neural network (ANN) demonstrated a classification error rate of 7.62% by accurately classifying different consumer types. In contrast, the K-means algorithm had a slightly higher error rate of 9.26%, while ANFIS reached an error rate of 11.11% by failing to detect the initial type of anomaly [12]. Pengwah et al. developed a weighted least squares approach for predicting non-technical losses by utilizing voltage sensitivity coefficients and residual values obtained from the ordinary least squares method. In this study, voltage measurements from smart meters and the predicted sensitivity coefficients were used to estimate the actual consumption of customers. The differences between the measured and predicted consumption values were evaluated against a threshold; if the difference exceeded this threshold, the customer was labeled as a "fraudulent customer" [13]. Jené-Vinuesa et al. demonstrated that a Random Forest classifier trained for the detection of non-technical losses effectively identifies types of fraud with a weighted F1 score of 0.859. Additionally, an unsupervised detection model integrating clustering and correlation methods has facilitated the accurate identification of tampered meters. The study presented two adjustable parameters that enable utilities to finely tune their meter tampering detection strategies based on economic factors. High-accuracy fraud detection was achieved using the Fuzzy C-Means algorithm, which obtained an F1 score of 0.9 [14]. Souza et al. used real electricity consumption data to detect non-technical losses and analyzed additional statistical and temporal features based on this data. In the study, these features were utilized to improve the detection rates of various types of NTL. Furthermore, a model that combines the electricity consumption data with these additional features was developed, achieving higher detection rates for all types of fraud considered [15]. Kara et al. proposed gradient boosting decision tree-based models, LightGBM, XGBoost, and CatBoost, to detect illegal electricity usage from smart meter data of consumers. In the study, the CatBoost model achieved accuracy and AUC scores of 78.10% and 74.17%, respectively, while the LightGBM model achieved a sensitivity performance of 72.48% [16]. Saeed et al. used a dataset containing records of both honest customers and those who engaged in illegal energy use. They employed Pearson's chi-square algorithm to select the most relevant features from the data. Subsequently, the Boosted C5.0 Decision Tree (DT) algorithm was applied to classify honest and fraudulent consumers based on these features. To assess the effectiveness of their proposed electricity theft detection method, its performance was compared with several state-of-the-art machine learning algorithms, including Random Forest (RF), Support Vector Machine (SVM), Artificial Neural Network (ANN), and Extreme Gradient Boosting (XGBoost). The proposed Non-Technical Loss (NTL) detection method outperformed these algorithms, achieving an accuracy of 94.6%, a precision of 78.1%, a specificity of 98.2%, an F1 score of 84.9%, and an overall performance of 93.2% [17].

Chatterjee et al. tried to detect electricity theft using Recurrent Neural Networks (RNN), a state-of-the-art artificial intelligence algorithm. The algorithm utilized Long Short-Term Memory (LSTM) units to process sequential electricity consumption data. They proposed a model that can be used to shortlist potential electricity theft consumers in real-time [18]. Khan et al. proposed two schemes for detecting electricity theft by predicting illegal usage. Both schemes combined Autoregressive Integrated Moving Average (ARIMA) and machine learning techniques to effectively model consumer behavior related to electricity theft. Extensive simulations on real-world electricity consumption datasets demonstrated that the proposed schemes outperformed the latest solutions, achieving 98% accuracy, 98.6% precision, 98.2% recall, 97.9% AUC, and a 98.4% F1 score [19]. Xing et al. employed the Maximal Information Coefficient algorithm to capture the global and periodic patterns in consumption data to prevent electricity theft. Extensive experiments conducted under various attack scenarios demonstrated the effectiveness of the proposed method [20].

Barros et al. used the Rotation Forest algorithm to detect electricity theft and the eXtreme Gradient Boosting (XGBoost) algorithm to predict energy recovery. The study analyzed a dataset of 261,489

consumers from a public utility in Brazil. The results indicated that the proposed approach increased the financial return of field inspections by up to 11.5 times [21]. Saeed et al. proposed a new approach for theft detection in Electricity Distribution Companies (EDC) using the Ensemble Bagged Tree (EBT) algorithm. Their model generates a list of suspicious consumers based on irregularities in consumption data for further investigation. The EBT algorithm demonstrated an accuracy of 93.1% in detecting electricity theft [22].

Shih-Che Huang et al. proposed a state estimation-based approach for load forecasting at distribution transformers to detect theft. They used the overall fit of estimated values to feeder bar measurements, based on customer meter readings collected at distribution transformers, to identify irregularities in electricity usage. The results from state estimation were then analyzed using variance analysis (ANOVA) [23]. Yurtseven proposed multiple linear regression models to estimate non-technical losses energy losses caused by theft and fraud by third parties in electricity distribution systems. These models aim to quantify the impact of such losses on the operations of electricity organizations [24]. Sook-Chin Yip et al. proposed two regression-based algorithms to assess anomaly coefficients for analyzing consumers' energy usage behaviors and detecting energy theft caused by meter tampering, as well as identifying faulty smart meters. The model incorporated categorical variables and detection coefficients to pinpoint periods and locations of energy theft and faulty meters. Simulations demonstrated that the proposed algorithms successfully identified all fraudulent consumers [25]. Esther Villar-Rodriguez et al. presented an algorithmic approach that combines probabilistic data mining and time series analysis concepts to identify consumption outliers in smart grids [26].

In order to detect leakage in electricity meters, it is quite difficult to detect leakage in manual/physical inspections. In order to overcome this difficulty, it is inevitable to use artificial intelligence tools developed in a situation where there are millions of meters. In this study, three different leakage electricity meter data and non-leakage electricity meter data were classified using both deep learning architectures and traditional methods (SVM, k-NN). The data set used for Convolutional Neural Networks (CNN), one of the deep learning architectures, was transformed from one dimension to two dimensions. The obtained matrices were given to the proposed CNN architecture and Long-Short Term Memory (LSTM) architecture. In traditional methods, the feature matrix was created by taking the mean, standard deviation, maximum and minimum values from the data set in the pre-processing phase. These obtained features were evaluated in SVM and k-NN classifiers. The original aspects of this study are given below.

- This study involved the development of a unique dataset tailored to address multiple types of illegal electricity usage, specifically designed to capture voltage leakage, current leakage, and combined voltage-current leakage scenarios. Unlike datasets used in prior studies, this dataset incorporates diverse leakage types, providing a robust foundation for machine learning models to identify and classify distinct patterns of non-technical losses (NTLs) in electrical grids.
- For the first time in the literature, this study presents an artificial intelligence-based method capable of detecting and classifying multiple leakage types within electrical distribution systems. This approach leverages advanced deep learning techniques to process and analyze complex consumption patterns, allowing for improved accuracy and adaptability in identifying non-technical losses, a significant step beyond traditional detection methods focused on single leakage types.
- The study introduces a novel approach by transforming the dataset into a two-dimensional matrix format, enabling more effective analysis through deep learning architectures like Convolutional Neural Networks (CNN). This matrix-based data processing method is particularly suited to extracting spatial patterns inherent in the data, enhancing the model's ability to differentiate between leakage types and improving overall classification performance. This methodology represents a pioneering effort in leveraging data structure transformation to optimize AI model efficacy in NTL detection.

2. Method

In this study, three different leakage data and non-leakage electricity meter data were classified using both deep learning architectures and traditional methods (SVM, k-NN). The data set was transformed from one dimension to two dimensions using deep learning architectures such as Convolutional Neural Network (CNN) and Long-Short Term Memory (LSTM). The flow diagram suggested in this study is given in Figure 1.

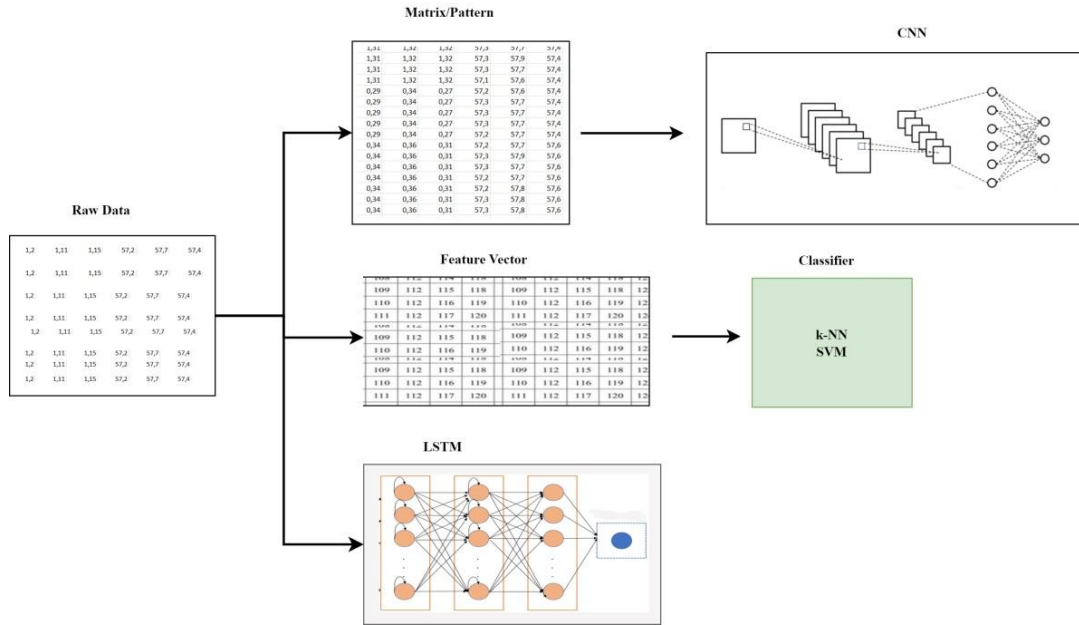


Figure 1. Classification methods proposed in this study

The obtained matrices were classified in the proposed CNN architecture. In traditional methods, the feature matrix was created by obtaining the mean, standard deviation, maximum and minimum values from the data set in the pre-processing stage. These obtained features were evaluated in SVM and k-NN classifiers.

2.1. Dataset

In the study, current and voltage information of 400 electricity meters were taken hourly and daily. Each of these data contains 100 electricity meter data and there are 3 different types of leakage. These are: 1-Voltage Leakage, 2-Current Leakage, 3-Current-Voltage Leakage. The remaining 100 electricity meter data consists of data without leakage. Each meter data from these data is 300x6 in size. Columns (6 piece) in the data set consist of current and voltage data drawn by the meters. Information on the types of leakage in the data set is given below. The consumption values of an electricity meter belonging to a customer consuming electricity are obtained by multiplying the Current X Voltage X Hourly data. The leakage methods examined are; 1-Voltage Leakage, 2-Current Leakage, 3-Current-Voltage Leakage, respectively.

Voltage Leakage is a leakage method that occurs when a customer consuming electricity intervenes in the measurement system and the voltage peaks fed to the electricity meter and included in the consumption calculation of the used electrical energy fall to zero value or to values lower than the required values.

Current Leakage, This leakage method, which has similar features to Voltage Leakage, is a leakage method that occurs when the current values corresponding to the electricity consumed by the customer on the electricity meter are intervened in the measurement system and the current values are reduced to zero or to lower values than they should be.

Current-Voltage Leakage, this leakage method, unlike the other two leakage methods, is a leakage method that occurs when both current and voltage values are intervened in the measurement system from outside,

and the current and voltage values that should be zero or lower than the values that should be passed through the electricity meter in order to bill the consumer less or not billed at all for the electricity used. The types of leaked data and non-leaked data are given in Table 1.

Table 1. Sample class data

Class	Current I1	Current I2	Current I3	Voltage L1	Voltage L2	Voltage L3
Voltage Leakage	0.53	0.59	0.53	0	59	58.5
	0.54	0.63	0.53	0	59	58.5
	0.54	0.62	0.55	0	59.1	58.8
	0.57	0.67	0.61	0	59.1	58.8
	0.75	0.73	0.001	57.4	57.8	57.7
Current Leakage	0.9	0.88	0	57.6	58	57.7
	0.69	0.69	0	57.4	57.8	57.8
	0.84	0.86	0	57.4	57.8	57.7
	0	0	1.52	0	57.7	57.3
Voltage-Current Leakage	0	0	1.57	0	57.7	57.5
	1.55	0	1.67	0	57.9	57.6
	1.63	0	1.65	58.2	57.9	0.01
	1.77	1.57	1.52	58.7	58.1	57.8
	1.77	1.57	1.52	58.7	58.1	57.8
Non-Illegal	1.77	1.57	1.52	58.7	58.1	57.8
	1.77	1.57	1.52	58.7	58.1	57.8
	1.77	1.57	1.52	58.7	58.1	57.8

2.2. Convolutional neural network architecture

In the traditional methods used in previous studies of deep learning networks, data losses are high in the feature acquisition phase [27]. Especially the positive developments in computer hardware have paved the way for the use of deep learning architectures. Deep learning architectures consist of layers [27]. Each layer has different functions. In general, an CNN architecture consists of convolution, activation, pooling and a full layer, which is a classical neural network [27]. In the convolution layer, the data is subjected to data convolution with a specified filter. After the convolution process, the data is subjected to the activation process. The pooling layer is a subsampling process. Here, the largest value or average of the data in the frame obtained as a result of stepping and stepping is taken. Feature maps are created as a result of these processes. A CNN architecture can consist of many layers depending on the data size. Finally, the data is classified in the fully connected layer, which has a classical artificial neural network structure. In CNN architectures, the lower layers contain general features, while the upper layers obtain more specific features. The CNN structure proposed in this study is shown in Figure 2.

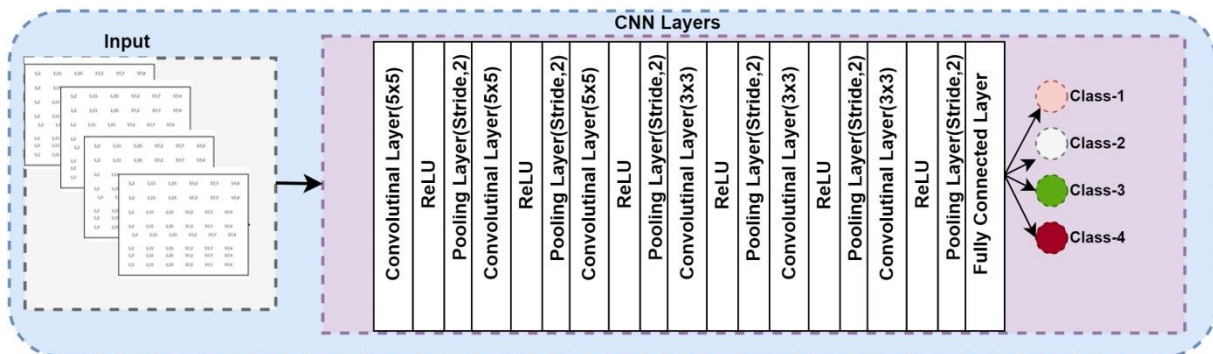


Figure 2. CNN structure proposed in this study

In the study, 6 convolution layers were used in the CNN architecture. 5x5 filters were used in the first three convolution layers, and 3x3 filters were used in the last three layers. A ReLu activation function and a pooling layer were added after each convolution layer. 250 neuron inputs were used in the fully connected layer. From the CNN architecture parameters, learning rate was set as 0.001, batch size as 2 and number of epochs as 100. This study was performed on a computer with 12th Gen Intel(R) Core(TM) i5-1235U 1.30 GHz and 16 GB RAM capacity.

2.3. Long-short term memory architecture

The UKSB architecture is an CNN architecture. It is mostly used in processing one-dimensional data [28]. Its features have come to the fore in the field of language processing. It has been proposed to overcome the shortcomings of continuous recurrent (RNN) networks. In the UKSB architecture, a previous state and input information are kept in memory cells [29]. This memory combines the current and previous inputs. In this way, it ensures the continuity of the data series. In the study, 4 3x3 filtered 2D LSTM convolution layers were used. 40 feature maps were obtained in each layer. LSTM memory blocks are given Figure 3.

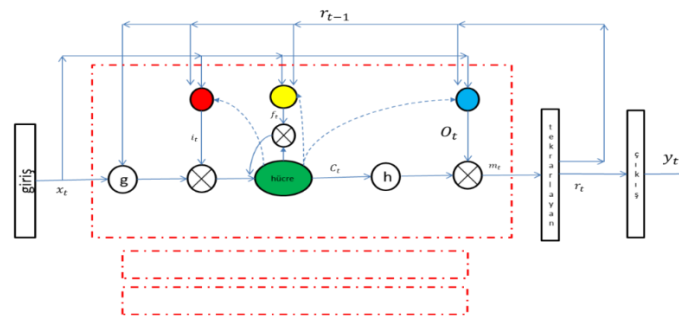


Figure 3. LSTM memory blocks [30]

2.4. k-EN nearest neighbor algorithm

The K-NN classifier algorithm is widely used in classification problems[31]. It is an algorithm that can give very good results even in noisy data. It is a supervised machine learning method. The K-NN classifier algorithm compares a test data and calculates the distance metric k between the features of the test data and the features of the closest classes. In this study, the k value is determined as 3. The K-nearest neighbor (KNN) classification for sample data is given in Figure 4.

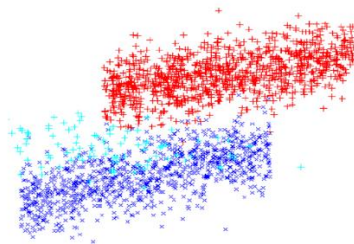


Figure 4. The K-nearest neighbor (KNN) classification for sample data [32]

2.5. Support vector machine

Support Vector Machine (SVM) is a supervised machine learning method [33]. It is a vector space-based approach that identifies the decision boundary between two classes, aiming to maximize the margin between the boundary and the nearest points in the training data [34]. Hyper plane structure of support vector machines (SVM) is given Figure 5.

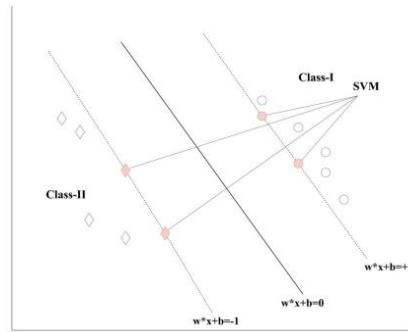


Figure 5. Hyper-plane structure of support vector machines (SVM) [35]

3. Results

In the study, 80% of the dataset was used for training and 20% for testing. Additionally, 10% of the training data was set aside for validation. Three different classifiers were employed in the study. The training accuracy and loss graphs for the convolutional neural network (CNN) architecture are shown in Figure 6.

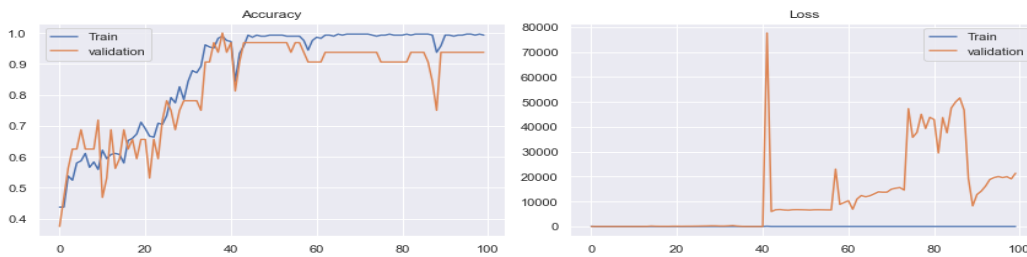


Figure 6. The training accuracy and loss graph of the convolutional neural network architecture

The classification accuracy obtained in the convolutional neural network is 97.50%. The classification performance metrics obtained on a class basis are given in Table 2.

Table 2. Performance measurements obtained from CNN architecture

Class	Precision	Recall	F1- Score
Voltage Leakage	1.00	0.92	0.96
Current Leakage	1.00	1.00	1.00
Voltage-Current Leakage	1.00	1.00	1.00
Non-Illegal	0.88	1.00	0.94
Average	0.97	0.98	0.975

Among the metrics obtained in the table 3, the precision metric of Voltage Leakage, Current Leakage and Voltage-Current Leakage was found to be 1.00. The recall metric was obtained as 1.00 in the Current Leakage, Voltage-Current Leakage and Non-Leakage classes. The F-1 score was found as 1.00 in the Current Leakage and Voltage-Current Leakage classes. The study revealed an average brightness of 0.97% .The confusion matrix obtained as a result of the classification is given in Table 3.

Table 3. Performance measurements obtained from CNN architecture

Actual Class	Predicted Class			
Voltage Leakage	24	0	0	0
Current Leakage	0	21	0	10
Voltage-Current Leakage	0	0	18	0
Non Leakage	2	0	0	15

In the study, only 2 of the test data given to the CNN classifier were classified as Voltage Free Leakage class. The test data of all other classes were classified as error-free.

Table 4. Performance metrics obtained from the LSTM architecture.

Class	Precision	Recall	F1- Score
Voltage Leakage	0.54	0.62	0.58
Current Leakage	0.63	0.61	0.62
Voltage-Current Leakage	0.77	0.69	0.73
Not Illegal	0.60	0.62	0.61
Average	0.635	0.635	0.635

As can be seen in the table 4, in the Voltage Leakage, Current Leakage, Voltage-Current Leakage and No Leakage sensitivity metrics, the lowest value was obtained as 0.54 for Voltage Leakage, while the highest value was obtained as 0.77 for Voltage-Current Leakage. In the recall metric, in the Voltage Leakage, Current Leakage, Voltage-Current Leakage and No Leakage classes, the lowest value was seen as 0.61 for Current Leakage, while the highest value was seen as 0.69 for Voltage-Current Leakage. When we look at the F-1 score values, in the Voltage Leakage, Current Leakage, Voltage-Current Leakage and No Leakage classes, Voltage Leakage showed the lowest value with 0.58, while the highest value was obtained as 0.73 for Voltage-Current Leakage. The study revealed an average brightness of 0.635%

Table 5. Confusion matrix obtained from LSTM architecture

Actual Class	Predicted Class			
	Voltage Leakage	Current Leakage	Voltage-Current Leakage	Non Leakage
Voltage Leakage	15	0	15	1
Current Leakage	0	17	0	10
Voltage-Current Leakage	8	0	27	0
Non Leakage	1	11	0	18

In the confusion matrix obtained in the LSTM classifier, 8 out of 24 Voltage Leakage test data were classified as Voltage-Current Leakage, while 1 was classified as Not Leakage. 11 out of 28 Current Leakage data were classified as Not Leakage, 12 out of 29 Voltage-Current Leakage test data were classified as Voltage Leakage, 10 out of 29 No Leakage test data were classified as Current Leakage, and 1 was classified as Voltage Leakage.

In the study, in the classification made with k-NN classifier, the data was divided into 5 parts and one part at a time was used as test data. In this way, 5 cross-validation (k-Fold) was performed. The classification accuracy obtained from each cross-validation in the study is given in Table 5.

Table 6. K-Fold performance values of K-NN classifier

K-Fold-1	K-Fold-2	K-Fold-3	K-Fold-4	K-Fold-5
71.25	65	58.75	75	67.5
Average	67.5			

When Table 6, is examined, it is seen that the highest success is Fold-4 and the lowest success is Fold-3. An average of 67.5% classification accuracy was obtained in the study.

Table 7. K-Fold performance values of SVM classifier

K-Fold-1	K-Fold-2	K-Fold-3	K-Fold-4	K-Fold-5
67.5	55	62.5	0.6	66.25
Average	62.25			

When the results given in Table 7, are examined, it is seen that the highest value is Fold-1 with 67.5% and the lowest value is Fold-4 with 0.6%. As a result of the study, an average accuracy of 62.25% is observed.

Table 8. Comparison of the classification accuracy of the classifiers used in the study.

Classifier	Accuracy
CNN	97.50
K-NN	67.50
LSTM	64.17
SVM	62.25

Table 8, compares the classification accuracy performance of the classifiers used in the study. It was observed that the highest classification accuracy was obtained from the CNN architecture, whereas the lowest performance was obtained from the SVM classifier.

In deep learning architectures, no feature method was used. On the other hand, in classical methods, the feature method was used. Therefore, in deep learning architectures, all of the data was given to the classifier without any data loss. In classical methods, data loss occurs due to the features obtained. As a result, it can be said that deep learning processes more data, whereas classical methods process less data. At the same time, this is the reason for this performance difference.

In Table 9, the accuracy rates and other performance metrics of this study are compared with previous studies. This table aims to reveal the performance of this study by comparing the results obtained with the results of various studies in the literature.

Table 9. Comparison with studies in the literature

Study	Method	Success(%)	Disadvantages
Çelikpençe.[8]	Classifications made with traditional methods	68.6	The success of the study depends on the accuracy and completeness of the data used. Data in electricity distribution networks may be incomplete or incorrect, which will negatively affect the accuracy of the model.
Jené-Vinuesa et al.[14]	Algorithmic and regression-based approaches	90	How the model works and why it makes certain predictions may not be easily understood by users. This will create transparency and reliability issues.
Kara et al.[16]	Algorithmic and regression-based approaches	78.10-74.17	Although using gradient boosting decision trees to detect illegal electricity usage with smart meter data, the data quality, risk of overfitting, and lack of transparency of the model
Saeed et al.[17]	Algorithmic and regression-based approaches	94.6	Boosted C5.0 algorithm requires more computational power. This can increase processing time when working with large datasets
Khan et al.[19]	Algorithmic and regression-based approaches	98	Hybrid approaches are often more complex and can create additional challenges in data processing, model training, and integration
Saeed et al.[22]	Algorithmic and regression-based approaches	93.1	can cause problems such as ensemble methods sometimes becoming too complex and overfitting the training dataset.
This study	Deep learning based approach	97.50	

The results obtained in this study achieved a higher accuracy rate compared to the studies conducted by Çelikpençe [8], Jené-Vinuesa et al. [14], Kara et al. [16], and Saeed et al. [17, 22]. On the other hand, a 0.50% lower accuracy rate was obtained compared to the study by Khan et al. [19].

4. Conclusion

Electrical energy has an important place all over the world. Electrical energy, which has become indispensable for modern life, is used in many areas such as health, transportation, industry, shelter (home),

etc. It is important that electrical energy, which has an important position in economic development, technology and production, is transmitted safely and healthily from its production to the final consumption point. Many negative situations occur in this cycle from the production point to the consumption point. Non-technical losses in distribution networks come to the forefront among these negativities. These losses have a negative effect both in terms of cost and the operation of the systems that transfer electrical energy. Many studies have been carried out in order to prevent these negativities. The cost of the studies carried out is also important. Artificial intelligence, which has become indispensable in the field of technology recently, provides serious gains in terms of both cost and labor in the face of such negative situations.

In this study, an artificial intelligence-based method based on the illegal electricity meter is proposed. A dataset consisting of different types of illegal electricity was created. The data obtained from this dataset was classified in different classifiers. The results obtained in this study show that different types of illegal electricity can be detected using machine learning methods. Thanks to the use of such artificial intelligence-based tools, electrical illegal electricity losses can be minimized. With this method, it is possible to obtain healthy, uninterrupted and efficient energy. The advantage of this study over other studies is that it automatically detects leaks from raw data. It has been observed that it gives good results in deep learning architecture without any preprocessing on the data. If this AI-based method is integrated into real-world systems, smart meters or real-time grid monitoring systems, it will make significant contributions to reducing illegal electricity use and increasing grid reliability. The next study aims to use Siamese networks to detect electrical leaks.

6. Acknowledgment

I would like to thank Diyarbakır Organized Industrial Zone Directorate for providing support during the conduct of this study.

7. Author Contribution Declaration

The authors contributed equally to the article.

8. Ethics Committee Approval and Conflict of Interest Declaration

There is no need to obtain ethics committee permission for the article prepared. "There is no conflict of interest with any person/institution in the article prepared.

9. References

- [1] L. J. Lepolesa, S. Achari, and L. Cheng, "Electricity theft detection in smart grids based on deep neural network," *IEEE Access*, vol. 10, pp. 39638–39655, 2022.
- [2] T. Sharma, K. K. Pandey, D. K. Punia, and J. Rao, "Of pilferers and poachers: Combating electricity theft in India," *Energy Res. Soc. Sci.*, vol. 11, pp. 40–52, 2016.
- [3] S. Sahoo, D. Nikovski, T. Muso, and K. Tsuru, "Electricity theft detection using smart meter data," in *Proceedings of the 2015 IEEE Power & Energy Society Innovative Smart Grid Technologies Conference (ISGT)*, Washington, DC, USA, 18–20 February 2015, pp. 1–5.
- [4] E. Villar-Rodriguez, J. Del Ser, I. Oregi, M. N. Bilbao, and S. Gil-Lopez, "Detection of non-technical losses in smart meter data based on load curve profiling and time series analysis," *Energy*, vol. 137, pp. 118–128, 2017.
- [5] H. O. Henriques, R. L. S. Corrêa, M. Z. Fortes, B. S. M. C. Borba, and V. H. Ferreira, "Monitoring technical losses to improve non-technical losses estimation and detection in LV distribution systems," *Measurement*, vol. 161, p. 107840, 2020.
- [6] E. S. Ibrahim, "Management of loss reduction projects for power distribution systems," *Elect. Power Syst. Res.*, vol. 55, pp. 49–56, 2000.
- [7] K. M. Ghorı, M. Imran, A. Nawaz, R. A. Abbasi, A. Ullah, and L. Szathmary, "Performance analysis of machine learning classifiers for non-technical loss detection," *J. Ambient. Intell. Humaniz. Comput.*, pp. 1–16, 2023.
- [8] M. Çelikpençe, "Elektrik dağıtım şebekelerinde teknik olmayan kayıp kaçakların makine öğrenmesi ile tespiti," 2023.
- [9] K. M. Ghorı, R. A. Abbasi, M. Awais, M. Imran, A. Ullah, and L. Szathmary, "Performance analysis of different types of machine learning classifiers for non-technical loss detection," *IEEE Access*, vol. 8, pp. 16033–16048, 2019.
- [10] G. Figueroa, Y. S. Chen, N. Avila, and C. C. Chu, "Improved practices in machine learning algorithms for NTL detection with imbalanced data," in *Proceedings of the 2017 IEEE Power & Energy Society General Meeting*, pp. 1–5, 2017.
- [11] M. B. Capeletti, B. K. Hammerschmitt, R. G. Negri, F. G. K. Guarda, L. R. Prade, N. Knak Neto, and A. D. R. Abaide, "Identification of nontechnical losses in distribution systems adding exogenous data and artificial intelligence," *Energies*, vol. 15, no. 23, p. 8794, 2022.
- [12] M. Žarković and G. Dobrić, "Artificial Intelligence for Energy Theft Detection in Distribution Networks," *Energies*, vol. 17, no. 7, p. 1580, 2024.
- [13] A. B. Pengwah, R. Razzaghi, and L. L. Andrew, "Model-less non-technical loss detection using smart meter data," *IEEE Trans. Power Deliv.*, vol. 38, no. 5, pp. 3469–3479, 2023.
- [14] M. Jené-Vinuesa, M. Aragüés-Peñalba, and A. Sumper, "Comprehensive Data-Driven Framework for Detecting and Classifying Non-Technical Distribution Losses," *IEEE Access*, 2024.
- [15] M. A. Souza, H. T. Gouveia, A. A. Ferreira, R. M. de Lima Neta, O. Nóbrega Neto, M. M. da Silva Lira, and R. R. de Aquino, "Detection of Non-Technical Losses on a Smart Distribution Grid Based on Artificial Intelligence Models," *Energies*, vol. 17, no. 7, p. 1729, 2024.
- [16] Y. Kara and A. Aksu, "Tüketicilerde Kaçak Elektrik Kullanımının Akıllı Sayaç Verisi Üzerinden Gradyan Artırmalı Karar Ağacı Tabanlı Makine Öğrenmesi Yöntemleriyle Tespiti," *J. Investig. Eng. Technol.*, vol. 6, no. 1, pp. 1–12, 2023.
- [17] M. Salman Saeed, M. W. Mustafa, U. U. Sheikh, T. A. Jumani, I. Khan, S. Atawneh, and N. N. Hamadneh, "An efficient boosted C5.0 decision-tree-based classification approach for detecting non-technical losses in power utilities," *Energies*, vol. 13, no. 12, p. 3242, 2020.
- [18] S. Chatterjee, V. Archana, K. Suresh, R. Saha, R. Gupta, and F. Doshi, "Detection of non-technical losses using advanced metering infrastructure and deep recurrent neural networks," in *2017 IEEE International Conference on Environment and Electrical Engineering and 2017 IEEE Industrial and Commercial Power Systems Europe (EEEIC/I&CPS Europe)*, pp. 1–6, 2017.
- [19] H. M. Khan, F. Jabeen, A. Khan, S. A. Badawi, C. Maple, and G. Jeon, "Hybrid non-technical-loss detection in fog-enabled smart grids," *Sust. Energy Technol. Assess.*, vol. 65, p. 103775, 2024.

- [20] Y. Xing, L. Guo, Z. Xie, L. Cui, L. Gao, and S. Yu, "Non-technical losses detection in smart grids: An ensemble data-driven approach," in 2020 IEEE 26th International Conference on Parallel and Distributed Systems (ICPADS), pp. 563–568, Dec. 2020.
- [21] R. M. R. Barros, E. G. da Costa, and J. F. Araujo, "Maximizing the financial return of non-technical loss management in power distribution systems," *IEEE Trans. Power Syst.*, vol. 37, no. 2, pp. 1634–1641, 2021.
- [22] M. S. Saeed, M. W. Mustafa, U. U. Sheikh, T. A. Jumani, and N. H. Mirjat, "Ensemble bagged tree based classification for reducing non-technical losses in Multan Electric Power Company of Pakistan," *Electronics*, vol. 8, no. 8, p. 860, 2019.
- [23] S. C. Huang, Y. L. Lo, and C. N. Lu, "Non-technical loss detection using state estimation and analysis of variance," *IEEE Trans. Power Syst.*, vol. 28, no. 3, pp. 2959–2966, 2013.
- [24] Ç. Yurtseven, "The causes of electricity theft: An econometric analysis of the case of Turkey," *Utilities Policy*, vol. 37, pp. 70–78, 2015.
- [25] S. C. Yip, K. Wong, W. P. Hew, M. T. Gan, R. C. W. Phan, and S. W. Tan, "Detection of energy theft and defective smart meters in smart grids using linear regression," *Int. J. Electr. Power Energy Syst.*, vol. 91, pp. 230–240, 2017.
- [26] E. Villar-Rodriguez, J. Del Ser, I. Oregi, M. N. Bilbao, and S. Gil-Lopez, "Detection of non-technical losses in smart meter data based on load curve profiling and time series analysis," *Energy*, vol. 137, pp. 118–128, 2017.
- [27] Y. LeCun, Y. Bengio, and G. Hinton, "Deep learning," *Nature*, vol. 521, no. 7553, pp. 436–444, 2015.
- [28] A. H. Mirza, "Low complexity efficient online learning algorithms using LSTM networks," M.S. thesis, Bilkent Univ., Ankara, Turkey, 2018.
- [29] Y. Yu, X. Si, C. Hu, and J. Zhang, "A review of recurrent neural networks: LSTM cells and network architectures," *Neural Comput.*, vol. 31, no. 7, pp. 1235–1270, 2019.
- [30] H. Sak, A. W. Senior, and F. Beaufays, "Long short-term memory recurrent neural network architectures for large scale acoustic modeling," in *Proc. ICASSP*, 2014.
- [31] P. K. Syriopoulos, N. G. Kalampalikis, S. B. Kotsiantis, and M. N. Vrahatis, "k NN Classification: a review," *Ann. Math. Artif. Intell.*, pp. 1–33, 2023.
- [32] Ö. Tomak and O. Ö. Mengi, "K-Nearest Neighbor Classification of Harmonics Using Akaike Information Criterion," *Karadeniz Fen Bilim. Derg.*, vol. 7, no. 1, pp. 1–8, 2017.
- [33] J. Ringelberg and E. Van Gool, "On the combined analysis of proximate and ultimate aspects in diel vertical migration (DVM) research," *Hydrobiologia*, vol. 491, pp. 85–90, 2003.
- [34] K. Blachowiak-Samolyk, S. Kwasniewski, K. Richardson, K. Dmoch, E. Hansen, H. Hop, et al., "Arctic zooplankton do not perform diel vertical migration (DVM) during periods of midnight sun," *Mar. Ecol. Prog. Ser.*, vol. 308, pp. 101–116, 2006.
- [35] Ö. Türk, "Classification of electroencephalogram records related to cursor movements with a hybrid method based on deep learning," *Int. J. Imaging Syst. Technol.*, vol. 31, no. 4, pp. 2322–2333, 2021.



Makine Öğrenmesi Tabanlı Regresyon Metotları ile Üç Boyutlu (3B) Baskı Parça Kalitesinin Tahmini

Ahmet Burak TATAR^{1*}

¹Mekatronik Mühendisliği, Mühendislik Fakültesi, Fırat Üniversitesi, Elazığ, Türkiye.
atatar@firat.edu.tr

Geliş Tarihi: 19.12.2024
Kabul Tarihi: 30.01.2025

Düzeltilme Tarihi: 26.12.2024

doi: <https://doi.org/10.62520/fujece.1604379>
Araştırma Makalesi

Alıntı: A.B. Tatar, “Makine öğrenmesi tabanlı regresyon metotları ile üç boyutlu (3b) baskı parça kalitesinin tahmini”, Fırat Üni. Deny. ve Hes. Müh. Derg., vol. 4, no 1, pp. 206-225, Şubat 2025.

Öz

Bu çalışmada farklı alanlarda kullanılacak ürünlerin üç boyutlu yazıcılarda imal edilirken baskı parametreleri dikkate alınarak kullanım amacına göre parçanın pürüzlülük oranı, yüke dayanımı ve çekme kuvvetine göre uzama gerilmesi verileri değerlendirilmiş ve ürün kalitesi makine öğrenmesi regresyon metotları ile optimize edilmiştir. Ürün kalitesinin tahmini için Kaggle platformundan elde edilen “3D Printer Material Requirement” açık kaynak veri seti kullanılmıştır. Bu veri setinde sisteme girdi olarak verilen; katman yüksekliği, duvar kalınlığı, dolgu yoğunluğu, dolgu deseni, nozul sıcaklığı, tabla (yatak) sıcaklığı, baskı hızı, baskı malzemesi (PLA ve ABS) ve fan hızı parametrelerine göre baskı sonucu ürünün pürüzlülüğü, yüke dayanım gücü ve çekme kuvvetlerinin etkisiyle ürünün uzama gerilmesi değerleri incelenmiştir. Bu değerler doğrultusunda da ürünün kullanım amacına göre kalitesi tahmin edilmeye çalışılmıştır. Katman yüksekliği, duvar kalınlığı, dolgu yoğunluğu, dolgu deseni, nozul sıcaklığı, yatak sıcaklığı, baskı hızı, baskı malzemesi ve fan hızı gibi parametreler, çıktı performansını etkileyen temel faktörler olarak kullanılmıştır. Bu çerçevede, Linear Regression (LR), Decision Tree (DT), Random Forest (RF), Support Vector Machine (SVM), Gaussian Process Regression (GPR), Multi-Layer Perceptron (MLP) tahmin modelleri geliştirilmiş ve model performansları, doğruluk (R^2), hata oranları (RMSE, MSE, MAE) ve işlem süresi gibi metrikler açısından değerlendirilmiştir. Bu yöntemler içerisinde GPR ile uzanım, gerilim mukavemeti ve pürüzlülük açısından en başarılı tahmin oranları sırasıyla 0,98, 0,9 ve 1 olarak elde edilmiştir. Elde edilen bulgular, 3B yazıcıların üretim süreçlerinde kalite tahmini ve optimizasyonu için makine öğrenmesi uygulamalarının etkili bir araç olduğunu göstermektedir. Ayrıca bu çalışma, 3B baskı süreçlerinde kalite kontrolü ve tasarım optimizasyonuna yeni bir perspektif sunmaktadır.

Anahtar kelimeler: 3D baskı, Makine öğrenmesi, Regresyon, Baskı parametreleri

*Yazışılan Yazar



Predicting Three-Dimensional (3D) Printing Product Quality with Machine Learning-Based Regression Methods

Ahmet Burak TATAR^{1*}

¹Mechatronics Engineering, Faculty of Engineering, Firat University, Elazığ, Türkiye.
atatar@firat.edu.tr

Received: 19.12.2024
Accepted: 30.01.2025

Revision: 26.12.2024

doi: <https://doi.org/10.62520/fujece.1604379>
Research Article

Citation: A.B. Tatar, "Predicting Three-Dimensional (3D) Printing Product Quality with Machine Learning-Based Regression Methods", *Firat Univ. Jour. of Exper. and Comp. Eng.*, vol. 4, no 1, pp. 206-225, February 2025.

Abstract

This study examines how printing parameters affect the roughness, tensile strength, and elongation of 3D-printed parts used in various applications. Machine learning-based regression models were employed to optimize product quality. The open-source "3D Printer Material Requirement" dataset obtained from the Kaggle platform was utilized to predict product quality. This dataset includes input parameters such as layer height, wall thickness, infill density, infill pattern, nozzle temperature, bed temperature, print speed, printing material (PLA and ABS), and fan speed. These parameters were analyzed for their impact on the product's roughness, load resistance, and elongation under tensile force. Based on these evaluations, product quality was estimated according to its intended use. Parameters such as layer height, wall thickness, infill density, infill pattern, nozzle temperature, bed temperature, print speed, printing material, and fan speed were identified as key factors influencing output performance. Within this framework, prediction models including Linear Regression (LR), Decision Tree (DT), Random Forest (RF), Support Vector Machine (SVM), Gaussian Process Regression (GPR), and Multi-Layer Perceptron (MLP) were developed, and their performances were assessed using metrics such as accuracy (R^2), error rates (RMSE, MSE, MAE), and computational time. Among these methods, GPR demonstrated the highest prediction accuracy for elongation, tensile strength, and roughness, with respective values of 0.98, 0.9, and 1. The findings indicate that machine learning applications are effective tools for quality prediction and optimization in the production processes of 3D printers. Furthermore, this study provides a novel perspective on quality control and design optimization in 3D printing processes.

Keywords: 3D printing, Machine learning, Regression, Printing parameters.

*Corresponding Author

1. Introduction

3D printing is an additive manufacturing process that creates physical three-dimensional objects from digital models by depositing materials layer by layer, offering advantages over traditional subtractive manufacturing methods [1]. Today, 3D printing has revolutionized design and manufacturing by enabling rapid prototyping, producing intricate geometries, and facilitating cost-effective small-scale production. This technology is widely adopted in both industrial and personal applications. The technology plays a significant role in areas such as prototype production, medical devices, and aerospace applications. However, the multitude of parameters influencing the quality of 3D-printed parts complicates process optimization. The printing process involves parameters that can impact print quality, microstructure, and certain properties [2]. These properties can be enhanced through the optimization of parameters such as layer height, infill density, nozzle temperature, and print speed. Nevertheless, traditional experimental approaches to understanding these parameters' effects are often time-consuming and costly. Machine learning algorithms, by analyzing multidimensional and complex datasets, offer the potential to predict these effects quickly and effectively.

The integration of data-driven artificial intelligence and its subset, machine learning (ML), accelerates the optimization of 3D printing parameter settings while reducing time and cost [3]. Recent advances in ML have opened new avenues to address these challenges. ML algorithms can uncover complex relationships between input parameters and output quality metrics, enabling more accurate predictions and optimizations. Leveraging these capabilities, this study aims to develop a predictive framework for 3D-printed part quality and reduce reliance on experimental trial-and-error methods.

This study utilizes the "3D-Printer Material Requirement" dataset available on Kaggle [4] to predict 3D printing part quality through machine learning-based regression methods. The results provide detailed insights into the effects of printing parameters on part quality and offer actionable outputs for quality optimization. Parameters such as layer height, wall thickness, infill density, infill pattern, nozzle temperature, bed temperature, print speed, printing material (PLA and ABS), and fan speed were analyzed for their effects on surface roughness, tensile strength, and elongation at break of the printed parts.

Optimizing these parameters to enhance product performance not only ensures material savings but also enables the production of higher-quality outputs. In addition, this study will ensure that the product to be printed on the 3D printer is manufactured with optimum accuracy according to its intended use. For example, a spur gearbox mechanical part that is expected to be resistant to loads and tensile forces that may occur, or a figurine that is constantly in a static state and is not exposed to any load but is expected to have minimum roughness and can be used as an ornament, will be obtained with optimum printing.

In this paper; Chapter 2 includes a literature review in which similar studies on the subject are researched and presented. Chapter 3 provides the contributions of this study to the literature and the originality of the study. Chapter 4 presents the materials and methods required for the implementation of this study. Chapter 5 provides experimental results as a result of the study and evaluates these results. Chapter 6 includes the evaluation of the success of the study according to the results obtained and its interpretation and conclusion.

2. Literature Review

The manufacturing of parts using 3D printing techniques and products (Figure 1) is widely applied for various purposes, including robotic applications [5-7], healthcare services [8-10], space exploration [11], aviation [12], mechanical fasteners [13], and diverse products offering practical solutions for everyday life [14]. These parts, whether designed to operate under static and dynamic loads or to perform tasks without being subjected to any loads, must be manufactured with high quality according to their intended use by employing the correct method and appropriate printing parameters. Therefore, optimizing product quality based on the intended application through different 3D printing parameters ensures the successful completion of the manufacturing process.

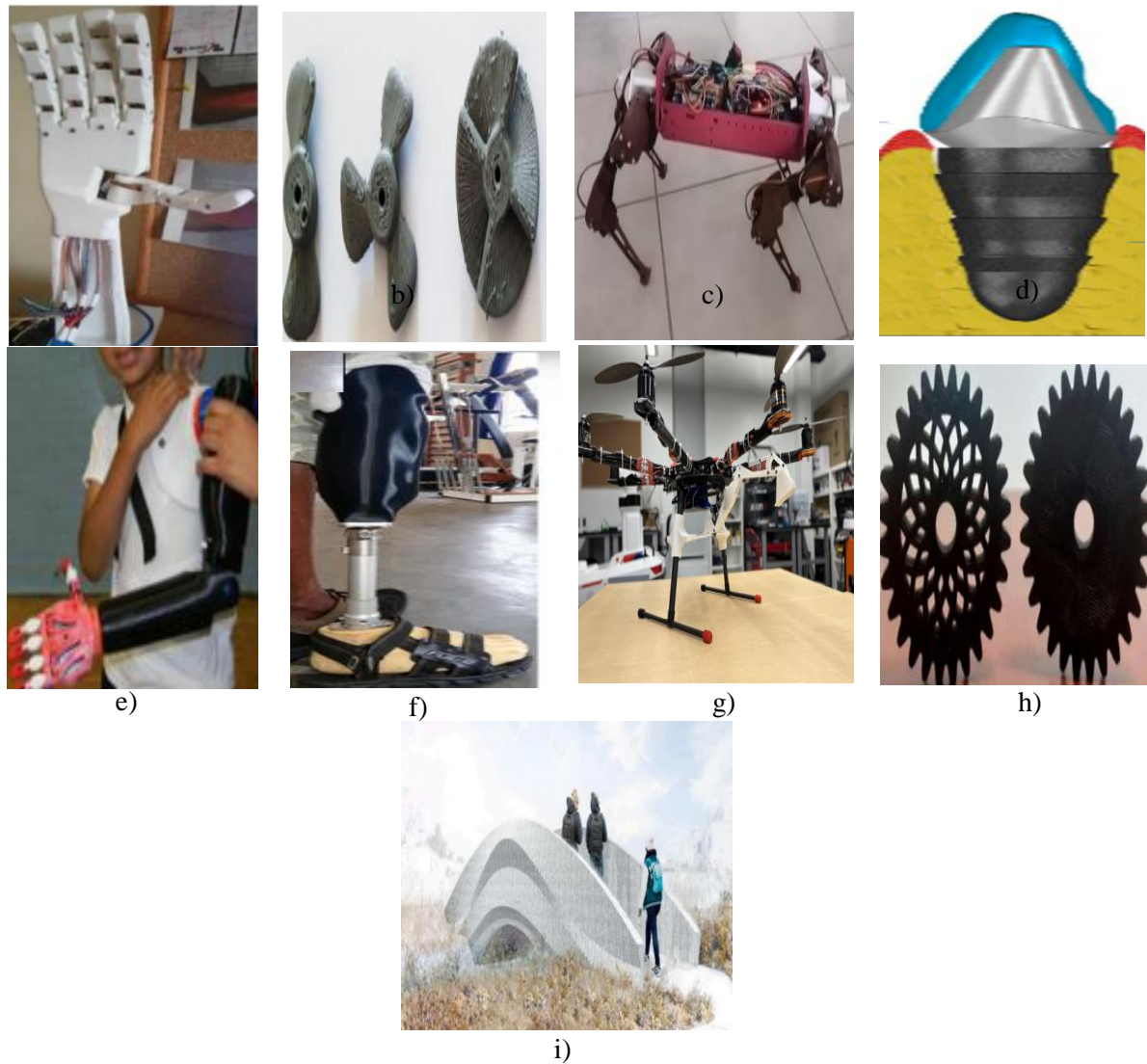


Figure 1. Examples of 3D-printed products; **a)** Prosthetic hand [5], **b)** Propeller [6], **c)** Quadraped robot [7], **d)** Dental implant [8], **e)** Prosthetic arm [9], **f)** Prosthetic leg [10], **g)** Drone [11], **h)** Spur gear [12], **i)** 3D-printed bridge [13]

Artificial intelligence algorithms can be leveraged to predict the quality of parts produced through 3D printing. By evaluating the effects of printing parameters on the output product, it becomes possible to optimize part quality. Recent studies have demonstrated the effectiveness of machine learning in optimizing 3D printing parameters [15-22, 27];

Omigdobun et al. [15] developed a predictive framework employing multiple machine learning regression algorithms to enhance the mechanical and thermal properties of PLA, a 3D printing material, for biomedical applications. They achieved high prediction accuracies, with R^2 metrics of 0.9173 and 0.8772 for compressive and tensile strengths, respectively. Kasim et al. [16] investigated the influence of infill density and print speed on the microstructure and tensile behavior of 3D-printed parts. Their results indicated that maintaining a print speed below the threshold of 40 mm/s positively impacts product quality, while higher infill percentages enhance the part's strength.

Zhang et al. [17] optimized the dynamic performance of 3D-printed spur gears using a Genetic Algorithm-based Artificial Neural Network for multi-parametric regression. By analyzing parameters such as nozzle temperature, print speed, bed temperature, and infill percentage, they concluded that wear performance improved threefold. Pereira et al. [18] evaluated parts produced with varying layer thickness, print speed, infill density, infill pattern, and material parameters through tensile, compression, and bending mechanical

tests. Their optimization aimed to minimize time and total weight, resulting in a 72.39% reduction in print time and a 9.06% increase in mass.

Sani et al. [19] emphasized the potential of Artificial Intelligence-Augmented Additive Manufacturing (AI2AM) technology in detecting defects, improving production quality, and minimizing risks of failure. The AI2AM framework proved effective in optimizing printer operations under ideal conditions. Sevli [20] focused on material selection for 3D printing using machine learning methods. By evaluating the impact of different materials on print parameters and outcomes, the study proposed a model for optimal material selection, achieving 100% accuracy in classification using the Logistic Regression algorithm.

Dabbagh et al. [21] employed Gradient Boosting Regression (GBR) to determine the optimum printing parameters for manufactured parts, achieving a prediction accuracy with an R^2 score of 0.954. Similarly, Jatti et al. [22] used a machine learning regression model to predict tensile, impact, and bending test outcomes for printed parts, achieving lower percentage errors of 3.109, 6.532, and 3.712, respectively.

Nair et al. [27], in a study similar to this one, performed the prediction of 3D model selection using various machine learning methods and evaluated the processes of elongation, roughness, and tensile strength. The success evaluation of the results they obtained has been compared with the success rates in the results section of this study.

These studies demonstrate the growing role of machine learning in enhancing the quality and efficiency of 3D printing, paving the way for advanced manufacturing solutions.

3. Contribution and Novelty

This study offers a novel perspective on the application of machine learning algorithms in 3D printing processes. The multidimensional structure of the dataset highlights the interactions among multiple printing parameters, enabling a deeper understanding of their effects on print quality. By comparing the performance of different regression models, the study identifies the most suitable algorithm, providing valuable contributions to both academic literature and industrial applications. The application of machine learning techniques, particularly regression methods, to predict 3D printer quality constitutes a noteworthy methodological contribution. Unlike traditional analytical methods, these models enable the modeling of more complex relationships and generate actionable predictions.

The proposed model captures the nonlinear effects of parameters, facilitating accurate adjustments to printer settings and improving quality in the production process. This is particularly advantageous for rapid prototyping, small-batch production, and personal manufacturing processes, yielding significant time and cost savings. Moreover, the study can serve as a decision-support tool for 3D printer users, assisting them in optimizing parameters ranging from material selection to print speed, thereby enhancing the overall printing experience and outcomes.

4. Material and Method

4.1. Feature of 3D printer dataset

In this study we used an open access dataset, which publish in kaggle platform (3D Printer Material Requirement- <https://www.kaggle.com/datasets/shubhamgupta012/3d-printer-material-requirement>) [4]. This dataset provides comprehensive information on various parameters and properties involved in the 3D printing process. It includes data on factors such as layer thickness, wall width, infill density, infill pattern, nozzle temperature, bed temperature, printing speed, material type, fan speed, surface roughness, tensile strength, and elongation. These variables are critical elements that can influence the quality, durability, and aesthetic appearance of 3D-printed objects. Researchers can analyze this dataset to understand how different printing parameters affect the final output. The data can be utilized to explore correlations between printing settings and the physical properties of printed objects, optimize printing conditions, and identify new trends in 3D printing techniques. The primary goal of this dataset is to facilitate the analysis and experimentation of

3D printing processes, enabling users to make informed decisions about printing settings to achieve desired results.

4.2. Regression analysis based machine learning methods

4.2.1. Multiple linear regression model

In the multiple linear regression model, the dependent variable y is predicted based on multiple independent variables ($x_1, x_2, x_3 \dots x_p$). Each of these independent variables is included in the model with a separate coefficient to explain its effect on the dependent variable. The general equation of the model is as follows [23]:

$$y = b_0 + b_1x_1 + b_2x_2 + \dots + b_px_p + \epsilon \quad (1)$$

y is the dependent target variable, $x_1, x_2, x_3 \dots x_p$ are the independent input variables, b_0 is the intercept term, $b_1, b_2, b_3 \dots b_n$ are the coefficients of each independent variable, and ϵ represents the error term. The objective is to determine the coefficients ($b_0, b_1, b_2 \dots b_n$) that best predict the dependent variable y . In multiple regression, the coefficients ($b_0, b_1, b_2 \dots b_n$) are estimated using the Ordinary Least Squares (OLS) method, as shown in Equation (2). The Residual Sum of Squares (RSS) cost function, defined in Equation (3), is minimized to calculate these coefficients.

$$b = (X^T X)^{-1} X^T y \quad (2)$$

$$RSS = \text{Minimize } \sum_{i=1}^n (y_i - \hat{y}_i)^2 \quad (3)$$

4.2.2. Decision tree regression model

The Decision Tree Regression Model is a widely used non-linear predictive modeling method valued for its interpretability and ability to manage both numerical and categorical data effectively. In this study, the Decision Tree algorithm [24] was applied to evaluate its performance in predicting target variables such as roughness, tensile strength, and elongation, using independent variables including layer height, wall thickness, infill density, nozzle temperature, bed temperature, print speed, and fan speed.

The model operates by iteratively dividing the dataset into smaller subsets based on feature values, resulting in a tree-like structure. At each decision point, the algorithm identifies the feature and threshold that minimize the variance within the resulting partitions. This splitting process continues until predefined conditions, such as maximum tree depth or a minimum number of samples per leaf, are met. The predicted value for each terminal node is the mean value of the target variable for the data points in that subset.

In this study, hyperparameters like maximum tree depth and minimum samples per split were fine-tuned to balance prediction accuracy and prevent overfitting. The Decision Tree Regression Model effectively captured non-linear relationships between the independent variables and the target outcomes, providing valuable insights into the factors significantly influencing roughness, tensile strength, and elongation.

4.2.3. Random forest regression model

The Random Forest (RF) regression technique constructs an ensemble of decision trees to perform regression tasks. In this approach, multiple regression trees are generated, and their predictions are combined to produce a final result, typically by averaging their outputs [25]. This method operates by recursively dividing the input data into subsets through binary splits, creating a hierarchical structure resembling a forest. At each split, the algorithm identifies the feature and threshold that best separate the data into smaller, more homogeneous groups. This process minimizes the sum of squared deviations within the resulting partitions [25]. The regression tree algorithm focuses on optimizing the partitioning at each node by solving the following minimization problem :

$$\arg \min [P_l \text{Var}(Y_l) + P_r \text{Var}(Y_r)] \quad x_j = x_j^R, j = 1, 2, 3 \dots, M \quad (4)$$

In Eq. (4), P_l and P_r represent the probabilities of the left and right child nodes, respectively. M denotes the total number of features in the dataset. X_j and x_j^R indicate the feature and its optimal split point. $\text{Var}(Y_l)$, $\text{Var}(Y_r)$ correspond to the variance of the target variable in the left and right child nodes. The algorithm seeks to achieve the optimal split by minimizing the weighted variance of the target variable across the two partitions. This approach is notably robust to outliers and variations in the dataset, making it effective for regression tasks where data quality may vary. By leveraging the strengths of multiple decision trees, Random Forest regression provides a more stable and reliable prediction compared to individual regression trees.

4.2.4. Supported vector machine regression model

Support Vector Machines (SVMs) are supervised learning methods applied to both classification and regression problems [20]. When adapted for regression tasks, the dataset can be represented as [24]:

$$D = \{(x_1, y_1), (x_2, y_2), \dots, (x_l, y_l)\} \quad (5)$$

Here, x_i represents the N -dimensional input features, and y_i denotes the corresponding output variable. The regression function is defined as:

$$f(x) = \langle w, x \rangle + b \quad (6)$$

In this equation, w is the weight vector (also known as the normal vector), x is the input vector, and b is the bias term. The dot product $w \cdot x$ ensures that the inputs and weights are isodimensional. The goal in Support Vector Regression (SVR) is to determine a function $f(x)$ that estimates the output values y_i with a maximum allowable deviation ϵ , while minimizing the distance between two parallel planes surrounding the data. To achieve this, the optimization problem involves minimizing the norm of the vector w , formulated as:

$$\min \frac{1}{2} \|w\|^2 + C \sum_{i=1}^l (\xi_i + \xi_i^*) \quad (7)$$

$$y_i - \langle w, x_i \rangle - b \leq \epsilon + \xi_i \quad (8)$$

$$\langle w, x_i \rangle + b - y_i \leq \epsilon + \xi_i^* \quad (9)$$

$$\xi_i, \xi_i^* \geq 0 \quad (10)$$

Here, ξ_i, ξ_i^* are slack variables that allow deviations beyond ϵ . C is a regularization constant greater than 0, balancing the trade-off between the model's complexity and the tolerance for errors. Compared to traditional neural network-based supervised learning methods, SVMR employs the principle of **structural risk minimization**. This approach not only minimizes the empirical error (training error) but also reduces the generalization error's upper bound, making the model robust and effective for unseen data.

4.2.5. Gaussian process regression (GPR)

Gaussian Process Regression (GPR) is a non-parametric machine learning technique designed to predict the values of continuous response variables. This method models the output variable as a Gaussian process by establishing covariance relationships with the input features. A key advantage of GPR lies in its flexibility, as it offers a range of covariance (kernel) functions, enabling the selection of the most appropriate function for the specific problem at hand. This adaptability allows the creation of models capable of capturing relationships of varying complexity. A Gaussian process extends the Gaussian distribution concept from random variables to functions. While a Gaussian distribution describes the distribution of random values, a Gaussian process represents the distribution over functions. The Gaussian process function $f(x)$ is defined using a mean function $m(x)$ and a covariance function $k(x, x')$ as shown below [26]:

$$m(x) = E(f(x)) \quad (11)$$

$$k(x, x') = E(f(x) - m(x))(f(x') - m(x')) \quad (12)$$

Here, $k(x, x')$ represents the kernel or covariance function that describes the relationship between different points in the input space. The function $f(x)$ can be expressed as:

$$f(x) = GP(m(x), k(x, x')) \quad (13)$$

Typically, the mean function $m(x)$, is assumed to be zero for simplification. The relationship between the input vector x_i and the output variable y_i in GPR can be described as:

$$y_i = f(x_i) + \varepsilon \quad (14)$$

In this equation, $f(x)$ represents the regression function, while ε denotes the noise term, typically modeled as Gaussian noise. The covariance matrix for the Gaussian process is defined by $k_{i,j}$ which specifies the covariance between two points $f(x_i)$ and $f(x_j)$ in the input space as Eq.(15). The covariance matrix can be represented as Eq.(16)

$$k_{i,j} = k(x_i, x_j) \quad (15)$$

$$k = \begin{pmatrix} k(x_1, x_1) & k(x_1, x_2) & k(x_1, x_n) \\ \vdots & \vdots & \vdots \\ k(x_n, x_1) & \dots & k(x_n, x_n) \end{pmatrix} \quad (16)$$

This covariance structure allows GPR to capture the relationships between inputs, making it a robust approach for modeling complex patterns in data. By leveraging this framework, GPR can provide accurate predictions while accounting for uncertainty in the data.

4.2.6. Multi-layer perceptron regression model

The MLP (Multi-Layer Perceptron) regression model is an artificial neural network model designed to predict a numerical target value by working through multiple layers of nonlinear transformations from input to output. The independent variables in the model's input are represented by the vector $\mathbf{x} = [x_1, x_2, \dots, x_d]^T$, and this vector is passed to the first hidden layer. At each hidden layer, the following transformation is performed [24]:

$$\mathbf{z}^{(l)} = g(\mathbf{W}^{(l)} \cdot \mathbf{z}^{(l-1)} + \mathbf{b}^{(l)}) \quad (17)$$

Here: l , layer number, $\mathbf{z}^{(l-1)}$ is the output of the previous layer. $\mathbf{W}^{(l)}$, Weight matrix of l -th layer, $\mathbf{b}^{(l)}$, The bias vector of the l -th layer, g is the activation function (ReLU, Sigmoid, Tanh, vb.). While activation functions are generally used to add nonlinearity in hidden layers, activation function is generally not applied in the output layer because of the regression problem. The output is;

$$\hat{y} = \mathbf{W}^{(o)} \cdot \mathbf{z}^{(L)} + \mathbf{b}^{(o)} \quad (18)$$

$\mathbf{W}^{(o)}$, is the weight vector from the last hidden layer to the output layer, $\mathbf{b}^{(o)}$ bias term of the output layer, $\mathbf{z}^{(L)}$ is the output of the last hidden layer. A loss function is defined based on the difference between the model's prediction and the actual values. N , total number of data, y_i actual target value, \hat{y}_i , is the model's predicted value.

$$L = \frac{1}{N} \sum_{i=1}^N (\hat{y}_i - y_i)^2 \quad (19)$$

Model weights and bias values are optimized via derivatives of the loss function. $\delta^{(o)}$, represents the error signal in the output layer. The error signal in the hidden layers is calculated by the chain rule, the learning rate is η . $g'(\mathbf{z}^{(l)})$ is the derivative of the activation function. \odot expresses element-wise multiplication.

$$\delta^{(o)} = \hat{y} - y \quad (20)$$

$$\delta^{(l)} = (\mathbf{W}^{(l+1)})^\top \delta^{(l+1)} \odot g'(\mathbf{z}^{(l)}) \quad (21)$$

$$\mathbf{W}^{(l)} = \mathbf{W}^{(l)} - \eta \cdot \delta^{(l)} \cdot (\mathbf{z}^{(l-1)})^\top \quad (22)$$

$$\mathbf{b}^{(l)} = \mathbf{b}^{(l)} - \eta \cdot \delta^{(l)} \quad (23)$$

4.3. Selected parameters of ML methods

In this study, the dataset was evaluated using 10-fold cross-validation to ensure robust training and testing. This method splits the data into 10 equal parts, using 9 folds for training and 1 fold for testing iteratively, thus maximizing the use of the dataset while minimizing bias and variance in performance evaluation. The parameters employed in the regression models are detailed in Table 1, showcasing the specific configurations used for each model. This approach ensures a comprehensive and fair comparison of model performance across varying conditions.

Table 1. Parameter of used regression models

Multiple Linear Regression (MLR)		Preset: Robust Linear Term: Linear Robust option: On Preset: Fine
Decision Tree (DT)		Min. leaf size:4 Surrogate decision splits: Off Preset: Boosted Trees
Random Forest (RF)		Min. leaf size:8 Number of learners:30 Learning rate:0.1 Preset: Cubic
Support Vector Machine (SVM)		Kernel function: Cubic Kernel scale: Auto Box constraint: Auto Epsilon:Automatic Standardize data: True Preset: Exponential GPR Basis function: Constant Kernel function: Squared Exponential Use Isoteric kernel true
Gaussian Process Regression (GPR)		Kernel scale: Automatic Signal standard deviation: Automatic Sigma: Automatic Standardize: True Optimize numeric parameters: True Preset: Medium Number of fully connecte layer: 1
Multi-Layer Regression (MLP)	Perceptron	First layer size: 25 Activation: ReLu Iteration limit:1000 Regularization streght: 0 Standardize data: True

4.4. Performance evaluation metrics

In this study, the performance of the regression models was assessed using six metrics, which are essential for evaluating the models' accuracy and generalizability. To determine performance, the

regression coefficient (R^2), mean absolute error (MAE), mean squared error (MSE), and root mean squared error (RMSE) were calculated. These metrics are described mathematically as Eq. (24-27).

$$MAE = \frac{1}{n} \sum_{i=1}^n |y_i - \hat{y}_i| \quad (24)$$

This metric calculates the average of the absolute differences between actual (y_i) and predicted (\hat{y}_i) values. A low MAE indicates that the model's predictions closely match the actual values.

$$MSE = \frac{1}{n} \sum_{i=1}^n (y_i - \hat{y}_i)^2 \quad (25)$$

This metric takes the average of the squared differences between actual and predicted values, giving greater weight to larger errors. A lower MSE indicates higher model accuracy.

$$RMSE = \sqrt{\frac{1}{n} \sum_{i=1}^n (y_i - \hat{y}_i)^2} \quad (26)$$

The RMSE provides the average size of prediction errors in the original measurement units. A low RMSE suggests that the model makes precise predictions.

$$R^2 = \frac{\sum (y_i - \hat{y}_i)^2}{\sum (y_i - \bar{y})^2} \quad (27)$$

This metric explains the proportion of variability in the dataset accounted for by the model. Values close to 1 indicate that the model has high explanatory power, effectively capturing the patterns in the data. N is the number of samples, \hat{y} is predicted value of y , \bar{y} is mean of experimental results of y .

5. Experimental Results and Discussion

In this study, all solutions were tested on a workstation with an Intel Core i7-9700K, RAM: 16 GB DDR4, GPU: NVIDIA GTX 1660 Ti and 64-bit Windows 11 Pro features. MATLAB 2023a version was used for all applications within the scope of the study.

5.1. Description of the datasets

The characteristics of the dataset are illustrated in Figure 2. The horizontal line connected to the dashed line represents the minimum and maximum values within the dataset. The blue box indicates the interquartile range, with its upper and lower boundaries corresponding to the 75th and 25th percentiles, respectively. Additionally, outliers are depicted as small circular markers positioned outside the minimum and maximum distribution, highlighting data points that deviate significantly from the central range. This visualization provides a comprehensive overview of the dataset's spread, variability, and outlier presence.

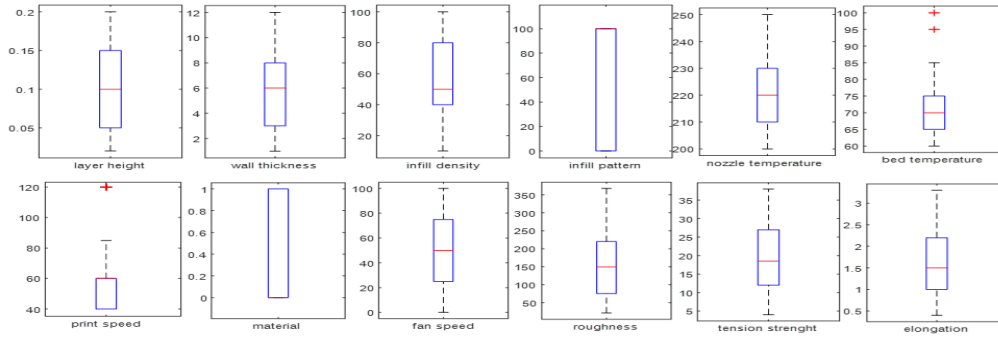


Figure 2. The analysis of the variables

In Table 2, specific statistical parameters have been calculated and presented for a comprehensive analysis of the dataset. Parameters such as layer height and wall thickness exhibit relatively homogeneous distributions, with low standard deviations (0.0626 and 2.95, respectively). In contrast, parameters like infill density and fan speed show higher standard deviations (27.55% and 35.83%, respectively), reflecting a wider variation. This indicates that some parameters were optimized within specific limits, while others were tested across a broader range. Nozzle temperature and bed temperature exhibit controlled variations, with standard deviations of 15.09 and 8.65, respectively, suggesting that these parameters were adjusted according to material compatibility. Regarding outputs, roughness (standard deviation 95.70) and tensile strength (standard deviation 9.20) demonstrate significant variability, indicating differences in mechanical performance and surface quality. On the other hand, elongation values vary within a narrower range (standard deviation 0.76), indicating more consistent results in terms of flexibility.

Table 2. Statistical analysis of the dataset

Feature	Count	Mean	Std	Min	25%	50%	75%	Max
Layer Height	132	0,098182	0,062608	0,02	0,0525	0,1	0,15	0,2
Wall Thickness	132	5,583333	2,952943	1	3	6	8	12
Infill Density	132	54,72727	27,54551	10	40	50	80	100
Nozzle Temperature	132	222,2727	15,09411	200	210	220	230	250
Bed Temperature	132	70,37879	8,651839	60	65	70	75	100
Print Speed	132	64,24242	28,59858	40	40	60	60	120
Fan Speed	132	48,5303	35,83433	0	25	50	75	100
Roughness	132	160,5455	95,7039	21	78,25	149,5	220	368
Tension Strength	132	19,75758	9,202108	4	12	18,5	27	38
Elongation	132	1,625	0,762498	0,4	1,025	1,5	2,175	3,3

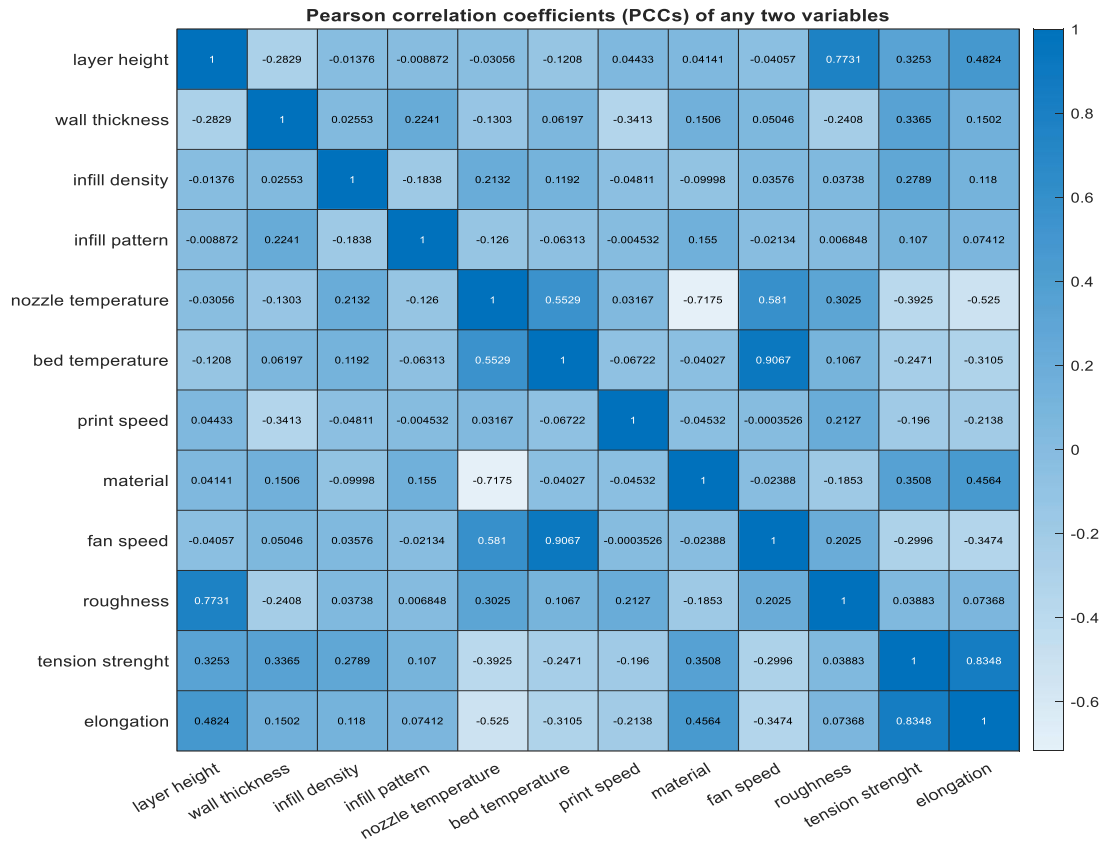


Figure 3. Coefficients of Pearson Correlation (PCC) of roughness, tension strength and elongation

Figure 3 presents the Pearson Correlation Coefficients (PCCs), which measure the strength and direction of linear relationships between pairs of variables. Upon analysis, it becomes evident that roughness, tensile strength, and elongation exhibit weak or insignificant linear correlations with other independent variables, such as layer height, wall thickness, infill density, nozzle temperature, bed temperature, print speed, and fan speed. This lack of strong linear associations suggests that these target variables may be influenced by more complex, non-linear interactions among the independent variables, which are not adequately captured through simple correlation metrics. The absence of significant linear relationships highlights the limitations of using basic statistical tools to understand the underlying patterns within the dataset. It indicates that the interactions between the variables are likely more intricate, requiring advanced methods to fully uncover and interpret their effects. For example, roughness may depend on a combination of layer height, print speed, and fan speed, but in a way that does not manifest as a straightforward linear relationship. Similarly, tensile strength and elongation could be affected by multiple features simultaneously, with interactions and thresholds that are not evident in linear analyses. In light of these findings, it became necessary to employ regression models capable of capturing complex, non-linear dependencies. To address this, three different machine learning models were developed as part of this study. These models aim to provide a more detailed understanding of the relationships between the independent variables and the target outputs. By leveraging machine learning techniques, the models are designed to identify hidden patterns, interactions, and trends that are not discernible using traditional linear approaches. This approach ensures a more robust and comprehensive analysis, offering valuable insights into the factors influencing roughness, tensile strength, and elongation, and ultimately supporting the optimization of 3D printing parameters for improved performance.

5.2. Single-variable partial dependence visualization for printed prototype of roughness, tension strenght and elongation

Single-variable partial dependence plot is a type of plot that visualizes the effect of an independent variable on a target variable. This plot focuses on the analysis of only one independent variable and aims to isolate the effect of the selected variable on the target variable, holding the effect of all other independent variables constant. In this work, it has been used to increase the "explainability" of machine learning models (e.g., random forest, gradient boosting models) and understand how the model responds to that variable. In Figure 4, Figure 5 and Figure 6, the effect of 'layer height, wall thickness, infill density, infill pattern, nozzle temperature, bed temperature, print speed, material, fan speed on roughness, tension strenght and elongation are presented based on the result of partial dependency analysis.

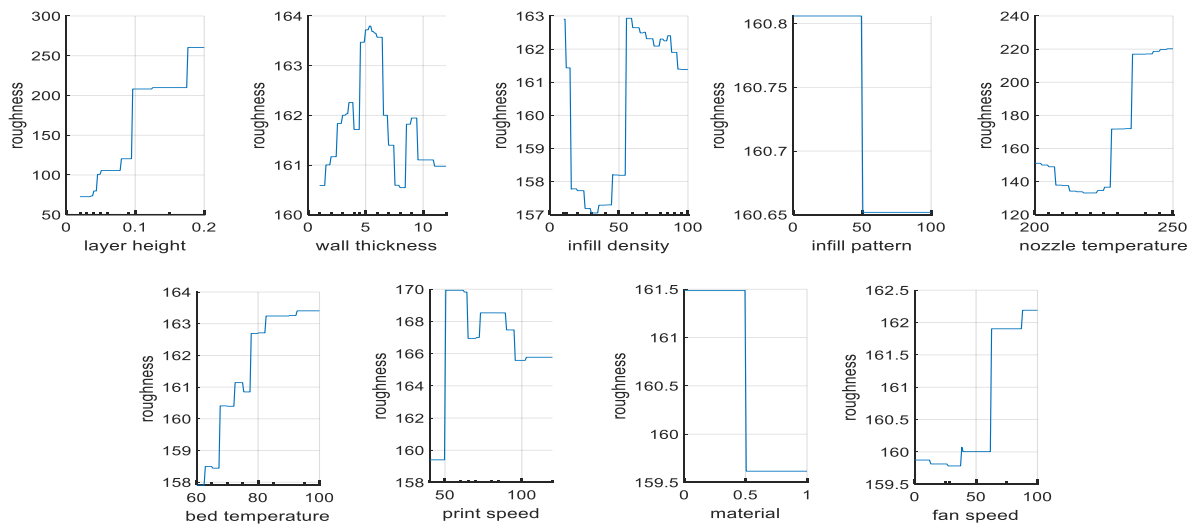


Figure 4. Single-variable partial dependence visualization for roughness

Figure 4 shows the effect of the specified parameters on roughness. When the graphs are considered, one of the most obvious changes is the increase in roughness as the layer height increases. In addition, an increase in roughness value is seen when the nozzle temperature exceeds 225°C.

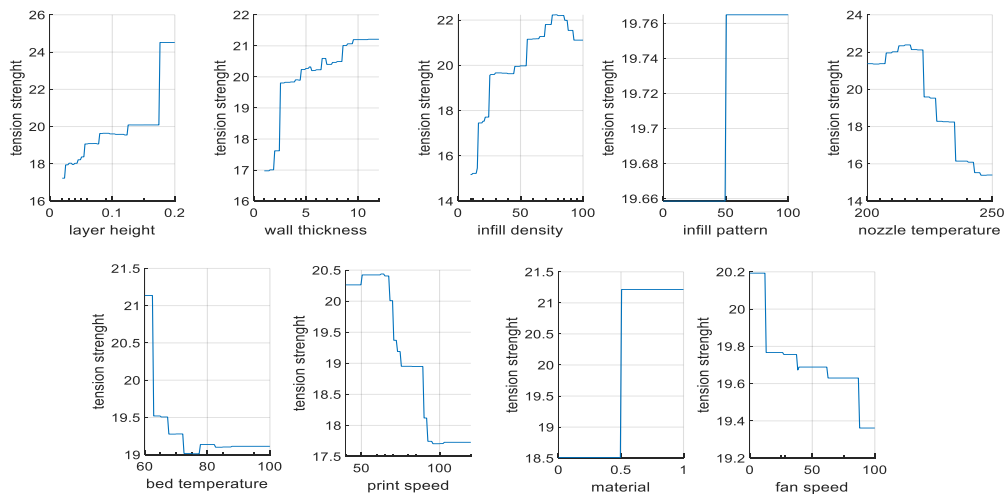


Figure 5. Single-variable partial dependence visualization for tension strenght

Figure 5 shows the effects of the input parameters on tension strength. The increase in fan speed, printing speed, nozzle temperature and bed temperature leads to a decrease in tension strength. It is seen that the optimum nozzle temperature is approximately 210 C and the optimum filling ratio is 90% for the specified conditions to obtain the highest tension strength. The increase in layer height and wall thickness also increases tension strength.

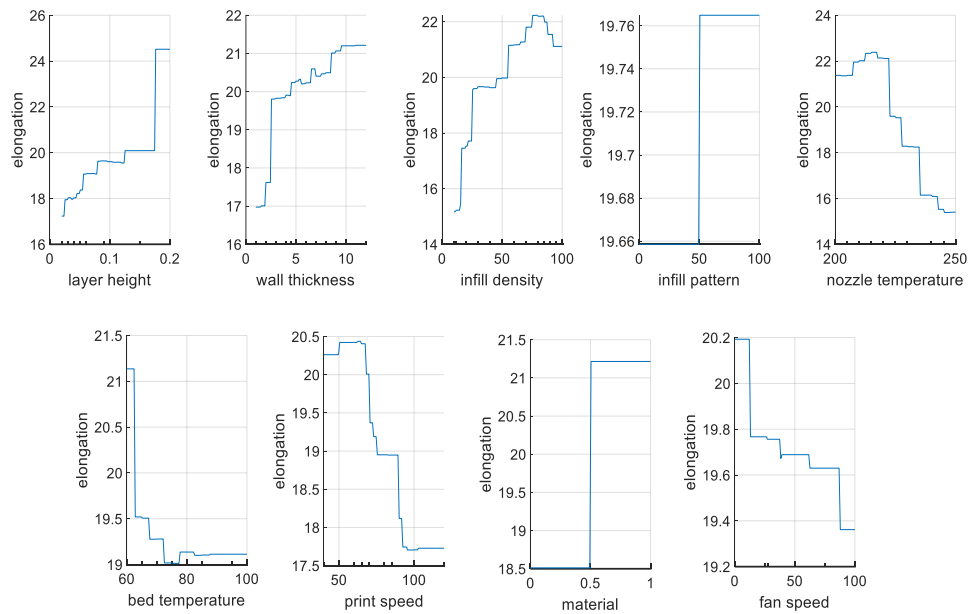


Figure 6. Single-variable partial dependence visualization for elongation

Figure 6 shows the results of the elongation effect according to these parameters. When the graphs are examined, it is seen that similar results are obtained to the effects seen in tension strength.

The success comparison of the methods according to the parameters of R^2 , RMSE, MSE, MAE, estimation rate, training time is presented in Table 3.

Table 3. Performance metrics for *Elongation, Tension strength, Roughness* prediction

Parameter	Method	RMSE	R-Squared	MSE	MAE	Prediction Speed (obs/sec)	Training Time (sec)	Model Size (kB)
Elongation	MLR	0.51526	0.54	0.26549	0.40592	4900	5.9446	11
	DT	0.36187	0.77	0.13095	0.24103	2300	0.7988	9
	SVM	0.23887	0.90	0.057059	0.15823	2700	1.0253	10
	RF	0.30746	0.84	0.09453	0.21588	1600	2.4777	167
	GPR	0.10417	0.98	0.010852	0.027385	5400	1.0999	19
	MLP	0.2485	0.89	0.061754	0.062839	6200	2.0725	14
Tension strength	MLR	4.911	0.71	24.118	3.0868	1600	1.7326	53
	DT	5.3234	0.66	28.339	3.7534	4100	0.76664	8
	SVM	4.1156	0.80	16.938	2.6388	4100	0.67843	10
	RF	4.6571	0.74	21.688	3.0317	1700	2.0643	167
	GPR	2.833	0.90	8.0257	0.78883	5900	1.3456	19
	MLP	4.5639	0.75	20.829	1.5082	6700	3.1345	9
Roughness	MLR	51.458	0.71	2647.9	42.569	4000	1.1285	11
	DT	24.405	0.93	595.62	17.749	4700	1.4112	9
	SVM	10.745	0.99	115.46	9.8676	3600	0.80012	8
	RF	21.089	0.95	444.73	14.805	1200	4.7927	167
	GPR	1.3543	1.00	1.8341	0.24223	4200	2.3904	19
	MLP	4.8427	1.00	23.452	0.87258	6700	3.5984	9

According to Table 2, Gaussian Process Regression (GPR) emerges as the most accurate method overall. GPR consistently achieves the lowest error rates (RMSE, MSE, MAE) and the highest R^2 values across all parameters. For instance, in elongation, it achieves an RMSE of just 0.10417 and an R^2 of 0.98, demonstrating superior predictive performance. Similarly, in tension strength, GPR achieves an RMSE of 2.833 and an R^2 of 0.90, while in roughness, it reaches an RMSE of 1.3543 and an R^2 of 1.00, indicating exceptional accuracy. As alternatives, Support Vector Machine (SVM) and Artificial Neural Networks (MLP) also deliver commendable results in many cases. SVM, for example, performs well in predicting elongation and tension strength, with R^2 values of 0.90 and 0.80, respectively. MLP, on the other hand, matches GPR in terms of accuracy for roughness with an R^2 value of 1.00 while excelling in prediction speed. For instance, MLP achieves the fastest prediction speed at 6700 obs/sec. Meanwhile, Random Forest (RF) provides reasonably accurate results, though slightly less precise compared to GPR and SVM. RF's R^2 values for elongation, tension strength, and roughness are 0.84, 0.74, and 0.95, respectively. However, its large model size (167 kB) and relatively slow prediction speed can be disadvantages in scenarios with large datasets. In contrast, Multiple Linear Regression (MLR) and Decision Tree (DT) methods generally perform worse in terms of accuracy compared to other methods. Linear Regression has the lowest performance in terms of RMSE and R^2 . For example, in roughness, it records an RMSE of 51.458 and an R^2 of only 0.71. Similarly, DT offers faster prediction speeds but is limited in accuracy. So, Gaussian Process Regression (GPR) yielded the highest prediction accuracies: 0.98 for elongation, 0.90 for tensile strength, and 1.00 for roughness.

In conclusion, GPR is recommended for the highest accuracy and reliability, while MLP is ideal for speed-focused predictions. The combination of GPR's accuracy advantage and MLP's speed superiority highlights that the choice of method should depend on the requirements of the specific application. SVM offers a balanced option between accuracy and speed, whereas RF may face limitations in memory usage and prediction time with larger datasets.

Figure 7, Figure 8 and Figure 9 show the effect of the 3D printer's operating parameters, namely layer height, wall thickness, infill density, infill pattern, nozzle temperature, bed temperature, print speed, material, fan speed on the roughness, tension strength and elongation of the prototype part, which are predicted graphs in Figure 7. The predicted results of the MLR (a), DT (b), SVM (c), RF (d), GPR (e), MLP (f) models are presented with graphs, respectively. The x-axis represents the actual experimental data, and the y-axis represents the predicted values. The fact that the points are on the linear line shows the high success of the prediction.

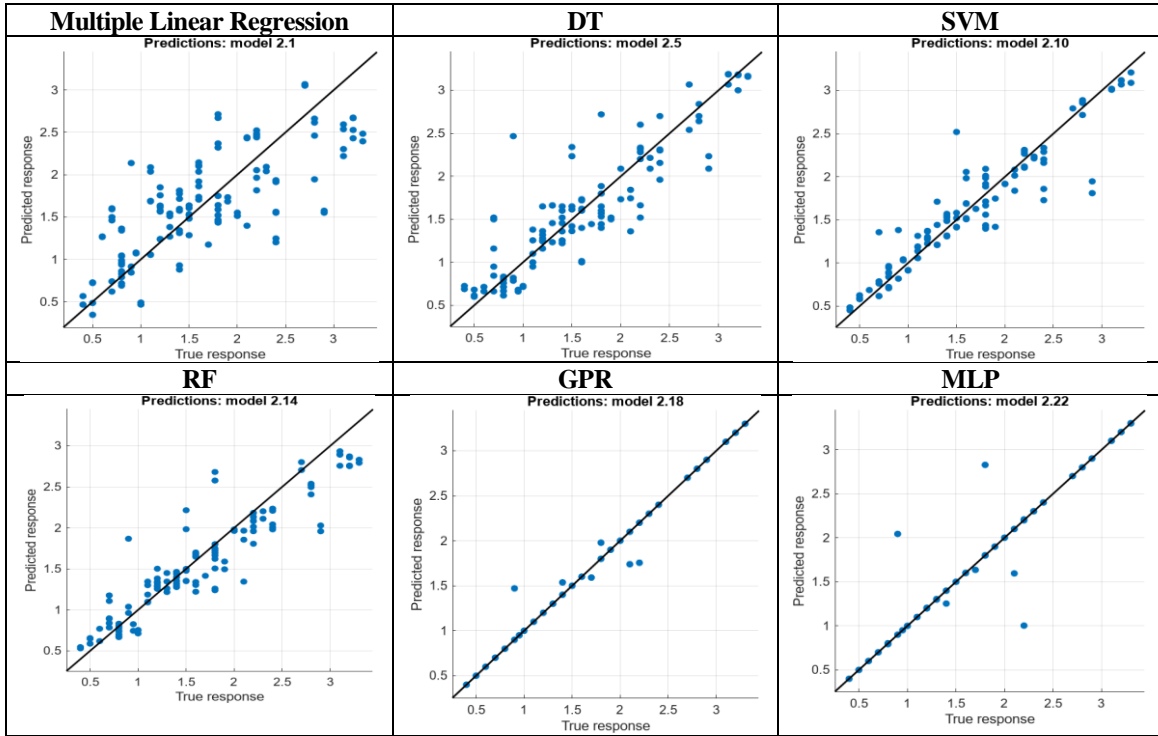


Figure 7. Prediction performance plots for elongation

Figure 7 shows the results of the prediction performance for elongation. According to the graphs, the most successful results are obtained with the GPR, SVM and MLP methods.

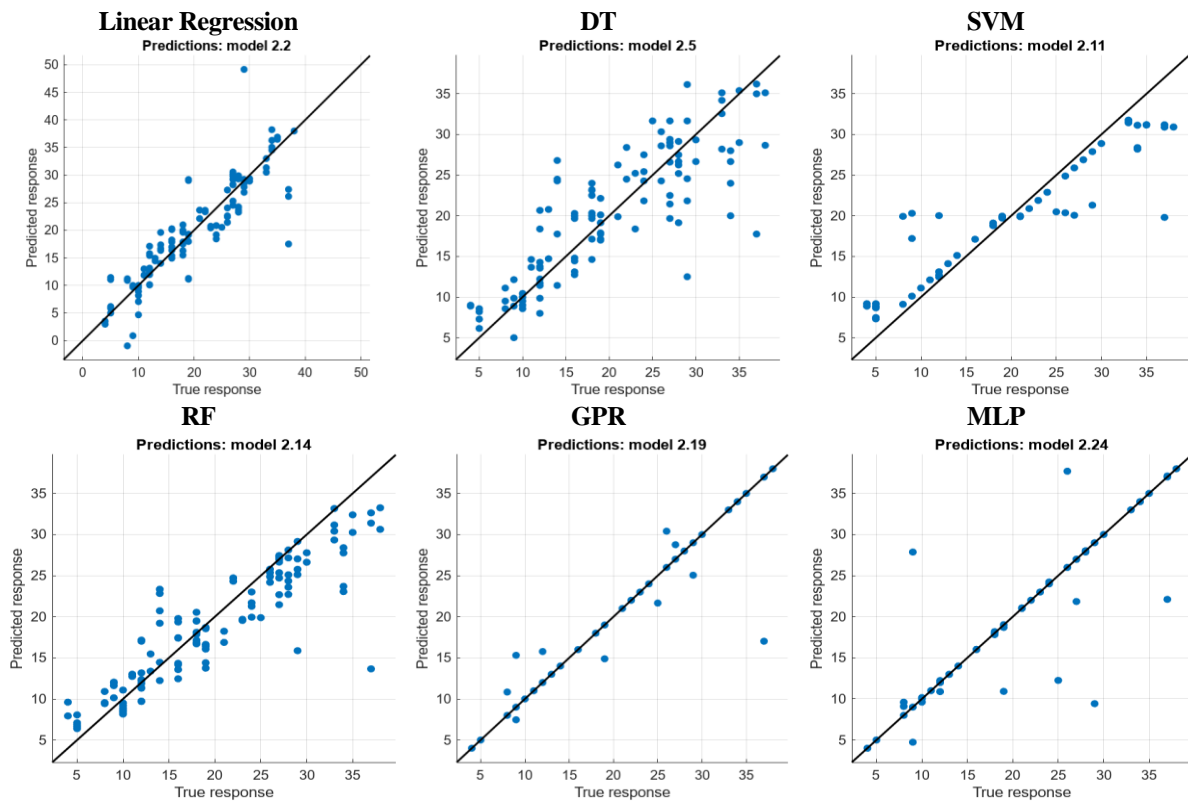


Figure 8. Prediction performance plots for tension strength

Figure 8 shows the results of the estimation performance for roughness. According to the graphs, the methods that make the estimation with maximum accuracy are GPR and MLP.

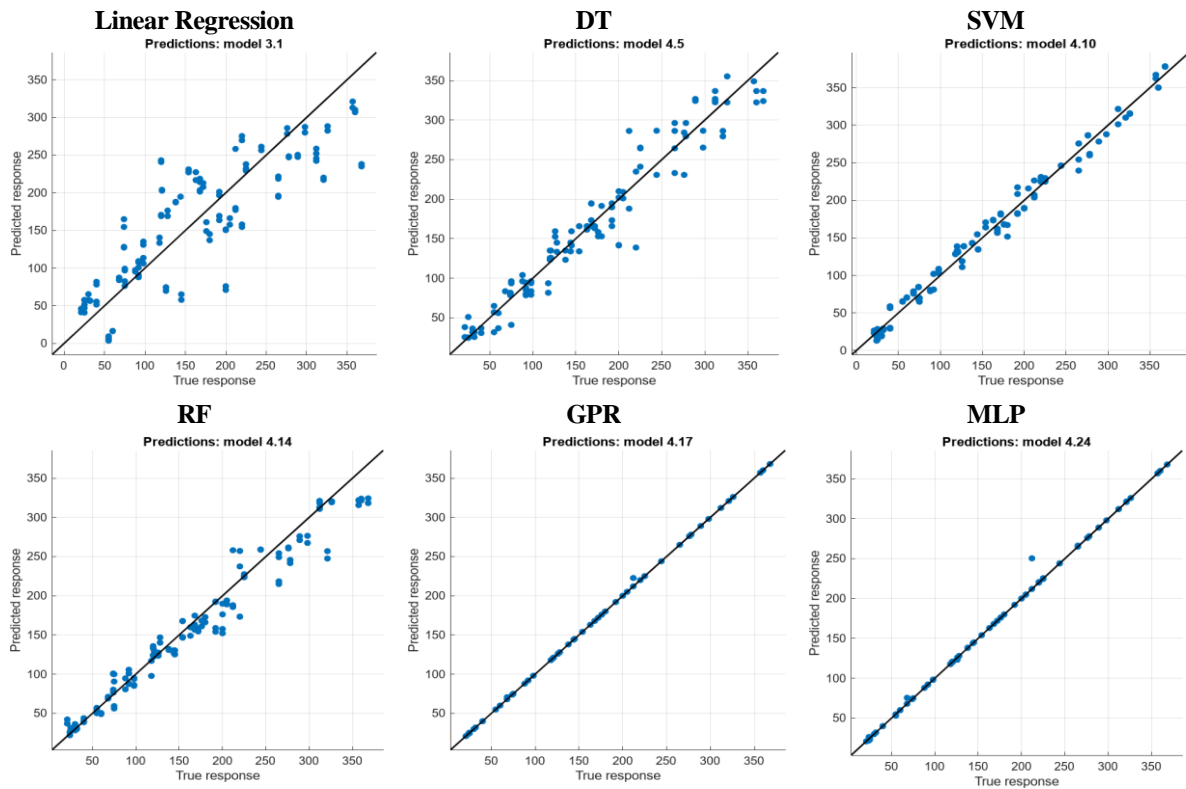


Figure 9. Prediction performance plots for roughness

In this study, only one work in the literature was identified that predicts the three performance metrics (elongation, tension strength, roughness) of parts produced using the same dataset. Table 4 was prepared to compare the results obtained using our methods with those reported by Nair et al. [27]. In their study, Nair and colleagues [27] utilized 29 different ML regression models and reported the lowest prediction errors for each output variable (elongation, roughness, tension Strength) based on Mean Absolute Error (MAE) values as follows: 0.3421 for the Elongation parameter using the Radial Basis Function Regression method, 39.2895 for the Roughness parameter using the Additive Regression method, and 5.2789 for the Tension Strength parameter using the Random Forest method.

In this study, the best prediction error values obtained for all three parameters were lower than those reported by Nair et al. Specifically, the prediction errors achieved in this study were 0.2485 for elongation (using the MLP method), 2.833 for tension strength (using the GPR method), and 1.3543 for roughness (using the GPR method).

Table 4. Performance comparison with studies using the same dataset

Parameter	Method	RMSE Value in [23]	RMSE Value in this study
Elongation	MLR	0.595	0.51526
	DT	0.732	0.36187
	SVM	-	0.23887
	RF	0.4908	0.30746
	GPR	-	0.10417
	MLP	0.5584	0.2485
	MLR	6.0349	4.911
Tension Strength	DT	11.3935	5.3234
	SVM	-	4.1156
	RF	5.8104	4.6571
	GPR	-	2.833
	MLP	10.0624	4.5639
	MLR	58.7044	51.458
	DT	68.348	24.405
Roughness	SVM	-	10.745
	RF	49.5023	21.089
	GPR	-	1.3543
	MLP	52.879	4.8427

6. Conclusion

In this study, a comprehensive machine learning-based analysis was conducted to evaluate the effects of various 3D printing parameters on the mechanical and aesthetic properties of printed outputs. Key parameters such as layer height, wall thickness, infill density, nozzle temperature, bed temperature, print speed, and fan speed were systematically varied, and their impacts on critical output characteristics, including surface roughness, tensile strength, and elongation, were assessed. The material type, particularly PLA and ABS, plays a crucial role in determining the roughness, tensile strength, and elongation of 3D-printed parts. PLA, known for its rigidity and ease of printing, typically produces smoother surfaces due to its lower melting temperature and better layer adhesion, resulting in reduced roughness. On the other hand, ABS exhibits higher elongation and better impact resistance due to its ductile nature, making it ideal for parts subjected to mechanical stresses. The choice between PLA and ABS thus directly influences the trade-offs between surface quality, strength, and flexibility, requiring careful consideration based on the intended application of the printed part.

The interplay between these parameters demonstrates the complex relationship between printing conditions and material performance, highlighting the need for fine-tuning to achieve a balance between surface quality, strength, and flexibility in 3D-printed parts.

The most successful methods in this study were estimation errors obtained using the MLP method for elongation, 0.2485, For tensile strength, it was obtained as 2.833 using the GPR method and for roughness, it was obtained as 1.3543 using the GPR method. This study demonstrates that machine learning models, particularly Gaussian Process Regression (GPR) and Multi-Layer Perceptron (MLP), provide highly accurate predictions of 3D-printed part quality. These findings highlight the potential for AI-driven optimization in additive manufacturing, reducing trial-and-error in material selection and print parameter adjustment.

7. Author Contribution Statement

The author processed the data. Interpreted the results and wrote manuscript.

8. Ethics Committee Approval and Conflict of Interest

There is no conflict of interest with any person/institution in the prepared article.

9. References

- [1] J. Park, M. Chang, I. Jung, H. Lee, K. Cho, "3D Printing in the design and fabrication of anthropomorphic hands: A review.", *Adv. Intell. Syst.*, vol. 6, pp. 1-13, 2024.
- [2] M. Sovetova, J. K. Calautit, "Influence of printing parameters on the thermal properties of 3D-printed construction structure", *Energy*, vol. 305, no. 132265, pp. 1-12, 2024.
- [3] E. S. Chen, A. Ahmadianshalchi, S. S. Sparks, C. Chen, A. Deshwal, J. R. Doppa, K. Qiu, "Machine learning enabled design and optimization for 3D-Printing of high fidelity presurgical organ models", *Adv. Mater. Technol.*, vol. 2400037, pp. 1-11, 2024.
- [4] 3D Printer Material Requirement, URL: <https://www.kaggle.com/datasets/shubhamgupta012/3d-printer-material-requirement/data>.
- [5] B. Taşar, A. Gülten, "EMG-Controlled Prosthetic hand with Fuzzy Logic Classification algorithm", vol. 321, pp. 321-341, 2017.
- [6] O. Yaman, T. Tuncer, B. Taşar, "DES-Pat: A novel DES pattern-based propeller recognition method using underwater acoustical sounds", *Appl. Acoust.*, vol. 175, no. 107859, pp. 1-13, 2021.
- [7] A. K. Tanyıldızı, "Prototype design and manufacturing of a four-legged exploration robot with a three-dimensional (3D) printer", *Int. J. 3D Print. Technol. Digit. Ind.*, vol. 7, no. 2, pp. 233-242, 2023.
- [8] H. Ma, Y. Kou, H. Hu, Y. Wu, Z. Tang, "An investigate study on the oral health condition of individuals undergoing 3D-Printed customized dental implantation", *J. Funct. Biomater.*, vol. 15, no. 156, pp. 1-12, 2024.
- [9] F. Gorski, R. Wichniarek, W. Kuczko, M. Zukowska, "Study on properties of automatically designed 3D-printed customized prosthetic sockets", *Mater.*, vol. 14, no. 18, 2021.
- [10] M. van der Stelt, M. P. Grobusch, A. R. Koroma, M. Papenburg, I. Kebbie, C. H. Slump, T. J. J. Maal, L. Brouwers, "Pioneering low-cost 3D-printed transtibial prosthetics to serve a rural population in Sierra Leone – an observational cohort study", *EClinicalMedicine*, vol. 35, pp. 1-9, 2021.
- [11] M. Mao, Z. Meng, X. Huang, H. Zhu, L. Wang, X. Tian, J. He, D. Li, B. Lu, "3D printing in space: from mechanical structures to living tissues", *Int. J. Extreme Manuf.*, vol. 6, no. 023001, pp. 1-10, 2024.
- [12] A. Zaman, J. Seo, "Design and control of autonomous flying excavator", *Machines*, vol. 12, no. 23, pp. 1-17, 2024.
- [13] O. Doğan, M. S. Kamer, "Optimum spur gear design and production with additive manufacturing method", *Bitlis Eren Univ. J. Sci.*, vol. 10, no. 3, pp. 1093-1103, 2021.
- [14] M. Yang, C. Li, H. Liu, L. Huo, X. Yao, B. Wang, W. Yao, Z. Zhang, J. Ding, Y. Zhang, X. Ding, "Exploring the potential for carrying capacity and reusability of 3D printed concrete bridges: Construction, dismantlement and reconstruction of a box bridge", *Case Stud. Constr. Mater.*, vol. 20, no. e02938, 2024.
- [15] F. T. Omigdobun, N. O. Uwagboe, A. G. Udu, B. I. Oladapo, "Leveraging machine learning for optimized mechanical properties and 3D printing of PLA/cHAP for bone implant", *Biomimetics*, vol. 9, no. 587, pp. 1-23, 2024.
- [16] M. Kasim, B. Owed, "The influence of infill density and speed of printing on the tensile properties of the three-dimension printing polylactic acid parts", *J. Eng. Sustain. Dev.*, vol. 27, no. 1, pp. 95-103, 2023.
- [17] Y. Zhang, K. Mao, S. Leigh, A. Shah, Z. Chao, G. Ma, "A parametric study of 3D printed polymer gears", *Int. J. Adv. Manuf. Technol.*, vol. 107, pp. 4481-4492, 2020.
- [18] R. J. R. Pereira, F. A. de Almeida, G. F. Gomes, "A multiobjective optimization parameters applied to additive manufacturing: DOE-based approach to 3D printing", *Structures*, vol. 55, pp. 1710-1731, 2023.
- [19] A. R. Sani, A. Zolfagharian, A. Z. Kouzani, "Artificial Intelligence-augmented additive manufacturing: insights on closed-loop 3D printing", *Adv. Intell. Syst.*, vol. 6, pp. 1-19, 2024.
- [20] O. Sevli, "Prediction of the Material to be Used in 3D Printing with Machine Learning Techniques", *Int. J. 3D Print. Technol. Digit. Ind.*, vol. 5, no. 3, pp. 596-605, 2021.
- [21] S. R. Dabbagh, O. Ozcan, S. Tasoglu, "Machine learning-enabled optimization of extrusion-based 3D printing", *Methods*, vol. 206, pp. 27-40, 2022.

- [22] V. S. Jatti, M. S. Sapre, A. V. Jatti, N. K. Khedkar, V. S. Jatti, "Mechanical properties of 3D-Printed components using fused deposition modeling: optimization using the desirability approach and machine learning regressor", *Appl. Syst. Innov.*, vol. 5, no. 112, pp. 1-15, 2022.
- [23] N. Çelik, S. Kapan, B. Taşar, "Effects of various parameters on entropy generation and exergy destruction in a coil wire inserted heat exchanger by using deep learning neural network method", *Int. Commun. Heat Mass Transf.*, vol. 161, no. 108481, 2025.
- [24] N. Çelik, B. Taşar, S. Kapan, "Performance optimization of a heat exchanger with coiled-wire turbulator insert by using various machine learning methods", *Int. J. Therm. Sci.*, vol. 192, no. 108439, 2023.
- [25] M. Li, S. Yin, Z. Liu, H. Zhang, "Machine learning enables electrical resistivity modeling of printed lines in aerosol jet 3D printing", *Sci. Rep.*, vol. 14, no. 1, 2024.
- [26] M. R. Ebers, K. M. Steele, J. N. Kutz, "Discrepancy Modeling Framework: Learning missing physics, modeling systematic residuals, and disambiguating between deterministic and random effects", *arXiv:2203.05164v2 [stat.ML]*, 2023.
- [27] A. Nair, J. Jebakumar, K. Raj, "Machine learning model selection for performance prediction in 3D printing", *J. Inst. Eng. India Ser. C*, vol. 103, no. 4, pp. 847-855, 2022.